CRANFIELD UNIVERSITY

DACKSON MASIYANO

USE OF DIFFUSE REFLECTIONS IN TUNABLE DIODE LASER SPECTROSCOPY

SCHOOL OF ENGINEERING

PhD THESIS

CRANFIELD UNIVERSITY

SCHOOL OF ENGINEERING
ENGINEERING PHOTONICS GROUP

PhD THESIS

Academic Year 2005 - 2008

DACKSON MASIYANO

Use of diffuse reflections in tunable diode laser spectroscopy

Supervisors: Dr Jane Hodgkinson, Prof Ralph Tatam

January 2009

This thesis is submitted in partial fulfilment of the requirements for the degree of Doctor of Philosophy.

© Cranfield University, 2008. All rights reserved. No part of this publication may be reproduced without the written permission of the copyright holder.

ABSTRACT

Tunable diode laser absorption spectroscopy (TDLAS) is an optical gas sensing technique in which the emission frequency of a laser diode is tuned over a gas absorption line of interest. A fraction of the radiation is absorbed by the sample gas and this can be determined from measurements of initial intensity and the intensity transmitted through the sample. The amount of light absorbed is related to the gas concentration. Additional modulation techniques combined with phase sensitive detection allow detection of very low gas concentrations (several parts per million).

The advantages of using TDLAS for trace gas sensing include; fast response times, high sensitivity and high target gas selectivity. However, the sensitivity of many practical TDLAS systems is limited by the formation of unintentional Fabry-Perot interference fringes in the optical path between the source and detector. The spacing between the maxima of these fringes, in particular those generated in gas cells, can be in the same wavelength range as Doppler and pressure-broadened molecular line widths. This can lead to (1) interference fringe signals being mistaken for gas absorption lines leading to false concentration measurements or (2) distortion or complete obscuring of the shape and strength of the absorption line, such that the sensitivity of the instrument is ultimately limited by the fringes.

The interference fringe signals are sensitive to thermal and mechanical instabilities and therefore can not be removed by simple subtraction techniques. Methods that have been proposed by previous workers to reduce the effects of interference fringes include careful alignment of optical components and/or mechanically jittering the offending components.

In general the alignment of the optical components is critical. This often leads to complex and fragile designs with tight tolerances on optical component alignment, and can therefore be difficult and expensive to maintain in field instruments.

This thesis presents an alternative approach based on the deliberate use of diffusely scattering surfaces in gas cells as a means of eliminating spurious signals due to Fabry-Perot etalons. However, their use introduced laser speckle that contributed an intensity uncertainty to gas detection measurements. A methodology for investigating the laser speckle related intensity uncertainty has been developed and confirmed. The intensity uncertainty has been quantified for the different gas cell geometries employing diffusely scattering surfaces including integrating spheres. Methods for reducing the speckle related intensity uncertainty were also investigated and are presented.

It has been shown that under the right circumstances robust gas cell designs that do not suffer from Fabry-Perot etalon effects and are relatively easy to align can be realised. The performance was found to be comparable to a conventional cell design (e.g. 3ppm detection limit for a 10cm standard cell and 11ppm for a 10cm diffusive cell). The technique could potentially simplify instrument design, thereby aiding the transfer of technology to industry.

Acknowledgements

This thesis is dedicated to the memory of my parents Mary and Overton, to whom I owe the deepest gratitude.

I would like to thank the following people for their contributions:

My academic supervisors Jane Hodgkison and Ralph Tatam for their help and guidance throughout my studies; Dan Francis for many useful discussions on speckle; and Steve Staines for his technical support.

The Hampson family, in particular, Patricia and Caroline for looking after my daughter Tiyamike.

Finally, I would like to thank my dear wife Mary and my daughter Tiyamike for their love, support and understanding over the past three years.

This work was supported by an EPSRC (Engineering and Physical Sciences Research Council) grant (GT/T04601).

Table of contents

List of Figures

List of Tables

Notation

a_{min}	minimum detectable absorbance
α_0	absorption coefficient at ν_0 corresponding to the centre of the absorption line
$\alpha(\nu)$	specific absorption coefficient with units of ppm^{-1} m^{-1}
B	detection bandwidth
B	frequency dependence of the laser excess
β	coherence factor of a speckle pattern
b_c	pressure broadening coefficient
C	gas concentration
D	diameter of illuminated area
ε	Speckle size
ε_0	objective speckle size
ε_s	subjective speckle size
F#	f-number (ratio of focal length to clear aperture of lens
I	irradiance
<I>	average intensity of a speckle pattern
i_{ex}	rms current
i_m	amplitude of the current modulation
IM-FM	intensity modulation-frequency modulation
i_0	average laser current
I_0	average brightness of a speckle pattern
$i_p(t)$	photocurrent
$I(\nu)$	output intensity
J_0	Bessel
k	Boltzmann's constant
k_v	spectral absorption coefficient
L	the distance during which the laser light interacts with the gas
m	Modulation index
η	intensity modulation index
NA	Numerical aperture
P_1, P_2	magnitudes of the first (P_1) and second harmonic (P_2)
P_0	average laser output power
$P(\nu)$	transmitted intensity after passage through an absorbing sample
$P_0(\nu)$	initial intensity
p	gas pressure
P	laser output power
P_0	initial laser power
P_{abs}	pressure of the absorbing species
P_{AP}	absorbed power
P_{ex}	defines the magnitude of the laser power fluctuations at $1Hz$ in a 1-Hz bandwidth
$\rho(I)$	probability distribution of irradiance

$\delta\theta$	correlation coefficient
Π	magnification of lens
Q	Multiplication factor
$\varphi(\nu - \nu_0)\ (m)$	the line shape function
r	Ratio of reference beam to speckle beam
RAM	residual amplitude modulation
RIN	laser relative intensity noise
R_{sh}	shunt resistance
σ	standard deviation
S	gas absorption line strength
$S(T)\ (cm^{-2}\ atm^{-1})$	temperature dependent line strength of the transition
T	transmittance given by $\ln(P_0/P)$
ν	frequency
$\nu_{\frac{1}{2}}$	absorption half width frequency
ν_0	frequency at the line centre
$\Delta\nu_D$	the Doppler full width at half maximum
$\Delta\nu_L$	Lorentzian full width at half maximum
ν_{line}	frequency at gas absorption line centre
ν_{Lm}	amplitude of the frequency modulation
$\nu_{L0}(= c / \lambda_{L0})$	average laser carrier frequency
ν_m	modulation frequency
$\Delta\nu_v$	Voigt full width at half maximum
$\delta\nu$	half-width at half-maximum (HWHM) of the absorption line
$x = \nu_{Lm} / \delta\nu$	modulation index
Y	Optical feedback parameter

Chapter 1 Introduction

This chapter begins with a description of the background to the project. This is followed by a statement of the aims and objectives of the research. An outline of the thesis is also presented.

1.1 Background to gas sensing

The need for gas detection is driven by a wide variety of reasons. Some of the important reasons include:

- Personal health and safety (e.g. some gases toxic to human health).
- Safety concerns and economic reasons in the oil and gas industry (risk of explosion, losses due to leaking gas).
- Environmental monitoring (global warming effect of green house gases e.g. Figure 1-1, carbon trading).
- Compliance with government regulations (e.g. vehicle emissions, Kyoto Protocol).

1875 photo courtesy H. Slupetzky/University of Salzburg

Figure 1-1: (a) The Pasterze, Austria's longest glacier, was about 2 kilometres longer in the 19th Century, but is now completely out of sight if viewed from Grossglockner High Road. Images taken from website[1].

Gas measurement can be used in several ways including: (a) to determine accurately the amount of gas present and (b) to simply establish the presence or absence of a particular gas. The applications that this thesis is targeting are leak detection for gas distribution companies and trace gas detection for environmental monitoring. In these applications, methane gas is one of the important gases of interest and has therefore been chosen as the target gas in this project.

1.1.1 Methane gas

Methane (CH_4) is the most abundant organic gas in the atmosphere[2]. Scientific and industrial interest in methane makes it a good candidate for a gas detection case study. Methane is a greenhouse gas with a concentration of 1.7-1.9 parts per million (*ppm*) in natural air[2]. Carbon dioxide, another major greenhouse gas, is 200 times higher in concentration at 350-370ppm. However, the Global Warming Potential (GWP*) of methane is 23 times larger over a time horizon of 100 years[3]. The global methane concentration growth rate in the atmosphere was 11.5 ppb/year for 1984–1990 and 2.8 ppb/year for 1995–2005[4]

"According to some estimates, methane is responsible for a third of current global warming, and reductions in methane emissions may be the quickest and cheapest way of slowing climate change"[5].

Methane is released into the atmosphere through natural and unnatural processes and processes resulting from human activities. The main contributors are summarised in Table 1-1.

Table 1-1: Main sources of Methane. Figures based on Wuebles[2] and references within

NATURAL PROCESSES		HUMAN ACTIVITIES	
Process	As a % of total natural processes	Process	As a % of total human contribution
Wetlands	72%	Fossil fuel extraction	29%
Termites	13%	Domestic ruminants (cattle, sheep, etc)	23%
Other	9%	Waste decomposition	17%
Oceans	6%	Rice cultivation	17%
		Biomass burning	14%
Total	160TgCH_4/year	Total	375TgCH_4/year

Natural gas comprises of mainly methane. Methane is explosive at concentrations between 5% and 15% volume in air[6]. If a leak occurs, it is considered as a safety hazard because of its explosive potential.

Leak detection and monitoring of methane is of interest for several industrial applications including natural and liquefied gas handling, storage, pipeline transport, biogas, coal mining and landfill.

Emission of methane from landfill sites provides an opportunity to use methane as a renewable source of energy. Landfill gases (LFG) are released when organic matter breaks down in the absence of oxygen.

** Is defined as the total impact over time of adding a unit of a greenhouse gas to the atmosphere[3]

Figure 1-2: (a) Leaking gas on the North Sea oil rig Piper Alpha ignited on 6 July 1988, causing a blaze in which 167 of the 226 people on board perished. Picture taken from BBC website[7].

The following figures reported in this paragraph were obtained from a website of the Department for Business and Enterprise and Regulatory Reform (BERR)[*]. Typical composition of LFG is: Methane (30-50%), Carbon dioxide (30-60%), Nitrogen; 0-10%. With 62% of domestic waste still directed to landfill, capturing and using methane is an important aspect of combating global warming. BERR estimates that methane from landfill accounted for 3% of total greenhouse gas emission in 2005 in the UK. Landfill energy production from methane made up 33% of all renewable energy in the UK compared to 8.2% from wind (in 2005).

Methane is also traded under the Kyoto protocol; this places an obligation on industries producing the gas to measure it.

1.2 Methane detection

The method of detection employed depends on the application. In the leak detection and trace concentration measurement applications the important instrument criteria are;

- Large dynamic range of detection sensitivity; in leak detection an instrument that can work at both the %LEL[†] (Lower Explosive Limit) and *ppm* (parts per million) scale is highly desirable.
- High selectivity of the target gases.
    - Immunity from cross sensitivity to other gases is important.
    - In some cases instruments that respond to both methane and ethane are desirable in natural gas detection.
- Measurement accuracy and long-term stability.

---

[*] http://www.berr.gov.uk/energy/statistics/publications/in-brief/page17222.html

[†] %LEL: A combustible gas will cause an explosion if its concentration builds up to a value above its LEL. As an illustration, methane concentration between 5% and 15% in air will explode if exposed to a flame. The LEL of methane in air is therefore taken to be 5% and a concentration of 100% LEL is equivalent to 5% volume.

- Explosion safety; the operation of the instrument must not introduce a risk of an explosion.
- Portability.
- High speed of response (< 10 seconds; in practice limited by time to fill or evacuate gas cell).
- Low cost of ownership; many instruments are required by gas distribution companies.

The methane detection techniques can be broadly categorised into optical and non optical techniques.

Optical sensors rely on the absorption of light by the target gas. Different gases absorb light of a specific wavelength (Figure 1-3). At wavelengths other than this, there is essentially no absorption. Specific gases can therefore be targeted by selecting light sources of suitable wavelength or using appropriate filters with broadband sources. The amount of absorbed light corresponds to the concentration of the gas.

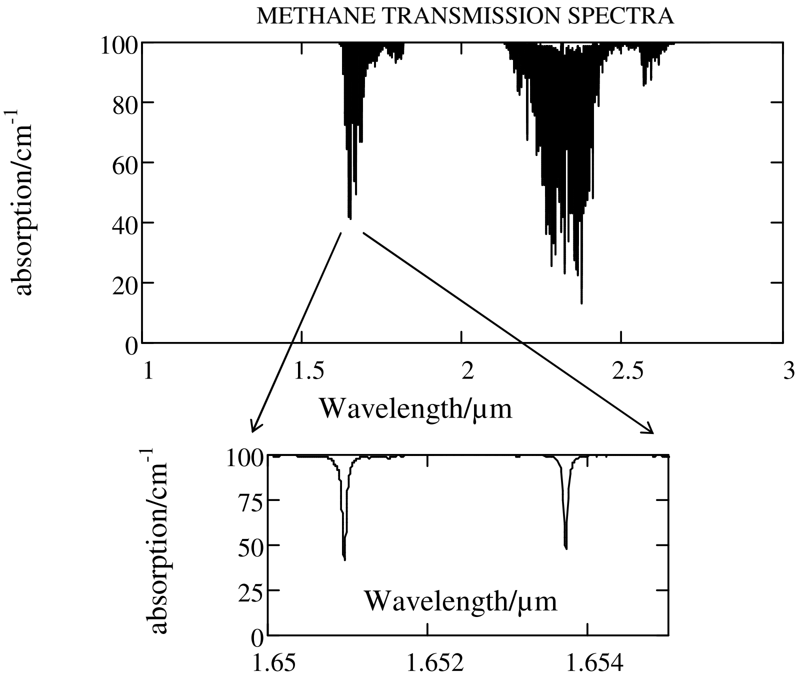

Figure 1-3: Theoretical methane (100% volume) absorption bands in the near Infrared region of the spectrum using data from the Hitran data base[8].

The principle and operation of the common detection techniques will be dealt with in detail in chapter 2; a brief introduction follows.

In the natural gas and oil industry, non optical techniques that have been traditionally used and are still in common use are the flame ionisation detectors (FIDs) and Pellistor sensors. Both the FID and Pellistor sensor provide a measure of gas concentration that is inherently related to the combustibility of the gas. Pellistor sensors are mainly used for measurements requiring accuracy on the %LEL and %volume gas scales, while the high sensitivity of the FID makes it most suitable for work on the *ppm* scale[9].

An example of a common traditional optical technique is Non Destructive Infrared (NDIR). NDIR sensors measure the absorption of infrared light. Incandescent light bulbs are often used as the light source. Wavelength selection is achieved by using appropriate wavelength filtering.

The traditional instruments briefly described above have some operational limitations that make them unsuitable for the applications that this project is targeting. The resolution of NDIR sensors is set by the bandwidth of the wavelength selection filter (typically 100nm around the chosen wavelength); and they are therefore incapable of resolving the fine structure of absorption lines. As an illustration, at atmospheric pressure and room temperature, methane absorption lines are approximately 0.04nm in width. Both the FID and Pellistor cross-respond to a variety of flammable gases and vapours and are therefore not suitable for specific species measurements; an important requirement in trace gas detection for environmental monitoring. Additionally, due to limited dynamic range the instruments have to be used in combination to cover both the %LEL (Pellistor) and *ppm* (FID) scales.

Optical absorption sensors based on tunable diode laser spectroscopy (TDLAS) can overcome some of the limitations of the conventional instruments as well as introduce new capabilities such as remote sensing[10]. A brief description of TDLAS is provided in the following section.

1.3 Introduction to gas sensors based on tunable diode laser spectroscopy

Optical absorption sensors based on tunable diode laser spectroscopy (TDLAS) have the potential to meet the instrument requirements listed in section 1.2. TDLAS works by making a measurement of a single gas absorption line (absorption lines are covered detail in section 2.3.3) at very high resolution. This is possible because the lasers employed have line widths (typically tens of Megahertz) that are typically three orders of magnitude narrower than a single gas absorption line (typically several Gigahertz at room temperature). The shape of the gas absorption line can be measured directly by scanning the laser diode wavelength across it (illustrated in Figure 1-4).

One main disadvantage of TDLAS is that the use of narrow line width (long coherence length*) lasers can lead to the formation of optical interference fringes between parallel reflecting surfaces in the optical path. The formation of fringes is shown in Figure 1-5.

---

* The mean length over which interference effects can be observed in the axial direction

Fringes occurring in the sensing path will appear in the measured spectrum and may be interpreted as the gas absorption signal itself. If the interference fringe signal is larger than the detector noise, it becomes the limiting factor of the detection sensitivity.

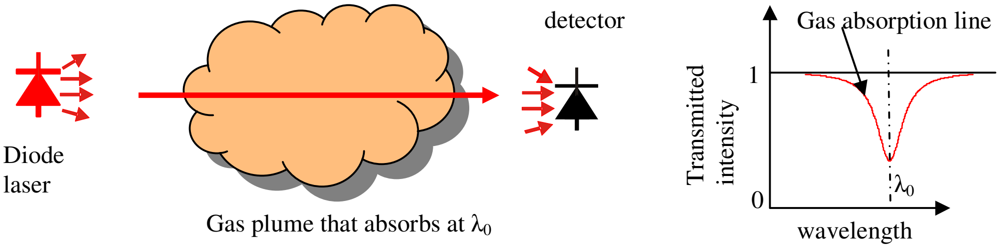

Figure 1-4: Principle of optical absorption.

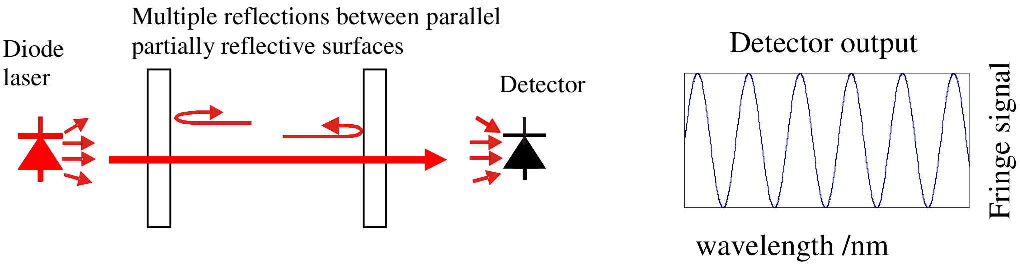

Figure 1-5: Illustration of formation of interference fringes: reflections from parallel surfaces can lead to formation of a periodic signal at the detector.

Indeed, the sensitivity of many practical TDLAS systems is limited by the formation of unintentional Fabry-Perot interference fringes in the optical path between the source and detector[11,12]. Thermal and mechanical instabilities mean that fringes can not be removed by simple subtraction.

A number of techniques for eliminating or reducing the amplitude of the fringe signal exist. The operation and limitations of these techniques are discussed in detail in chapter 2.

In general, these measures are effective in limited circumstances, add to instrument complexity and/or can be difficult to maintain in field instruments. This results in instruments that are complex, expensive and sensitive to misalignment.

In recent years, there has been interest in using diffuse reflections within the optical path in the following diverse areas; use of remote laser pointer style gas detectors where the light is backscattered from a rough surface at ground level[13-15] and use of integrating spheres as multi-path gas cells[16-19].

This project will take this concept further by investigating the deliberate use of diffuse reflections in TDLAS, known in some circumstances to reduce interference fringes[18]. This approach has several potential benefits.

- Improved detection sensitivity.
- Reduced complexity and costs in instrument manufacture.
- Making systems less susceptible to misalignment thereby increasing field robustness.

However, the use of diffuse reflections introduces laser speckle that can contribute a random, rather than periodic, uncertainty to gas detection measurements.

Speckle is formed when an optically rough surface (surface with height deviations comparable to the illuminating wavelength) is illuminated by a coherent and monochromatic light source such as a laser; the reflected components interfere and the surrounding region is filled with a complex interference pattern.

The formation of laser speckle is illustrated in (Figure 1-6).

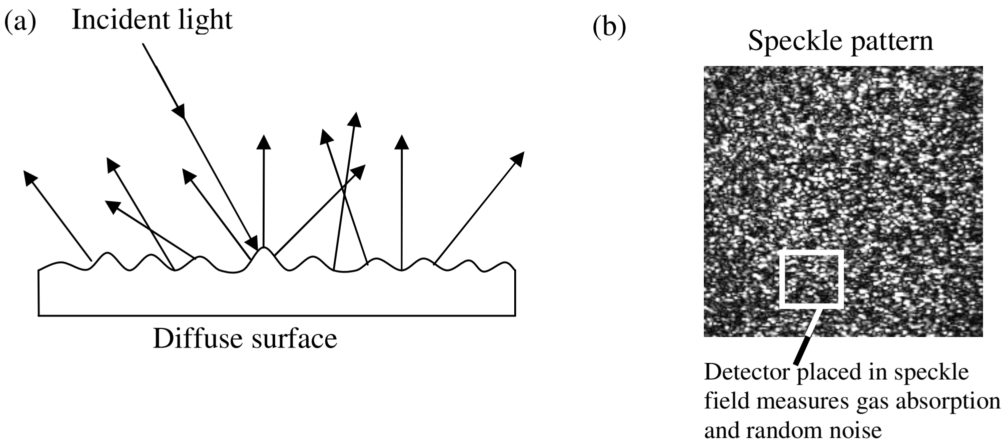

Figure 1-6: (a) diffuse reflection of light caused by an optically rough surface. (b) Speckle pattern; bright spots and dark spots correspond to where the interference has been highly constructive and destructive respectively.

Intensity measurements of a speckle field have an intensity uncertainty associated with the speckle.

1.4 Thesis Objectives

This research program is focused on investigating the use of diffuse reflections in TDLAS in the optical path between the source and the sensor as a means of reducing the effects of interference fringes. The TDLAS modulation scheme employed in this project is Wavelength Modulation Spectroscopy (WMS). Methane was chosen as the gas for the case study because of its importance to both the environmental monitoring and natural as leak detection applications. The specific aims of the project are outlined below.

- Developing an understanding of both the potential and limitations of WMS.

- Developing a standard WMS methane detection system with a target detection sensitivity of approximately 2 *ppm.* This is the background atmospheric concentration of methane.
- Investigating the use of diffuse reflections in TDLAS by;
    - Developing a good understanding of speckle theory.
    - Developing a theoretical framework for conducting speckle related investigations.
    - Developing a methodology for investigating the use of diffuse reflections in TDLAS and conducting experimental investigations of the use of diffuse reflections in TDLAS.
    - Design and evaluation of gas cells utilising diffuse reflections.

1.5 Thesis outline

Chapter 2 reviews methane detection methodology. Optical and non optical techniques that are commonly used to detect methane are described. The merits and demerits of the different techniques are also discussed. Among the optical techniques considered in this thesis, particular attention will be paid to those based on TDLAS. Several TDLAS techniques are considered including a detailed analytical treatment of WMS. WMS is one of the widely implemented forms of TDLAS and is also implemented in this project. Justification for implementing WMS is presented. Noise sources influencing the detection limit of WMS are discussed and evidence is presented to show that WMS is limited by interference fringes. The operation and limitations of current techniques employed to reduce the interference fringes are discussed.

The purpose of Chapter 3 is to establish a theoretical framework for investigating the use of diffuse reflections (speckle effects) in TDLAS. A detailed review of relevant speckle theory is presented. The properties of speckle that influence the speckle related intensity uncertainty are considered. Additionally, conditions under which speckle can give rise to interference effects are investigated.

Chapter 4 is concerned with experimental investigation of the implications of the theoretical framework developed in Chapter 3 on the use of diffuse reflections in TDLAS. A methodology for investigating the consequent introduction of intensity uncertainty associated with laser speckle that is developed is presented. A systematic experimental study of the use of diffuse reflections in TDLAS is reported.

The results obtained in this chapter will be used in designing and evaluating the performance of a diffuse gas cell for use in a TDLAS instrument.

The development of a WMS instrument is covered in Chapter **5**. The various design stages are reported. Experimental work conducted to characterise and evaluate the performance of the instrument is also presented in this chapter.

Chapter 6 reports a systematic investigation of the interferometric effects caused by optical feedback (i.e. where a portion of the laser emission is feedback into the laser cavity). To the author's knowledge, this is the first time such a systematic study of the interferometric effects due to optical feedback has been reported in TDLAS.

The focus of Chapter 7 is on the design and evaluation of gas cells employing diffusive surfaces. The designs are based on the knowledge developed in chapter 4. A comparison of the performance of the gas cells with standard cells is presented.

Chapter 8 investigates the feasibility of using integrating spheres as multipass optical cells in TDLAS. An integrating sphere is a spherical cavity with highly reflective surfaces that is used to contain and diffuse input light so that it is evenly spread over the entire surface area of the sphere. When used as a gas cell, the high reflective coating of the internal sphere surface allows multiple reflections through the sample and results in an equivalent absorption path length much larger than the diameter of the sphere.

A discussion and conclusion of the thesis is given in Chapter 9**.** Also presented in this Chapter are suggestions for further work. This is followed by a list of publications arising from this research and appendices.

1.6 References

[1] Gary Braasch Photography, *Glaciers and Glacial Warming, Receding Glaciers* [Web Page] (Available at http://www.worldviewofglobalwarming.org/pages/glaciers.html, accessed 1 November 2009).

[2] Wuebbles, D. J. and Hayhoe, K. (2001), 'Atmospheric methane and global change', *Earth-Science Reviews*, V57, pp. 177-210.

[3] Watson R T 2001 *Climate Change 2001: Synthesis Report. A Contribution of Working Group 1, 2 and 3 to the Third Assessment Report of the Intergovernmental Panel on Climate Change* (New York: Cambridge University Press).

[4] Nikiforova O Yu, Kapitanov V A and Ponomarev Yu N 2008 *Applied Physics B: Lasers and Optics* **20** 263.

[5] F. Pearce (2006), 'Kyoto promises are nothing but hot air', *New Scientist.*, V 190, N2557, pp. 10.

[6] Coward H F and Jones G W 1952 *Bulletin 503* (Washington: US Govt Printing Office).

[7] *1988: Disaster in the North Sea* [Web Page] (Available at http://news.bbc.co.uk/onthisday/hi/witness/july/6/newsid_3036000/3036510.stm, accessed 1 November 2009).

[8] Rothman *et al,* L. S (1992), 'The HITRAN molecular database: editions of 1991 and 1992', *Journal of Quantitative Spectroscopy and Radiative Transfer*, V48, pp. 469–507.

[9] Fackrell, J. E. (1980), 'A flame ionisation detector for measuring fluctuating concentration', *Journal of Physics E (Scientific Instruments)*, V13, N8, pp. 888-93.

[10] Uehara, K. and Tai, H. (1992), 'Remote detection of methane with a 1.66-um diode laser', *Applied optics*, V31, N6, pp. 809-813.

[11] Schiff H I, Mackay G I and Bechara J 1994 *Air Monitoring by Spectroscopic Techniques* Editor Sigrist M W (New York: John Wiley and sons) pp 239-333.

[12] Nadezhdinskii, A. and others (1999), 'High sensitivity methane analyzer based on tuned near infrared diode laser ', *Spectromica Acta Part A*, V55, N10, pp. 2083-2089.

[13] Iseki, T., Tai, H., and Kimura, K. (2000), 'Portable remote methane sensor using a tunable diode laser', *Measurement Science and Technology*, V11, N6, pp. 594-602.

[14] van Well, B., Murray, S., Hodgkinson, J., Pride, R., Strzoda, R., Gibson, G., and Padgett, M. (2005), 'An open-path, hand-held laser system for the detection of methane gas', *Journal of Optics A: Pure and Applied Optics*, V. 7, pp. 420-4.

[15] Frish M B, Wainner R T, Green B D, Laderer M C and Allen M G 2005 *Infrared to Terahertz Technologies for Health and the Environment, Oct 24-25 2005* 6010

Proceedings of SPIE - The International Society for Optical Engineering (Boston, MA, United States: International Society for Optical Engineering, Bellingham WA, WA 98227-0010, United States) p 60100.

[16] Abdullin, R. M. and Lebedev, A. V. (1988), 'Use of an integrating sphere as a multipass optical cell', *Soviet Journal of Optical Technology*, V55, N3, pp. 139-41.

[17] Tanaka H, Matsuura M, Tai H and Uehara K Tokyo Gas Co, LTD Tokyo Japan (13 April 1993), *Gas Detection Device*. USA. 5202570.

[18] Tranchart, S, Bachir, I. H., and Destombes, J-L. (1996), 'Sensitive trace gas detection with near-infrared laser diodes and an integrating sphere', *Applied Optics*, V35, N36, pp. 7070-7074.

[19] Hawe, E. and others (2007), 'An investigation into the use of an integrating sphere as a gas absorption cell', *Journal of Applied Optics A: Pure and Applied Optics*, V9, pp. S12-S18.

Chapter 2 Methane Detection methodology

The importance of detecting methane has been previously discussed in Chapter 1. This chapter describes the common non optical and optical gas detection techniques that are used for methane detection.

2.1 Non optical techniques

The non optical techniques described in the following paragraphs are flame ionisation detectors (FID), catalytic sensors and solid state sensors.

2.1.1 Flame ionisation detectors (FID)

The FID is based on the measurement of changes in the number of ions generated in a hydrogen/air diffusion flame due to the presence of trace quantities of organic compounds. It was first described by McWilliam in 1958[1]. The detector is still commonly used for the quantification of organic compounds in gas chromatography experiments and in portable gas leak detection instruments today.

The FID responds to most compounds that contain carbon. A typical FID instrument consists of a hydrogen/air flame and a collector plate (Figure 2-1).

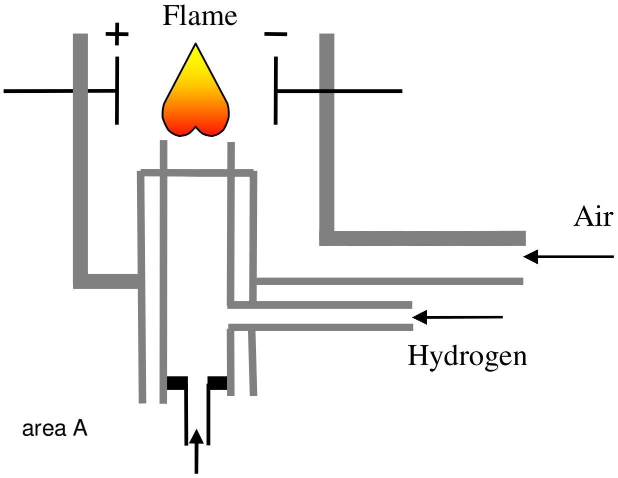

Figure 2-1: Schematic diagram of a Flame Ionisation Detector.

The sampled gas is burned in the flame. The organic compounds are reduced into carbon fragments and become ionised. The ions are collected on a biased electrode above the flame. The generated current is measured across the collector and the metal jet. This signal is amplified for subsequent processing. The FID is extremely sensitive (1 to 50,000ppm[2]) and linear over many orders of magnitude (between 3 and 5[3]).

The disadvantages are that it destroys the sample and instruments are complex - they need hydrogen and a stable environment for the flame. The technique is non selective between organic compounds.

2.1.2 Catalytic sensor

Flammable gas sensors are in common use in oil and gas plants, both onshore and offshore. They are used to detect combustible gases such as methane. They are designed to set off warning signals if the combustible gases accumulate to explosive levels.

Traditionally, the catalytic sensor or Pellistor has been employed for this type of detection. The Pellistor is a miniature calorimeter used to measure the energy liberated on oxidation of a combustible gas[4]. The combination of high heats of oxidation and a ready supply of oxygen make catalytic sensors very suitable for monitoring flammable gases in air.

Many Pellistor beads consist of a coil of fine platinum wire surrounded by porous alumina. Pellistors are manufactured as pairs, a sensitive (or catalytically active) element and a non-sensitive (or compensating) element[4]. The sensitive and the compensating elements are treated with catalysts that enhance and inhibit oxidation respectively. The bead is heated by passing a current through the platinum wire coil to a temperature (around 500°C) at which oxidation occurs at the sensitive element. The oxidation results in further temperature increase, with a consequent increase in the resistance of the platinum coil in the sensitive element. This leads to a difference in resistance between the two beads and for most gases, this output change is linear with concentration. A Wheatstone Bridge circuit is often employed to sense this difference in temperature[4]. The sensitive element therefore responds to gas whilst the compensating element allows for the effect of environmental change. Figure 2-2 shows a typical Wheatstone bridge circuit for detecting a change in resistance**.**

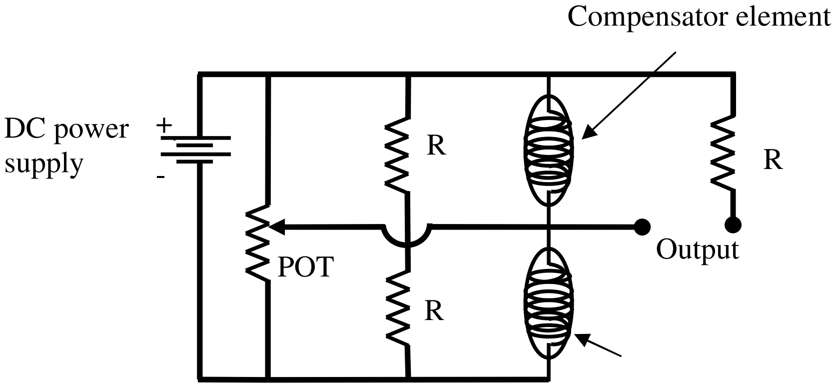

Figure 2-2: A typical Wheatstone bridge circuit for detecting a change in resistance. After Jones[4]. Key: R, resistance; POT, variable resistor.

The sensors have a long life but are considered to have the following disadvantages:

- Pellistor sensors are not very sensitive. They are typically used for measurements requiring accuracy on the %LEL (lower explosive limit, with 5% methane concentration corresponding to 100% LEL) and %VOL (volume) scale[5]. They are unreliable to be used on the *ppm* scale due to short term drift.
- Pellistors are 'poisoned' by contaminating chemicals (e.g. silicones, sulphur compounds, chlorine compounds, heavy metals)[6]. These chemicals react with the catalyst during oxidation causing an inert layer to build up on the bead surface resulting in degradation of the sensor. They are also irreversibly damaged by water.
- Pellistor sensors cross-respond to a variety of flammable gases and vapours.

2.1.3 Metal oxide semiconductor (solid state)

Solid state sensors exploit the phenomenon of electrical conductivity changes induced in semiconducting materials by adsorption of gases on the solid surface[7]. The solid state sensor is often made up of a tin oxide bead that is formed around two thin coils of platinum wire. Heating the bead using one of the coils results in oxidation of the gas on the bead surface. This has the effect of changing the electrical conductivity as measured between the heated and unheated coils. This sensor responds to many oxidisable gases. The sensors are attractive because they are inexpensive, rugged and show high sensitivity to some gases.

The main disadvantages of the solid state sensor are:

- Sensors have poor gas selectivity
- Sensor instability and irreproducibility leads to difficulty in the interpretation of positive readings and the potential for false positive alarms[8].
- Sensors are effective over a limited range of relative humidity. As humidity increases, sensor output increases as well. Water vapour affects both the conductance in air and sensitivity to other gases[7].
- Response to gases is nonlinear as a function of concentration[7].
- Sensor response times are very temperature dependent (being shorter at high temperatures)[7].

2.2 Optical absorption spectroscopy

In this section the underlying principle of optical absorption spectroscopy is outlined, and a discussion of gas absorption lines with emphasis on methane absorption lines is given.

2.2.1 Fundamentals of optical absorption spectroscopy

Many gases have useful characteristic absorption lines throughout the electromagnetic spectrum. Gas molecule absorption spectra can be classified into three separate types of spectra: rotational, vibrational, and electronic spectra. Selection of an optimal wavelength region for gas measurement is application specific and is based on a variety of parameters that includes strength of absorption, avoidance of spectral interferences from other gases, availability of light sources, and the detection requirements. Table 2-1 below shows the regions of the electromagnetic spectrum and the associated spectroscopic techniques.

Table 2-1: Regions of the electromagnetic spectrum and the molecular processes associated with each region as defined by Banwell and McCash[9]

	FREQUENCY	**WAVELENGTH**	**TRANSITION**	**SPECTROSCOPY TECHNIQUE**
Radio frequency region	3×10^{6}-3×10^{10}Hz	10m-1cm	Reversal of spin of a nucleus or electron	Nuclear magnetic resonance(n.m.r) or Electron spin resonance (e.s.r)
Microwave region	3×10^{10} - 3×10^{12}Hz	1cm-100μm	Transitions between different rotational levels	Rotational spectroscopy
Infra-red region	3×10^{12} - 3×10^{14}Hz	100μm-1μm	molecular vibrational modes	Vibrational spectroscopy
Visible and ultra-violet	3×10^{14} - 3×10^{16}Hz	1μm-10nm	Transitions between energies of valence electrons	Electronic spectroscopy
X-ray	3×10^{16}-3×10^{18}Hz	10nm-100pm	Energy changes involving inner electrons of atoms or molecules	

Many optical techniques concentrate on transitions in gases in the near (0.8-2.5μm) to mid infrared (2.5-14μm) regions of the spectrum. The transitions are due to molecular bond vibrations combined with rotational "fine structure". The optical techniques can be grouped according to;

- Techniques that measure the intensity of the transmitted beam (illustrated in Figure 2-4) at the wavelengths characteristic of a particular target gas. Two in common use are non-dispersive infrared (NDIR) and tunable diode laser absorption spectroscopy (TDLAS).
- Techniques based on what happens to the absorbed or scattered photon.
  - Temperature and pressure change in the gas (e.g. photothermal and photoacoustic spectroscopy).

- Re-emission or scattering at a different wavelength (e.g. fluorescence, Raman spectroscopy).

Molecules of gas only absorb energy at specific wavelengths (gas absorption lines) in the electromagnetic spectrum. Figure 2-3 below shows methane transmission spectra in the 1.65μm region.

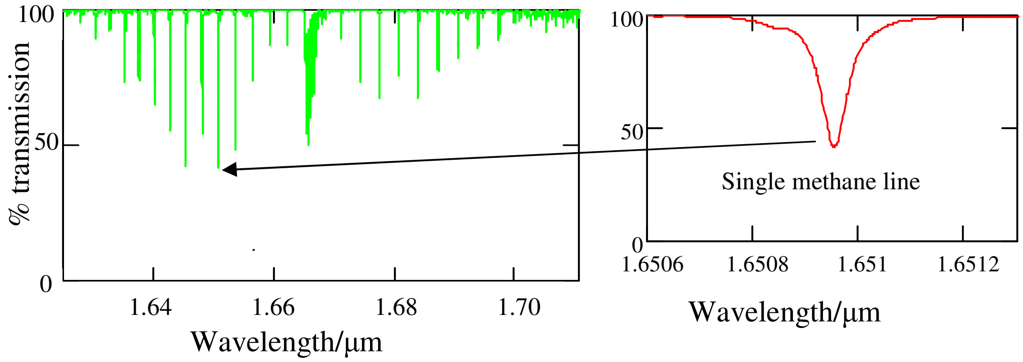

Figure 2-3: Theoretical methane (100% volume) transmission spectrum in the 1.65μm region using data from the Hitran data base [10]. The pathlength is 1cm.

The basic principle of absorption-based gas detection is shown in Figure 2-4 in which a transmission-type sensor is illustrated. When a laser beam of frequency ν and intensity $P_0(\nu)$ passes through a gas sample, the output intensity $I(\nu)$ may be expressed according to Beer-Lambert law[9] as

$$P(\nu) = P_0(\nu)\exp[-\alpha(\nu)CL] \tag{2-1}$$

where C is the gas concentration in ppm (parts per million), L is the distance over which the laser light interacts with the gas conveniently expressed in metres m**,** the constant $\alpha(\nu)$ with units of ppm^{-1} m^{-1} represents the specific absorption coefficient due to gas absorption. The concentration-path length product CL is sometimes referred to as the absorption factor or optical depth.

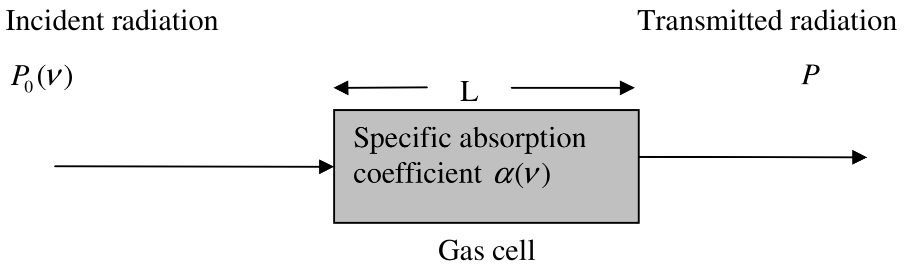

Figure 2-4: Illustration of Beer's Law.

The amount of light absorbed is usually measured by transmittance $T = P / P_0$. For single wavelength light sources and at low gas concentration the term $\exp[-\alpha(\nu)CL]$ is approximately equal to $1-\alpha(\nu)CL$ such that transmittance can be expressed as

$$T = \exp[-\alpha(\nu)CL] \cong 1-\alpha(\nu)CL \qquad \textbf{(2-2)}$$

Equation (2-2) is often expressed as absorbance; $A = \ln(1/T)$.

$$A = \alpha(\nu)\, CL \qquad \textbf{(2-3)}$$

This is a more convenient form as the relationship between absorbance and concentration, *C,* is linear.

2.2.2 Absorption line shapes

Characteristics that are important in atmospheric measurements are the gas absorption line strength (*S*), and the line shape and width. The width and shape of the gas absorption lines depend on both the temperature and pressure. For some gases, the lines are well separated under normal atmospheric pressures and temperatures. The absorption lines of other molecules are broadened by pressure resulting in an overlap of the lines (Figure 2-5). Overlapping lines from different gases can lead to cross interference in high resolution spectroscopy measurements.

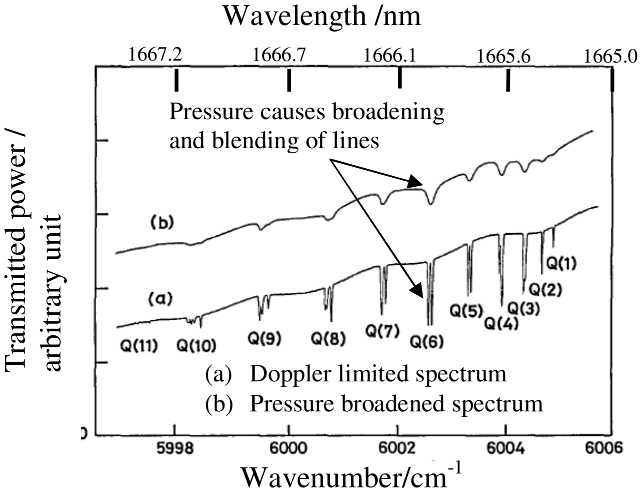

Figure 2-5: Absorption spectra of the Q branch of the $2\nu_3$ band of methane obtained by Uehara[11]. (a) Low pressure or Doppler limited spectrum and (b) atmospheric pressure (Lorentzian) . The spectrum was obtained by temperature tuning a 1.66µm DFB laser. The methane pressure was 4 Torr in both traces but 1-atm air was added in (b). The absorption cell length was 50cm, and (b) was deliberately shifted upward for clarity.

The product of the specific absorption coefficient $\alpha(\nu)$ and concentration C is termed the spectral absorption coefficient k_ν in m^{-1}. The spectral absorption coefficient is related to the pressure of the absorbing species P_{abs} (*atm*), the temperature dependent line strength of the transition *S(T)* (cm^{-2} atm^{-1}), and the line shape function $\varphi(\nu-\nu_0)$ (*m*) according to the following relationship[12].

$$k_\nu = P_{abs} S(T)\varphi(\nu-\nu_0) \qquad \textbf{(2-4)}$$

The dependence of the line shape and width on temperature and pressure is usually grouped into three pressure regimes; Doppler broadening, pressure broadening and the Voigt regime.

Doppler broadening is due to the random thermal motion of the gas molecules and is dominant at pressures below about 10 Torr. The line shape of a Doppler broadened line is a Gaussian function that depends on the linewidth $\Delta\nu_D$ (defined as the full width at half maximum).

$$\Delta\nu_D = 7.16\times10^{-7}\nu_0(T/M)^{1/2} \qquad \textbf{(2-5)}$$

where ν_0 is the frequency at the line centre; T, the temperature in Kelvin; and M, the molecular mass[13]. For example, methane (M=16, ν_0=6057cm^{-1} or 1651nm) at a temperature of 298K has $\Delta\nu_D$= 18.7×10^{-3}cm^{-1}. At the line centre the specific absorption coefficient $\alpha(\nu)_0$ of a Doppler broadened line is given by[13]

$$\alpha(\nu_D)_0 = 0.94\times S(T)/\Delta\nu_D \qquad \textbf{(2-6)}$$

from which the absorption cross section of gases of interest can be calculated to lie in the range 10^{-18}-10^{-16}cm^{-2}molecule^{-1}.

Pressure broadening generally applies to pressures above 100 Torr. The line shapes and widths are governed by collision-induced broadening and the line shape is defined by a Lorentzian function. For a given temperature, the linewidth $\Delta\nu_L$ increases linearly with pressure

$$\Delta\nu_L = 2b_c p \qquad \textbf{(2-7)}$$

Where *p* is the gas pressure; and b_c is the pressure broadening coefficient. At the line centre the specific absorption coefficient $\alpha(\nu)_0$ of a pressure broadened line is given by

$$\alpha(\nu_L)_0 = 2S(T)/\pi\Delta\nu_L = S(T)/\pi b_c p \qquad \textbf{(2-8)}$$

Pressure broadened linewidths are typically on the order of 0.1cm^{-1} (3GHz) at atmospheric pressure. This is approximately 1-2 orders of magnitude larger than purely

Doppler limited linewidths. Pressure broadening results in much smaller peak specific absorption coefficients and in progressive overlapping and blending of the molecular absorption lines of many large molecules[13] (Figure 2-5). This limits the measurements to light molecules (diatomic e.g. NO or CO or light polyatomic e.g. CH_4 or NH_3). Due to absorption of atmospheric pressure broadened lines of some gases such as H_2O and CO_2, which are present in large concentrations (e.g. approximately 370ppm for CO_2, compared to 2ppm for methane), measurements are further limited to so called windows (spectral regions free of H_2O and CO_2).

In the pressure region between 10 and 100 Torr or at altitudes between 10 and 40km, designated as the Voigt regime, the line shape and width are described by a convolution of Doppler and pressure broadened line shapes[13]. The Voigt regime linewidth is computed numerically and can be approximated (to a claimed accuracy of 2 parts in 10,000) by[14]

$$\Delta \nu_v = C_1 \Delta \nu_L + (C_2 \Delta \nu_L{}^2 + \Delta \nu_D{}^2)^{1/2} \qquad \textbf{(2-9)}$$

where $C_1 = 0.5346$ and $C_2 = 0.2166$. At the line centre the specific absorption coefficient $\alpha(\nu)_0$ of a pressure and collision broadened line is given by

$$\alpha(\nu_v)_0 = \frac{S(T)}{2\Delta \nu_v (1.065 + 0.447x + 0.058x^2} \qquad \textbf{(2-10)}$$

Typical linewidths for atmospheric species in the Voigt pressure regime fall in the range 5×10^{-3} to $5\times10^{-2}cm^{-1}$ (150-600 MHz). This is smaller than the spacing of rotational lines of many molecules of interest; therefore operation in this regime increases sensitivity and specificity and allows measurements in the spectral regions where H_2O and CO_2 have strong absorptions[13]. The disadvantage is that measurements are limited to point sampling because of the need for a vacuum pump, or high altitudes.

The pressure regime that applies to this work is the atmospheric pressure broadened regime. The gas measurements will be performed at atmospheric pressure on the light polyatomic molecule methane around 1650nm.

2.2.3 Methane absorption lines

Most gas molecules including methane have fundamental bands of vibrational transition in the mid-infrared (2-14μm) region, whereas overtone and combination bands lie in the near infra-red (0.75-2μm) region. The tetrahedral CH_4 molecule has four fundamental vibrational modes (Figure 2-6).

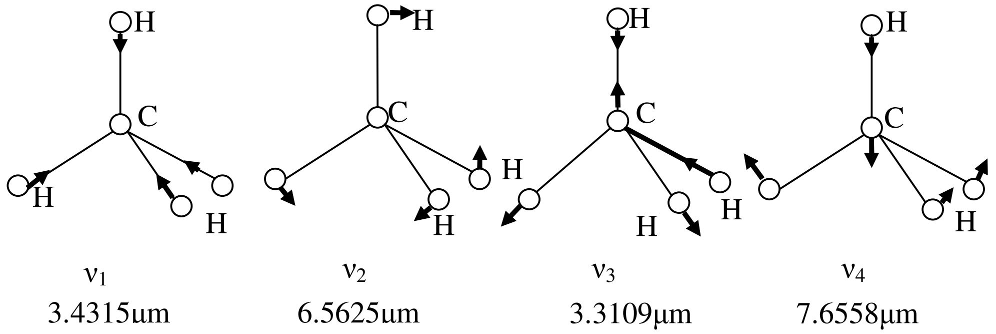

Figure 2-6: Four fundamental vibration modes of the CH_4 molecule. After Ikegami *et al*[15].

In general, the fundamental bands have much stronger absorption intensities than the overtone bands. The strongest methane vibrational absorption bands are the fundamental bands centred at 3.3μm and 7.6μm. The strongest band of methane below 2 μm is the $2\nu_3$ band (an overtone of ν_3 at 3.3μm illustrated in Table 2-2 and Table 2-3), whose centre is located at 1.665 μm and whose absorption strength is approximately 25 times smaller than the fundamental 3.392 μm[11]. This band occurs in a spectral region relatively free of water and other interferences making it a good potential candidate for CH_4 measurement. Vibrational overtone line strengths in the near infrared are approximately two to three orders of magnitude lower compared to the fundamental lines in the mid infrared region[16].

In the near infra red region, diode lasers can be fabricated to a specific wavelength at a relatively low cost. Near infra red diode lasers have the advantages of single-longitudinal mode output at milliwatt power and room temperature operation. In addition the benefits from availability of fibre optic technology and inexpensive auxiliary equipment, such as thermoelectric coolers, lenses, low noise current drivers and detectors primarily developed for the telecoms industry outweigh the disadvantage of working with the weaker overtone and combination bands.

The strong methane absorption lines below 2μm are listed in Table 2-2 below and those of the $2\nu_3$ band around 1.65μm are listed in Table 2-3.

The relative magnitudes of the R0-R4 branches of the $2\nu_3$ band of Methane around 1650nm are illustrated in Figure 2-7 below. The laser diode used in this project can access the R3 and R4 branches of the $2\nu_3$ band of methane. The individual lines of the R4 branch (shown in Table 2-3) overlap at atmospheric pressure to give the appearance of a single line (Figure 2-7).

Table 2-2: The overtone band classification in the 2µm region as suggested by Norris and Unger[17]

BAND µm	WAVENUMBER cm^{-1}	CLASSIFICTION
1.1350	8800	$\nu_1 + 2\nu_3 = 8819 cm^{-1}$
1.1620	8606	$3\nu_3 = 8661\ cm^{-1}$
1.1873	8423	$2\nu_1 + 2\nu_4 = 8434 cm^{-1}$
1.3305	7516	$\nu_2 + 2\nu_3 = 7548 cm^{-1}$
1.6645	6008	$2\nu_3 = 6028\ cm^{-1}$
1.7335	5769	$\nu_1 + \nu_2 + \nu_4 = 5737\ cm^{-1}$
1.7898	5587	$\nu_1 + 2\nu_4 = 5521 cm^{-1}$

Table 2-3: The R branch classification of the 2v3 band of methane in the 1.65µm region as suggested by Margolis[18]

BRANCH	WAVENUMBER /cm^{-1}	WAVELENGTH/nm	STRENGTH OF BRANCH @296K $10^{-3}cm^{-2}atm^{-1}$
R0	6015.66435	1662.326789	14.39
R1	6026.22743	1659.412977	14.12[1]
R2	6036.65362	1656.546926	30.84
	6036.65841	1656.545612	
R3	6046.94195	1653.72846	77.84
	6046.95275	1653.725507	
	6046.96474	1653.722228	
R4	6057.07779	1650.961131	96.59
	6057.08609	1650.958869	
	6057.09977	1650.95514	
	6057.12733	1650.947628	

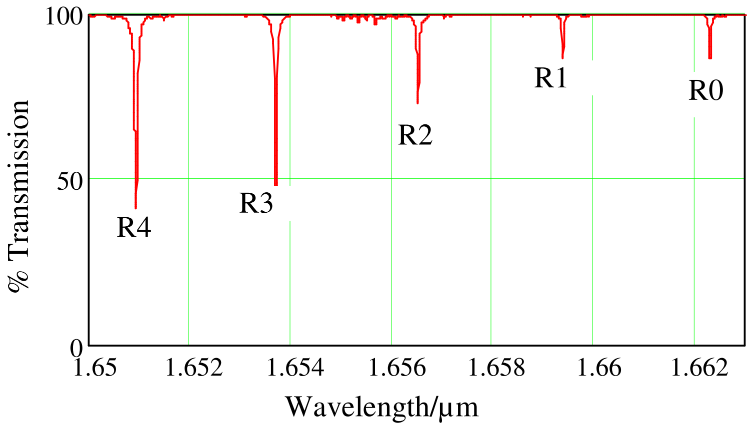

Figure 2-7: Theoretical Methane transmission spectra of the R branch of the $2\nu_3$ band of methane in the 1.65μm region as obtained from the Hitran database[10].

In the past, the laser sources used for absorption measurements were not stable enough to provide a high signal to noise ratio*[19,20]. Lack of adequate laser frequency stabilisation necessitated frequent calibration of the systems' response whilst multimode behaviour led to nonlinearities in the response[19]. This led to the popularity of other techniques such as flame ionisation and photo-acoustic spectroscopy (using broad band light sources) in trace analysis. Now however, single longitudinal mode semiconductor lasers are readily available and there emission frequency can be stabilised using their operating current or temperature.

In the following sections, optical absorption techniques that are in common use, particularly those employing tunable diode lasers, are discussed.

2.3 Non dispersive infra red (NDIR)

The technique is 'non-dispersive' because it does not resolve the spectrum. Narrow-band optical filters are used to select an absorbing region of the spectrum[21]. NDIR is typically used in the mid IR where signal strengths are very high. Filament lamps or light emitting diodes are used as light sources and are often modulated either mechanically or electronically. A schematic diagram of a basic NDIR sensor is shown in Figure 2-8.

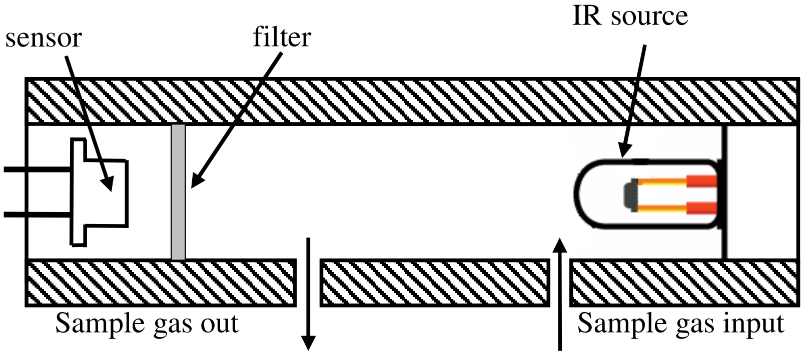

Figure 2-8: Schematic diagram of an NDIR sensor. After SIRA Technology LTD[21]

A reference beam derived from a second filter with a pass band at a different wavelength from the measurement wavelength, such that it is not absorbed by the target gas, can be used to correct for variations in the source intensity, detector efficiency and the performance of the optics[21].

The advantages are that the technique is simple to implement and the cost is low to moderate. The disadvantages include:

- Light source and detector both subject to drift.

---

* In this case defined as the ratio of measured quantity to the spurious optical signals produced by the source

- Lack of very fine spectral selectivity; therefore susceptible to cross-response to other gases.
- Dirt on the windows can be interpreted as gas absorption.

2.4 Photo-acoustic Spectroscopy (PAS)

Illuminating a gas with the light of a frequency that matches one of its resonant vibration frequencies results in partial absorption. The molecules of the gas that are excited to a higher vibration energy state as a result of the absorption will in time relax back to the initial state through a number of processes (Figure 2-9). For vibration excitation, the primary relaxation process is vibration to translation energy transfer which results in increased heat energy of the gas molecules and therefore a temperature and/or pressure increase in the gas[22]. Only the nonradiative relaxation contributes to the heat production and thus to the PAS signal[23]. The PA (photoacoustic) process is therefore complementary to fluorescence and additional nonthermal decay processes, as illustrated in Figure 2-9.

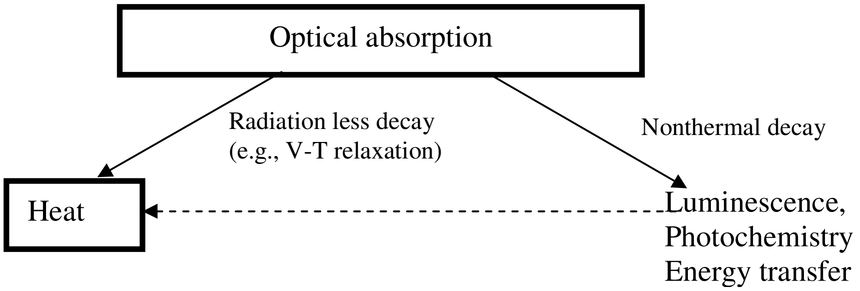

Figure 2-9: Principle of the Photoacoustic effect. After Sigrist[23]. Key: V-T, vibrational to translational

If the incident radiation is modulated, then the temperature and pressure will be as well. The modulated pressure will result in an acoustic wave, which can be detected with a sound measuring device, such as a microphone[22]. A schematic diagram of a typical PAS set up is shown in Figure 2-10 below.

The generated acoustic waves are detected by the microphone. The microphone signal is fed to a lock-in amplifier locked to the modulation frequency. The average laser power can be recorded simultaneously by a power meter. This can be used to normalise the microphone signal as shown in Figure 2-10.

The amplitude of the acoustic wave will depend upon such factors as the geometry of the gas cell, incident light intensity, absorbing gas concentration, absorption coefficient, and the background gas.

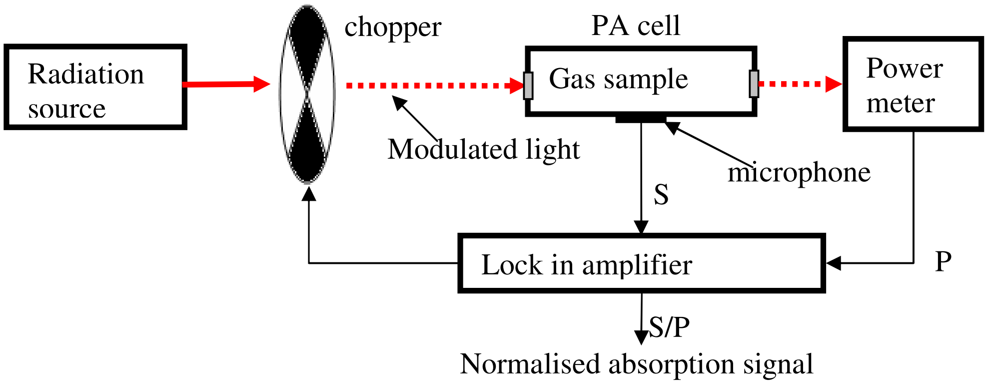

Figure 2-10: Schematic diagram of a PAS system. Key: S, microphone signal; P, Laser power. After Sigrist[23].

Gas concentration measurements are performed by calibrating the photoacoustic signal. Often a linear behaviour of the signal is observed in a large dynamic range more than five orders of magnitude[22]. This makes PAS suitable for applications in trace gas analysis and pollution monitoring. Advantages of PAS include:

- Selective and quantitative measurement of a specific gas in a mixture of gases can be achieved by using a broad band source with an appropriate optical filter.
- Very high sensitivity can be achieved.
- Instruments are stable; microphones have demonstrated a very low drift equivalent to <10% in 100 years[24].
- Instruments have a large dynamic range, up to 10^5 times the detection limit can be achieved for a specific gas[24]. Therefore the same instrument can be used at extremes of the concentration scale without recalibration.

2.5 TDLAS spectroscopy techniques

TDLAS employs diode lasers with narrow linewidths (tens of megahertz) that are narrower than Doppler linewidths and can be continuously tuned over a desired wavelength region (up to tens of GHz).

The use of narrow linewidth lasers has a particular advantage in atmospheric measurements where very high spectral resolution is required to avoid interference between species, particularly from water and carbon dioxide (absorption lines of H_2O and CO_2 are widely occurring). Individual rotational-vibrational features have linewidths of typically $2\times10^{-3}cm^{-1}$ (60MHz). Instruments with broad-band light sources such as NDIR (section 2.4) are generally incapable of such high resolution[13]. Sources such as CO_2 and CO lasers that are commonly used in PAS (section 2.5) have narrow linewidths but rely on accidental resonance between laser emission lines and the gas absorption lines[13]. On the contrary, diode lasers, particularly in the near infrared, can be fabricated to a specific wavelength at relatively low cost.

In addition to specificity, TDLAS offers many other advantages including:

- High sensitivity (sub *ppm*); allowing measurement of trace species or trace constituents in complex gas mixtures.
- fast response times; allowing rapid surveys or gas flux measurements.
- portable instrumentation; allowing vehicle based or hand held TDLAS systems that are in use in the gas utility industry.
- Large dynamic range; the same instrument is capable of measuring %Vol, LEL and *ppm* scale.

TDLAS systems have been used in a variety applications including; air pollution monitoring, research tools to study atmospheric processes and process control. A comprehensive review of applications of TDLAS techniques can be found elsewhere in the literature[25]. Due to the specificity and freedom from interferences of TDLAS, it has been used as a standard over which other less definitive techniques can be compared and calibrated[13].

TDLAS can be implemented in a number of ways. The main TDLAS techniques include: direct spectroscopy, wavelength modulation spectroscopy (WMS), frequency modulation spectroscopy (FMS) and two tone frequency modulation spectroscopy (TTFMS). There has been a lot of work, both theoretical and practical, in comparing the different TDLAS techniques[26-28]. These techniques are described in the following sections.

2.5.1 Direct Spectroscopy

In fixed wavelength optical absorption techniques that measure the transmitted intensity after passage of light through the gas cell, the signal beam is attenuated by absorption of the gas under investigation, but also by other processes such as scattering or dirt on the gas cell windows. It is therefore not possible to determine to which extent the attenuation can be attributed to the influence of the absorber. However, when the wavelength of the light source is tuned over the absorption feature of interest, the proportion of absorption that is linked to the concentration of the molecule is wavelength dependent and can therefore be distinguished from the attenuation of the light due to other processes that tend to have broader spectral absorption features. The absorption due to gas peaks at the gas absorption line centre. The signal and its background (to both sides of the absorption feature) are recorded almost simultaneously; therefore, absorption due to other processes will appear as base line shift.

A schematic diagram of a typical experimental setup for laser diode based direct absorption spectroscopy is shown in Figure 2-11. The laser diode frequency is stabilised at the peak of the absorption line by controlling its operating temperature and current. A low frequency (hundreds of Hz or several kHz) saw tooth waveform with suitable amplitude is then added to the laser D.C. operating current. This has the effect of scanning the laser frequency across the gas absorption line. A proportion of the laser intensity is absorbed in the gas cell. The transmitted light is collected and the detected signal is amplified. The signal can then be monitored on an oscilloscope. The signal on the oscilloscope (Figure 2-11) has a sloping background because the saw tooth wave form has the undesirable side effect of ramping the laser diode intensity. The disadvantages of this technique are the strongly sloping background signal, which make it very difficult to identify small absorptions, and the vulnerability of the scheme to small drifts in the laser output power[29]. The background signal is directly related to the incident laser power. This problem can be reduced by normalising the measured signal by a signal obtained without gas in the cell.

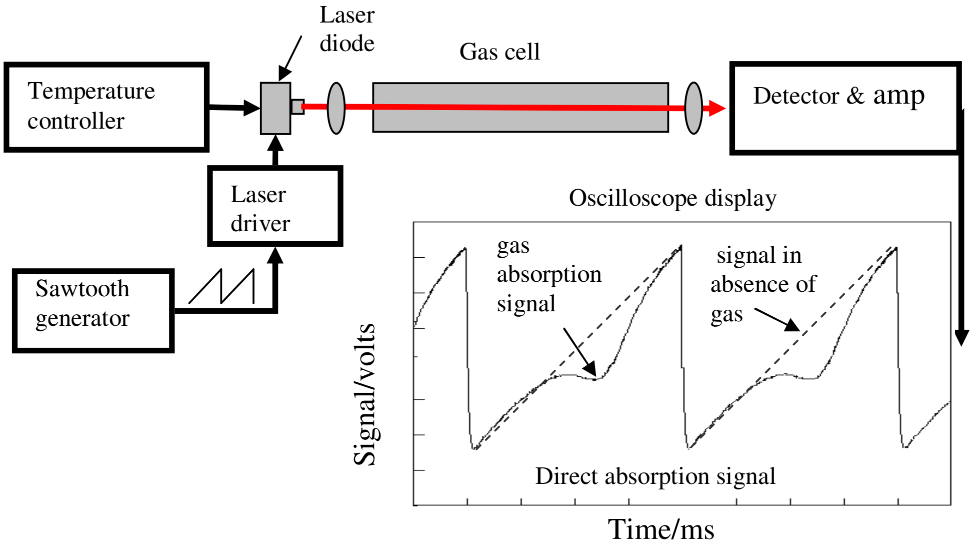

Figure 2-11: A schematic diagram of a typical experimental setup for laser diode based direct absorption spectroscopy.

The amplitude of the saw tooth waveform must be chosen carefully to avoid having any instantaneous currents that are below the threshold for lasing, above the permitted upper current limit, or in a region where mode hops are induced.

Sensitivity can be improved by increasing the path length over which absorption occurs in the gas cell. Multipass cells such as the White[30-31] or Herriott[32-33] cells are often used.

Direct spectroscopy is limited to measurement of peak absorbances A (defined in equation (2-3)) greater than 10^{-3}, by uncertainties in subtracting two large numbers (I and I_0)[13]. The sloping background and the laser excess noise of the diode itself at the relatively low modulation frequency (a few kilohertz) limit the detectable signal. Another uncertainty contribution comes from spurious signals generated in the optical path.

The removal of the sloping background and reduction of the laser excess noise can be achieved by applying additional modulation techniques; permitting routine absorption measurements of better than 10^{-5} according to Gharavi and Buckley[12]. The additional modulation techniques are described below.

2.5.2 Wavelength modulation spectroscopy (WMS)

WMS is essentially a more sophisticated version of the direct absorption method. It combines the scanning of the laser frequency across the absorption line with an additional higher frequency modulating waveform of suitable amplitude; most typically a low amplitude sine wave[13]. The interaction of the modulated light with the absorption line leads to the generation of signals at different harmonics of the modulation frequency. The signal at a given harmonic can be measured with phase sensitive detection and is directly proportional to the absorption. The principle of WMS is illustrated in (Figure 2-12) below.

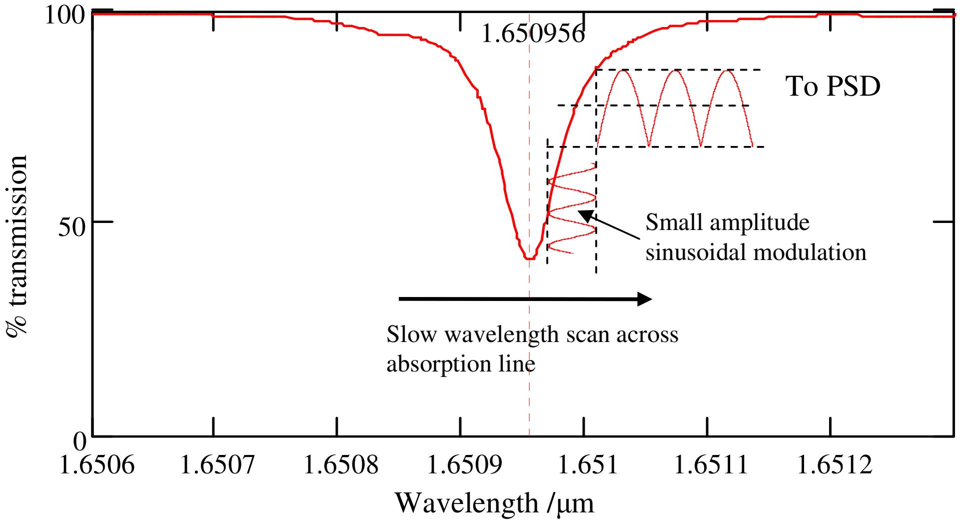

Figure 2-12: Schematic diagram of the principle of WMS; the laser wavelength is scanned across the gas absorption line whilst being simultaneously modulated by a small amplitude sine wave of the order of several kHz. Key: PSD, phase sensitive detector.

An important advantage of this technique is to shift the detection to higher frequencies, at which the laser excess noise (1/*f* noise) is reduced[34].

WMS was first used by Tang *et al* in 1974[35] in conjunction with continuous dye lasers. In 1980, Reid *et al*[36] used the technique to detect the strong ν_3 band of NO_2 that occurs at $1600 cm^{-1}$; they described the modulation technique in detail and the noise mechanisms that limited the detectable absorption coefficients to approximately $10^{-7} m^{-1}$.

A thorough explanation of WMS is given in section 2.7. Only a brief description is given in this section. The schematic diagram of a typical experimental setup for generating WMS signals using diode lasers is shown in (Figure 2-13) below.

The laser wavelength is modulated by varying the drive current at a frequency ν_m of several kilohertz. The modulation frequency is much less than the half width, $\nu_{1/2}$, of the absorption line of interest (typically several GHz). WMS can be characterised by $\nu_m / \nu_{1/2} << 1$. The laser wavelength is simultaneously slowly scanned across the absorption line at a frequency $f << \nu_m$. The resulting signal is then demodulated by a phase sensitive detector at the modulating frequency ν_m or at harmonics of this.

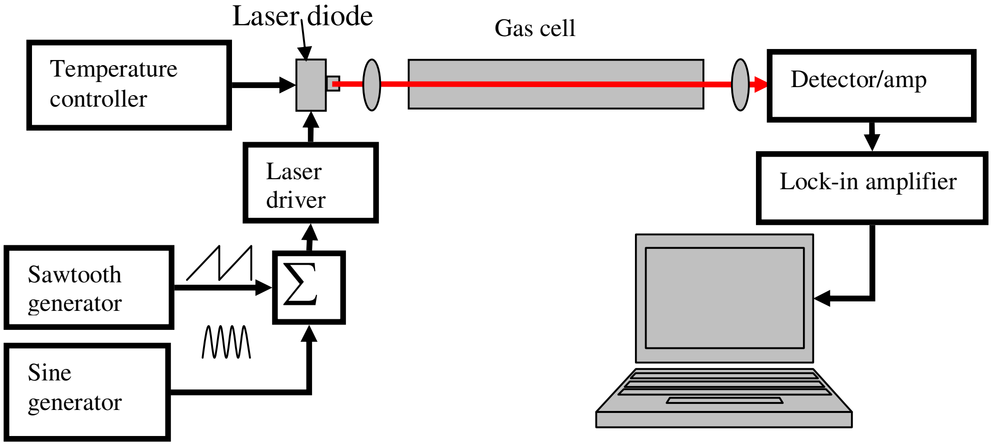

Figure 2-13: Schematic diagram of a typical experimental setup for diode laser based WMS

Detection is usually made at the first three harmonics (1f, 2f and 3f), also referred to as derivatives. One of the reasons for using low modulation frequencies (<10 kHz is typical) and detection at the lower harmonics is to take advantage of the simple and cheap detection circuits that are readily available in the audio frequency band.

Most WMS implementations use the 2f signal for measuring the gas concentration because the noise is relatively low, the signal peaks at the absorption line centre, base lines are usually flat (compared to the 1f as shown in Figure 2-14) and most lock-in amplifiers have a 2f detection feature. Absorbance sensitivities as low as 5×10^{-6} have been achieved[28,37] (1Hz bandwidth) at kilohertz modulation frequencies.

The strongly sloping background in the direct absorption signal (Figure 2-11), known as residual amplitude modulation (RAM), produces a significant D.C offset in the first derivative (1f) trace. The magnitude of this offset is proportional to the laser power incident on the detector[29]. The first derivative is therefore susceptible to fluctuations in the laser power. The 1f signal can be used for normalisation[34] and frequency stabilisation of the laser if the D.C offset is accurately known and constant. The 3f signal can also be used for frequency stabilisation of the laser[38] (frequency stabilisation techniques are discussed in detail in section 2.9). Detection at the second harmonic produces a significantly reduced D.C. offset and further reduces the effect of laser power fluctuations. The residual D.C. offset in the second harmonic signal is related to nonlinearity in the power versus current curve of laser diodes[20]. In some cases this residual background is eliminated by electronic subtraction techniques[39]or by detecting at higher even harmonics[40]. However, detecting at higher harmonics offers improved signal to noise ratios only in cases where the loss of the signal efficiency (the signal decreases with increasing detection harmonic, Table 2.4) is compensated by reduced laser noise available at the detection frequency or less RAM induced noise at the higher detection harmonic[28].

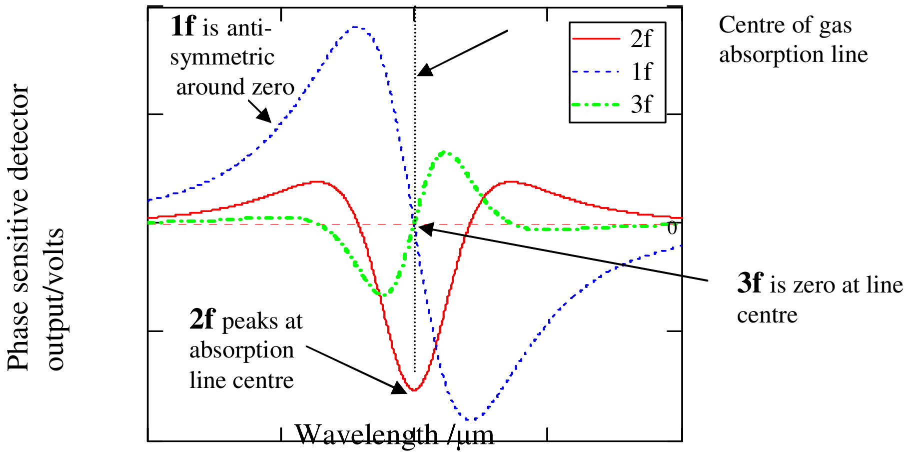

Figure 2-14: WMS harmonic signals obtained as the laser wavelength is tuned through the gas absorption line by current tuning: The 1f signal is large but has a large DC offset. The 2f signal peaks at the absorption line centre. The 3f signal is zero at the gas absorption line centre. The plots were generated from real experimental data obtained by the author.

One disadvantage of WMS is the loss of information about the unabsorbed laser power. One solution to this problem is to use a dual beam system in which the unattenuated laser power is measured separately and simultaneously. Another common solution is calibrating the system with a known concentration of the target gas[13] or to zero it periodically in clean air.

To improve on the detection limit imposed by laser excess noise, a high frequency modulation technique, FMS, similar in principle to WMS was developed in the early 1980s. A brief description of the technique follows.

2.5.3 Frequency Modulation Spectroscopy (FMS)

In FMS the laser diode is modulated at a very high frequency ν_m (typically hundreds of megahertz[41,42]). The modulation frequency ν_m is larger than the absorption half width frequency $\nu_{1/2}$ of the target gas. FMS is therefore characterised by $\nu_m / \nu_{1/2} >> 1$.

The technique was pioneered by Bjorklund in 1980[43]. The advantages of this technique are increased detection speed and increased detection sensitivity. These result from the radio frequency (RF) modulation of the diode laser and hence subsequent detection in a region where the laser 1/f noise is negligible, so that detector-limited sensitivities of the order of 10^{-7} - 10^{-8} are possible[44-45].

It has been shown that 1/f laser noise can be substantially reduced by using high frequency modulation techniques. With a ring dye laser, Hall *et al* [46] found that the noise level at 1 MHz is lower by 80 dB than at 10 kHz. For lead-salt diode lasers, similar measurements carried out by Werle *et al*[47] showed that the noise level decreased by 40 dB between 2 and 200 MHz. According to Werle *et al*[47], in terms of sensitivity, modulation techniques operated at 200 MHz should improve the SNR by 2 orders of magnitude. This improvement is reduced to one order of magnitude when multipass cell are used[48]. This is probably due to interference noise signals generated in the multipass cells (interference effects, the focus of this project, are discussed in section 2.7.1.

One may choose from among several methods of implementing FM spectroscopy using diode lasers, including what are known as one-tone[41] (OTFMS) and two-tone[49] (TTFMS) techniques. These are distinguished by, among other things, the number of distinct RF components that are supplied to the diode laser. OTFMS and TTFMS are described next.

2.5.4 One Tone Frequency Modulation Spectroscopy (OTFMS)

In single-tone FM spectroscopy, the laser diode frequency is modulated by a single RF signal, resulting in one or more sidebands separated by the modulation frequency ν_m. Mixing the detector photocurrent with a local oscillator at ν_m and scanning the laser across the absorption line results in an output spectrum that exhibits positive and negative peaks proportional to the original absorption line shape[50]. The signals in single-tone FMS have odd symmetry and, with a suitable choice of local oscillator phase, appear against a zero background. The complete theory of line shapes and signal-to-noise analysis for single-tone FM in different conditions is given by Bjorklund[43].

The output spectrum consists of a strong carrier at ν_c and two sidebands, of the same amplitude but 180 degrees out of phase, and displaced by the modulation frequency ν_m from the carrier[42] (Figure 2-15). When there is no absorption present, the beat signal at ν_m between the carrier and the upper sideband exactly cancels the beat signal between the carrier and the lower sideband. If, however, the laser frequency is tuned over an absorption line, so that one of the sidebands is absorbed, the imperfect cancellation of the two beats produces an FMS signal. The signal can be detected at the modulation frequency ν_m through heterodyne detection[42]. OTFM spectroscopy is essentially a differential absorption technique, thus for optimum sensitivity the modulation frequency must exceed the width of an absorption feature so that only one sideband is absorbed at a time[42]. To investigate broad spectral features, such as absorption lines broadened to 2-3 GHz (0.067 -0.1cm^{-1}) by atmospheric pressure, the modulation frequencies must be correspondingly high. Unfortunately, detectors with such bandwidths are complex to implement. To reduce the detection bandwidth requirement, the two-tone technique, described below, is employed.

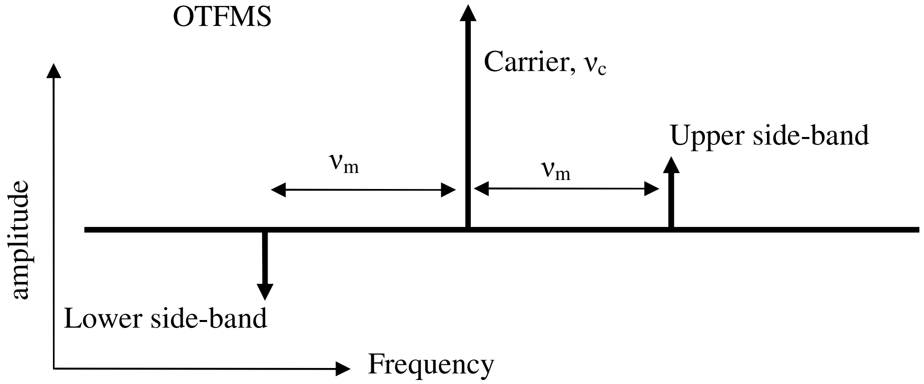

Figure 2-15: Schematic diagram showing the spectral distribution of the electric field of the laser in One Tone Frequency Modulation Spectroscopy. After Wang *et al*[42].

2.5.5 Two Tone Frequency Modulation Spectroscopy (TTFMS)

This technique was first demonstrated by Janik *et al* in 1986[49] using very high modulation frequencies (16GHz, 0.5cm^{-1}). Two radio frequency (RF) signals, closely spaced in frequency, ν_{m1} and ν_{m2}, are supplied to the diode laser, and the beat tone between them is monitored as the laser carrier frequency is scanned through an absorption line. The processing of the signal occurs at the beat frequency $|\nu_{m1} - \nu_{m2}| << \nu_{m1}, \nu_{m2}$ (Figure 2-16).

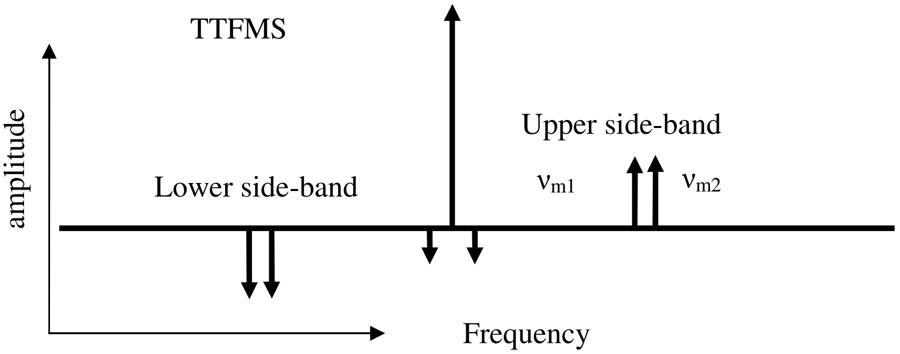

Figure 2-16: Schematic diagram showing the spectral distribution of the electric field of the laser in Two Tone Frequency Modulation Spectroscopy. After Wang *et al*[42].

The two-tone absorption signal arises from the difference between the absorption of the carrier and the sum of the absorptions of the sidebands. The signal peaks at the absorption line centre, and has even symmetry.

The primary advantage is that the detector bandwidth need only be in the 1-10MHz range rather than >150MHz, allowing the use of relatively inexpensive detectors[50].

2.5.6 Brief summary of common methane detection methods

The important points on direct spectroscopy, WMS, OTFMS and TTFMS are summarised in Table 2-4 below.

Table 2-4: A brief summary of TDLAS techniques.

DETECTION METHODOLOGY	PRINCIPLE	ADVANTAGES	DISADVANTAGES
Direct spectroscopy or Amplitude modulation	Laser frequency scanned across absorption line,	• simple to implement • provides absolute calibration compared to the other TDLAS techniques that only provide relative absorption values	• relatively low sensitivity • fluctuations in incident radiation can affect the measured signal
Wavelength Modulation Spectroscopy	Modulation at several kHz. Detection at harmonics usually 2f	• high sensitivity. • Simple modulation and detection circuitry	• 1/f noise in laser emission is significant • calibration required
One Tone Frequency Modulation Spectroscopy	R.F. modulation signal. Detection at R.F. frequencies	• Negligible 1/f noise • Increased detection sensitivity	• Requires complex modulation electronics and complex detector electronics • unsuitable for measurements at atmospheric pressure
Two Tone Frequency Modulation Spectroscopy	Modulation at two R.F. signals with detection at beat frequency	• Negligible 1/f noise • Increased detection sensitivity • Reduced detection bandwidth	• Requires complex modulation electronics

A summary of the methane detection methodologies described in the previous sections is provided in Table 2-5 for the reader’s convenience.

Table 2-5: Comparison of the commonly used methane detection methodologies.

DETECTION METHODOLOGY	PRINCIPLE	ADVANTAGES	DISADVANTAGES
FID	• measurement of changes in number of ions generated in a hydrogen/air flame due to trace organic compounds	• high sensitivity • high dynamic range •used in the range 1-50000ppm	• complex instruments • destroys sample • need hydrogen and stable environment for flame • non selective between organic compounds
catalytic sensor/Pellistor	• measures energy liberated on oxidation of a combustible gas • typically used for %LEL and %volume scales	•very suitable for monitoring flammable gases in air (used on LEL scale with 5%Vol equal to 100%LEL • sensors have a long life	• low sensitivity; not suitable for ppm scale • cross sensitivity to other flammable gases and vapours • sensor poisoning
solid state or metal oxide semiconductor	measures changes in electrical conductivity induced in semiconducting materials by adsorption of gases on surface	• responds to many oxidisable gases • inexpensive • rugged • high sensitivity to some gases	• poor gas selectivity • nonlinear response to gas concentration • sensor instability and irreproducibility
NDIR	• measures absorbed light. • Wavelength selection by filtering broadband light. • Spectral width typically 100nm	• simple to implement • moderate cost • no competing technologies for CO_2 detection	• source and detector subject to drift • cross sensitivity
PAS	• measures increase in pressure in PAS cell due to gas absorptions	• high sensitivity • high dynamic range	• sensitive to external acoustic noise and vibration
TDLAS	• Laser frequency scanned across absorption line, detection at fundamental frequency	• high sensitivity • high specificity • fast response times	• sensitivity limited by optical interference noise • sources expensive compared to the above techniques • limited to regions of the spectrum free of H_2O and CO_2

2.5.7 Justification for implementing WMS over other TDLAS techniques

WMS and FMS are closely related techniques, which operate at different values of the modulating frequency and the depth of modulation[51]. FM techniques avoid the excess noise of diode lasers by modulation of the diode lasers beyond the excess noise region, so theoretically a sensitivity limited by shot noise can be achieved, but the FM technique is complex to apply and is expensive.

In their experimental comparison of the modulation techniques using lead salt lasers Bomse *et al*[28] found that both OTFMS and TTFMS gave relatively poor results due to inefficient coupling of the very high frequency modulation waveform to the laser current. In 1992 Pavone and Inguscio[52] compared experimental WMS and FMS using an AlGaAs diode laser. They came to the conclusion that the advantage of using FMS was less pronounced because semiconductor lasers exhibit less excess noise compared to dye laser that were used in early studies.

Several other studies have concluded that, under ideal conditions, better ultimate sensitivity for absorption detection is obtained in the FMS regime than in the WMS regime[42]; however, in practice the sensitivity is expected to be limited mainly by optical interference effects (covered in detail in section 2.7.1) which are comparable in both cases[53]. In most practical applications, the question of ultimate sensitivity may be irrelevant until these spurious signals that limit the detection sensitivity are resolved. The purpose of this project is to make a contribution in this area.

Some studies have implemented high frequency (hundreds of kilohertz) WMS (HFWMS) to take advantage of the benefits offered by both WMS and FMS. HFWMS, in which the modulation frequency is less than but approaching the value of the absorption linewidth, can have the same sensitivity as OTFMS or TTFMS but with fewer operational complications[50]. Wavelength modulation detection using commercial lock-in amplifiers or discrete components is easy to implement. It avoids the impedance matching difficulties and RF leakage problems associated with the FMS techniques.

In this project, WMS with *2f* detection has been chosen because of lower cost and ease of implementation. This makes WMS the most likely technique for commercialisation. It offers the sensitivity targeted by the project without the technical challenges encountered in implementing FMS techniques. The background methane concentration is approximately 2ppm; therefore for most applications there is no need to have an instrument with sensitivity better than the background concentration. In addition WMS has been used in trace gas detection for many years; as a result there is an abundance of reference literature. As both WMS and FMS are known to suffer from interference fringes, it is prudent to implement the simplest of these techniques to investigate potential methods of reducing such fringes. WMS is the subject of the following sections.

2.6 Wavelength Modulation Spectroscopy

In the following sections a detailed theoretical description of WMS is given, and some of the common problems in practical implementation of WMS are also discussed.

2.6.1 Theoretical description of WMS

The theoretical description of WMS below is based on the assumption that modulating the laser diode current gives rise to pure frequency modulation (FM, Figure 2-17(b)). In reality, the output intensity of the laser is also modulated (Figure 2-17(a)). The intensity modulation (IM) is an undesirable side effect in WMS and is ignored in the following description.

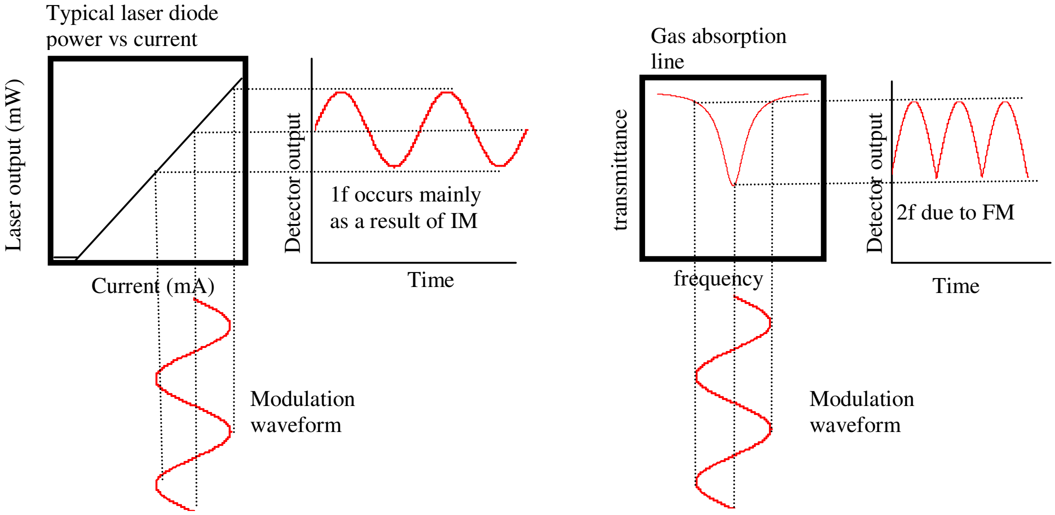

(a) Intensity modulation (IM) (b) Frequency modulation (FM)

Figure 2-17: Illustration of (a) intensity modulation IM and (b) frequency FM effects on WMS signals. After Iseki[54].

Jin *et al*[55] have shown that the light intensity after passing through the gas cell is approximately given by (see Appendix A for the detail)

$$P(t) = P_0[1+\eta \sin \omega t - \alpha(\nu_0 + \nu_m \sin \omega t)CL] \qquad \textbf{(2-11)}$$

by making two assumptions;

- $\alpha(\nu)CL << 1$, justified by the fact that in most practical situations the concentration of the gas being measured is small
- $\eta << 1$, usually the residual intensity modulation is also small

where P_0 and $\nu_0 (= c/\lambda_0)$ represent, respectively, the average laser output power and the average laser carrier frequency. ν_m is the amplitude of the frequency modulation and η is an intensity modulation index.

Under atmospheric pressure, the gas absorption line is collision broadened and the line shape is given by a Lorentzian distribution, i.e.

$$\alpha(\nu) = \frac{\alpha_0}{1 + \left(\dfrac{\nu - \nu_{line}}{\delta\nu}\right)^2} \tag{2-12}$$

where α_0 is the absorption coefficient at ν_{line} corresponding to the centre of the absorption line (maximum absorption) and $\delta\nu$ is the half-width at half-maximum (HWHM) of the absorption line. The Lorentzian distribution is plotted in Figure 2-18 below.

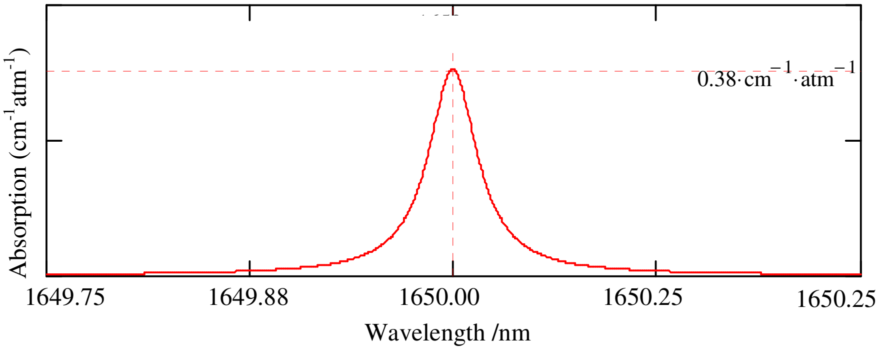

Figure 2-18: Theoretical Lorentzian distribution gas absorption line. The graph was plotted by substituting the following values in equation (2-16): α_0 = 0.38cm^{-1}atm^{-1} (1atm=1.013×10^{5}Pa); $\delta\nu$ =2GHz (0.067cm^{-1}); ν_{line}=1650nm (6061cm^{-1}).

The signal intensity is given by[28] (see appendix A for details).

$$P(t) = P_0\left[1 + \eta\sin\omega t - \frac{\alpha_0 CL}{1 + \left(\dfrac{\nu_0 - \nu + \nu_m \sin\omega t}{\delta\nu}\right)^2}\right] \tag{2-13}$$

If the average frequency of the laser diode is locked to the centre of the absorption line using frequency stabilisation locking techniques (covered in section 2.8)[15, 56], we have $\nu_0 = \nu$ and $P(t)$ may be written as

$$P(t) = P_0\left[1 + \eta\sin\omega t - \frac{\alpha_0 CL}{1 + x^2\sin^2\omega t}\right] \tag{2-14}$$

where $x = \nu_m / \delta\nu$ is known as the modulation index. The magnitudes of the first (P_1) and second harmonic (P_2) Fourier components of this equation were calculated by Jin *et al*[55]. These are presented below

$$P_1 = AI_0\eta \tag{2-15}$$

$$P_2 = -2Ak\alpha_0 CLI_0 \tag{2-16}$$

where A (collection efficiency) accounts for losses in the system and *k* is given by

$$k = \frac{2\,[2 + x^2 - 2(1+x^2)^{\frac{1}{2}}]}{x^2(1+x^2)^{\frac{1}{2}}} \qquad \textbf{(2-17)}$$

The value of x can be tuned to maximise the second-harmonic signal. The maximum occurs when $\partial k / \partial x = 0$, which gives a value of approximately 2.2. Under this optimal condition, $k = 0.343$ (Figure 2-19).

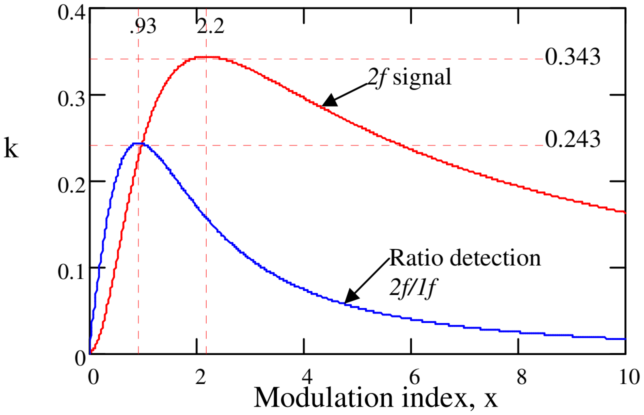

Figure 2-19: Plot of the value of k in equation 2-17 versus the modulation index x. The maximum 2f signal occurs when x= 2.2 giving *k=0.343*. For the ratio method the corresponding values are *x=0.93*and *k=0.243*.

In systems where the collection efficiency or the initial laser power can change, the ratio of P_2 to P_1 is utilised as the output of the sensor to removed the dependency on I_0 and A[57],[58]

$$\frac{P_2}{P_1} = \frac{-2k}{\eta}\alpha_0 CL \qquad \textbf{(2-18)}$$

To achieve the best sensitivity with the ratio detection, x is tuned to maximise the ratio P_2/P_1 rather than P_2. For the ratio-detection method the optimum modulation index, x, is 0.93 and the corresponding value of k is 0.243[55,58,59].

Optimum values of the modulation index and corresponding peak heights for the Lorentzian profile as computed by Silver[50] are shown in Table 2-6 below.

The important conclusion from the above analysis is that the signal strength depends on the modulation index and that there is an optimum modulation index for maximum and minimum signal.

The main drawback of the WMS technique is that the detection limit is frequently limited by various background signals[20,59]. These were briefly mentioned in section 2.6.2, and include residual amplitude modulation, non-linearity in the laser wavelength versus current tuning characteristics and interference fringes. These are discussed in more detail in the following sections.

Table 2-6: Computed peak heights and optimal modulation indices for WMS. After Silver[50].

HARMONIC	MODULATION INDEX	PEAK
1	2.0	0.509
2	2.2	0.345
4	3.9	0.179
6	7.4	0.146

2.6.2 Residual amplitude modulation (RAM)

In Figure 2-17, it was illustrated that modulation of the injection current in a semiconductor laser produces a combined frequency modulation (FM) and intensity modulation (IM) of the emitted light, with a phase difference between the two modulations. A change in the injection current gives rise to a change in carrier density. The carrier density is related to the number of photons and therefore output intensity. A change in the carrier density leads to a change in the effective refractive index and therefore laser emission frequency. However, for laser diodes modulated at frequencies less than 10MHz, the current/frequency transfer function is dominated by thermal effects (i.e. refractive index change and therefore laser emission frequency caused by current heating) rather than carrier effects (chapter 5 in ref 70). The thermal effect time constant gives rise to the IM-FM phase shift.

Some investigations of theoretical models of WMS only treated pure FM and ignored the associated IM[51,60]. Phillipe and Hanson[61] proposed the first model to take into account simultaneous FM and IM in 1993. The IM–FM phase shift depends on the laser structure and modulation frequency, but typical values in DFB lasers decrease from 0 degrees at low frequencies (where thermal effects are dominating) to -180 degrees at high frequencies (where carrier effects dominate)[62].

In WMS, the detected signals are mainly due to the FM of the laser emission, whereas IM, often referred as RAM in the literature is an unwanted effect that distorts the signals. This distortion also depends on the IM–FM phase shift, so that this parameter should be known precisely for a detailed and accurate description of the WMS signals[34]. The IM–FM phase shift can be determined experimentally[34], but for completeness a theoretical description of WMS that includes the IM–FM phase shift is given in Appendix B.

Johnstone *et al*[63] proposed a very simple but apparently effective technique of eliminating the RAM signal. The lock-in amplifier detection phase was set to null the RAM signal using the experimentally determined FM-IM phase shift (Figure 2-20). This technique can only be implemented with dual phase lock-in amplifiers.

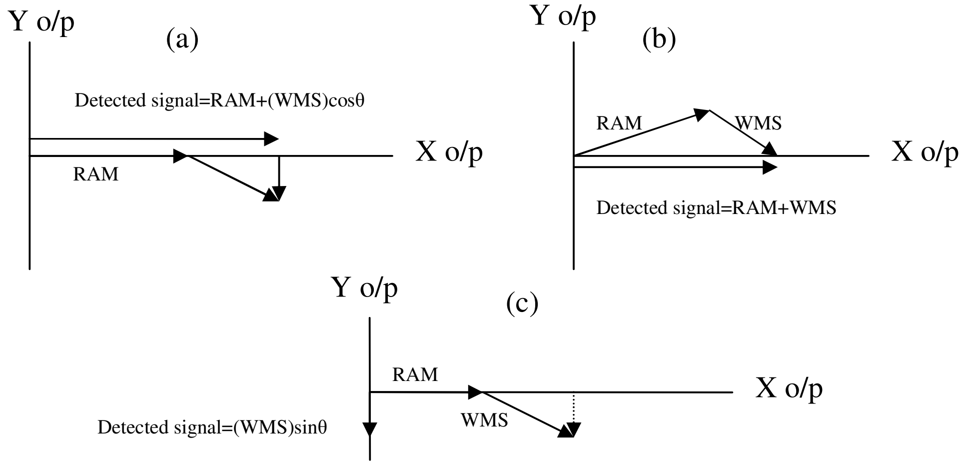

Figure 2-20: "Phasor diagrams showing the lock-in amplifier detection phase set to a) maximise RAM on the X output, b) maximise the resultant of the RAM and the gas signal on the X output, C) detect only the sinθ component of the gas signal on the Y output with the RAM signal nulled on the Y axis (maximised on the X)". After Johnstone *et al*[63].

2.6.3 Background signal from nonlinearity in the laser power versus current curve

It was mentioned in section 2.5.2 that the second harmonic signal has an offset due to nonlinearities in the laser power versus current curve. Cassidy *et al*[20] and Schilt *et al*[34] observed that this second harmonic background signal increased at higher modulation depth. This is consistent with the fact that nonlinearity of the power versus current curve of the laser diode is more appreciable at the increased modulation depth, as the laser current has to be tuned over a wider range. This also explains why the residual D.C offset of the *2f* signal (which is due to the nonlinearity in the wavelength versus current curve of the laser) in is larger in studies at atmospheric pressure, where the absorption lines are broadened (the required modulation depth is large, several GHz).

2.7 Noise sources and detection limits

Tunability, low cost, simplicity, and continuous wave operation at room temperature have made diode lasers widely used in laser absorption spectroscopy for trace species detection. Despite these advantages, the practical implementation of WMS using diode lasers is limited by detector noise, laser excess noise, laser sensitivity to optical feedback, injection current fluctuations, and optical interference fringes. These limitations are discussed in more detail in the following subsections. Injection current fluctuations can be reduced by using low noise current sources, temperature stabilisation and frequency stabilisation techniques.

Sensitivity of the detection system is determined by the minimum detectable signal that is distinguishable from noise or other unwanted signals appearing at the output of the detection system[13]. It is often defined in terms of the minimum absorbed power, corresponding to unity signal to noise ratio (S/N=1). The signal S is the average electrical signal corresponding to the absorbed power P_{AP} and is given by

$$S = Qge\eta P_{AP} / h\upsilon_o \qquad \textbf{(2-19)}$$

where g and η are the detector gain and quantum efficiency respectively; e is the electronic charge; and Q, a multiplication factor equal to 1 for amplitude modulation techniques and to less than 1 for wavelength modulation techniques[13].

2.7.1 Interference fringes in WMS

Many practical implementations of WMS have shown that the detection sensitivity is limited by interference fringes and not by the theoretical limit given by detector noise[64].

The interference fringes stem from Fabry-Perot etalons between reflecting or scattering surfaces such as mirrors, lenses, optical fibre end faces, detector and laser head windows, semiconductor surfaces, and components of multipass cells[13]. The background signals from the etalon effects depend on the reflectivity of the surfaces, the path difference of the etalon, the angle of incidence, the centre frequency around which the laser light is modulated, the modulation amplitude, and the mode of detection[59].

The etalons often exhibit a free spectral range similar to the linewidth of the absorbing species and appear as periodic spectral features with sufficient amplitude to obscure weak absorption signals[65]. Bomse *et al*[28] suggested that gas cell windows are often the worst culprits. Figure 2-21 below illustrates the formation of interference fringes in a gas cell and their influence on direct spectroscopy. Figure 2-22 shows the effects of interference fringes on WMS signals.

Experiments using DFB diode lasers are particularly prone to interference fringes because the narrow laser linewidths (tens of megahertz) translate into long coherence lengths (tens of metres). The fringe spacing, $\Delta\nu$ or FSR (free spectral range), corresponding to an etalon thickness l is given by

$$\Delta\nu = \frac{c}{2nl} \qquad \textbf{(2-20)}$$

where c is the free space speed of light and n is the refractive index of the etalon. For example, an etalon formed between the windows of a gas cell with a typical length of 10cm will give rise to fringes with a spacing of approximately 1GHz (0.033cm^{-1}). This is comparable to pressure broadened gas absorption linewidths. For methane at atmospheric pressure the worst etalon spacing would be 5cm or 2GHz; the width of the absorption line.

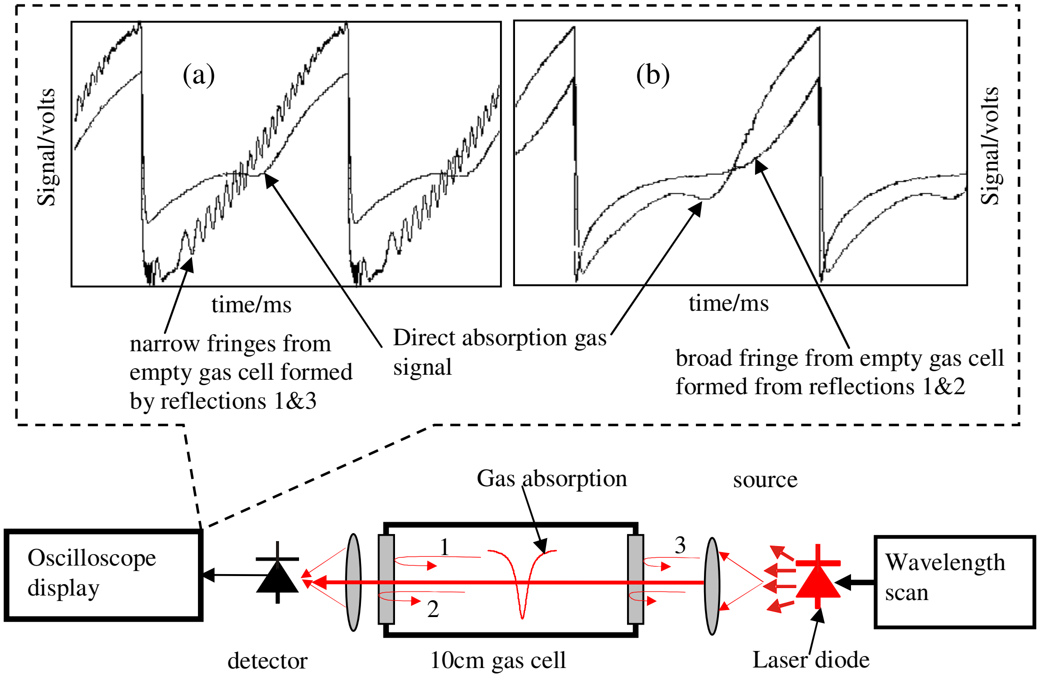

Figure 2-21: Illustration of formation of interference fringes in direct absorption spectroscopy: reflections from laser windows, detector windows, lenses, and gas cell windows can lead to the formation of interference fringes. (a) Gas absorption signal and interference fringe signal from an etalon created between two windows; (b) gas absorption signal and interference fringe signal from an etalon created between the two faces of one window.

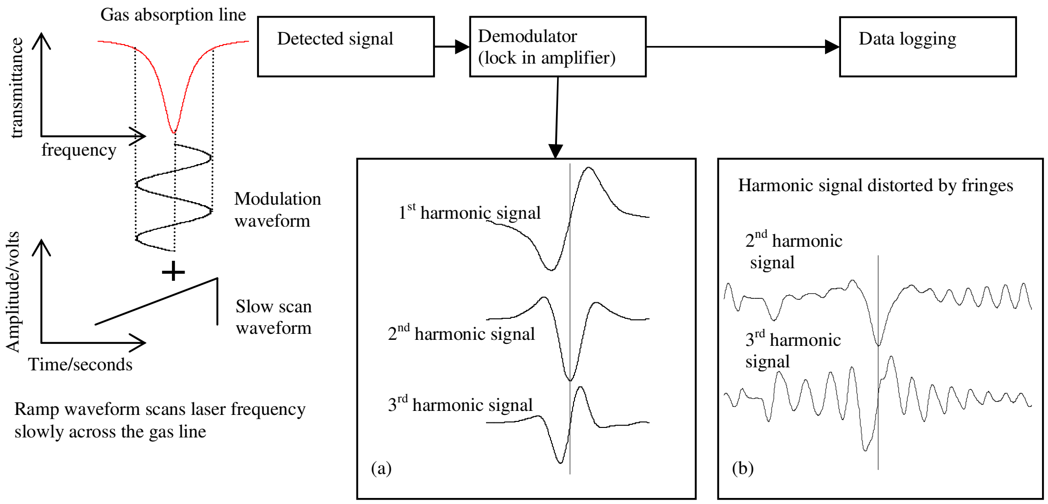

Figure 2-22: Illustration of the principle of WMS and effect of interference fringes on WMS signals. (a) Harmonic signals generated in the absence of interference fringes. (b) Harmonic signals distorted by interference fringes.

An early quantitative analysis of the effects of interference fringes on detection sensitivity was carried out by Reid *et al* in 1978[29]. In their study, the authors estimated that they could improve the detection sensitivity by at least a factor of 5 if they could eliminate the fringe signal.

Design techniques to reduce etalon formation include the use of reflective optics to avoid on-axis scattering from lenses, wedging and angling of all windows, antireflection coating of windows and lens surfaces, and angle polishing optical fibre ends.

In the following paragraphs a number of techniques that have been employed to reduce the effects of interference fringes by previous workers are discussed.

In some studies, the background signal is taken to be constant and electronic subtraction techniques are used to eliminate the fringe signal[34,39]. These techniques rely on subtracting a reference signal (this is usually taken in clean air simultaneously over a separate path that is closely matched to the main signal path) from the main signal to remove signals that are common to both arms. However, in practice it is difficult to match exactly the signal and reference paths. In their study Cassidy and Reid[20] found that the background signal was not reproducible and therefore could not be used as a baseline from which to make reliable measurements. They suggested that it was more effective to detect at higher harmonics as the background signal decreases faster with harmonic order than the harmonic signal efficiency (Table 2-6 lists the relative magnitude of the peak signal for the 1st, 2nd, 4th and 6th harmonics).

Interference fringe noise can not be eliminated by simple subtraction of a reference signal taken in clean air because thermal and mechanical instabilities of the optical system will modify the etalon fringe with time.

Reid *et al*[36] used a jitter method to reduce fringe amplitude. They used, in addition to the normal modulating current, a second modulating wave at frequencies not harmonically related to the basic modulation frequency to sweep the laser wavelength over several fringe periods. When the frequency swing precisely matches the FSR, the integrated signal goes to zero, thus eliminating the fringe signal. However, this averaging also decreases the absorption signal and can not be used for fringes with FSR similar to absorption linewidth.

Iguchi[66] and Sano *et al*[67] have suggested alternative modulation waveforms after finding that the waveform of the modulating signal affects the relative magnitude of the absorption signal and etalon fringes. Iguchi[66] found that a triangular waveform generally gave a larger 2f signal amplitude and a better suppression of a fine pitch etalon fringe signal, compared to the use of a sine wave. This approach appears to be advantageous, as it does not involve the use of an additional modulation waveform or dithering of optical components, or a precise knowledge of the FSR.

Both the jitter and waveform selection methods are efficient in suppressing etalons with etalon spacing either much larger or smaller than the molecular linewidth. However, for fringes comparable to the linewidth, they are inefficient and tend to reduce the signal[13]. Another limitation is that the specific implementation depends on the laser tuning characteristics which vary from one laser to another[64].

Mechanical methods of averaging out the fringes by oscillating the path length with an external device have also been proposed. Bomse *et al* [28] suppressed all etalon frequencies including those having widths comparable to the absorption signal by using longitudinal dithering of optical elements. They attached piezoelectric transducers to the mirrors of a Herriott cell used in the study. Webster[68] utilised a Brewster-plate spoiler to suppress optical fringes by a factor of 30 in a single pass absorption experiment. An angular oscillation was applied to a transmitting plate (tilted at Brewster angle) inserted within the offending etalon to vary its effective optical path. Suppression of the fringes due to averaging occurs when the optical path change is greater than the FSR (as given by equation (2-44)) of the fringes. The effectiveness of the Brewster spoiler depends on closely matching the transmission, refractive index and tilt[71]. Transmission losses and alignment difficulties may make this method unsuitable for most multipass cells[71].

Silver and Stanton[64] used an oscillating mirror driven by a piezoelectric transducer asynchronously to the modulation frequency. The mirror was placed within or bounding the interference fringe region. The amplitude of oscillation along the optical axis was adjusted to obtain a change in path length greater than $\lambda/4$ or half the fringe separation, resulting in effective fringe averaging. Chou *et al*[69] claimed to have achieved a 20-fold reduction in fringe amplitude by using a mirror mounted on a speaker driven at audio frequencies. The advantage of the mirror over the Brewster plate is that a broader range of wavelengths can be used if the mirror is broadband AR coated and there are no transmission losses.

Electronic or digital filtering can be applied post-detection where the signal and interference spectra are distinguishable in the frequency domain. Cappelani *et al* used Fourier transform digital filtering to remove interference spectra. Cooper and Carlisle[44] used electronic low pass filtering combined with rapid laser scanning, which they demonstrated to be effective in removing high-frequency fringes. In systems employing high frequency modulation, a high pass filter is used to reject low-frequency noise, fluctuations, and interference fringes[13].

It has been claimed that in general, etalon suppression techniques reduce unwanted fringes approximately 100-fold[28] compared to the main signal. It is difficult to compare the effectiveness of the different techniques described above because they have been used in experiments using different lasers (with different coherence lengths) and different experimental setups. These fringe-reduction techniques do not actually eliminate the etalons; they vary the etalon spacing in a time-dependent manner so that fringes average to zero or, in the Cooper and Carlisle example, the demodulated signal is processed to remove the etalon contribution[28].

In summary, the efforts described above to reduce the effects of interference signals fall into three broad categories. In the first group of approaches, a frequency jitter is applied to the laser diode and the signal is integrated. In the second group, the fringe spacing is mechanically modulated and the resultant signal is integrated to average zero, or to minimise the contribution of the fringes to the absorption signal. While effective, this approach limits the detection bandwidth because of the mechanical motion and signal integration required and adds to system complexity. The techniques also require prior knowledge of the FSR. The third group involves post detection filtering; electronic filtering techniques are not useful in cases where the fringe spacing is too close in frequency to the spectral feature of interest.

This project aims to investigate a novel method of removing interference fringes that does not have the disadvantages of the above techniques.

2.7.2 Optical feedback to the DFB laser

Numerous studies have investigated both the detrimental and beneficial effects of optical feedback on the operation of semiconductor lasers; linewidth narrowing and broadening[70], reduction of laser chirp[70], mode hopping[71], oscillation frequency shift[70,72], coherence collapse and intensity noise degradation[73].

For GaAs semiconductor lasers, a 3% feedback of the emission power has been shown to affect significantly the current and voltage across the laser junction, as well as causing changes in the output power[74]. One possible cause for the generation of excess noise is given by so-called mode competition theory[75]. A resonating mode (e.g. in the laser cavity) is significantly influenced by the fluctuation of neighbouring modes (e.g. caused by feedback external to the cavity) due to a strong coupling effect, leading to fluctuation of the spontaneous emission. In the presence of optical feedback, so-called external cavity modes are built up, whose frequencies are determined by a standing wave between the reflecting point and the laser facet[75]. This external mode interacts with the resonating mode; this is what gives rise to the laser excess noise according to the mode competition theory.

A recent study of optical feedback noise in TDLAS has reported degradation of the shape and extensive broadening of the absorption spectra due to lasing longitudinal mode instability and coherence collapse in the laser diode respectively[76]. These effects were observed in the presence of relatively strong optical feedback. However, in a practical TDLS system, the amount of backscattered or back reflected light that is unintentionally coupled into the source is likely to be weak, because of the use of AR coated optics, off axis parabolic mirrors, angle polished fibres and isolators. This is also the case for the use of diffusely scattering surfaces in TDLS[77]; for example in laser pointer style gas sensors where the light is backscattered from the topography[78-80] and the use of integrating spheres (see refs[81,82]) where the source can be directly mounted onto the sphere.

If a fraction of light backscattered or back reflected from optical components or a remote target is coupled into the laser cavity, both the amplitude and frequency of the lasing field may be modulated[83]. Periodic signals will be generated by relative motion between the laser and the remote target or tuning the laser by ramping the injection current or operational temperature. The signals display similar properties to those generated by a Fabry-Perot etalon[84]. In fact, this phenomenon is employed in so-called self-mixing or induced modulation interferometry, in which the laser source acts as a sensitive detector for distance, velocity and displacements measurements[83].

In so called self-mixing interferometry the light back reflected or backscattered by a remote target is deliberately coupled back into the laser cavity[83]. This causes interference with light already present in the cavity, resulting in a modulation of both the amplitude and the frequency of the emitted light.

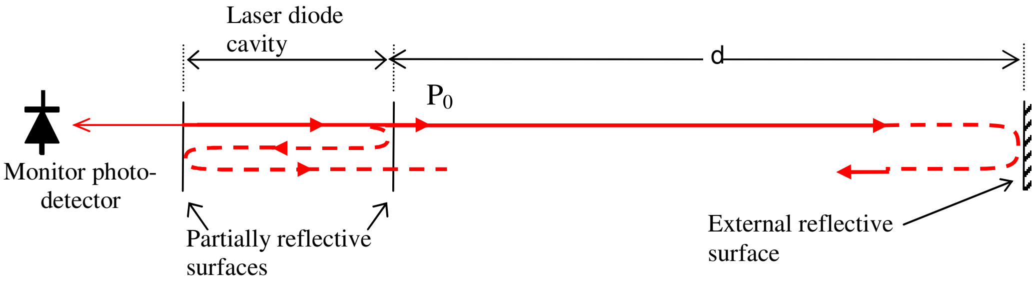

Figure 2-23: Schematic diagram of a conventional self-mixing configuration employing a laser diode. After Giuliani *et al*[83].

The power emitted by a laser diode with very low feedback (<0.05%)[76] is given by

$$P(\phi) = P_0[1 + m\,F(\phi)] \tag{2-21}$$

where P_0 is the power emitted without feedback, *m* the modulation index and $F(\phi)$ is a periodic (2π) function of ϕ[83]. The phase ϕ is given by

$$\phi = 4\pi s / \lambda \tag{2-22}$$

where *s* is the distance to the external reflector or diffuser[83]. The modulation index *m* and the form of $F(\phi)$ depend on a characteristic parameter Y, which is a measure of the relative strength of the optical feedback[83,85]

$$Y = \frac{ks\sqrt{1+\alpha^2}}{L_{las}n_{las}} \tag{2-23}$$

where α is the linewidth enhancement factor, L_{las} is the cavity length and n_{las} is the cavity refractive index. k is given by

$$k = \frac{\varepsilon}{\sqrt{A}}\frac{1-R_2}{\sqrt{R_2}} \tag{2-24}$$

where ε (<< 1) accounts for a mismatch between the reflected and the lasing modes, A is the total optical power attenuation in the external cavity and R_2 is the reflectivity of the laser output facet (see Figure 2-23). The Y parameter therefore depends on both target reflectivity and distance s. Giuliani *et al*[83] have used the Y parameter to distinguish between different feedback regimes as follows:

Table 2-7: Classification of different feedback regimes based on the feedback parameter Y (After Giuliani[83])

VALUE OF Y	FEEDBACK REGIME	EFFECT ON $F(\phi)$	EFFECT ON MODULATION INDEX *m*
Y << 1	very weak	is a cosine	proportional to $1/\sqrt{A}$
0.1 < Y < 1	weak	distorted, non symmetric	proportional to $1/\sqrt{A}$
1 < Y < 4.6	moderate	bistable (2 stable and 1 unstable state) interferometric signal becomes saw-tooth like and exhibits hysteresis	increases for decreasing $\sqrt{A}$ but no longer inversely proportional
Y > 4.6	strong	Some laser diodes suffer mode hopping or even coherence collapse. interferometric measurement are no longer possible	

Optical feedback external to the laser must be avoided in high resolution spectroscopy. If the laser is multimoding, then cross sensitivity to other absorption lines in the vicinity may occur. Sufficient broadening of the laser linewidth can occur such that the gas absorption line can not be resolved. In addition, the output power fluctuations due to optical feedback can give misleading gas absorption measurements.

In general, the use of reflecting optics, proper alignment (or misalignment) of optical components, and the use of optical isolators and apertures can reduce the problem, although a reduction in laser power can result.

2.7.3 Laser excess noise

The sensitivity of TDLAS measurements is often limited by fluctuations in laser power, particularly when relatively high laser power and low modulation frequencies are employed[13]. The power fluctuations, usually referred to as laser excess noise, are either due to the inherent behaviour of the laser diode or to external effects such as injection current noise, temperature instabilities and optical feedback.

Intrinsic laser noise is produced by photon and carrier density fluctuation, refractive index fluctuation, and partition noise resulting from mode competition in multimode lasers[86]. It depends greatly on the manufacturing process and design of the laser and on the operating current and temperature[13].

Laser excess noise due to injection current and temperature instabilities can be minimised by using either battery powered or highly stabilised current sources together with temperature stabilisation, and by line locking the laser to an absorption feature with a low noise control loop[13].

The rms current i_{ex} at the detector, caused by laser excess noise, can be expressed as

$$i_{ex} = (e\eta P_{ex} / h\upsilon)(B / f^{b})^{1/2} \quad \textbf{(2-25)}$$

where B defines the frequency dependence of the laser excess noise and ranges between 0.8 and 1.5, and P_{ex} defines the magnitude of the laser power fluctuations at $1Hz$ in a 1-Hz bandwidth; P_{ex} is approximately proportional to laser power and depends on the intrinsic noise of the diode laser and on the external effects of the particular measuring system[13]. According to Schiff *et al*[13] careful system design and laser diode selection can limit P_{ex} to fractions of 10^{-4}-10^{-5} of the laser power, P.

The amount of optical noise present in an optical source is described by a parameter known as the relative-intensity-noise, *RIN*[71]. *RIN* is defined as the ratio of the mean-square noise power to the mean power squared.

$$RIN = \frac{\left\langle \delta P^{2} \right\rangle}{\left\langle P^{2} \right\rangle} \quad \textbf{(2-26)}$$

To measure *RIN* the optical power is converted to a current after the receiving photodiode and the noise of this photocurrent may be easily measured with a spectrum analyser[71]. This procedure is correct as long as no additional noise is added in the receiver.

According to Alexander[87], the expression for *RIN* in terms of the measured current can be given by

$$RIN(\omega) = i_{n}^{2}(\omega) / i_{p}^{2} \quad \textbf{(2-27)}$$

where $i_n^2(\omega)$ is the measured current-noise power spectral density in amps^2/Hz that is associated with the average DC photocurrent i_p. *RIN* has units of inverse frequency and can also be expressed in decibels per hertz as

$$RIN(\omega) = [10\log(i_{n}^{2}(\omega) / i_{p}^{2})] dB / Hz \quad \textbf{(2-28)}$$

2.7.4 Detector noise

The principal components of detector noise are Johnson (or thermal) noise, shot noise, and 1/f noise[88]. Figure 2-24 below shows a simple detector noise model that includes the principal noise sources in a detector.

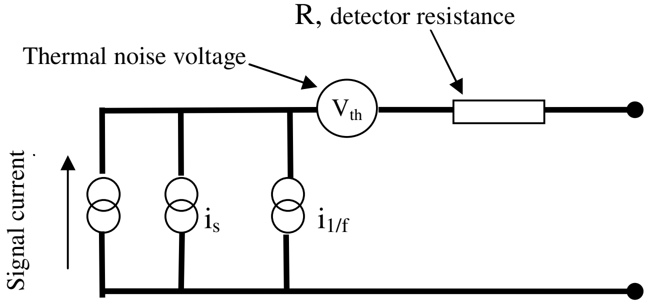

Figure 2-24: Detector noise model.

Thermal noise is due to random fluctuations of the electronic charges and is present in all resistive components of the detection system including the preamplifier. The thermal noise current of the detection system, i_T, is given by

$$i_T = (4kTB/R)^{1/2} \tag{2-29}$$

where k is the Boltzmann's constant; T, the temperature; B, the detection bandwidth; and R, the component resistance[13]. Johnson noise depends on temperature and the detection bandwidth but not on the frequency of the light intensity or the detection frequency (therefore referred to as "white noise").

Shot noise is due to the random arrival times of photons. The rms (root mean square) shot noise current is given by

$$i_S = (2e^2\eta BP/h\upsilon)^{1/2} \tag{2-30}$$

where P is the transmitted power and $h\upsilon$ is the photon energy[13]. Shot noise is independent of modulation frequency but is proportional to the square root of the laser power and of the detection bandwidth.

Detector *1/f* noise is thought to be caused by potential barriers in semiconductors and semiconductor contacts and depends greatly on manufacturing procedures, particularly with respect to contacts and surfaces[13]. The general expression of *1/f* noise takes the form:

$$i_{1/f} = (B/f)^{1/2}(e\eta P/h\upsilon) \tag{2-31}$$

The total detector noise is i_{total} is given by

$$i_{total}^2 = i_T^2 + i_S^2 + i_{1/f}^2 \tag{2-32}$$

The three noise sources depend linearly on the square root of the detection bandwidth. The bandwidth and therefore the noise can be reduced by filtering or signal integration. However this has to be balanced against the resulting increase in system response time.

2.7.5 Detection limit estimation

The sensitivity of a WMS system can be defined in terms of the minimum detectable absorption ($a=P_{AP}/P_0$) for a signal to noise ratio, *S/N*, equal to 1[13]. The general expression of the total rms noise current i_N is obtained by taking the square root of the quadrature summation of the noise contributions from detector Johnson noise, detector shot noise, detector 1/f noise and laser excess noise. The assumption is that the interference fringes have been reduced to a negligible level.

According to Schiff *et al*[13], under shot noise limited conditions, the minimum detectable absorbance a_{min} is given by

$$a_{\min} = (2Bh\upsilon / \eta P_0)^{1/2} \qquad \textbf{(2-33)}$$

and the minimum detectable absorption for atmospheric measurements at frequencies below 200 kHz utilising the 2f detection technique can be approximated as

$$a_{\min} = (P_{ex} / P_0)(B / f)^{1/2} \qquad \textbf{(2-34)}$$

where the terms have been defined in equation (2-59). This is based on the assumption that the detection limit is determined by the *1/f* noise.

The *2f* signal is much smaller than the *1f* signal when the concentration-path length product (or optical depth) of methane is small. The noise current on the photo detector can be assumed to be white noise below $2f = 12kHz$, therefore only the *2f* component is taken into account for estimating the detection limit[80]. According to Iseki *et al*[80] the *2f* signal current is given by

$$I_s = \frac{sP_{dc}k\alpha_0 CL}{\sqrt{2}} \qquad \textbf{(2-35)}$$

where I_s is the rms of the *2f* signal current (in Amperes) and *s* is the responsivity of the detector (AW^{-1}). The noise current is given by[80]

$$I_N = \sqrt{\left(\left(s^2(RIN)P_{dc}{}^2 + 2e(sP_{dc} + I_{dark}) + 4k\,T / R_{sh}\right)B\right)} \qquad \textbf{(2-36)}$$

where I_N is the rms of the *2f* noise current (in Amperes), *e* is the charge of an electron (in coulombs), *RIN* is the related intensity noise of the laser (Hz^{-1}), I_{dark} is the detector dark current (in amperes), R_{sh} is the detector parallel resistance (in ohms) and *B* is the bandwidth (in Hertz). If we define the detection limit, CL_{limit} , as the range-integrated concentration for which the signal-to-noise ratio (SNR) equals unity, CL_{limit} is given by[80]

$$CL_{\mathrm{lim}it} = \frac{1}{k\alpha_0}\left[\left(\frac{RIN}{2}+\frac{e}{sP_{dc}}+\frac{eI_{dark}+2k_BT/R_{sh}}{(sP_{dc})^2}\right)B\right]^{\frac{1}{2}} \tag{2-37}$$

The theoretical detection limit is plotted in Figure 2-25 below for various limiting factors.

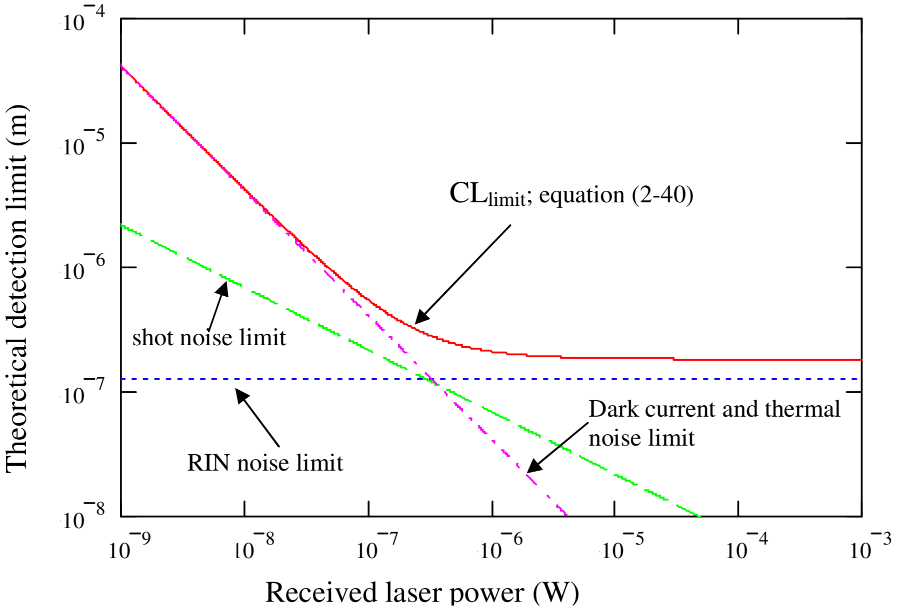

Figure 2-25: Theoretical detection limit versus the received laser power. The following values were used in calculations: α_0=0.38atm^{-1}cm^{-1}, RIN=10^{-12}Hz^{-1} (typical figure for DFB lasers), k=0.343, detector sensitivity PD=1.1AW^{-1}, detector dark current I$_{\mathrm{dark}}$=100nA, detector temperature 300K, detector parallel resistance R$_{\mathrm{shunt}}$=500kΩ and B=5Hz.

For a RIN of RIN=10^{-12}Hz^{-1}, (typical figure for DFB lasers), the ultimate detection limit for 10cm path will be approximately 2ppm which is the target sensitivity identified in chapter 1. Above 10µW the power level has little impact on the signal to noise ratio.

2.8 Wavelength stabilisation

The instantaneous lasing frequency of the laser diode depends on its operating current and temperature. The temperature coefficient of the wavelength shift of peak emission of DFB lasers is determined by the refractive index variation with temperature as well as by expansion/contraction of the feedback grating and is typically 0.1nm/°C (or 11GHz (0.4cm^{-1})/°C at 1650nm). The current dependency is typically 0.01nm/mA (1GHz/mA). Noise on the supply current to the laser and ambient temperature drifts will result in fluctuations in the laser operating frequency. Considering that the FWHM of the $2\nu_3$ absorption band of methane is approximately 4GHz (0.133cm^{-1}), to achieve high resolution spectroscopy it is vital that the laser frequency is stabilised so that the residual frequency jitter is much less than the absorption line FWHM.

In practical use, semiconductor lasers are temperature-stabilised by using peltier-electric coolers. To stabilise the oscillation frequency of the laser diode, it is necessary to compare the centre frequencies of the laser to a frequency reference. To date, several frequency stabilisation schemes for semiconductor lasers have been proposed involving the use of; Fabry-Perot interferometers[89], molecular absorption lines[56,90,91] and controlling the operating voltage[92].

Using Fabry-Perot interferometers achieves higher short term stabilities than simply using temperature and current controllers; however, long term stabilities are hard to attain, due to long-term cavity length fluctuations caused by temperature effects, unless the interferometer itself is stabilised with a gas laser[93]. A frequency lock employing atomic or molecular absorptions lines is more suitable than one using a Fabry-Perot etalon for maintaining the long term stability of the error signal[56]. A typical arrangement for frequency locking using molecular absorption lines is shown in Figure 2-26. In this case, the gas used to provide the frequency lock is identical to the measurement target gas, ensuring correspondence between the locked wavelength and the absorption line of interest.

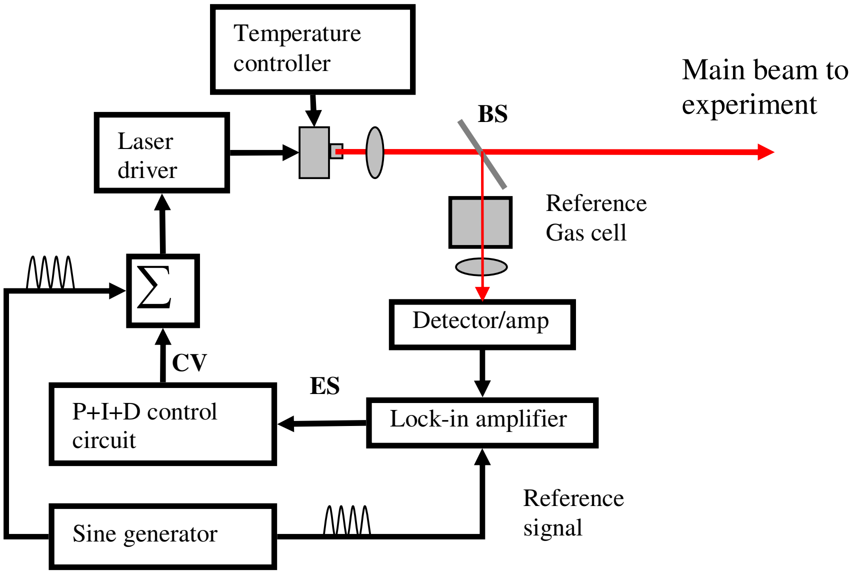

Figure 2-26: Atypical arrangement for frequency stabilisation using a gas molecular line. Key: ES, error signal; CV, correction voltage; BS, beam splitter; P+I+D, proportional + integral + derivative

In such schemes it is common to use the 1f or 3f signal from the lock-in amplifier as the error signal for locking to the peak of the 2f signal.

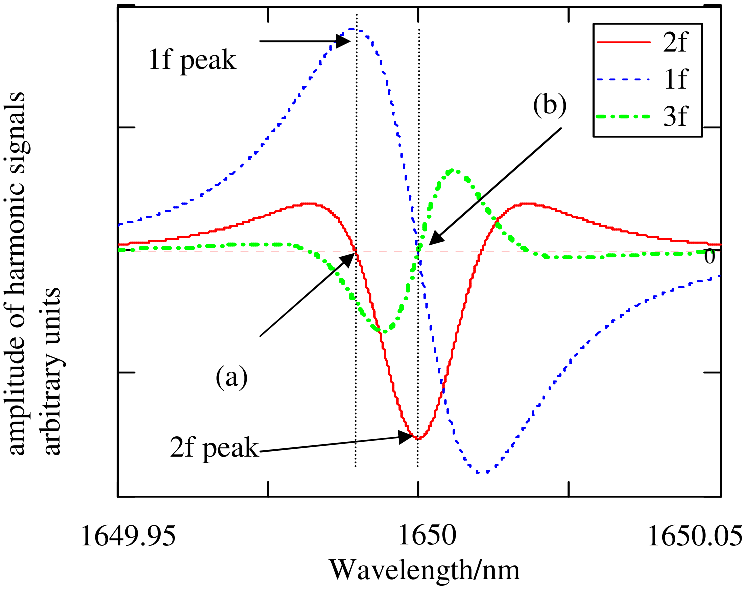

Figure 2-27: Plots of harmonic signals; 1f, 2f and 3f. Odd harmonics are zero at the line centre and even harmonics peak at the line centre.

The advantage of using the 1f component over the 3f component is that the 1f function is available on all lock-in amplifiers whilst the 3f is only available on the more sophisticated digital models. Using the 1f signal requires the DC offset to be stable. The DC offset can also be nulled by using the technique proposed by Johnstone *et al*[63] (see Figure 2-20). This requirement is not necessary if 3f lock is employed. This is because the 3f signal is zero at the line centre (Figure 2-27). If the laser frequency deviates from the line centre, the 3f signal or 1f with DC offset removed is non-zero (positive or negative). The 3f or 1f signal therefore provides the error signal as long as the error excursions are within a restricted region in the vicinity of the zero crossing. The feedback control (usually PID) circuit uses this error signal to supply a voltage to the laser driver to reduce the error (3f) signal to zero. This has the desired effect of locking the laser frequency to the peak of the absorption line centre.

In a less common implementation, the 2f signal can be used to provide the error signal for locking to the peak of the 1f signal. The laser is locked to the zero crossing of the 2f signal at the inflection points (point (a) in Figure 2-27). This corresponds to the peak of the 1f signal. The advantage of 1f detection with 2f lock is that it can be implemented with cheap lock-in amplifiers (i.e. no 3f or dual phase lock capability). The disadvantages of 1f detection have been outlined in section 2.5.2.

The next paragraph presents the frequency stabilities achieved using molecular absorption lines by previous workers (summarised in Table 2-8 below).

2.8.1 Brief summary of the frequency stabilities achieved using molecular absorption lines by previous workers

Bowring *et al*[56] reduced the frequency jitter of a 780nm GaAlAs laser diode from 80MHz to 0.8MHz by locking to acetylene absorption lines. Yanagawa *et al*[94] stabilised the frequency of 1.5µm InGaAsP DFB laser to NH_3 absorption lines. They reduced a frequency drift of about 100MHz under free running conditions to less than 2MHz. Sudo *et al*[91] reduced a peak to peak fluctuation of an InGaAsP DFB laser of about 200MHz to less than 500kHz by locking to the molecular absorption line of C_2H_2.

Table 2-8: Performance of frequency stabilisation schemes based on locking the laser frequency to a gas molecular absorption line

WORKERS	LASER USED	GAS LINE USED	FREE RUNNING STATE JITTER	FREQUENCY STABILISED JITTER
Bowring *et al*[56]	780nm GaAlAs	Acetylene	80MHz	0.8MHz
Yanagawa *et al*[94]	1.5µm InGaAsP DFB	Ammonia NH_3	100MHz	<2MHz
Sudo *et al*[91]	InGaAsP DFB laser	Acetylene C_2H_2	200MHz	500kHz

This level of stability (hundreds of kHz to several MHz) will be used as a bench mark for the frequency locking system to be developed. For example, a frequency stabilised jitter of 1MHz is approximately 3 orders of magnitude smaller than the HWHM of a Lorentzian linewidth. In this project, the 3f lock technique using a methane absorption line is employed. The 3f lock has been chosen over the 1f lock because it allows the flexibility of experimenting with various levels of incident power without the need to adjust the set point in the PID loop or having to null the offset using the method established by Johnstone *et al*[63] every time electronic equipment is changed.

Using a frequency reference that is the same as the gas that is being detected has the added advantage of ensuring absolute wavelength calibration.

2.9 Summary

In this chapter, non optical and optical techniques that are commonly used for methane detection have been reviewed. A summary of the different techniques is presented in Table 2-5. The advantages of TDLAS techniques include; fast response times, high sensitivity, high target gas sensitivity and instrumentation portability. Different TDLAS schemes were considered in section 2.5 and compared in Table 2-6.

This project has opted to implement the WMS technique with *2f* signal demodulation because of lower cost and ease of implementation. This decision was justified in section 2.5.7. WMS offers the sensitivity targeted by the project without the technical challenges encountered in implementing FMS techniques. As both WMS and FMS are known to suffer from interference fringes, it is prudent to implement the simplest of these techniques to investigate potential methods of reducing such fringes.

A thorough theoretical description of WMS was presented in section 2.7. Noise sources that limit the detection sensitivity of WMS were considered in section 2.7 and showed that the sensitivity of TDLAS including WMS is often limited by noise from optical interference fringes. A thorough review of the prior art in interference fringe reduction schemes was presented in section 2.7.1. It has been found that many of the schemes are effective in limited circumstances and often lead to complicated and fragile instruments. This presents a barrier in transferring the technology from the laboratory to the industry.

This project aims to investigate an alternative technique for eliminating interference fringes. The technique could potentially simplify instrument design, thereby aiding the transfer of technology to industry. The technique is based on using diffuse reflections (laser speckle) in the optical path as means of suppressing interference effects. The principle of the technique and the theory of speckle are presented in the following chapter.

2.10 References

[1] McWilliam, I. G. and Dewar, R. A. (1958), 'Flame Ionisation Detector for Gas Chromatography', *Nature*, V181, N4611, pp. 760.

[2] RAE systems inc (2004), *Comparison of photo ionisation detectors and flame ionisation detectors, Application note AP-226,* available at: http://www.raesystems.com/~raedocs/App_Tech_Notes/App_Notes/AP-226_PID_vs_FID_Comparison.pdf (accessed 2006).

[3] IUPAC Compendium of Chemical Terminology *flame ionization detector (in gas chromatography),* available at: http://www.iupac.org/goldbook/F02410.pdf (accessed 26th February 2006).

[4] Jones. E (1987), 'The Pellistor Catalytic Gas Detector', in Moseley, P. T. and Tofield, B. C. *Solid State Gas Sensors*, IOP Publishing, England, pp. 17-31.

[5] *INQ3. Technical specification for portable gas detectors* (1995), British Gas Transco,

[6] Gentry, S. J. and Walsh, P. T. (1987), 'The Theory of Poisoning of Catalytic Flammable Gas-sensing Elements', in Moseley, P. T. and Tofield, B. C. *Solid State Gas Detectors*, Adam Hilger, England, pp. 32-50.

[7] Jones, T. A. (1987), 'Characterisation of Semiconductor Gas Sensors', in Moseley, P. T. and Tofield, B. C. *Solid State Gas Sensors*, IOP Publishing, England, pp. 51-70.

[8] Occupational Safety and Health Administration (OSHA), U. S. D. o. L. 'Workshop - What to Look for in Gas Detection and Measurement Instrumentation ', in *53rd Annual Federal Safety and Health Conference* at Los Angeles;

[9] Banwell, C. N. and McCash, E. M. (1994), *Fundamentals of Molecular Spectroscopy* (4th edition), McGraw-Hill, London.

[10] Rothman *et al,* L. S. (1992), 'The HITRAN molecular database: editions of 1991 and 1992', *Journal of Quantitative Spectroscopy and Radiative Transfer*, V48, N5-6, pp. 469–507.

[11] Uehara, K. and Tai, H. (1992), 'Remote detection of methane with a 1.66-um diode laser', *Applied optics*, V31, N6, pp. 809-13.

[12] Gharavi, M. and Buckley, S. G. (2005), 'Diode laser absorption spectroscopy measurement of line strengths and pressure broadening coefficients of the methane $2v_3$ band at elevated temperatures', *Journal of Molecular Spectroscopy*, V229, N1, pp. 78-88.

[13] Schiff, H. I., Mackay, G. I., and Bechara, J. (1994), 'The use of tunable diode laser absorption spectroscopy for atmospheric measurements', in Sigrist, M. W. (Editor), *Air monitoring by spectroscopic techniques*, John Wiley and sons, New York, pp. 239-333.

[14] Olivero, J. J. and Longbothum, R. L. (1977), 'Empirical fits to the Voigt line width: a brief review', *Journal of Quantitative Spectroscopy and Radiative Transfer*, V17, N2, pp. 233-6.

[15] Ikegami, T., Sudo, S., and Sakai, Y. (1995), *Frequency Stabilisation of Laser Diodes*, Artech House, INC, Norwood, USA.

[16] Engelbrecht, R. (2004), 'A compact NIR fiber-optic diode laser spectrometer for

CO and CO2: analysis of observed 2f wavelength modulation spectroscopy line shapes', *Spectrochimica Acta Part A*, V60, N14, pp. 3291–3298.

[17] Norris, W. V. and Unger, H. J. (1933), 'Infrared Absorption Bands of Methane', *Physical Review*, V43, N6, pp. 467-72.

[18] Margolis, J. S. (1988), 'Measured line positions and strengths of methane between 5500 and 6180 cm^{-1}', *Applied Optics*, V27, N19, pp. 4038-51.

[19] Chaney, L., Rickel, D., Russwurm, G., and McClenny, W. (1979), 'Long-path laser monitor of carbon monoxide: system improvements ', *Applied Optics*, V18, N17, pp. 3004-9.

[20] Cassidy, D. T. and Reid, J. (1982), 'Atmospheric pressure monitoring of trace gases using tunable diode lasers', *Applied Optics*, V21, N7, pp. 1185-90.

[21] SIRA Technology LTD (2005), *Gas detector selection and calibration guide* (1st edition), Witherbys, London.

[22] Hess, P. (1989), 'Principles of Photoacoustic and Photothermal Analysis', in Hess, P. *Photoacoustic, Photothermal and Photochemical Processes in Gases*, Springer-Verlag, Berlin, pp. 1-13.

[23] Sigrist, M. W. (1994), 'Air monitoring by laser photoacoustic spectroscopy', in Sigrist, M. W. *Air monitoring by spectroscopic techniques*, John Wiley and Sons, Inc, New York,

[24] Innova Airtech Instruments (2005), *Measuring Gases with the Help of Microphones – Photoacoustic Effect,* available at: http://www.innova.dk/1412_details.gas_monitoring4.0.html (accessed 2006).

[25] Webster, C. R., Menzies, R. T., and Hinkley, E. D. (1988), 'Infrared laser absorption: Theory and applications', in Measures, R. M. *Laser Remote Chemical Analysis*, Wiley, New York, pp. 163-272.

[26] Werle, P. (1996), 'Tunable diode laser absorption spectroscopy: recent findings and novel approaches', *Infrared Physics and Technology*, V37, N1, pp. 59-66.

[27] Song, K. and Jung, E. C. (2003), 'Recent developments in modulation spectroscopy for trace gas detection using tunable diode lasers', *Applied spectroscopy reviews*, V38, N4, pp. 395-432.

[28] Bomse, D. S., Stanton, A. C., and Silver, J. A. (1992), 'Frequency modulation and wavelength modulation spectroscopies: comparison of experimental methods using a lead-salt diode laser', *Applied Optics*, V. 31, N6, pp. 718-30.

[29] Reid, J., Shewchun, J., Garside, B. K., and Ballik, E. A. (1978), 'High sensitivity pollution detection employing tunable diode lasers', *Applied Optics*, V17, N2, pp. 300-7.

[30] White, J. U. (1942), 'Long Optical Paths of Large Aperture', *Journal of Optical Society of America*, V32, N5, pp. 285.

[31] White, J. U. (1976), 'Very long optical paths in air', *Journal of Optical Society of America*, V66, pp. N5, 411–416.

[32] Herriott, D. R., Kogelnik, H., and Kompfner, R. (1964), 'Off-Axis Paths in Spherical Mirror Interferometers', *Applied Optics*, V3, N4, pp. 523.

[33] Herriott, D. R. and Schulte, H. J. (1965), 'Folded Optical Delay Lines', *Applied Optics*, V4, N8, pp. 883.

[34] Schilt, S., The´venaz, L., and Robert, P. (2003), 'Wavelength modulation spectroscopy: combined frequency and intensity laser modulation', *Applied Optics*, V42, N33, pp. 6729-36.

[35] Tang, C. L. and Telle, J. M. (1974), 'Laser modulation spectroscopy of solids ', *Journal of Applied Physics*, V45, N10, pp. 4503-5.

[36] Reid, J., El-Sherbiny, M., Garside, B. K., and Ballik, E. A. (1980), 'Sensitivity limits of a tunable diode laser spectrometer, with application to the detection of NO2 at the 100-pptv level', *Applied Optics*, V19, N19, pp. 3349-54.

[37] Bruce, D. M. and Cassidy, D. T. (1990), 'Detection of oxygen using short external cavity GaAs semiconductor diode lasers ', *Applied Optics* , V29, N2, pp. 1327-32.

[38] Iseki, T. (2004), 'A portable remote methane detector using an InGaAsP DFB laser', *Environmental Geology*, V46, N8, pp. 1064-9.

[39] Zhu, X. and Cassidy, D. T. (1995), 'Electronic subtracter for trace-gas detection with InGaAsP diode lasers ', *Applied Optics*, V34, N36, pp. 8305-8.

[40] Dharamsi, A. N. (1996), 'A theory of modulation spectroscopy with applications of higher harmonic detection', *Journal of Physics D: Applied Physics*, V29, N3, pp. 540-9.

[41] Cooper, D. E. and Warren, R. E. (1987), 'Frequency modulation spectroscopy with lead-salt diode lasers: a comparison of single-tone and two-tone techniques', *Applied Optics*, V26, N17, pp. 3726-32.

[42] Wang, L., Riris, H., Carlisle, C. B., and Gallagher, T. F. (1988), 'Comparison of approaches to modulation spectroscopy with GaAIAs semiconductor lasers: application to water vapor', *Applied Optics*, V27, N10, pp. 2071-7.

[43] Bjorklund, G. C. (1980), 'Frequency-Modulation Spectroscopy: a New Method for Measuring Weak Absorptions and Dispersions', *Optics Letters*, V5, N1, pp. 15,

[44] Carlisle, C. B., Cooper, D. E., and Prier, H. (1989), 'Quantum noise-limited FM spectroscopy with a lead-salt diode laser ', *Applied Optics*, V28, N13, pp. 2567-76.

[45] Werle, P., Slemr, F., Gehrtz, M., and Braeuchle, C. (1989), 'Quantum-limited FM-spectroscopy with a lead-salt diode laser', *Applied Physics B: Photophysics and Laser Chemistry*, V49, N2, pp. 99-108.

[46] Hall, J. L., Baer, T., Hallberg, L., and Robinson, H. G. (1981), 'Precision Spectroscopy and Laser Frequency Control Using FM Sideband Optical Heterodyne Techniques', in McKellar, A. R. W. et al. *Laser Spectroscopy V*Springer-Verlag, Berlin , pp. 16.

[47] Werle, P., Selmr, F., Gehrtz, M., and Brauchle, C. (1989), 'Wideband noise characteristics of a lead-salt diode laser: possibility of quantum noise limited TDLAS performance', *Applied Optics*, V28, N9, pp. 1638.

[48] Werle, P. and Slemr, F. (1991), 'Signal-to-noise ratio analysis in laser absorption spectrometers using optical multipass cells ', *Applied Optics*, V30, N4, pp. 430-4.

[49] Janik, G. R. , Carlisle, C. B., and Gallagher, T. F. (1986), 'Two-Tone Frequency-Modulation Spectroscopy', *Journal of the Optical Society of America*, VB , N3,

pp. 1070.

[50] Silver, J. A. (1992), 'Frequency-modulation spectroscopy for trace species detection: theory and comparison among experimental methods', *Applied Optics*, V31, N6, pp. 707-17.

[51] Supplee, J. M., Whittaker, E. A., and Lenth, W. (1994), 'Theoretical description of frequency modulation and wavelength modulation spectroscopy', *Applied Optics*, V33, N27, pp. 6294-302.

[52] Pavone, F. S. and Inguscio, M. (1992), 'Frequency- and Wavelength-Modulation spectroscopies: Comparison of Experimental Methods Using an AlGaAs Diode Laser', *Applied Physics B*, V56, pp. 118-22.

[53] Goldstein, N., Adler-Golden, S., Lee, J., and Bien, F. (1992), 'Measurement of molecular concentrations and line parameters using line-locked second harmonic spectroscopy with an AlGaAs diode Laser', *Applied Optics*, V31, N18, pp. 3409-15.

[54] Iseki, T. *LASERMETHANE^{TM}. A Portable Remote Methane Detector*, available at: http://www.gas.or.jp/english/letter/images/02/pdf/igrc_tg-2.pdf#search=%22LASER%20METHANE%E2%80%94%20A%20Portable%20Remote%20Methane%20Detector%22

[55] Jin, W., Xu, Y. Z., Demokan, M. S., and Stewart, G. (1997), 'Investigation of interferometric noise in fiber-optic gas sensors with use of wavelength modulation spectroscopy', *Applied Optics*, V36, N28, pp. 7239-46.

[56] Bowring, N. J., Lit, D., and Baker, J. G. (1994), 'Frequency stabilization of a 0.78 pm GaAIAs laser diode to acetylene absorption lines ', *Measurement Science and Technology*, V5, N10, pp. 1313-6.

[57] Tanaka, H., Matsuura, M., Tai, H. and Uehara, K. (inventors) Tokyo Gas Co, L.T.J., (Apr 13, 1993), *Gas detection device*. USA. 5202570.

[58] Iseki, T. (2003), 'Calculation of the ratio between the second and first harmonic signals in wavelength-modulation spectroscopy for absorption measurement', *Optical Review*, V10, N1, pp. 24-30.

[59] Kluczynski, P., Lindberg, S., and Axner, O. (2001), 'Characterization of Background Signals in Wavelength-Modulation Spectrometry in Terms of a Fourier Based Theoretical Formalism ', *Applied Optics*, V40, N6, pp. 770-82.

[60] Reid, J. and Labrie, D. (1981), 'Second-Harmonic Detection with Tunable Diode Lasers-Comparison of Experiment and Theory', *Applied Physics B*, V26, N3, pp. 203-10.

[61] Philippe, L. C. and Hanson, R. K. (1993), 'Laser diode wavelength-modulation spectroscopy for simultaneous measurement of temperature, pressure, and velocity in shock-heated oxygen flows', *Applied Optics*, V32, pp. 6090-103.

[62] Jacobsen, G., Olesen, H., Birkedahl, F., and Tromborg, B. (1982), 'Current/frequency-modulation characteristics for directly optical frequency modulated injection lasers at 830nm and 1.3μm', *Electronic letters*, V18, N20, pp. 874-6.

[63] Johnstone, W., Duffin, K., McGettrick, A., Stewart, G. , Cheung, A., and Moodie, D. (2005), 'Tuneable diode laser spectroscopy over optical fibres for gas measurements in harsh Industrial environments', in Jaroszewicz, L. R. et al.

Optical Fibers: Applications, V5952 International Society for Optical Engineering, United States, Warsaw, Poland, pp. 1-8.

[64] Silver, J. A. and Stanton, A. C. (1988), 'Optical interference fringe reduction in laser absorption experiments ', *Applied Optics*, V27, N10, pp. 1914-16.

[65] Werle, P. (1998), 'A review of recent advances in semiconductor based gas monitors', *Spectrochimica Acta Part A*, V54, N2, pp. 197-236.

[66] Iguchi, T. (1986), 'Modulation waveforms for second-harmonic detection with tunable diode lasers', *Journal of the Optical Society of America B (Optical Physics)*, V3, N3, pp. 419-23.

[67] Sano, H., Koga, R., and Kosaka, M. (1983), 'Analytical description of tunable diode laser derivative spectrometry ', *Japanese Journal of Applied Physics, Part 1 (Regular Papers & Short Notes)*, V22, N12, pp. 1883-8.

[68] Webster, C. R. (1985), 'Brewster-plate spoiler: a novel method for reducing the amplitude of interference fringes that limit tunable-laser absorption', *Journal of Optical Society of America B*, V2, N9, pp. 1464-70.

[69] Chou, S., Baer, D. S., and Hanson, R. K. (1997), 'Diode laser absorption measurements of CH_3Cl and CH_4 near 1.65µm', *Applied Optics*, V36, N15, pp. 3288-93.

[70] Petermann, K. (1988), 'Semiconductor lasers with optical feedback', in Petermann, K. *Laser diode modulation and noise*, Kluwer Academic Publishers, London, pp. 250-90.

[71] Petermann, K. (1988), *Laser diode modulation and noise*, Kluwer, Boston.

[72] Vodhanel, R. S. and Ko, J.-S. (1984), 'Reflection induced frequency shifts in single-mode laser diodes coupled to optical fibres', *Electronics Letters*, V20, N23, pp. 973-4.

[73] Kawano, K., Mukai, T., and Mitomi, O. (1986), 'Optical output power fluctuation due to reflected lightwaves in laser diode modules', *Journal of Lightwave Technology*, VT-4, N11, pp. 1669-77.

[74] Burke, W. J., Ettenberg, M., and Kressel, H. (1978), 'Optical feedback effects in cw injection lasers ', *Applied Optics*, V17, N14, pp. 2233-8.

[75] Yamada, M. and Suhara, M. (1990), 'Analysis of excess noise induced by optical feedback based on mode competition theory', *The transactions of the IEICE*, VE, N73, pp. 77-82.

[76] Fukuda, M., Ooyama, S., Utsumi, A., Kondo, Y., Kurosaki, T., and Masuda, T. 'Effect of optical feedback noise on tunable diode laser spectroscopy', *Applied Physics B: Lasers and Optics*, V90, No2, pp. 269-272 (2008)

[77] Masiyano D, Hodgkinson J, and Tatam R P, Use of diffuse reflections in tunable diode laser absorption spectroscopy: Implications of laser speckle for gas absorption measurements, *Applied Physics B: Lasers and Optics*, V90, No2, pp. 279-288 (2008).

[78] van Well, B., Murray, S., Hodgkinson, J., Pride, R., Strzoda, R., Gibson, G., and Padgett, M. (2005), 'An open-path, hand-held laser system for the detection of methane gas', *Journal of Optics A: Pure and Applied Optics*, V7, N6, pp. 420-4.

[79] Frish, M. B., Wainner, R. T., Green, B. D., Laderer, M. C., and Allen, M. G. (2005), 'Standoff gas leak detectors based on tunable diode laser absorption

spectroscopy', in *Infrared to Terahertz Technologies for Health and the Environment, Oct 24-25 2005,* V6010 International Society for Optical Engineering, Bellingham WA, WA 98227-0010, United States, Boston, MA, United States, pp. 60100.

[80] Iseki, T., Tai, H., and Kimura, K. (2000), 'Portable remote methane sensor using a tunable diode laser', *Measurement Science and Technology*, V11, N6, pp. 594-602.

[81] Tranchart, S., Bachir, I. H., and Destombes, J.-L. (1996), 'Sensitive trace gas detection with near-infrared laser diodes and an integrating sphere', *Applied Optics*, V35, N36, pp. 7070-4.

[82] Hawe, E., Fitzpatrick, C., Chambers, P., and Lewis, E. (2007), 'An investigation into the use of an integrating sphere as a gas absorption cell', *Journal of Applied Optics A: Pure and Applied Optics*, V9, N6, pp. S12-S18.

[83] Giuliani, G. , Norgia, M., Donati, S., and Bosch, T. (2002), 'Laser diode self-mixing technique for sensing applications', *Journal of Optics A: Pure and Applied Optics*, V4, N6, pp. 283-94.

[84] Schilt, S. and Thevenaz, L. (2004), 'Experimental method based on wavelength-modulation spectroscopy for the characterisation of semiconductor lasers under direct modulation', *Applied Optics*, V43, N22, pp. 4446-53.

[85] Acket, G. A. , Lenstra, D., den Boef, A. J., and Verbeek, B. H. (1984), 'The influence of feedback intensity on longitudinal mode properties and optical noise in index-guided semiconductor lasers', *IEEE Journal of Quantum Electronics*, VQE-20, N10, pp. 1163-9.

[86] Welford, D. and Mooradian, A. (1982), 'Observation of linewidth broadening in (GaAl)As diode lasers due to electron number fluctuations', *Applied Physics Letters*, V40, N7, pp. 560-2.

[87] Alexander, S. B. (1997), *Optical Communication Receiver Design*, V. IEE Telecommunications Series V. 37, IEE , London.

[88] Kruse, P. W. (1977), 'The photon detection process', in *Optical and infrared detectors*, Springer-Verlag, pp. 5-69.

[89] Picque, J.-L. and Roizen, S. (1975), 'Frequency-controlled cw GaAs tunable laser', *Applied Physics letters*, V27, N6, pp. 340.

[90] Yamaguchi, S. and Suzuki, M. (1982), 'Frequency locking of an InGaAsP semiconductor laser to the first overtone vibration-rotation lines of hydrogen flouride', *Applied Physics letters*, V41, N11, pp. 1034-6.

[91] Sudo, S., Sakai, Y., Yasaka, H., and Ikegami, T. (1989), 'Frequency-Stabilised DFB Laser Module Using 1.53159μm Absorption Line of C_2H_2', *IEEE Photonics Technology Letters*, V1, N10, pp. 281-4.

[92] Uehara, K. and Katakura, K. (1988), 'New method of frequency stabilisation of semiconductor lasers', *Japanese Journal of Applied Physics*, V27, N2, pp. 244-6.

[93] Tako, T., Ohtsu, M., and Tsuchida, H. (1981), 'Frequency stabilization of AlGaAs lasers based on the H_2O and Rb-D_2 lines', in *Third Symposium on Frequency Standards and Metrology, 12-15 Oct. 1981: Journal de Physique Colloque,* V42 Aussois, France, pp. 83-8.

[94] Yanagawa, T., Saito, S., and Yamamoto, Y. (1984), 'Frequency stabilisation of

1.5µm InGaAsP distributed feedback laser to the NH_3 absorption lines', *Applied Physics letters*, V45, N8, pp. 826-8.

Chapter 3 Laser Speckle

3.1 Background

The primary aim of this research is to investigate the use of scattering surfaces in the optical path of a TDLAS instrument as a means of reducing the effects of interference fringes. The formation, prevention and elimination of interference fringes were discussed in chapter 2 section 2.8.1. To reiterate; gas cell windows are one of the main sources of the interference fringes (illustrated in Figure 3-1 (a)). The fringe signals can cause misleading gas concentration readings and often limit the detection sensitivity. Measures taken to prevent the formation of fringes (e.g. careful alignment of optics) and to reduce interference fringe signals (e.g. mechanically dithering offending components) often lead to complicated, expensive and fragile designs; making the instruments unsuitable for field applications.

Under certain circumstances it has been claimed that using a diffuse reflector in the gas cell can prevent the formation of interference fringes[1-3]. This is the approach the project aims to explore. It has the potential to reduce instrument design complexity and lead to more robust designs.

The formation of fringes and the principle of the proposed approach are illustrated in Figure 3-1 below. Light from a laser diode is coupled into a fibre coupler. One arm is directed onto a detector after passing through a gas cell. As shown in Figure 3-1 (a), multiple reflections can lead to formation of interference fringes.

Figure 3-1(b) shows a proposed experimental system, designed to characterise speckle in a gas cell geometry. Light reflected from the diffuse surface end of the gas cell is imaged by the lens onto the CCD chip via the beam splitter and displayed on the monitor. The image on the monitor comprises a random interference or laser speckle. If the CCD camera is replaced by a detector, the detector measures gas absorption and random noise rather than the systematic noise (interference fringes).

The focus of this chapter is developing the theoretical framework for the investigation. Firstly, a qualitative description of laser speckle is given, followed by a brief account of the origins of speckle. Following that is a discussion of the fundamental properties of speckle that are relevant to the project. These include; factors that govern size, brightness distribution, and contrast of speckle patterns. Particular attention is paid to interference of speckle patterns.

(a) Basic TDLAS setup employing a 1650nm DFB laser

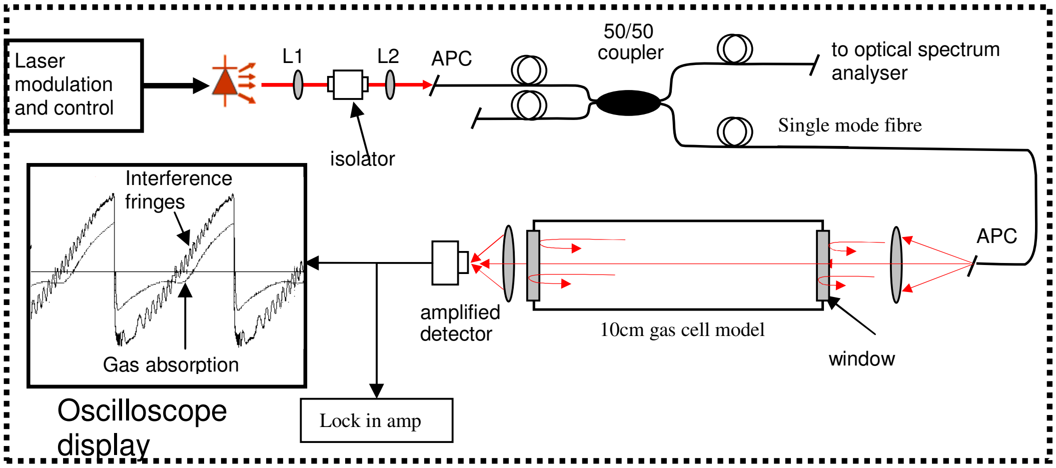

(b) Proposed experimental model at 823nm

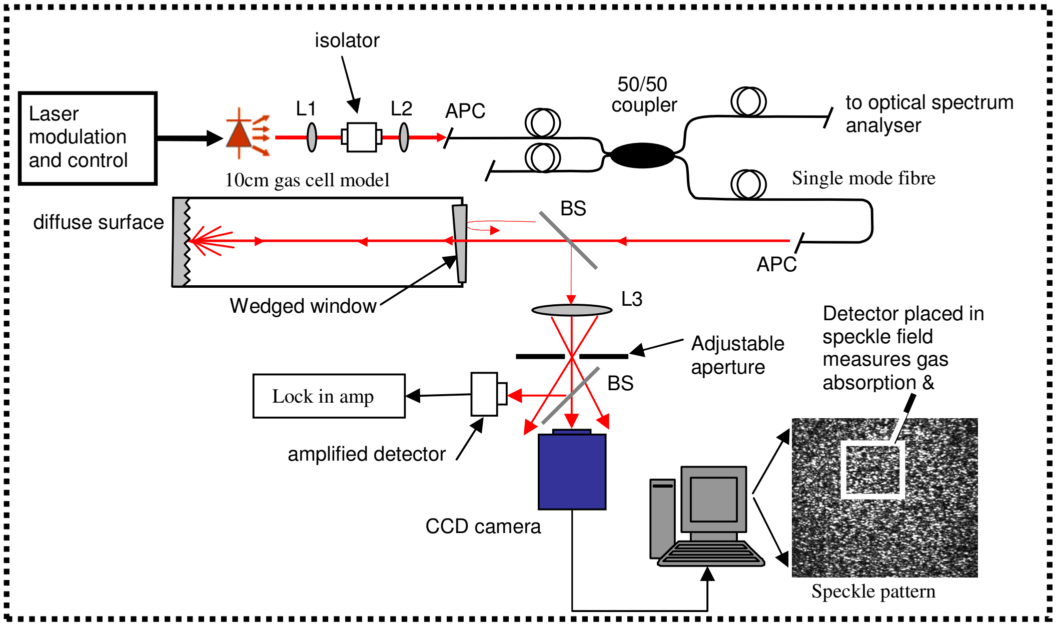

Figure 3-1: (a) demonstration of the formation of fringes in a gas cell, (b) Experimental setup for investigating the use of diffuse surfaces as a means of reducing interference fringes in WMS. Key, L_1, L2: lens; APC: angle polished connector; BS: beam splitter.

3.2 Statistical properties of laser speckle patterns

3.2.1 Introduction to speckle

The reflection of light incident on an optically rough surface, i.e. where the surface height deviations are greater than the wavelength of light, is not specular. Instead, the light is scattered in random directions dictated by the topography of the surface, as illustrated in Figure 3-2.

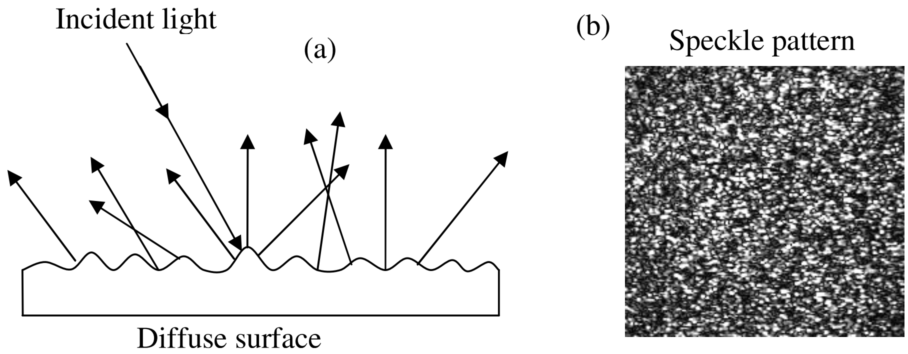

Figure 3-2: (a) diffuse reflection of light caused by an optically rough surface. (b) Speckle pattern; bright spots and dark spots correspond to where the interference has been highly constructive and destructive respectively.

When the source of illumination is coherent and monochromatic, such as a laser, the reflected components interfere and the surrounding region is filled with a complex, stationary, interference pattern. The pattern appears disordered, and has a grainy appearance (see Figure 3-2 (b)). The complex pattern bears no obvious relationship to the macroscopic properties of the object illuminated[4]. The picture of the observed effect was perhaps most vividly painted by Gabor[5] "A white sheet of paper appears as if it is crawling with ants. The crawling is put into it by the restless eye, but the roughness is real"

The wave reflected from an optically rough surface illuminated by a coherent monochromatic light source consists of contributions from many independent scattering areas. Wavelets that are scattered from different parts of the surface experience differences in their path lengths due to the topography of the surface. When two wavelets from different points on the surface intersect, they interfere and produce a fringe pattern. Since the light has high coherence, any pair of points can produce interference fringes, each pair's fringes being at different orientations and with different fringe separations. The resulting speckle pattern is a complex mix of a multitude of bright spots and dark spots where the interference has been highly constructive and destructive respectively.

3.2.2 Historical perspective of speckle

Although the speckle phenomenon has been known since the time of Newton, it came into prominence with the advent of the laser. It was first described by Oliver[6] in 1963 in a paper titled "Sparkling spots and random diffraction" in which he gave a qualitative explanation of speckle. This was summarised by Gabor[7]; "It arises by a diffraction effect at the receiving end or, more exactly, by the limitation of the amount of light admitted for image formation by the optical instrument or by eye". In other words, the speckle pattern is dependent on the image forming aperture.

Speckle has been long recognised as the “Enemy Number One” of holography[7]. Holographic reconstructions were often submerged in a very annoying speckle background and this was considered a bane of holographers[8]. Considerable efforts were made to eliminate the speckle from holograms[7].

The turning point occurred when it was realised that speckles could be used as a random pattern that carried information about the object surface. Gabor[9], who received a Nobel prize for discovering holography, made an insightful comment on speckle: “The novelty in holography is speckle noise. This has really nothing to do with holography; it is a consequence of coherence. It has a special standing among noise phenomena because it is not really noise but unwanted information. When we put a sheet of white paper into laser light, the reflected light conveys to us information on the roughness of the paper in which we are not at all interested. I am glad that Dr. J.M. Burch[10] has shown that we can make some use of this information”. Burch had presented his paper at the same conference.

The information-carrying capacity of speckle was fully utilised for interferometry measurements on real objects. This gave rise to a field known as speckle interferometry (SI)[8]. A concise description of SI was provided by Leendertz[11]; “If two speckle patterns are superimposed the distribution of intensity in the resultant pattern depends on the relative phases of the component patterns. By measuring the correlation between the resultant patterns at two different times a change of relative phase is detected. This leads to a versatile method of measuring either the normal or in-plane components of displacement over the whole of a surface at one time”. Speckle is therefore both a nuisance and a useful measuring tool in different applications.

Initially, SI was performed using photo-emulsions as recording medium; this was replaced by electronic imaging devices such as vidicon tubes and later charge- coupled devices (CCD) array detectors. Traditional photographic methods have been reviewed by Ennos[12]. Film-based methods are problematic owing to difficulties in the processing and final placement of the film sheets. The use of video methods in recording and correlating the speckle patterns was recognised early[13,14]. Due to its versatility, video recording has in recent years replaced many of the film-based methods[15]. The video-based method is referred to as Electronic Speckle Pattern Interferometry (ESPI). ESPI was originally developed for vibration analysis using time-average techniques from holography and was then successfully extended to static displacement measurements, heterodyning and stroboscopic techniques to recover the vibrational phase information and surface profile measurement[16]. ESPI enables displacements to be measured in real-time to a sensitivity of the order of a wavelength of light and surface shape to be measured over a range of sensitivity from a few micrometers to several millimetres[17]. The power of ESPI is demonstrated by the diversity of its applications[8,16,18].

Advances in electronic recording and computer processing of interferometric speckle patterns have made ESPI a powerful, relatively inexpensive, tool for laboratory and industrial use. Details of developments in the optoelectronic technology used in SI instrumentation can be found in a review paper by Tatam[19]. A typical ESPI configuration employing a laser diode and optical fibres is shown in Figure 3-3.

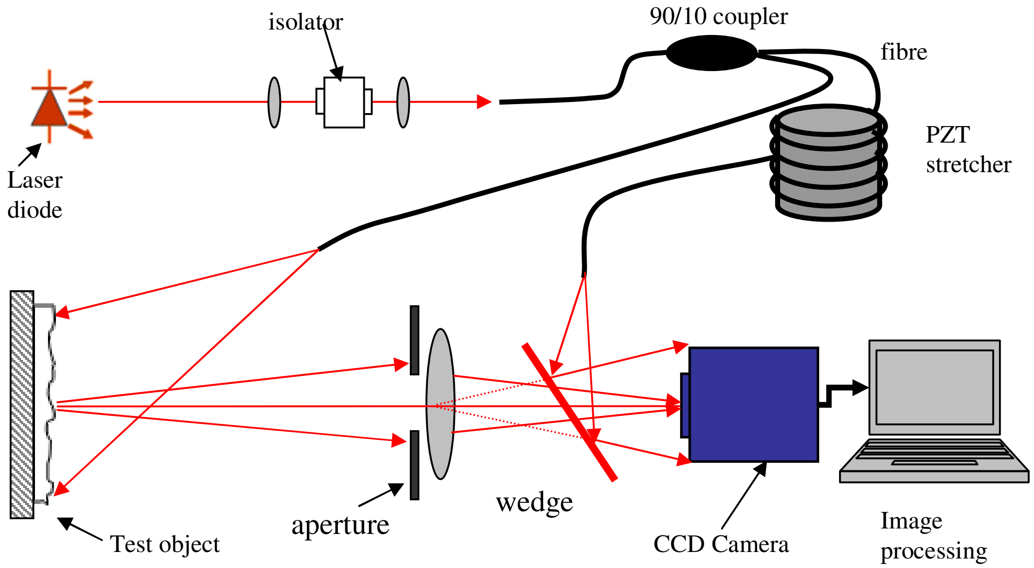

Figure 3-3: A typical ESPI setup employing optical fibre. After Tatam[20].

A coherent light source is coupled into a single mode fibre through an isolator. The isolator prevents optical coupling back to the laser diode. The coupler provides the reference and object beam, with the majority of the coupled light incident on the test object. The scattered light is collected by the lens and imaged onto a CCD camera through a beam splitter. The reference beam is directed onto the CCD through the same beam splitter, where it is mixed with the imaged scattered light from the object surface to form an interferometric speckle pattern. The PZT stretcher provides a phase shift between the interferometric speckle patterns before and after object displacement. The interferometric speckle patterns can be stored electronically for subsequent computer processing.

The following sections cover the fundamentals of speckle relevant to the project. These include;

1. size of speckles; if a detector is placed in a speckle field, the speckle related intensity uncertainty is expected to be related to the number of speckles and therefore speckle size,
2. polarisation; only light in the same polarisation state can interfere,
3. behaviour of speckle under wavelength modulation.

3.2.3 Size of an objective speckle field

The size of laser speckles, a statistical average of the distance between adjacent regions of maximum and minimum brightness, is always related to the aperture angle that the radiation giving rise to it subtends at the plane defining the speckle field[12]. The formation of objective speckle is illustrated in Figure 3-4.

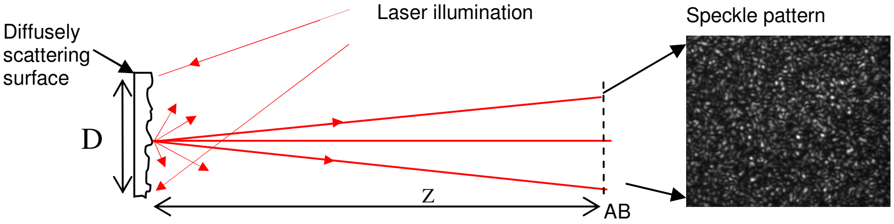

Figure 3-4: Illustration of the formation of objective speckle at screen AB. Key: D; the illuminated area, Z; the distance to the observation plane AB.

The size (diameter) ε_0 of the objective speckles formed on the screen AB at a distance Z, by the scattering of coherent light from a circular region of diameter D is given approximately by

$$\varepsilon_o = 1.2\lambda Z / D \qquad \textbf{(3-1)}$$

where λ is the wavelength of light[12]. This relationship can be can be visually confirmed by stopping the pupil of the eye (squinting) whilst observing a white sheet of paper illuminated by coherent light. “Squint and the grains grow in size; step toward the screen and they shrink; take off your glasses and the pattern stays in perfect focus”[21].

3.2.4 Size of a subjective speckle field

If, alternatively, the speckle is formed by collecting the scattered radiation field with a lens and focussing it on to the screen CD (Figure 3-5), a ‘subjective’ speckle pattern is formed[12].

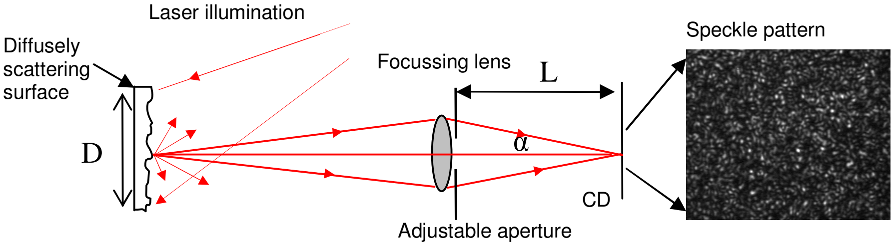

Figure 3-5: Illustration of the formation of objective speckle at screen AB and subjective speckle at screen CD. Key: D; CD; the image plane.

The size of the individual speckles at the screen CD is then related to the effective numerical aperture N.A. of the lens by[12]

$$\varepsilon_s = 0.6\lambda / N.A \tag{3-2}$$

It is often useful to relate the speckle size to the f-number (F#, ratio of the focal length to aperture) and to the magnification Π at which the lens is operating. According to Ennos[12], the speckle size is then

$$\varepsilon_s = 1.2(1+\Pi)\lambda F\# \tag{3-3}$$

Speckle size is an important parameter particularly when the speckle data is recorded on a CCD array. For ESPI the speckles must be large compared with the pixel size so that the speckle intensity variations can be resolved[22]. However a large number of speckles in each image sample are necessary for meaningful statistical evaluation, requiring that their size be kept to a minimum.

The speckle size can be matched to the pixel size of the CCD array by choosing a collecting lens with an appropriate f-number. The smallest speckles have diameters ε that are of the order of the magnitude of the diffraction pattern of the image forming-lens. Francon[23] has shown that if the diameter of the image-forming lens in Figure 3-5 is *2a* and the distance *L* between the lens and the plane of observation is such that $\alpha=a/L$, then the smallest speckle size is given by

$$\varepsilon = \lambda / \alpha \tag{3-4}$$

3.2.5 Effects of polarisation on speckle formation

Since the speckle phenomenon is itself an interference one, a true ‘fully developed’ speckle pattern can derive only from interference of light that is all polarised in the same manner[12]. If the light illuminating the interferometer comes from a linearly polarised laser, and the diffuse reflections do not depolarise the light, then the field where the lens forms images of the two surfaces will contain a high contrast speckle pattern[24]. Surfaces at which polarised light is singly scattered generally give rise to a polarised speckle field, as do also lightly-scattering transmission elements, such as ground glass. On the other hand, surfaces into which light penetrates and is multiply scattered, such as matt white paint or opal glass, depolarise the light and thus do not generate a fully developed speckle pattern[12]. The brightness of distribution of this type of speckle pattern is markedly different from that of a ‘fully-developed’ speckle[12]. Brightness distribution is defined in the following section.

3.2.6 Brightness distribution of a single speckle field

Another important statistical property of a speckle pattern is the likelihood of observing a bright peak or a dark null in the irradiance at a given point (the probability distribution of the irradiance *I*). It has been shown by several authors [4,8,12] that the distribution of the brightness among the speckles of a fully developed pattern is governed by the negative exponential relationship

$$\rho(I) = \begin{pmatrix} (1/I_0)\exp(-I/I_0), & I > 0 \\ 0, & \text{otherwise} \end{pmatrix} \quad \textbf{(3-5)}$$

where $\rho(I)$ is the probability that a speckle has brightness between the values I and $(I + \Delta I)$, and I_o is the average brightness. The probability density function is plotted in Figure 3-6 below.

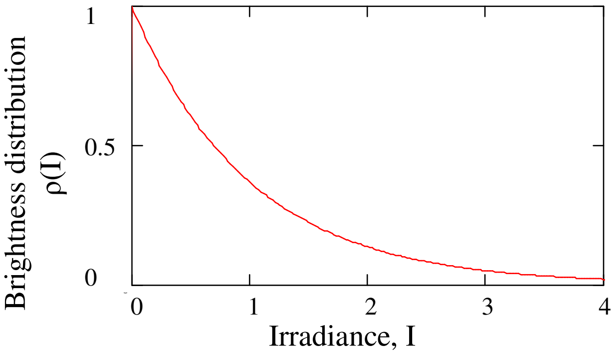

Figure 3-6: Theoretical plot of the probability density function of the brightness distribution of a polarised speckle pattern (equation 3-5).

The most probable brightness of a speckle is zero; in other words, there are more dark speckles in the field than speckles of any other brightness[12]. It is this property that is of the greatest importance in distinguishing a fully-developed speckle pattern from one less well-developed (or washed out), especially when it is observed visually[12].

3.2.7 Coherent combination of speckle and uniform fields

A simple interferometer can be made by combining a uniformly bright field of coherent radiation (a reference beam) with a speckle field. It is necessary for the rays of the reference beam to be directed along the axes of the speckle-forming rays (see Figure 3-3). The addition of the reference field will have an effect both upon the size and the brightness distribution of the speckles[12]. The diameter of a speckle approximately doubles when a reference field is added to the speckle pattern[12]. According to Ennos[12], the reason for this doubling in speckle size can be understood by considering the interference effect of adding a single strong wave to the speckle-forming waves in the direction of their axis. “The size of a speckle without the addition of the reference beam corresponds roughly to the spacing of the interference fringes generated by waves coming from the opposite ends of a diameter of the speckle-forming pupil. When the strong reference wave is introduced, the principal interference effects will take place with respect to this central strong ray, so that the maximum angle between interfering rays is halved, thus doubling the interference fringe spacing. On this reasoning the diameter of the speckles is also doubled”[12].

Dainty[25] has considered the statistical distribution of brightness of the resultant pattern when the uniform field is added to the speckle pattern in varying proportions. When the average speckle brightness is equal to the reference field brightness, the intensity distribution is expressed by

$$\rho(I) = (r+1)\exp[-r - I(r+1)]J_0\left(2\sqrt{Ir(r+1)}\right) \tag{3-6}$$

where J_0 is the modified Bessel function of zero order with imaginary argument, and r is the ratio of the uniform (I_u) beam to the average intensity of the speckle alone (I_0)[12]. This relationship is plotted as curve 2 in Figure 3-7 below for different values of r.

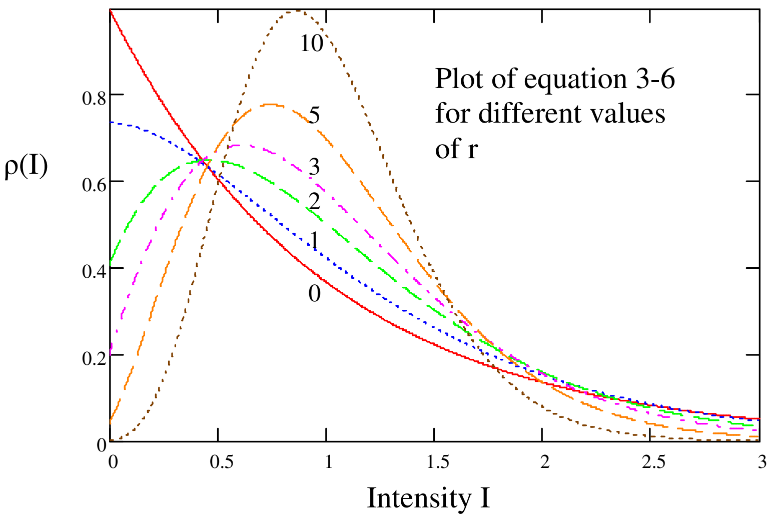

Figure 3-7: The normalised probability density function of the brightness distribution of a polarised resulting from the coherent combination of a speckle field and uniform field, for beam ratios, r, equal to 0, 1, 2, 3, 5, 10.

The significance of equation (3-6) is that when *r=0*, it resembles the distribution curve for the speckle pattern alone, equation (3-5). The most probable brightness is still zero, so that its texture can be readily recognised[12]. For *r>1* the most probable brightness is not zero. To facilitate comparison between the two equations ((3-5) and (3-6)) it should be noted that

$$r+1 = \frac{I_u + I_0}{I_0} \tag{3-7}$$

and that the total intensity (I_u+ I_0), is unity, giving $r+1 = 1/I_0$[25].

3.2.8 Contrast of a speckle pattern

The contrast C or normalised standard deviation of a polarised speckle pattern is defined as

$$C = \frac{\sigma_I}{I_{av}} \tag{3-8}$$

where I_{av} is the average irradiance and σ_I is the standard deviation of the irradiance given by

$$\sigma = \left[\beta \sum_{i=1}^{N} \frac{(I_i - I_{av})^2}{N-1} \right]^{1/2} \qquad \textbf{(3-9)}$$

where β is the coherence factor that accounts for the finite size of the detection area and the depolarisation of light in the medium[26]. The coherence factor approaches one only if a polarisation filter and a point detector are used[27].

The irradiance of a speckle pattern obeys negative exponential statistics (see equation (3-5)) , with the important consequence that its standard deviation equals the mean[4]. The contrast of a fully developed static (no relative motion between scattering surface and CCD camera) speckle pattern in equation (3-8) above is therefore always equal to $\beta^{1/2}$ or unity if β =1. Relative motion can lead to temporal intensity fluctuations with a time constant given by the local velocity[27]. In this case a time averaged quantity can be measured by choosing a certain camera exposure time T[27]. The average speckle contrast reduces according to

$$C^2 = (\beta / T) \int_0^T 2(1 - t/T) C(t) dt \qquad \textbf{(3-10)}$$

where C(T), given by $\langle I(0) I(\tau) \rangle / \langle I \rangle^2$, is the intensity correlation function[27].The contrast reduces to[27]

$$C = \sqrt{\beta \frac{e^{-2(T/\tau_c)} - 1 - 2(T/\tau_c)}{2(T/\tau_c)^2}} \qquad \textbf{(3-11)}$$

for a simple exponential decay, i.e. ($C(t) = \exp(-\tau/\tau_c)$.

A speckle pattern can be suppressed by adding many uncorrelated speckle patterns on an irradiance basis[4]. This results from the probability theory; "the sum of M identically distributed, real-valued, uncorrelated random variables has a mean that is M times the mean of one component, and a standard deviation which is $\sqrt{M}$ times the standard deviation of one component"[4]. Thus the contrast of the resultant speckle pattern is reduced by $1/\sqrt{M}$ by making appropriate substitutions in equation (3-8);

$$C = \frac{\sigma_I}{\sqrt{M} I_{av}} \qquad \textbf{(3-12)}$$

If a smooth reference beam of average intensity I_u is added to the speckle pattern as described in section 3.2.7, the contrast of such a speckle pattern has been shown by Goodman[28] to be

$$C = \frac{\sigma_I}{I_{av}} = \frac{\sqrt{1+2r}}{1+r} \qquad \textbf{(3-13)}$$

where I_{av} is the average total irradiance of the combined beams, $r = I_u / I_0$, and I_0 is the mean intensity of the speckle pattern alone. The contrast of such as pattern is plotted in Figure 3-8 and shows that the irradiance fluctuation may be quite large even for high beam ratios.

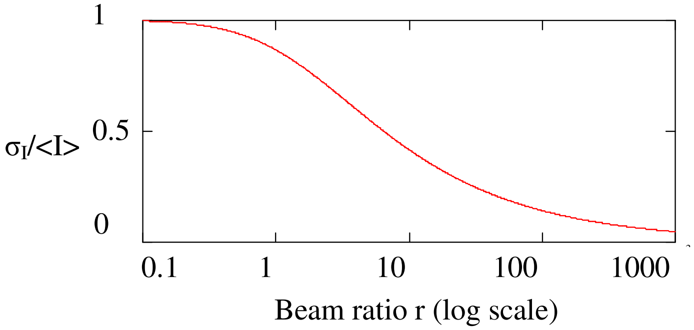

Figure 3-8: The standard deviation of the irradiance fluctuation relative to the total average irradiance as a function of the beam ratio r

3.2.9 Speckle patterns produced under a change of wavelength

In the system shown in Figure 3-5, if the wavelength of the incident radiation is changed from λ to λ_1 without disturbing the setup, there will be a phase difference δ introduce in the speckle patterns at the observation plane *AB* associated with the wavelength change $\Delta\lambda$. According to Francon[23] this difference in phase, δ, due to wavelength change is equal to

$$\delta = 2\pi\Delta_D \frac{\Delta\lambda}{\lambda^2} \qquad \textbf{(3-14)}$$

where Δ_D is a characteristic of the diffuse object and represents the average path difference due to the non uniformity of the thickness of the diffuser. Chromatic aberration of the lens is assumed to be small enough to have no effect and phase variations due to the thickness variations of the diffuse object are taken into account. The two speckle patterns corresponding to the two wavelengths λ and λ_1 are practically identical when

$$\Delta_D \frac{\Delta\lambda}{\lambda^2} << 1 \qquad \textbf{(3-15)}$$

3.2.10 Dependence of speckle statistics on surface roughness.

Fujii and Asakura[29] have investigated the effect of surface roughness on the statistical distribution of image speckle intensity. They have shown that the probability distribution and the standard deviation of the intensity fluctuations in image speckle patterns are strongly dependent on the surface roughness h. The probability distribution was found to vary from a negative exponential (Poisson) distribution for surfaces with h>λ to a blend of Poissonian and Gaussian distributions for decreasing value of roughness. They similarly found that the standard deviation of the intensity fluctuations increases almost linearly with increasing roughness and then levels off at a constant value corresponding to h>λ . This constant value corresponds to the fully developed speckle condition.

3.3 Speckle Interferometry

3.3.1 Addition of laser speckle fields

Speckle patterns can be added on either an amplitude basis or an intensity basis. In amplitude addition, there is no alteration in the statistics except for a scaling factor[8]. An example of addition of two speckle patterns on an amplitude basis is found in speckle shearing interferometry where two speckle patterns are spatially shifted and then are coherently superposed[8]. Addition on an intensity basis, for example if two speckle records are made on the same plate, changes the statistics, for example the most probable brightness of the speckle is no longer zero. Speckle statistics are now governed by a correlation coefficient.

Jones and Wykes[30] have shown that the correlation coefficient is given by (details in Appendix C).

$$\rho(\delta) = \frac{1 + r^2 + 2r\cos\delta}{(1+r)^2} \tag{3-16}$$

where $r = \frac{\langle I_2 \rangle}{\langle I_1 \rangle}$ is the ratio of the intensity of the two interferometric speckle patterns, and δ is the phase difference between them. The correlation coefficient is unity when the patterns have the same intensity and are in phase[8]. When the intensity ratio, r, is equal to one, equation (3-16) reduces to

$$\rho(\delta) = (1 + \cos\delta)/2 \tag{3-17}$$

This simple relationship shows that the correlation coefficient ranges according to a cosine relationship from 1 to 0 as δ evolves from in phase to out of phase.

The changes in phase of the light scattered from the surface can therefore be measured from the degree of the correlation between two speckle patterns acquired before and after deformation of an object. A good correlation of speckle intensities is observed from regions of the displaced surface that are in phase, whereas there is no correlation otherwise. A mapping of this correlation over the surface of the object results in a fringe pattern that contains information on the displacement of the object's surface.

3.3.2 The principle of speckle interferometry and correlation fringe formation

The first papers on the field of SI were presented by Leendertz in 1969[31] and 1970[11]. These two papers are credited with initiating the field of speckle interferometry[24]. SI is the basis of many well established techniques for the measurement of surface deformations or contours. Particular geometric setups are known to be predominantly sensitive to in-plane and out-of-plane displacement components, and in the case of speckle shearing interferometry to partial derivatives of the out-of-plane component[32]. It is common to all applications that they make use of the interference of a speckle object wave and a smooth or speckled reference wave. The effect of adding a smooth reference wave to a speckle pattern has been considered in section 3.2.7.

In this section the principle of speckle pattern correlation fringe formation is described with reference to Figure 3-9 below: A plane wave front U_0 incident on the beam splitter is split into two components of equal intensity that illuminate the optically rough surfaces *D1* and *D2*. The wave fronts scattered from *D1* and *D2* interfere on recombination at *B* and are recorded in the image plane of the lens-aperture combination.

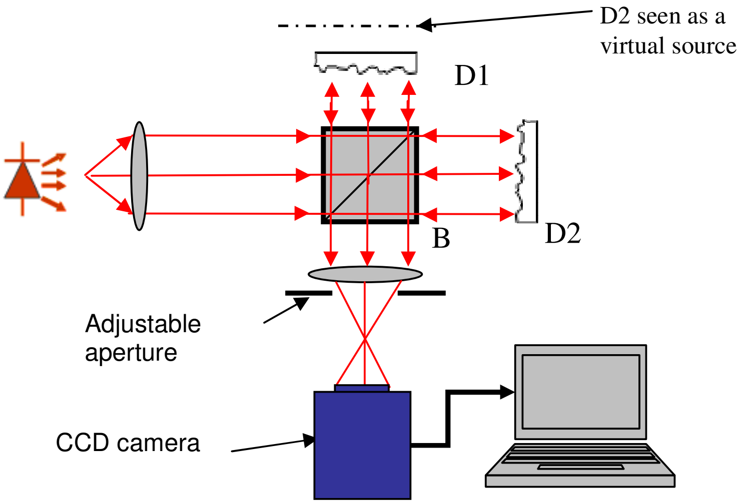

Figure 3-9: The Michelson arrangement of out of plane displacement sensitive speckle pattern correlation interferometer. After Jones and Wykes[30].

The intensity distribution in the image plane will consist of an interference pattern formed between the image-plane speckle patterns of *D1* and *D2* seen as a virtual source in the dashed position[30]. By letting

$$U_1 = u_1 e^{i\psi_1} \text{ and } U_2 = u_2 e^{i\psi_2} \tag{3-18}$$

be the complex amplitudes of these wave fronts where u_1, u_2 and ψ_1 , ψ_2 correspond to the randomly varying amplitude and phase respectively of the individual image-plane speckles. Jones and Wykes[30] showed that the intensity of a given point in the image plane is given by

$$I_a = I_1 + I_2 + 2\sqrt{I_1 I_2}\cos\Psi \tag{3-19}$$

where $I_1 = U_1 U_1^*$, $I_2 = U_2 U_2^*$ and $\Psi = \psi_1 - \psi_2$, where * represents the complex conjugate.

Unlike the situation in classical interferometry, this intensity distribution represents a speckle pattern rather than a fringe pattern because ψ_1 and ψ_2 are randomly variable from each speckle across the image In order to generate a fringe pattern, the object wave has to carry an additional systematic phase change that may arise due to deformation or displacement of the object[8]. When D_1 is displaced a distance d_1 parallel to the surface-normal, the resultant phase change is given by

$$\Delta\delta(d_1) = 4\pi d_1 / \lambda \tag{3-20}$$

This will change the intensity at a point to I_b, where

$$I_b = I_1 + I_2 + 2\sqrt{I_1 I_2}\cos(\Psi + \Delta\delta(d_1)) \tag{3-21}$$

Here the assumption is that that no decorrelation of the speckle pattern occurs because of object deformation. Here the term decorrelation refers to the speckle pattern after displacement "losing touch" with the original speckle pattern due to perhaps excessive displacement. If the addition of the two interferometric speckle patterns is done on an intensity basis the resultant intensity I will be the sum of the two intensities I_a and I_b and hence can be written as[8]

$$I = 2I_1 + 2I_2 + 4\sqrt{I_1 I_2}\cos(\Psi + \Delta\delta/2)\cos(\Delta\delta/2) \tag{3-22}$$

According to Sirohi[8] the first two terms represent a random intensity distribution and as such are due to the superposition of two speckle patterns. The third term is the intermodulation term in which $\cos(\Psi + \Delta\delta/2)$ shows a random speckle variation within an envelop defined by $\cos(\Delta\delta/2)$. The third term would be zero wherever $\cos(\Delta\delta/2) = 0$ and would have the maximum value when $\cos(\Delta\delta/2) = 1$. Therefore, as $\Delta\delta$ varies over the object surface, the intensity would show variation on a gross scale. This intensity variation is termed the fringe pattern but the fringes are highly speckled. There is a dark fringe whenever

$$\Delta\delta = (2n+1)\pi \quad n = 0,1,2... \tag{3-23}$$

and a bright fringe when

$$\Delta\delta = 2n\pi \quad n = 0,1,2.. \tag{3-24}$$

"In other words a bright fringe is formed when the two speckle patterns are fully correlated and a dark fringe is formed when they are not correlated. For this reason these are also called correlation fringes"[8] (Figure 3-10). This is the basis of electronic speckle pattern interferometry (ESPI).

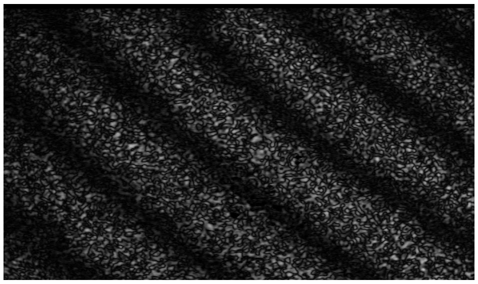

Figure 3-10: Fringes obtained using electronic speckle pattern interferometry, ESPI

According to Jones and Wykes[30] the maximum correlation occurs along lines where

$$d_1 = 1/2n\lambda \quad n = 0,1,2 \tag{3-25}$$

and the minimum correlation exists where

$$d_1 = \frac{1}{2(n+1/2)\lambda} \quad n = 0,1,2 \tag{3-26}$$

The contrast of these fringes can be increased considerably by removing the dc speckle component $2I_1+2I_2$ (equation (3-22)). This can be achieved by performing subtraction speckle interferometry[8]. This is possible when electronic detection processing is employed and is discussed in the next section.

3.3.3 Speckle pattern correlation fringe formation by electronic signal subtraction

Electronic Speckle Pattern Interferometry (ESPI) uses electronic signal processing to generate correlation fringes[30]. The basic measurement system consists of an optical head, CCD camera, host computer, image processing system and a display monitor (Figure 3-3). A specimen illuminated with an expanded laser beam forms a speckle pattern. The scattered speckle pattern is imaged onto a CCD. Since the speckle size can be controlled by the lens aperture (section 3.2.3), it can be matched to the resolution of the electronic detector. The analogue video signal from the CCD array is sent to an analogue-to-digital converter, which samples the video signal at a given rate and records it as a digital frame in the memory of the computer for further processing. A reference wave, which may or may not be speckled, is added at the observation plane to achieve interference between the object and reference waves. The resultant speckle pattern is stored in the processor and displayed on the monitor. The object deformation creates a path difference between the wave front scattered from its surface and the reference wave, and this modified speckle pattern is either subtracted or added to the previously stored pattern. The signal is rectified since the monitor cannot display negative values. The signal is also high-pass filtered in order to reduce the effect of the varying intensity of the laser beam across the field of view"[33]. The bright and dark fringes displayed on the monitor are referred to as correlation fringes and represent contour lines of constant surface displacement[34].

In subtraction ESPI the image from an object in its initial state is recorded and stored electronically. The object is then displaced and the digitised live camera signal of the deformed state of the object is subtracted pixel by pixel from the stored signal. Areas of the two images where the speckle pattern remains correlated will give a resultant signal of zero, while uncorrelated areas will give non-zero signals[30].

3.4 Summary

This chapter has presented the fundamental properties of speckle. Due to its random nature, speckle is described statistically. The statistical properties were presented in section 3.2. This knowledge of speckle statistics will facilitate the characterisation of speckle patterns of different materials that will be investigated and the quantification of speckle related intensity uncertainty.

As the primary motivation of the project is the reduction of interference fringes in TDLAS, conditions under which interference effects can occur in speckle were also considered (section 3.3). Under certain conditions, interference effects can occur due to coherent combination of a smooth wave and a speckle pattern or two speckle patterns.

Contrast of a speckle pattern can be reduced by $1/\sqrt{M}$ by averaging M uncorrelated speckle patterns.

The theory presented in this chapter will form the foundation for a methodology for investigating the use of speckle effects (diffuse reflections) in TDLAS. The development of the methodology is presented in the following chapter.

3.5 References

[1] Tranchart, S, Bachir, I. H., and Destombes, J-L. (1996), 'Sensitive trace gas detection with near-infrared laser diodes and an integrating sphere', *Applied Optics*, V35, N36, pp. 7070-7074.

[2] Atia W A and Flanders D C Axsun Technologies, Inc (27 March 2006), *Method and System for Reducing Parasitic Spectral Noise in Tunable Semiconductor Source Spectroscopy System*. USA. 20060187457.

[3] Owen, G. (1997), 'Suppression of interference effects in spectroscopy using an integrating sphere', *Review of Scientific Instruments*, V68, N3, pp. 1369.

[4] Goodman, J. W. (1976), 'Some fundamental properties of speckle', *Journal of Optical Society of America*, V66, N11, pp. 1145-1150.

[5] Gabor, D. (1972), 'Holography, 1948-1971', *Science*, V177, N4046, pp. 299-313.

[6] Oliver, B. M. (1963), 'Sparkling spots and random diffraction', *Proceedings of the IEEE*, V51, N1, pp. 220-221.

[7] Gabor D 1970 *Conference on Holography and the Computer, 10-12 Dec. 1969: IBM Journal of Research and Development* 14 *IBM J. Res. Dev. (USA)* (Houston, TX, USA pp 509-14.

[8] Sirohi, R. S. (2002), 'Speckle interferometry', *Contemporary Physics*, V43, N3, pp. 161-180.

[9] Gabor D 1971 *Proceedings of the SPIE Seminar on Developments in Holography, 14-15 April 1971 Proceedings of the SPIE Seminar on Developments in Holography* (Boston, MA, USA: Soc. Photo-optical Instrumentation Engrs) pp 129-33.

[10] Burch J M 1971 *Proceedings of the SPIE Seminar on Developments in Holography, 14-15 April 1971 Proceedings of the SPIE Seminar on Developments in Holography* (Boston, MA, USA: Soc. Photo-optical Instrumentation Engrs) pp 149-56.

[11] Leendertz, J. A. (1970), 'Interferometric displacement measurement on scattering surfaces utilizing speckle effect', *Journal of Physics E (Scientific Instruments)*, V3, N3, pp. 214-8.

[12] Ennos A E 1975 *Laser Speckle and Related Phenomena* (Berlin: Springer-Verlag) pp 203-53.

[13] Biedermann, K. and Ek, L. (1975), 'A recording and display system for hologram interferometry with low resolution imaging devices', *Journal of Physics E (Scientific Instruments)*, V8, N7, pp. 571-6.

[14] Lokberg, O. J. and Hogmoen, K. (1976), 'Vibration phase mapping using electronic speckle pattern interferometry', *Applied Optics*, V15, N11, pp. 2701-4.

[15] Schmitt, D. R. and Hunt, R. W. (1997), 'Optimization of fringe pattern calculation with direct correlations in speckle interferometry', *Applied Optics*, V36, N34, pp. 8848-57.

[16] Olszak, A. and Tatam, R. P. (1997), 'The calibration of the path-length imbalance in optical fibre ESPI systems employing source-wavelength modulation', *Measurement Science and Technology*, V8, N7, pp. 759-63.

[17] Varman, P. and Wykes, C. (1982), 'Smoothing of speckle and moire fringes by computer processing', *Optics and Lasers in Engineering*, V3, N2, pp. 87-100.

[18] Ford, H. D., Atcha, H., and Tatam, R. P. (1993), 'Optical fibre technique for the measurement of small frequency separations: application to surface profile measurement using electronic speckle pattern interferometry', *Measurement Science and Technology*, V4, N5, pp. 601-7.

[19] Tatam, Ralph P. (1999), 'Speckle interferometry: Optoelectronic developments and applications', *Proceedings of the Interferometry '99: Applications, Sep 20-Sep 23 1999: Proceedings of SPIE - The International Society for Optical Engineering*, V3745, pp. 114-133.

[20] Tatam, R. P. and others (1990), 'Holographic surface contouring using wavelength modulation of laser diodes', *Optics and Laser Technology*, V22, N5, pp. 317-21.

[21] Hecht, E. (1998), *Optics* (3rd edition), Addison Wesley Longman, England.

[22] Alexander, T L., Harvey, J. E., and Weeks, A. R. (1994), 'Average speckle size as a function of intensity threshold level: comparison of experimental measurements with theory', *Applied Optics*, V33, N35, pp. 8240-8250.

[23] Francon, M. (1979), *Laser Speckle and Applications in Optic*, Academic, London.

[24] Stetson, K. A. (1975), 'A review of speckle photography and interferometry', *Optical Engineering*, V14, N5, pp. 482-9.

[25] Dainty, J. C. (1972), 'Coherent addition of a uniform beam to a speckle pattern', *Journal of the Optical Society of America*, V26, N4, pp. 595-6.

[26] Rojas-Ochoa, L. F. and others (2004), 'Depolarization of backscattered linearly polarized light', *Journal of the Optical Society of America A: Optics and Image Science, and Vision*, V21, N9, pp. 1799-1804.

[27] Volker, A. C. 1 and others (2005), 'Laser speckle imaging with an active noise reduction scheme', *Optics Express*, V13, N24, pp. 9782-9787.

[28] Goodman J W 1975 *Laser Speckle and Related Phenomena* (Berlin: Springer-Verlag) pp 9-75.

[29] Fujii, H. and Asakura, T. (1974), 'Effect of surface roughness on the statistical distribution of image speckle intensity', *Optics Communications,* V11, N1, pp. 35-38.

[30] 1989 *Holographic and Speckle Interferometry* 2nd edn Jones R and Wykes C (Cambridge, UK: Cambridge University Press).

[31] Leendertz J A (1970) *Optical Instruments and Techniques, 14-19 July 1970 Optical Instruments and Techniques* (Reading, UK: Oriel Press) pp 256-64.

[32] Lehmann, M. (1995), 'Optimization of wavefield intensities in phase-shifting speckle interferometry', *Optics Communications*, V118, N3-4, pp. 199-206.

[33] Dainty J C 1976 *Progress in Optics, V.XI*: North-Holland) pp 3-46.

[34] Mohan, Nandigana Krishna and Rastogi, Pramod (2003), 'Recent developments in digital speckle pattern interferometry: Recent Developments in Digital Speckle Pattern Interferometry', *Optics and Lasers in Engineering*, V40, N5-6, pp. 439-445.

Chapter 4 Investigation of diffuse reflections in tunable diode laser absorption spectroscopy

The theory of laser speckle and speckle interferometry was presented in Chapter 3. This chapter is concerned with examining the implications of the theory on the use of diffuse reflections in TDLAS. The motivation for using diffuse reflections is to reduce the problem of interference fringes originating primarily from gas cell windows. A review of methods that have been proposed by other researchers to reduce the effects of interference fringes was presented in section 2.7.1. Evidence also suggests that in the right circumstances use of diffusely scattering materials may reduce fringes. Their use and the consequent introduction of random uncertainty associated with the generation of laser speckle has is investigated in this chapter.

The analysis is based on the experimental configuration shown in Figure 4-1 that includes: (i) a tunable diode laser (823nm) driven so as to simulate TDLAS based gas detection, (ii) a simulated gas cell containing a diffusely scattering surface in combination with one of a number of different types of window (a wedged window is illustrated), and (iii) an interrogation system employing a silicon CCD camera. The 823nm (rather than 1650nm) laser was used to allow use of a low cost silicon CCD.

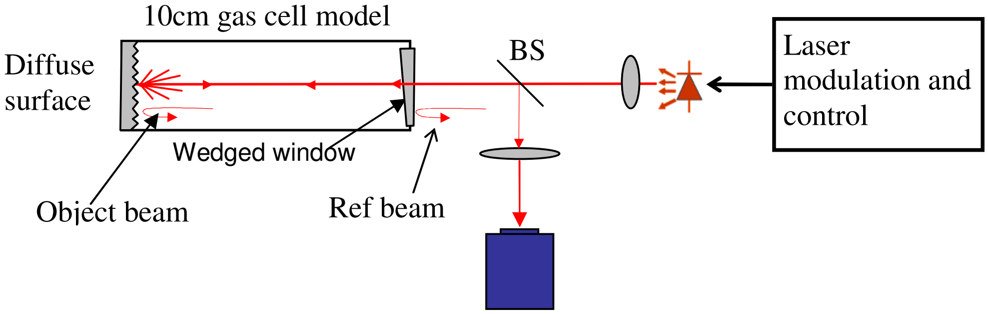

Figure 4-1: Experimental setup for investigating the use of diffuse reflections in TDLAS. Key: BS; beam splitter.

The experimental work has been grouped into three sections, namely;

1. development of the experimental methodology
2. experiments to confirm speckle behaviour and
3. experiments to investigate the use of diffuse reflections in TDLAS.

The diffuse objects used in the experiments have been deliberately restricted to those that could potentially be used in a practical instrument. Both bulk scatterers (multiply scattering) and surface scatterers (singly scattering) have been investigated.

First, for convenience, a summary of the important statistical properties of speckle is provided. After which, a methodology for investigating the use of diffuse reflections in TDLAS (in particular direct spectroscopy and WMS) is established and experimental investigations carried out.

4.1 Brief summary of theory of speckle

The lateral size ε of the individual objective speckles (ε_o, Figure 3-4) and subjective speckles (ε_s, Figure 3-5) in are given by[1]

$$\varepsilon_o = 1.22\lambda\ Z/D \tag{4-1}$$

$$\varepsilon_s = 1.22\lambda\ (1+\Pi)F\# \tag{4-2}$$

The scattered field amplitudes are randomly distributed and therefore the intensity values follow a negative exponential distribution

$$P(I) = \frac{1}{\langle I \rangle}\exp\left(-I/\langle I \rangle\right) \tag{4-3}$$

with the important consequence that its standard deviation σ equals the mean[2]. The normalised standard deviation or contrast C of a polarised speckle pattern is given by $C = \sigma/\langle I \rangle$. The contrast of a fully developed static speckle pattern is therefore always equal to unity. Adding M uncorrelated speckle patterns on an irradiance basis results in suppression of speckle contrast to $C = \sigma/\sqrt{M}\langle I \rangle$ [2].

The level of speckle intensity noise on a detector of size d x d is related to the number of speckles N and therefore the speckle size ε. The number of speckles can be approximated by d^2/ε^2. The level of speckle-related intensity noise, $\Delta I/I$, for a single speckle field is expected to be given by $1/\sqrt{N}$ or ε/d. From the above considerations, the speckle related uncertainty for a single static speckle field can be conveniently written in terms of equations (4-1) and (4-2) as

Objective speckle:
$$\frac{\Delta I}{I} = \frac{1.22\lambda Z/D}{\mathrm{d}} \tag{4-4}$$

Subjective speckle:
$$\frac{\Delta I}{I} = \frac{1.22\lambda\ (1+\Pi)F\#}{\mathrm{d}} \tag{4-5}$$

Interferometric speckle (a polarised speckle pattern coherently combined with a smooth reference wave or another speckle pattern) obtained at different wavelengths have a phase difference that is associated with the wavelength change. This applies only if the two interferometric speckle patterns remain spatially correlated in the measurement interval. Sirohi[3] has shown that the phase difference δϕ created between such interferometric speckle patterns is equal to

$$\delta\phi = 2\pi L\delta\lambda/\lambda^2 \tag{4-6}$$

where in this case, L is the physical path difference between the wedged window and the scattering surface in Figure 4-2. The value of $\delta\phi$ determines whether the observed speckle fields are in phase or out of phase, with the correlation coefficient being given by[3]

$$\rho(\delta\phi) = (1 + \cos \delta\phi) / 2 \tag{4-7}$$

From the above analysis, for a single static speckle field, the speckle related intensity uncertainty can be reduced by integrating many speckles over the detector aperture (i.e. small speckles for a given detector size or large area detector for a given speckle size. The contrast or normalised standard deviation of a speckle pattern can be reduced by averaging a number of statistically independent patterns. The following sections report experimental investigations of the above assertions.

4.2 Development of the experimental methodology

A model gas cell was established to enable different diffusely reflecting surfaces or transmitting windows to be investigated. A tunable diode laser (823nm) driven so as to simulate a TDLAS based gas sensor was used in the experiments. A CCD camera was used to image the reflected or transmitted light. A schematic diagram of the experimental set up is shown in Figure 4-2.

A 150mW single longitudinal mode laser diode (Spectra Diode Labs 5400 series) emitting at 823nm was coupled into a single mode fibre with angle cleaved end faces via a Faraday isolator (Halbo Optic), thus preventing feedback into the laser cavity which could have detrimental effects on the optical characteristics of the diode. The laser operating current and temperature were controlled by Profile LDC 202 and TED 200 controllers respectively. The light was divided by a 50:50 fibre optic coupler. One arm was passed to a Fabry-Perot scanning interferometer (Tec-Optics FPI25) for monitoring the laser diode emission. The other arm was directed to the gas cell model via a beam splitter. A proportion of the light was speculary reflected by a window in the modelled gas cell. This will be referred to as the reference beam (annotated in Figure 4-2). The reference beam intensity was controlled by using an appropriate antireflection coating on the window. Light reflected from the diffuse surface end of the gas cell will be referred to as the object beam (annotated in Figure 4-2).

The window on the modelled gas cell could be aligned such that the object and the reference beams combined interferometrically to form an interferometric speckle pattern or misaligned such that only the object beam (non-interferometric speckle) was imaged by the lens onto an 8 bit CCD camera (PearPoint P176). A calibrated variable aperture was used at the imaging lens to control the *F#* of the system. The video signal from the camera was transferred to a frame grabbing card (National Instruments IMAQ PCI 1408) housed in a computer. The image was displayed on the monitor after processing in the Labview$^{\text{TM}}$ software environment.

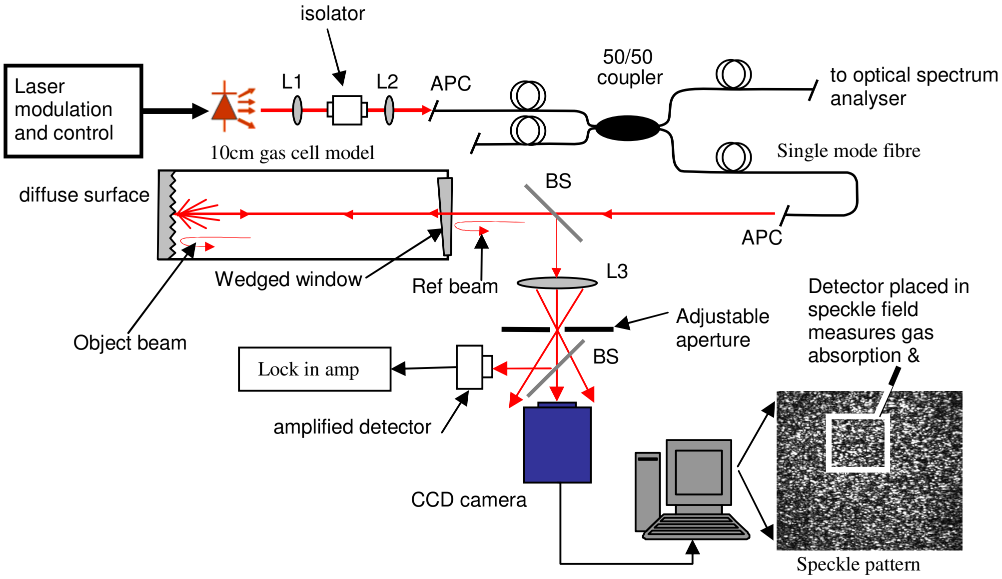

Figure 4-2: Experimental setup for investigating the use of diffuse reflections in TDLAS. Key: DFB; distributed feed back, SM; single mode, PSD; phase sensitive detection.

4.2.1 Elimination of optical feed back.

Optical feedback into the laser cavity was found to cause mode hopping of the laser operating frequency and/or multimode operation. These effects could be observed with an optical spectrum analyser that was set to have free spectral range of 5GHz (corresponding to a mirror separation of 3cm). The effect could also be observed in the 'twinkling' (instead of being stationary) of interferometric speckle at the camera when no change was applied to the phase of the interferometer (the simulated gas cell). A phase change could be introduced by displacing the diffuse reflector or changing the wavelength of the laser diode by changing the operating current or temperature. The 'twinkling' of interferometric speckle could therefore indicate a change in phase between successive interferometric speckle patterns. To confirm that there was an unwanted phase change in the interferometer, static frame subtraction (previously described in section 3.3.3 of chapter 3) was performed as follows.

An initial interferometric speckle pattern was stored in memory (as an 8 bit bitmap image) from which subsequent live images from the frame grabbing card were subtracted pixel by pixel. The difference images were converted into an array, each element representing the intensity level of each pixel (range of 0-255). The absolute intensity value $|x|$ of each element in the array was computed. The array of absolute values was then converted back into an image that was displayed on the monitor. This process was performed by a program written in Labview^{TM}. The program was run continuously allowing real time observation of the difference image. If there was no change between the reference frame and the live image, the displayed image would be black (Figure 4-3(a)). This would be the expected result were static frame subtraction to be carried out without any displacement applied to the interferometer (i.e. the laser operated at constant current and temperature and no displacement applied to the diffuse object). On the contrary, correlation fringes (Figure 4-3(b)) were observed and these were attributed to wavelength change due to laser mode hopping.

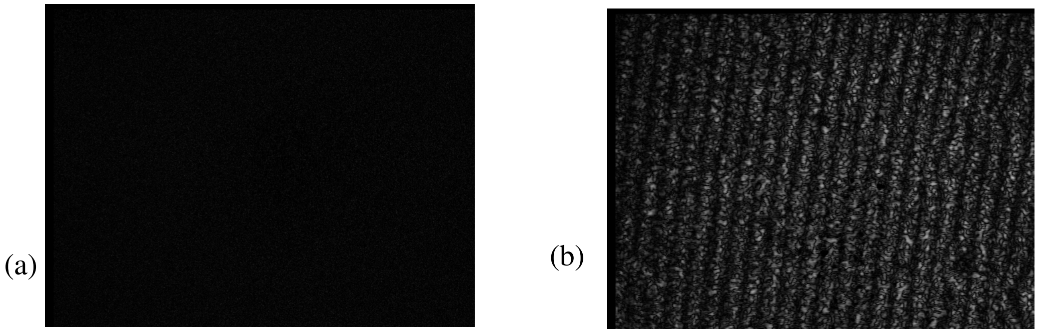

Figure 4-3: (a) A uniform black field corresponding to constant operating conditions(b) Correlation fringes caused by mode hopping of laser induced by optical feedback into the laser cavity.

Eliminating mode hopping by the use of a faraday isolator lead to the extinction of such fringes and the expected uniform black field could be observed. Independent confirmation was achieved by observing the output of the spectrum analyser on an oscilloscope display.

4.2.2 Reduction of fringes from unwanted Fabry-Perot etalons.

Fabry-Perot etalons created by parallel reflective surface in the optical system were found to cause interference (Figure 4-2). This introduced an undesirable uncertainty in intensity measurements with the camera.

Fringes of different pitch were observed; narrow fringes from long etalons (e.g. between fibre ends) and broad fringes from short etalons (e.g. between the fibre coupling lens and a fibre end face). Figure 4-4 illustrates fringes superimposed on a 100mHz saw tooth signal that was used to scan the laser frequency.

The CCD camera image also proved to be a useful diagnostic tool for fringe elimination, particularly for those originating from etalons in the optical path from fibre end (output) face to the CCD chip (Figure 4-2). A number of such fringes can be seen in interferometric speckle pattern in Figure 4-5(a). The broad fringes in the background were found to originate from a protective window in front of the CCD chip. The fringes marked a(2) and a(3) originated from etalons created by lenses L3, L4 and the wedged window. These could be seen more clearly by blocking the diffuse reflection such that only the specular reflection from the wedged window was imaged on the CCD (Figure 4-5 (b) and (c)).

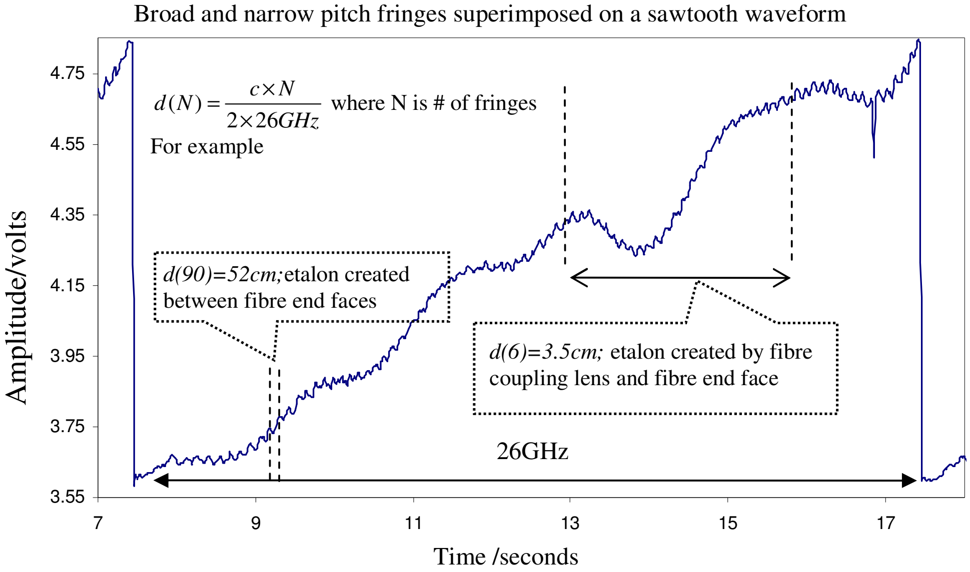

Figure 4-4: Example of fringes from unwanted etalons in the optical path; narrow fringes from long etalons (e.g. between fibre ends) and broad fringes from short etalons (e.g. between fibre coupling lens and fibre end face).

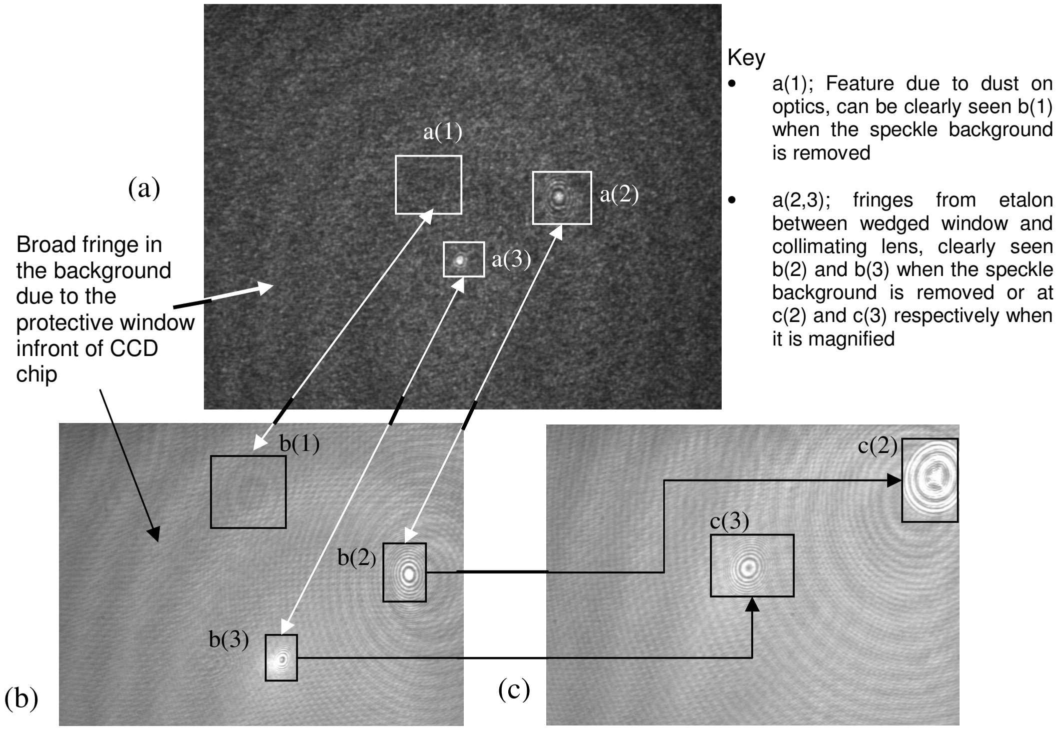

Broad fringe in the background due to the protective window infront of CCD chip

Key
- a(1); Feature due to dust on optics, can be clearly seen b(1) when the speckle background is removed
- a(2,3); fringes from etalon between wedged window and collimating lens, clearly seen b(2) and b(3) when the speckle background is removed or at c(2) and c(3) respectively when it is magnified

Figure 4-5: (a) interferometric speckle pattern. (b) Subsection of (a) with the speckle pattern removed, by removing diffuser in Fig 4-2. (c) Close up image of the specular image shown in part (b).

The fringes were removed by changing the camera lens from a multi element lens to a biconvex singlet lens (i.e. a lens with both surfaces curved) and removing the CCD cover window (Figure 4-6).

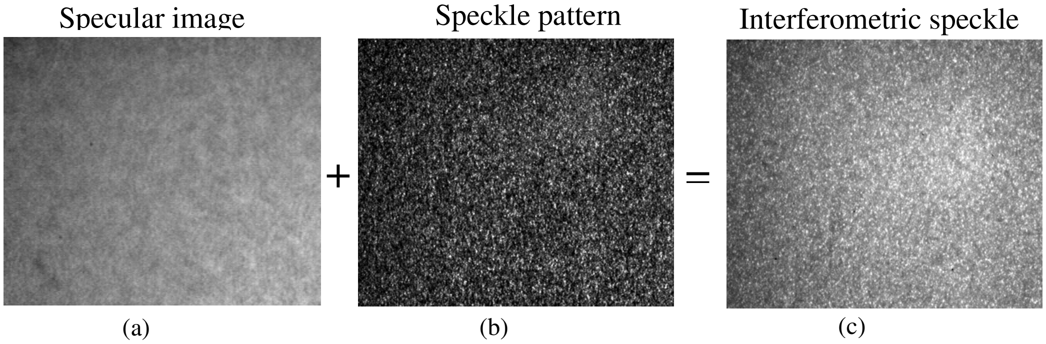

Figure 4-6: (a) Specular reflection. (b) Non interferometric pattern. (c) Interferometric speckle pattern, i.e. coherent combination of (a) and (b). Fringes that were observed in Figure 4-5 have been removed.

4.3 Experimental confirmation of speckle behaviour

The experimental setup (Figure 4-2) is different from a typical ESPI experimental configuration (Figure 3-3, chapter 3) in that the reference path and the object path are common. A series of experiments were therefore conducted to confirm speckle behaviour, verifying that the experimental setup was valid. Experiments were conducted to confirm;

a) The dependency of speckle size given by equations (4-1) and (4-2) on the optical geometry of Figure 4-2.
b) That interferometric speckle could be obtained with the experimental setup of Figure 4-2.

These experiments are described in the following subsections.

4.3.1 Confirmation of objective speckle behaviour

The size of objective speckle is given by $\varepsilon_o = 1.22\lambda\ Z/D$ (equation (4-1)). The dependence of speckle size on the illuminated area D was confirmed qualitatively by recording images of a diffuser (a gas turbine blade covered in retro reflective tape) for different values of D with fixed Z = 832mm (diffuser to camera distance). Figure 4-7 (a) and (b) show speckle images corresponding to (a) D = 4mm and (b) D = 110mm. The respective predicted speckle sizes are 161µm and 6µm (equation (4-1).

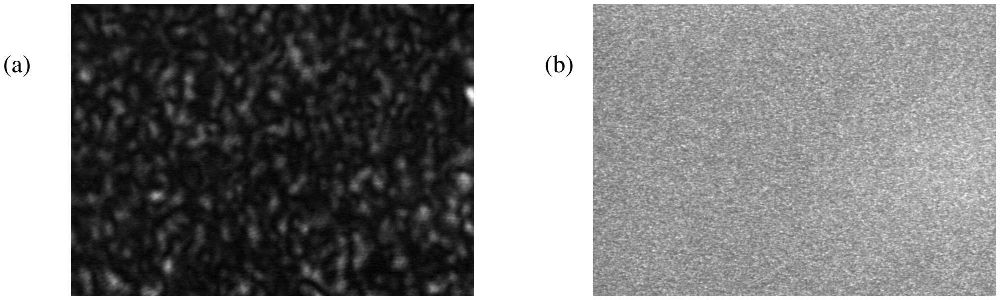
(a) diameter of illuminated area = 4mm

(b) diameter of illuminated area = 110mm

Figure 4-7: Effect of size of illuminated area on objective speckle. Speckle images of turbine blade covered with retro reflective tape illuminated by a beam diameter of (a) 4mm (b) 110mm.

4.3.2 Confirmation of subjective speckle behaviour

The size of subjective speckle is given by $\varepsilon_s = 1.22(1+\Pi)\lambda F\#$ (equation (4-2)). By varying the diameter of the adjustable aperture in Figure 4-2 and observing the speckle field formed, it was confirmed that the lateral speckle size of the subjective speckle was related to the F# according to the above equation. Speckle fields corresponding to various aperture diameters are shown in Figure 4-8 below.

(a) 0.3mm aperture

(b) 0.6mm aperture

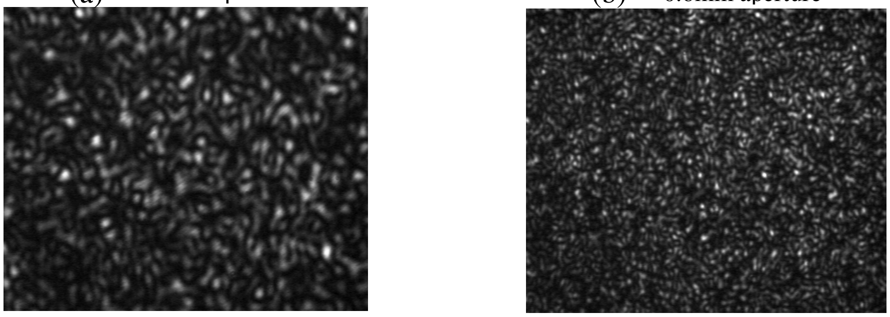

(c) 3mm aperture

(d) 6mm aperture

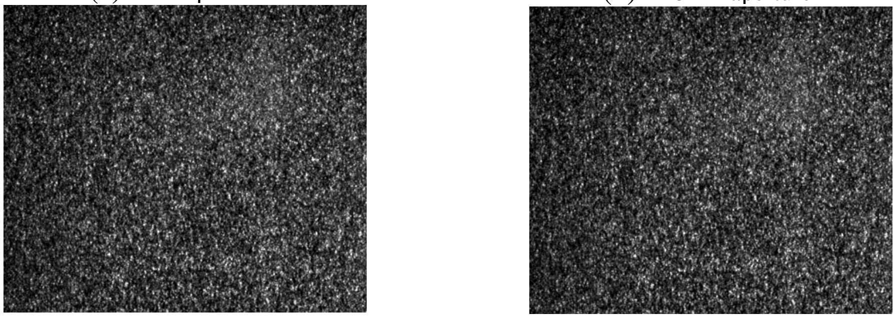

Figure 4-8: Effect of size of aperture on speckle size for subjective speckle. (a) Large speckles (0.3mm aperture). (b), Smaller speckles corresponding to a larger aperture (0.6mm). For apertures larger than 1mm speckle size can not be distinguished visually (e.g. (c) 3mm and (d) 6mm.

For aperture sizes less than 1mm, the lateral size of the subjective speckle was visually confirmed to be related to the F# of the imaging lens. However, at apertures larger than

1mm, changes in speckle size with aperture could not be confirmed visually. This could be attributed to the resolution of the system. The subjective speckle size is given by $\varepsilon_s = 2F\#(\mu m)$ for λ=823nm and $\Pi = 1$. The size of the pixels of the camera was 13.5µm ×11.5µm. The focal length of the lens used was 50mm. Therefore for F#< 20 (i.e. for apertures greater than 2.5mm), the speckle size was less than 40µm. For adequate sampling, 7-10 pixels spanning the diameter of the speckle are recommended[4]. This criterion is satisfied for speckle sizes >94.5µm (or F#> 47).

4.3.3 Confirmation of interferometric speckle

It is important to distinguish between non interferometric and interferometric speckle as defined in section 4.2 for the following reasons;

1. The statistical properties governing size, contrast and brightness distribution are different for the two cases.
2. The behaviour under wavelength modulation is different. In the case of interferometric speckle, the simulated gas cell can be modelled as a low finesse Fabry-Perot etalon. The implications of fringes that may arise from such an etalon on TDLAS gas measurements will have to be considered.

Additional practical considerations should be undertaken in the case of arranging an experiment to use interferometric speckle. Firstly, the relative intensity of specular and diffuse reflection has to be arranged such that neither one dominates the interferometric speckle pattern. In these experiments the magnitude of the specular reflection (the reference beam) was controlled by using wedged windows of different AR coatings. In standard ESPI configurations, beam intensity matching is achieved by appropriately attenuating the power in one path relative to the other.

Secondly, the location of the adjustable aperture is critical. To avoid truncation of the reference beam when the adjustable diaphragm is stopped down, it has to be located at the focal point as illustrated in Figure 4-2. Again this limitation is not encountered in standard ESPI configuration as the reference beam does not go through the aperture. The reference beam is introduced after the lens and aperture, (Chapter 3, Figure 3-3).

The experiment in the previous section, (4.3.2), can be taken to constitute confirmation of non interferometric speckle. To confirm that interferometric speckle could be obtained with the experimental configuration, the static frame subtraction procedure as described in section 4.2.1 was performed to obtain correlation fringes. Correlation fringes can only be obtained in the case of interferometric speckle. Correlation ESPI fringes obtained with the experimental set up are shown in Figure 4-9.

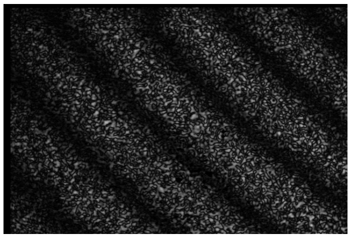

Figure 4-9: Correlation fringes obtained by performing static frame subtraction in ESPI.

The fringes were obtained by heating the diffuse surface and then performing static frame subtraction as the diffuse object cooled down. The dark regions correspond to areas of the two images where the speckle pattern remained in phase, while the light regions correspond to areas of the two images where the speckle patterns were out of phase. This confirms the presence of interferometric speckle.

4.4 Behaviour of speckle in practical systems

The statistical properties of speckle summarised in section 4.1 are based on the assumption that the surface height deviations of the diffuser are large in comparison to the wavelength of the radiation illuminating it, and that the resultant speckle field is completely polarised. In general surfaces at which polarised light is singly scattered give rise to polarised speckle; this includes lightly-scattering transmission elements, such as ground glass. Bulk diffusers (surfaces into which light penetrates and is multiply scattered) on the other hand, such as matt white paint or opal glass, depolarise the light and thus do not generate a fully developed speckle pattern[1]. The statistics of speckle from singly scattering surfaces with height deviations less than the illuminating wavelength have been shown to depend on the surface roughness[5]. The purpose of this section is to investigate the possibility of exploiting the characteristics of under developed speckle as a means of reducing the speckle related intensity uncertainty.

A number of diffusely scattering materials including PTFE (polytetrafluoroethylene, purchased from RS components), Macor^{TM} (white machinable ceramic), ground glass, opal glass, Spectralon^{TM} (a PTFE based material made by Labsphere), metallic surfaces painted with reflective paint (Reflect^{TM} made by Rocol) and retro reflective tape were investigated. Due to different levels of scattering and depolarisation in the different samples the speckle fields were expected to exhibit various levels of development ($0<C<1$, where C is contrast or normalised standard deviation). The speckle patterns generated by the various samples were characterised by plotting probability density function and contrast and observing the size of the speckle. For these experiments, a HeNe laser emitting at 632.8nm was used for convenience. The experimental setup is shown in Figure 4-10 (only the reflective geometry is illustrated).

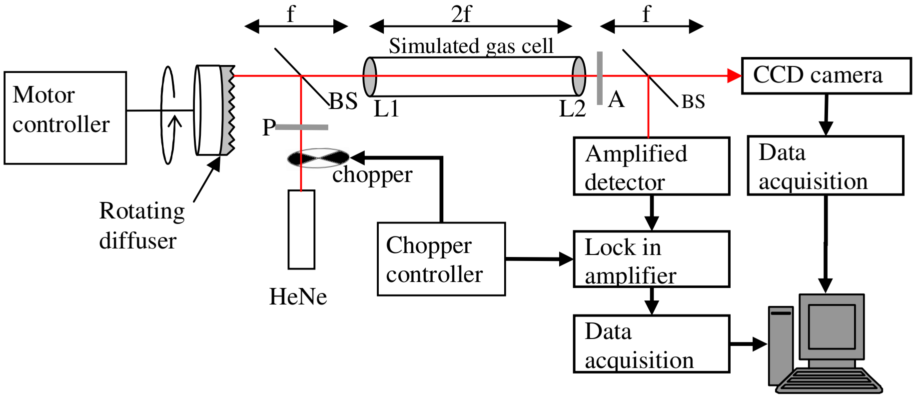

Figure 4-10: Experimental setup for characterising properties of speckle from various scattering materials. Key: P; polariser, A; analyser, BS; beam splitter, f; focal length of lens L1 and L2.

Light from a linearly polarised HeNe was directed onto the target samples. Transmitted or reflected light was then directed either to a detector or a CCD camera after passage through the gas cell model. Lenses were used as gas cell windows; L1 collimated the scattered light and L2 focussed the light on to the detector. The detector signal was then passed to a lock-in amplifier that was locked to the chopper frequency.

4.4.1 Dependence of speckle statistics on material type.

Images of speckle patterns from various static samples were captured under identical conditions, with L2 (Figure 4-10) removed. For most of the samples (Macor^{TM}, Spectralon^{TM}, spray painted surface, retro reflective tape), there were no visible differences in speckle size. However PTFE gave rise to visibly smaller speckle. The speckle images from the PTFE and Spectralon^{TM} are shown in Figure 4-11.

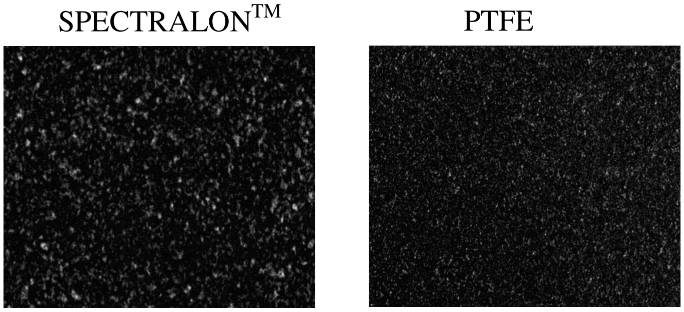

Figure 4-11: Dependence of speckle size on material type. (a) 10mm SPECTRALON^{TM} (460 ×460 pixels). (b) 10mm thick PTFE (460 ×460 pixels).

The images were captured with lens L1 operating at F# = 2.6. This appears to suggest that under certain circumstances speckle size depends on material type. There are several possible explanations for the phenomenon;

1. It has been reported that for diffusers with surface height deviations less than the wavelength of the illuminating light, speckle size depends on the surface height deviations (see section 3.2.10).
2. Differences in the bulk microstructure between the two samples.
3. Multiple scattering effects.

The important result from a practical perspective is that speckle contrast also depends on the type of diffuser and therefore speckle related intensity uncertainty can be reduced by judicious selection of diffuser.

4.4.2 Degree of polarisation (DOP).

Light emerging from a scattering medium illuminated by linearly polarised light consists of linearly and randomly polarised photons[6]. This is directly related to the number of scattering events experienced by the photons. In section 4.3.3 interference effects were demonstrated by coherently adding a reference beam (specular reflection) to a speckle pattern from a surface scatterer. This was possible because the speckle pattern had a high DOP (degree of polarisation). From a gas sensing point of view depolarised speckle is preferable for several reasons. Firstly, depolarised speckle is under developed; therefore the contrast is expected to be less than unity. Secondly, in comparison to polarised speckle, depolarised speckle will produce reduced visibility of interference effects in the case of interferometric speckle.

An experiment to measure the DOLP (degree of linear polarisation) of scattered light from the various samples was conducted. The DOLP is given by[6]

$$DOLP = \frac{I_P - I_C}{I_P + I_C} \tag{4-8}$$

where I_p and I_c are the mean intensities measured with parallel and crossed polarisers respectively[7]. The results are presented in Table 4-1 below.

Table 4-1: Degree of linear polarisation of light reflected or transmitted from various samples

MATERIAL	DEGREE OF LINEAR POLARISATION	CONTRAST
REFLECTIVE		
10mm thick PTFE	0.02	0.98
Spectraflect^{TM}	0.07	1.0
20mm thick Spectralon^{TM}	0.13	1.0
aluminium surface painted with a reflective paint	0.78	1.0
retro reflective tape	0.9	1.00
TRANSMISSIVE		
opal glass	0.2	1.00
ground glass	1	1.00

The *DOLP* was calculated from the measurements of I_p and I_c that were obtained with parallel and crossed polariser (P) and analyser (A) pair respectively (Figure 4-10). The polarisers were only used for this experiment. As expected the surface scatterers (aluminium surface, ground glass and retro reflective tape) exhibited a high *DOLP* compared to the bulk or volume scatters (PTFE, Spectraflect^{TM}, Spectralon^{TM} and opal glass). The results do not exhibit the expected reduction in the contrast of the speckle fiel. This could be due to inadequate sampling of the speckle field by the CCD. Ideally, 7-10 pixels should be used to sample one speckle[4]. In this experiment the speckles (approximately 2µm in size;estimated using $1.2\times\lambda\times F\#$ where $\lambda = 633$nm and $F\# = 2.6$) were smaller than the CCD pixels (11.3µm).

4.4.3 Effect of multiple scattering on speckle

The effect of multiple scattering on speckle size was investigated by recording speckle images of light transmitted after passage through PTFE samples of varying thickness (Figure 4-12).

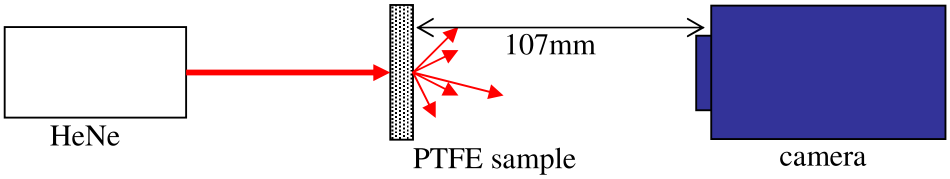

Figure 4-12: Experimental set up for recording multiply scattered speckle after passage through PTFE samples of varying thicknesses. The samples were placed 107mm from the CCD chip (measured from the exit face of the sample)

The captured images and the associated probability density functions (PDFs) are shown in Figure 4-13. Table 4-2 presents the calculated normalised standard deviation (contrast).

Table 4-2: Normalised standard deviation of speckle patterns obtained from light transmitted through PTFE of varying thickness.

IMAGE	CONTRAST OR NORMALISED STANDARD DEVIATION
PTFE: 2mm thick	0.157
PTFE: 5mm thick	0.103
PTFE: 10mm thick	0.08
PTFE: 20mm thick	0.062

This appears to show that multiple scattering effects lead to a reduction in speckle contrast.

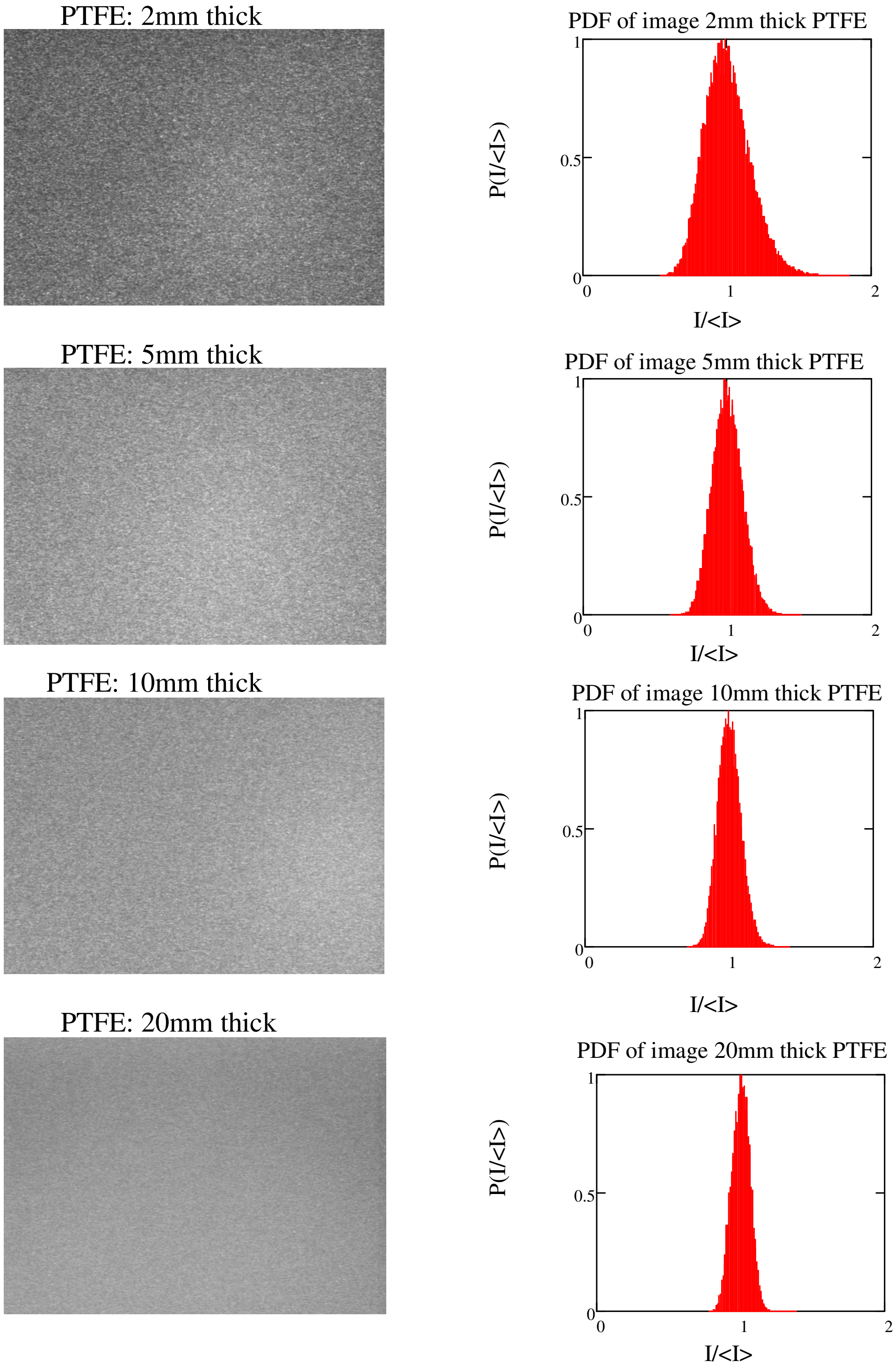

Figure 4-13: Dependence of speckle distribution on multiple scattering. Image and the associated probability density functions (PDFs) obtained by recording transmitted scattered light after passage through PFTE samples of various thicknesses. KEY: I is intensity of the individual pixels of the CCD and <I> is the average pixel intensity.

4.4.4 Integrated and blurred speckle.

In practice, speckle intensity measurements are made with detectors with finite apertures. As a result the measured intensity is an integrated version of the ideal point detector. Relative motion between the detector and the scattering surface can also lead to blurring of the speckles leading to reduction in contrast. The first-order statistics of integrated and blurred speckles have been considered by Goodman[8]. He has shown that for a non stationary speckle pattern, the mean of the measured intensity is equal to the true mean of the static pattern. Adding M independent speckle patterns has been shown to reduce the uncertainty by $\sqrt{M}$ [7].

In this work statistically uncorrelated speckle patterns were generated by capturing ten images (set 1) whilst the diffuser was rotated (rotation performed manually so that a different region of the diffuser was illuminated each time) using the experimental setup of Figure 4-10. From these images a set of nine images were generated by computing the average of K images where K= 2, 3…..10. Each of these images corresponded to averaging over K independent speckle patterns. The contrast of the average images was then calculated. As a control, ten images of the diffuser whilst stationary (set 2) at arbitrary time intervals between 30 seconds and 120 seconds were also taken. These were also subjected to the same processing as set 1.

The plot of contrast against number of images averaged for the two sets of images is shown in Figure 4-14.

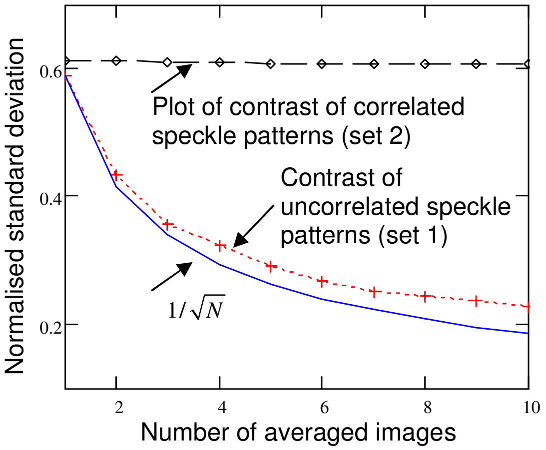

Figure 4-14: Variation of contrast or normalised standard deviation with the number of images averaged. Set 1; uncorrelated speckle patterns, Set 2; images taken from a static diffuser.

Figure 4-15 shows the averaged images and the plots of their corresponding probability density functions. Also shown in Figure 4-15 are the 3D representations of the intensity distribution corresponding to one speckle pattern and the average of ten speckle patterns.

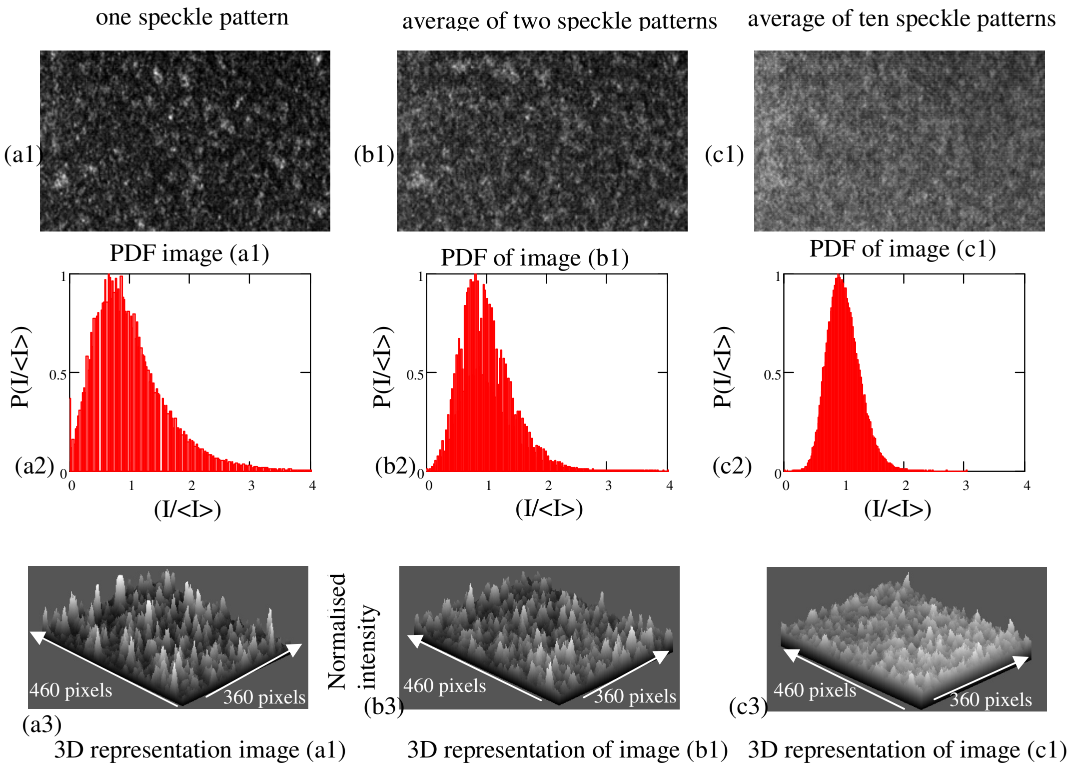

Figure 4-15: (a1), (b1) and (c1) are images (460 ×360 pixels) of speckle patterns; (a2), (b2), (c2) the associated probability density functions PDFs, (a3), (b3) and (c3) are 3D representations of images (a1), (b1) and (c1) respectively.

Averaging uncorrelated speckle patterns show behaviour similar to prediction (Figure 4-14). The offset in between the theoretical and experimental plots in Figure 4-14 could be due to a small level of background intensity.

The rotating diffuser was also used to blur the speckles via its motion. Figure 4-16 shows a static speckle image and blurred speckle image captured whilst the diffuser was rotated at 1 kHz.

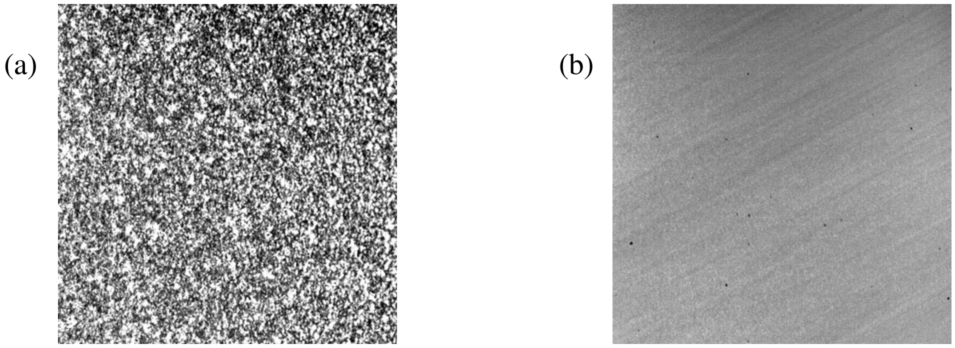

Figure 4-16: Blurring speckle using a moving diffuser. (a) image of a static diffuser, (b) image taken whilst rotating the diffuser.

The rotation speed of the diffuser could be set such that within the time period corresponding to 1 measurement (typically several seconds for WMS), the averaged image was equivalent to measuring over an area of M images (swept area). For a detector this reduces the uncertainty by a factor of $1/\sqrt{M}$. For example, if the speckle sizes in a static image have an average diameter of 2µm (i.e. λ = 823nm, Π=1 and F#=1 in equation 4-5), the speckle related intensity uncertainty is 2µm/1mm = 2×10^{-3}. To detect 10ppm gas concentration would require averaging 400 statistically independent speckle patterns.

4.5 Effect of wavelength modulation on speckle

Both direct spectroscopy and WMS techniques involve tuning the wavelength of the laser. Therefore speckle behaviour (interferometric and non interferometric) and the related intensity uncertainty requires investigation under wavelength modulation. The level of uncertainty that relates to wavelength modulation can be investigated by considering an intensity measurement made at one wavelength λ with a second measurement made within a short modulation period, at a second wavelength ($\lambda+\delta\lambda$).

The effect of the wavelength modulation on interferometric and non-interferometric speckle was investigated on a scale relevant to gas detection using direct spectroscopy and wavelength modulation spectroscopy.

4.5.1 Effect of wavelength modulation on non-interferometric speckle.

For non-interferometric speckle, the expected change in the speckle field due to a wavelength change can be estimated by evaluating the equation for speckle size, (4-2), at $\lambda_1$and $\lambda_1+\delta\lambda$. For example, substituting F# = 2.5, λ_1 = 1650nm, Π = 1 and $\delta\lambda$ = 0.09nm (10GHz or 0.334cm^{-1}); the proportional change in speckle related uncertainty is 6×10^{-5}. This level of uncertainty is relevant to differential measurements made at two different wavelengths or when scanning across the gas line to obtain the harmonic line shapes or for direct spectroscopy. The speckle related uncertainty due to wavelength change for non-interferometric speckle is therefore below the level of uncertainty for a static speckle field. The static speckle field uncertainty is given by equation (4.2), which is 4×10^{-3} for F# = 1, $\lambda = 1650$nm, $\Pi = 1$ and d=1mm.

Therefore in the case of a static speckle field, to detect 10ppm gas concentration, the speckle sizes must be approximately 10nm if a 1mm diameter detector is used. The geometry required to achieve such small speckles would be difficult to achieve in a practical gas detection experiment (e.g. large gas cell volume; instrument response time limited by time taken to fill or evacuate cell, very large beam diameter required; the illumination geometry required to achieve such a beam size may not be appropriate for many practical gas sensing systems). For example to achieve 10nm speckle sizes (i.e. 10ppm detection sensitivity), using the cell geometry shown in Figure 4-1:

a) In the case of an objective speckle configuration (equation 4-1) with Z = 150mm, the required diameter of the illuminated area is 30metres.

b) In the case of subjective speckle (equation 4-2) with $\Pi = 1$, the required *F#* is 2.5×10^{-3}.

4.5.2 Effect of wavelength modulation on interferometric speckle.

For experiments involving interferometric speckle, confirmation that the object and reference beams were combining interferometrically was achieved by obtaining correlation fringes using electronic speckle pattern interferometry as described in section 4.3.3.

Interferometric speckle patterns obtained at two wavelengths have a phase difference that is given by $\delta\phi = 2\pi L\delta\lambda / \lambda^2$ (Equation (4-6), section 4.1). For laser diodes sources, the wavelength change can be achieved by tuning the injection current. Equation (4-6) can therefore be rewritten as

$$\delta\phi = \frac{2\pi L}{c} k_v \Delta i \qquad \textbf{(4-9)}$$

where Δi is the change in laser current and k_v is a constant unique to a particular laser diode[9]. The equation above applies to individual speckles in an interferometric speckle pattern. Therefore when performing static frame subtraction ESPI whilst tuning the injection current, a plot of $I\text{-}I_0$ against Δi would be expected to take the form of a sinusoid. I_0 is the average intensity of an interferometric speckle pattern corresponding to $\Delta i = 0$.

An experiment was conducted to obtain a plot of the correlation of interferometric speckle patterns corresponding to different wavelength using a technique that was employed by Olszak and Tatam[9] to calibrate the path-length imbalance in optical fibre ESPI systems. The experimental setup of Figure 4-2 was used for this experiment.

The specular reflection from the wedged window (with reference to Figure 4-2) was used a reference smooth wave. A reference interferometric speckle pattern was stored for an initial injection current or wavelength value. The wavelength was scanned by a ramping the injection current, causing a corresponding change in the phase. New interferometric speckle patterns were acquired continuously. The subsequent images were then subtracted from the reference image pixel by pixel, the result rectified and the average intensity of the resultant image calculated. A plot of average intensity against current is shown in Figure 4-17.

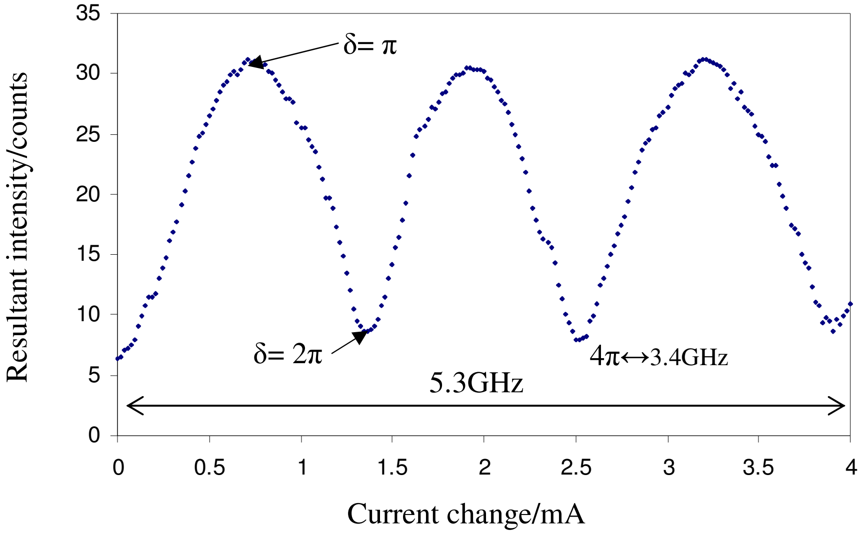

Figure 4-17: A plot of average intensity that maps the phase change of the interferometer with wavelength. The troughs correspond to $\delta\phi = 1$ (in phase) and the peaks correspond to $\delta\phi = 0$ (out of phase).

The x-axis can be converted to a frequency scale by characterising the frequency versus current tuning characteristics of the laser diode. From this, the wavelength change required to produce a 2π phase change for a given ΔL can be determined as follows.

The plot is on a sloping background due to simultaneous wavelength and intensity modulation. The period of the ramp waveform was 100 seconds. This allowed a sufficient number of frames to be captured in the interval $0 < \delta\phi < \pi$. When the phase shift equalled π the average intensity attained its maximum value and when it was 2π the average intensity was a minimum; that is, subtracting from a speckle image an identical speckle image results in a ‘black’ (zero-intensity) image. Approximately 16±0.5 maxima could be seen in a 26.6 GHz (0.9cm^{-1}) interval, yielding an etalon spacing of 9.2±0.2cm. The length of the simulated gas cell was 9cm. These observations are consistent with the fringes originating from the low finesse cavity formed by the simulated gas cell. This is an important result and shows that an interference fringe-like signal can occur due to wavelength modulation of interferometric speckle.

4.6 Estimation of speckle related uncertainty for direct spectroscopy and WMS

This section will consider the implications of the speckle (interferometric and non interferometric) related uncertainty on direct spectroscopy and WMS using the gas cell model illustrated in Figure 4-2. The effect of the wavelength modulation on speckle on a scale relevant to TDLS will be examined.

In direct spectroscopy the laser is tuned over the absorption line by either ramping the operating current or temperature. Direct spectroscopy was simulated by scanning the laser frequency over a 26GHz (0.9cm^{-1}) range. This was achieved by modulating the operating current with a low frequency ramp signal whilst continuously recording the speckle images and saving them to an AVI file.

For WMS, two scenarios have been considered. In the first case, the laser was simultaneously modulated at several kHz (modulation depth $\delta\lambda$, typically several GHz, for example $\delta\lambda = 4GHz$ for methane at atmospheric pressure) and scanned across the gas line at several Hz. In the second case, the scan was absent and the laser was locked to the peak of the gas line with a residual jitter of several MHz.

A number of programs were written in Labview^{TM} to read and process AVI files. One program converted the image frames into an array of individual pixel data. The array was then divided into grids (pixel binning) representing our detection system. The size of the bins could be chosen to match the size of our detectors or any arbitrary size (see Figure 4-18). Another program divided the image array into ten bins of user selectable size and origin (see Figure 4-18(b))

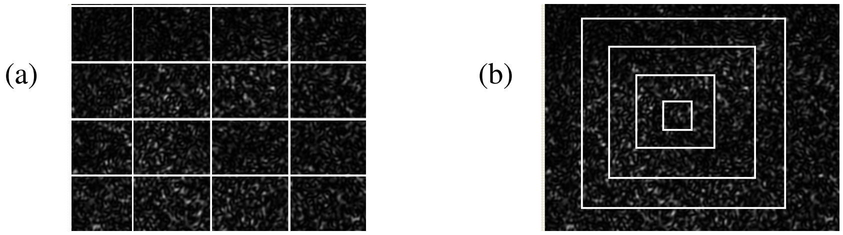

Figure 4-18: Illustrations of the different types of pixel binning that were employed. (a) Images were divided into equal bins size bins equivalent to detector size (b) different size bins used to evaluate the effect of averaging different number of pixel.

4.6.1 Non-interferometric speckle.

In section 4.5.1, it was established that the speckle related intensity uncertainty of non-interferometric speckle due to wavelength modulation is below the level of uncertainty of a static field. Therefore the level of noise in direct spectroscopy and WMS will be similar to that of a static field. According to equation (7-4) the speckle related intensity uncertainty of a static field is directly related to the effective *F#* of the image forming lens. In the experimental setup shown in Figure 4-2 the effective *F#* can be controlled by the iris diaphragm. The effect of speckle size on the intensity noise can therefore be investigated by conducting a series of experiments where the intensity noise is measured for different effective *F#* of the collecting lens. From equation (7-5), a reduction in intensity noise with decreasing *F#* is therefore expected.

The uncertainty of a static field was examined by considering the uncertainty associated with placing a detector of a particular size in different areas of the speckle field by using the binning method illustrated in Figure 4-18(a). For a given bin (or detector) size the speckle related measurement uncertainty was calculated from the mean intensity of each bin and the standard deviation of the mean intensities of all the bins. The exercise was conducted for various bin sizes and two different speckle sizes. The images shown in Figure 4-11 were used. The results are presented in Table 4-3. As expected, for small areas the uncertainty is higher.

Table 4-3: Speckle related intensity noise for various detector sizes.

		SPECTRALON^{TM}			PTFE		
detector or bin size (pixels)	Approximate bin area (mm2)	Mean intensity (counts)	Standard Deviation (counts)	Proportional Standard deviation	Mean intensity (counts)	standard Deviation (counts)	proportional Standard Deviation
40×40	0.25	19.4	3.5	0.18	19.4	2.8	0.14
80×80	1	19.8	2.8	0.14	19.4	2.5	0.13
120×120	2.2	19.4	1.8	0.093	19.3	2.2	0.11
160×160	4	19.1	1.2	0.063	19.0	1.3	0.07

4.6.2 Interferometric speckle.

In section 4.5.2, it was shown that modulation of interferometric speckle can result in interference fringe signals (Figure 4-17). The intensity uncertainty will be maximised if the induced phase change in the interferometer δ equals $(2n+1)\pi$.

The intensity of each pixel varies according to equation (4-7); however the phases of the pixels are randomly distributed. Therefore by averaging a sufficient number of pixels, a reduction in the visibility of the fringes is expected.

The effect of detector size on the visibility of the fringes was investigated. The area over which the speckles were averaged was varied by using the binning method illustrated in Figure 4-18(b). Shown in Figure 4-19 are the plots obtained for detector or bin sizes comprising of one pixel and a hundred pixels. The approximate maximum peak to peak intensity excursions for the different averaging areas are shown in Table 4-4 and plotted in Figure 4-20. As expected, a reduction in the modulation amplitude of the fringes is observed.

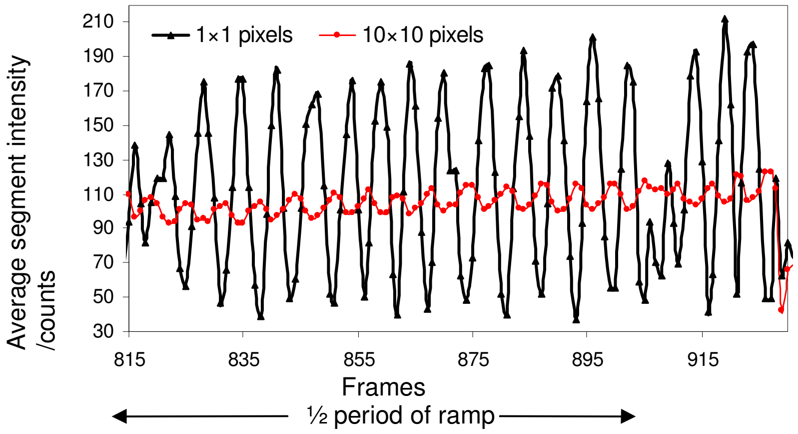

Figure 4-19: Reduction in the visibility of the interference fringes with increasing modelled detector size. Fringes were formed by modulating interferometric speckle. After a certain detector size, further increase of the detector size yields no detectable reduction in the amplitude of the interference fringes.

Table 4-4: Approximate peak to peak amplitude of the intensity modulation for different area averaging size.

Detector or bin size (pixels)	**Approximate pixel area** (mm^2)	**Maximum peak to peak intensity excursion** (counts)
1	1.6×10^{-4}	153
3×3	1.4×10^{-3}	127
5×5	3.9×10^{-3}	75
7×7	7.6×10^{-3}	20
10×10	0.016	14
40×40	0.25	12
80×80	1	6
120×120	2.2	4
160×160	4	4
200×200	6.2	4

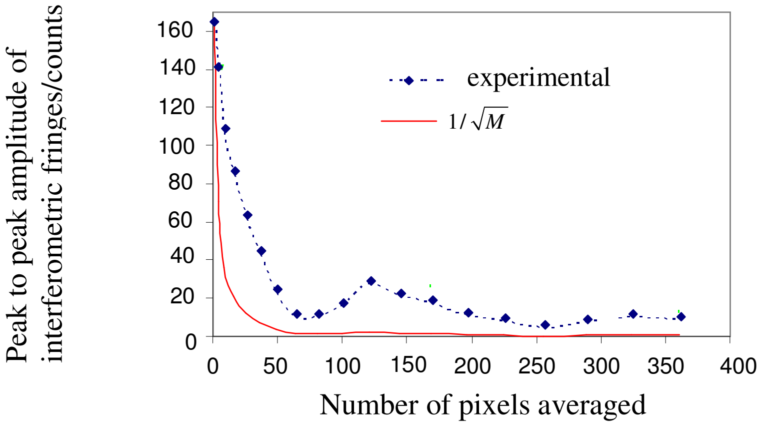

Figure 4-20: Plots showing a reduction in fringe visibility as the number of averaged pixels increase. Also shown is the 1/$\sqrt{M}$ plot for comparison

4.7 Discussion and conclusion

In this chapter a systematic study of the use of diffuse reflections in TDLAS has been reported. A methodology for investigating the consequent introduction of intensity uncertainty associated with laser speckle has been developed.

A relationship governing non interferometric speckle intensity uncertainty has been derived (equation (7-5) and experimentally confirmed. The uncertainty is reduced by integrating a large number of speckles over the detector area (Table 4-3) because of the statistical properties of speckle. The uncertainty can also be reduced by using multiply scattering surfaces that gives rise to a partially polarised (low contrast or washed out) speckle field.

In the case of objective speckle (assuming a fully developed speckle pattern) speckle sizes are governed by equation 4-1; $\varepsilon_o = 1.22\lambda\ Z/D$. If a 1mm detector is located 100mm from the diffuser, to detect 100ppm methane at 1650nm, the illuminated area diameter has to be approximately 200cm. The illumination geometry required to achieve such a beam size may not be appropriate for many practical gas sensing systems.

In the case of subjective speckle, the speckle size is determined by the f-number of the light collecting optic and by the magnification of the system. These can be configured to reduce the speckle size. For example Fresnel lenses with f# < 1 (commercially available at very low cost) can be used. The estimated speckle related intensity uncertainty is of the order of 1.5×10^{-3} (by using values of $\Pi = 0.5$, F# = 0.5 in equation 4-5; $\Delta I/I = 1.22\lambda\ (1+\Pi) F\#/d$).

Speckle noise can also be actively suppressed by averaging a sufficient number of uncorrelated speckles during the detector integration period. Adding M independent speckle patterns has been shown to reduce the uncertainty by $\sqrt{M}$ (Figure 4-14). Changes in the speckle pattern due to external factors (ambient vibrations, cooling fans in electronic equipment, pumps etc) will not worsen speckle noise for a sufficient number of speckles arriving at the detector. Although the speckles pattern will be non stationary, the detector will effectively 'see' the same number of speckles. On the contrary, environmental fluctuations can lead to reduced speckle uncertainty due to the averaging effect.

Interference fringes were observed in the case of interferometric speckle. The visibility of the fringes could be significantly reduced by integrating a large number of speckles over a detector area because of the random distribution of the phases of individual pixels (Figure 4-19 and Table 4-4). The peak to peak amplitude of the fringes detected at the CCD camera was reduced from 153 counts (measured in one pixel) to 6 counts by averaging over an area equivalent to a detector with a diameter of 1mm. The formation of such fringes can be partially avoided by using multiply scattering diffusers that gives rise to a depolarised speckle field. This reduces the finesse of the low finesse cavity giving rise to interferometric speckle. In practice, the specular component from the reference beam would be directed away from the camera or detector. In the experimental setup shown in Figure 4-2, it took considerable efforts to align the system to achieve interferometric speckle.

The results obtained in this chapter will be used in designing and evaluating the performance of a diffuse gas cell for use in a TDLAS instrument. The important design considerations based on results obtained in this chapter are outlined below.

- Speckle related intensity uncertainty has the following parameters
    - Dependent on optical geometry.
    - Dependent on the type of diffuser, under certain circumstances.
    - Largely independent of wavelength modulation (in the case of non interferometric speckle.
    - Interferometric speckle exhibits behaviour similar to Fabry-Perot etalon fringes.
- Speckle related uncertainty can be reduced by averaging
    - a large number of speckles N over a detector area in the case of a single static speckle pattern, $1/\sqrt{N}$ reduction
    - a number of uncorrelated speckle patterns M, yielding a $1/\sqrt{M}$ reduction

The following chapter describes the development of the TDLAS instrument employing the WMS technique.

4.8 References

[1] Ennos A E 1975 *Laser Speckle and Related Phenomena* (Berlin: Springer-Verlag) pp 203-53.

[2] Goodman, J. W. (1976), 'Some fundamental properties of speckle', *Journal of Optical Society of America*, V66, N11, pp. 1145-1150.

[3] Sirohi, R. S. (2002), 'Speckle interferometry', *Contemporary Physics*, V43, N3, pp. 161-180.

[4] Alexander, T L., Harvey, J. E., and Weeks, A. R. (1994), 'Average speckle size as a function of intensity threshold level: comparison of experimental measurements with theory', *Applied Optics*, V33, N35, pp. 8240-8250.

[5] Fujii, H. and Asakura, T. (1974), 'Effect of surface roughness on the statistical distribution of image speckle intensity', *Optics Communications,* V11, N1, pp. 35-38.

[6] Morgan, S. P. and Ridgway, M. K. (2000), 'Polarization properties of light backscattered from a two layer scattering medium', *Optics Express*, V7, N12, pp. 395-402.

[7] MacKerrow, E. P. and Schmitt, M. J. (1997), 'Measurement of integrated speckle statistics for CO_2 lidar returns from a moving, nonuniform, hard target', *Applied Optics*, V36, N27, pp. 6921-37.

[8] Goodman J W 1975 *Laser Speckle and Related Phenomena* (Berlin: Springer-Verlag) pp 9-75.

[9] Olszak, A. and Tatam, R. P. (1997), 'The calibration of the path-length imbalance in optical fibre ESPI systems employing source-wavelength modulation', *Measurement Science and Technology*, V8, N7, pp. 759-63.

Chapter 5 WMS instrument development

The purpose of this chapter to report the design and evaluation of the performance of a bench top demonstrator instrument based on the application of the WMS theory presented in chapter 2 (sections 2.7-2.9). The instrument will be used in the following chapters for investigating the use of diffuse reflections in TDLAS. The target detection limit of the instrument is the background methane concentration of approximately 2ppm. The various development stages of the instrument are reported. Experimental work that was conducted to characterise and evaluate the performance of the instrument is also presented in this chapter.

The following sections describe the main elements of the system and its operation.

5.1.1 Description of the main parts of the system

The instrument consisted of the following main elements;

1. Source and associated drive electronics
    a) A custom InGaAsP DFB laser diode module mounted in a standard 14 pin butterfly package, consisting of (with reference to Figure 5-1);
        i. a 1651nm DFB laser diode chip (NEL NLK1U5C1CA-TS) mounted on a thermoelectric cooler (TEC) element for heating or cooling the diode, to set the bulk emission wavelength.
        ii. a negative temperature coefficient thermistor (NTC) for sensing the operating temperature of the laser.
        iii. a commercially available monitor Ge photodiode enclosed in a standard TO package filled with methane, forming a reference cell with which the operating wavelength of the diode could be controlled. The 5mm (approximate) thickness of gas between the diode and package window gave an absorption of approximately 4% at 1651 nm[1].
        iv. a 4.5mm focal length aspheric lens (Light path 350230D) to collimate the main output beam (emission from the front facet).
    b) A laser current controller to supply the drive current to the laser and a temperature controller to provide bulk wavelength stabilisation of the laser (0.5Ω or 1mK stability over 24 hours if used with a 10kΩ thermistor at 25^0C).
    c) Signal generators to supply signals to the laser current or temperature controllers to tune or modulate the laser emission frequency.
2. A laser emission frequency stabilisation control circuit. A frequency stabilisation scheme is required to lock the emission frequency to the gas absorption line. This

utilised the reference gas cell and a feedback control loop (with proportional, integral, and derivative control actions).

3. A gas cell with a path length of 10cm. Conventional design techniques such as the use of AR coated and wedged windows were used to minimise interference effects.
4. A detection system comprising of an amplified detector and at least two lock-in amplifiers for phase sensitive detection. The second harmonic output of one lock-in amplifier (2f) was used as the system output. The third harmonic output (3f) of the second lock-in amplifier was used for frequency stabilisation.
5. Data acquisition system: the system had a means of transferring data from the instruments to a computer for post detection processing and storage. The acquisition was performed in the Labview^{TM} software environment.

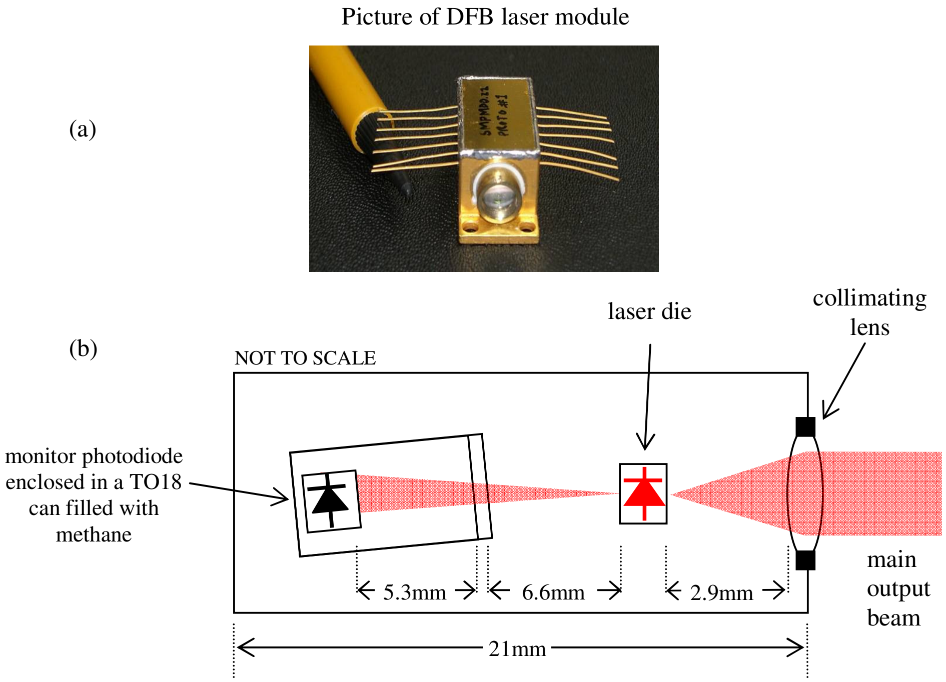

Figure 5-1: (a) Picture of the laser module. (b) Schematic diagram of the custom laser diode module.

5.1.2 Description of the operation of the initial bench top system

The laser emission could be coupled to the gas cell through free space or via single mode optical fibre. Fibre was utilised as it provided a flexible means of guiding light from the source to the gas cell. The fibre coupled system which is shown in Figure 5-2 is described here. The frequency stabilisation scheme is described separately in section 5.1.3. A picture of the drive circuitry is shown in Figure 5-3.

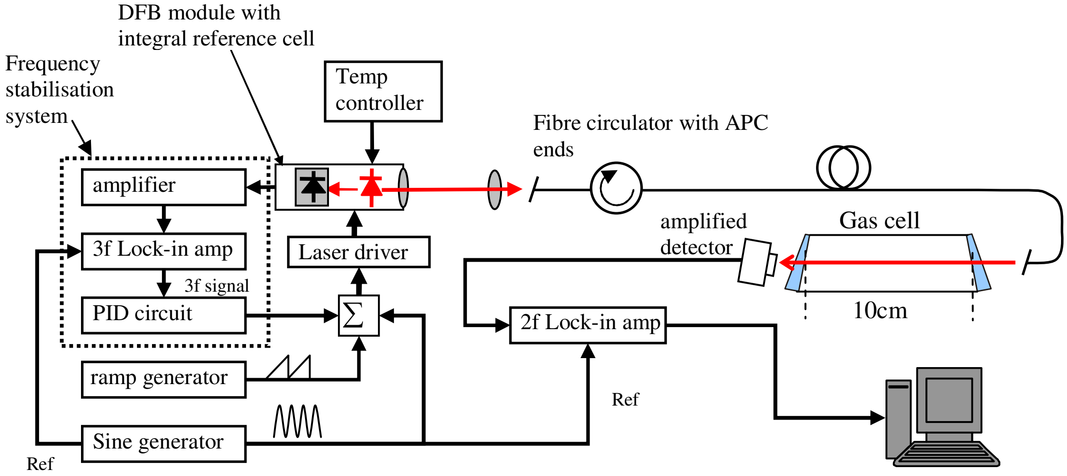

Figure 5-2: The experimental setup for methane gas detection using WMS. Key: SA, spectrum analyser; PID, proportional-integral-differential; APC, angle polished connector, Ref; reference signal supplied to the lock-in amplifiers.

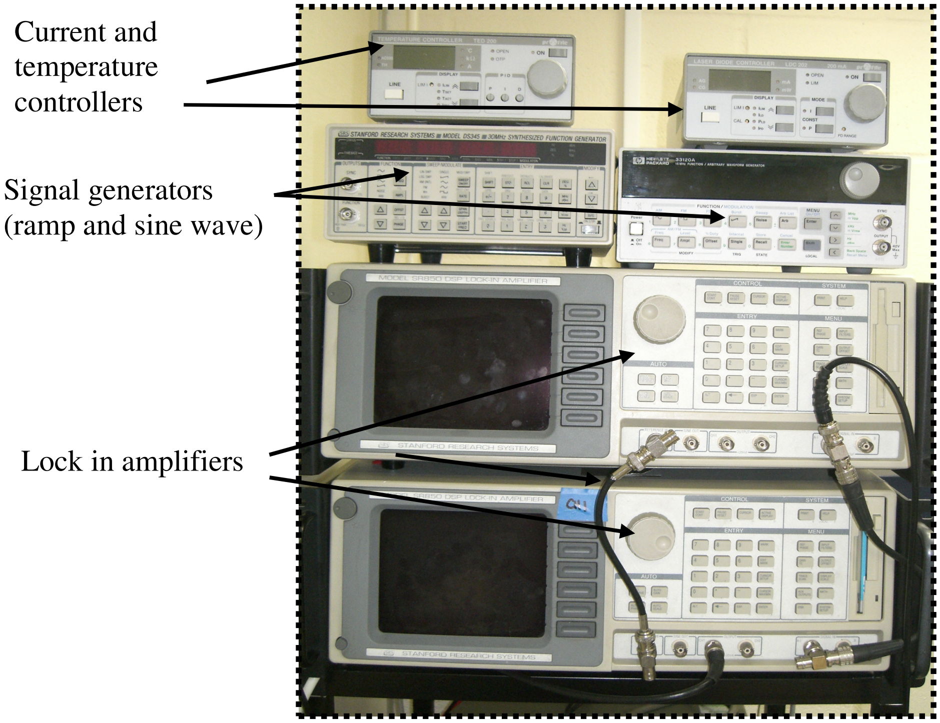

Figure 5-3: Picture of the bench top equipment for the WMS demonstrator. Current replacement cost >£16,000.

Modulated light from a frequency stabilised custom DFB laser diode (assembled by Semelab) was coupled into a single mode fibre circulator (FiberLogix FCIR-65-2-L-1) with angle polished connectors through an antireflection coated aspheric lens. The DFB laser was driven by a current controller (Thorlabs LDC 202) and a temperature controller (Thorlabs TED 200). Modulation of the DFB current was achieved by supplying the current controller with a 6kHz sine waveform from a signal generator (Hewlett Packard HP33120A). The 6 kHz modulation frequency was chosen because 1/f noise is negligible at such a relatively high frequency and the 2nd and 3rd harmonic components are within the audio frequency range allowing the use of cheap detection circuitry. This waveform was also supplied to lock-in amplifiers (Stanford Research Systems SR850) as a reference signal for phase sensitive detection. The return arm of the circulator was used for monitoring the returned power of the DFB laser by connecting it to a power meter (Ando AQ-2105) or monitoring the output spectrum by connecting to a confocal spectrum analyser (Toptica FPI 100) that had a free spectral range of 1GHz and a typical finesse of 1000.

The output light from the first arm of the circulator was collimated and directed onto an amplified detector (Thorlabs PDA400) after passage through a 10cm long gas cell with antireflection coated (Thorlabs C-coating, <0.25% reflectivity at 1650nm) and wedged windows (2 degrees beam deviation angle). The detector output was fed to a lock-in amplifier (Stanford Research SR850) for phase sensitive detection at 12 kHz (the second harmonic of the modulation frequency). The lock-in amplifier output could be observed on its graphic display, saved to a 3.5 inch floppy disk or transferred to a computer running Labview™ software through a high speed USB-GPIB interface (National Instruments HS-USBGPIB).

Test gases were fed to the gas cell from two certified cylinders (Scott Specialty Gases), one containing hydrocarbon (HC) free air and the other containing methane (three methane cylinders were used; 50ppm, 1010ppm and 2.5% volume in hydrocarbon free air). A bank of mass flow controllers (Teledyne Hastings HFC-302 with THPS-400 controller) was used to control flow rates from the two cylinders, with downstream mixing generating a series of mixtures of different concentrations from 0ppm to the concentration in the relevant methane cylinder.

5.1.3 Description of the frequency stabilisation scheme

Frequency stabilisation of the laser was achieved by locking the laser operating frequency to a methane absorption line via current control in the following manner. The operating wavelength of the laser was set to roughly coincide with the methane absorption line by setting the temperature controller to approximately 42^0C and the current controller to approximately 65mA. Within the DFB module, light from the rear facet of the DFB fell onto a Ge photodiode that was enclosed in a standard TO can containing 100% methane. This served as a reference methane gas cell. The photodiode signal was amplified by a home made transimpedance amplifier before being fed to a lock-in amplifier (Stanford Research SR850) where it was demodulated at 18 kHz (the third harmonic of the modulating signal). The laser frequency was accurately set to the methane line by simultaneously observing the 2f and 3f signals whilst adjusting the operating current (2f signal is maximum at line centre and 3f signal is zero, Figure 5-4).

A feedback control circuit (its design, build and evaluation process is reported in Appendix C) was then turned on to maintain the laser operating frequency on the gas absorption line. The control circuit used the 3f signal as an error signal. The home made circuit had proportional, integral and derivative control actions and supplied a voltage to the current controller that had the effect of locking the laser frequency to the gas absorption line.

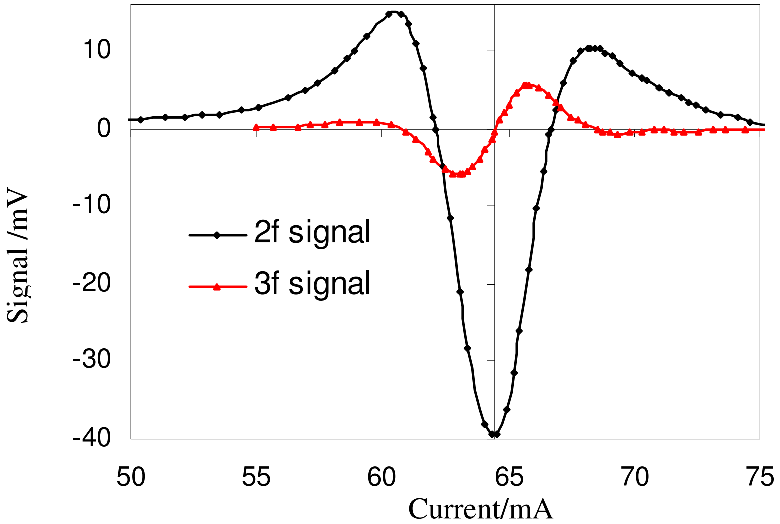

Figure 5-4: Experimentally measured second and third harmonic WMS signals; at the gas line centre the 2f signal had maximum amplitude and 3f signal was zero.

Figure 5-5 shows that the error fluctuation and drift in a free-running state, for which the PID control in the servo loop was switched off whilst the temperature was still stabilised, was reduced significantly when the PID control was on.

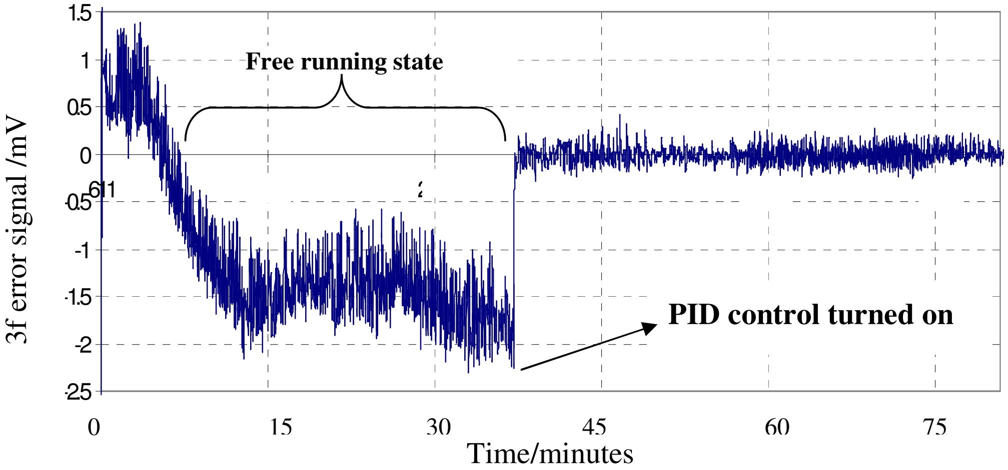

Figure 5-5: The recorded error (3f) signal from the lock-in amplifier; in the first part the PID is off. The y-axis is error signal in mV and the x-axis is time.

The recorded voltage output from the lock-in amplifier has been converted into a frequency scale (Figure 5-6) by using the known methane line width and the tuning characteristics of the diode (determined in section 5.2).

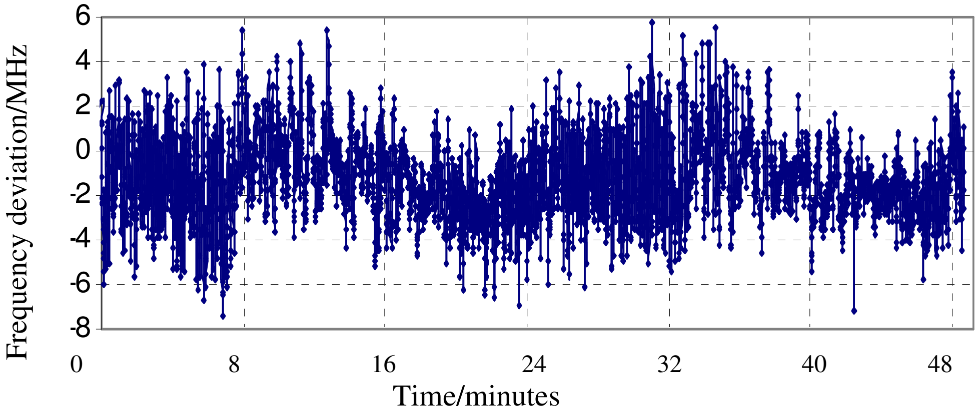

Figure 5-6: Graph of frequency jitter of the DFB laser under PID control over a period of 1 hour; the maximum deviation from the centre of the absorption line is less than 8MHz.

This gives an approximate degree of frequency stability. The residual frequency fluctuations of approximately 100 MHz (Figure 5-5), due to the stabilisation limitation of the temperature controller, have been reduced to less than 8 MHz by the frequency locking technique employed here. It is clear also from Figure 5-5 that the high frequency noise is located on a sloping background, suggesting that both differential and integral corrections of this signal are necessary. The frequency stability achieved by previous workers were in the range 500 kHz to 2MHz (Table 2.8).

An 8MHz jitter on the frequency signal would correspond to a potential uncertainty of 8μA (using a typical DFB laser tuning coefficient of 1GHz/mA) in the position of the peak in Figure 5-4. The uncertainty in the 2f signal depends on the modulation index (the 2f peak broadens with increasing modulation index).

5.2 Characterisation of the initial bench top demonstrator (MARK1)

This section describes the laboratory characterisation and development of the initial bench top WMS gas detection system. The characterisation experiments include; determining the DC laser current and temperature tuning coefficients, the optimum modulation amplitude or modulation index and intensity-frequency (IM-FM) modulation phase shift.

5.2.1 Determination of the optimum current modulation amplitude

The dependence of the amplitude of the peak 2f signal (the system output) on the modulation index (ratio of the HWHM of the line to the frequency modulation amplitude) was presented in chapter 2, Figure 2-19. This section reports two experiments that were conducted to determine the optimum frequency modulation amplitude.

The experiments involved measuring the frequency modulation amplitude that maximised the 2f output as described below.

In the first experiment, plots of the 2f signal as the wavelength was scanned across the gas absorption line for varying amplitudes of the 6 kHz modulation signal were recorded. The modulation amplitude was increased from an initial value of 100mV (2mA) to 1.3V (26mA) peak to peak in steps of 100mV (2mA). Figure 5-7 shows how the 2f signal waveform evolved with increasing modulation amplitude.

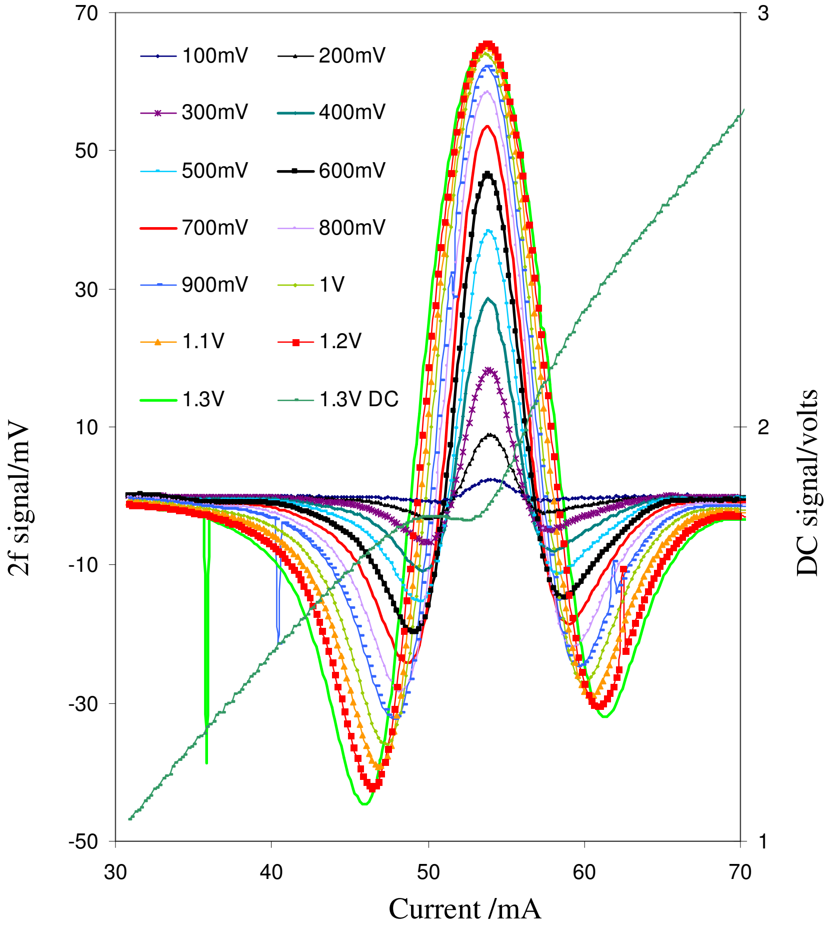

Figure 5-7: Plots of the 2f signal against current for different modulation amplitudes. The amplitude of the 2f signal initially increases with modulation amplitude and then saturates at a modulation amplitude of 1.2V peak to peak. Broadening of the measured line shape also increases with modulation amplitude.

The peak of the 2f plot initially increased approximately linearly with increasing modulation amplitude. The rate of increase declined as the 2f approached its maximum value. Further increase of the modulation amplitude only resulted in broadening of the 2f wave form and eventually a gradual decline of the amplitude of the 2f signal. The optimum modulation amplitude was then determined to be 12mA by inspection of Figure 5-7.

The second experiment involved locking the laser frequency to the centre of the gas absorption line and recording the 2f peak value as the modulation amplitude was varied as described in the first experiment. The modulation voltage supplied to the current controller was converted to a current modulation amplitude by using the controller's voltage to current conversion efficiency of 20mA/volt.

Figure 5-8 shows a plot of the peak amplitude of the 2f signal against the current modulation amplitude (broken line) and the fitted theoretical curve (equation 2-21).

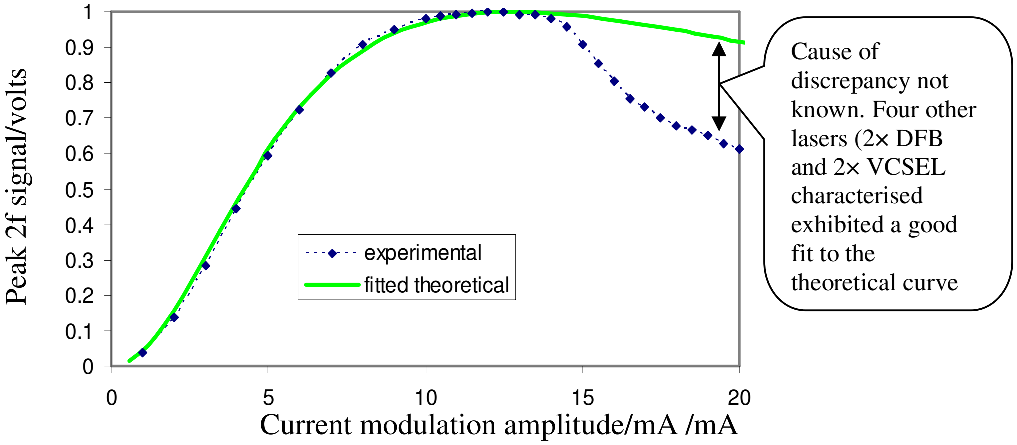

Cause of discrepancy not known. Four other lasers (2× DFB and 2× VCSEL characterised exhibited a good fit to the theoretical curve

Figure 5-8: Plots of the 2f signal against current modulation amplitude.

The optimum modulation current amplitude was determined from inspection of Figure 5-8 to be 12mA.

5.2.2 Determination of the frequency vs current tuning coefficient

The frequency against current tuning coefficient or frequency modulation coefficient of laser diodes, characterized by the parameter $\Delta \upsilon / \Delta i$ (GHz/mA), where Δi is the amplitude of the current modulation, is frequency dependent. The DC current tuning rate was determined from the slope of a plot of wavelength against current supplied by the manufacturer. The DC value is 0.66 GHz/mA at 25°C. This was confirmed from measurements obtained using a confocal spectrum analyser (Toptica, FPI 100).

The FM coefficient at a 6kHz modulation frequency (this is the fundamental modulation frequency of the instrument) was determined using an experimental procedure that was developed by Schilt and Thevenaz[2]. The efficiency was determined experimentally from the variation of the maximum of the second harmonic signal as a function of modulation amplitude Δi applied to the laser (Figure 5-8).

According to Schilt and Thevenaz[2] maximum 2f signal ($s_{2,\max}$) can be approximated by

$$s_{2,\max} = I_0 a_0 \left(\frac{-4}{m^2} + \frac{2}{m^2} \frac{m^2+2}{\sqrt{m^2+1}} \right) = kI_0 a_0\text{: for m = 2.2; k = 0.343} \qquad \textbf{(5-1)}$$

where I_0 is the optical power at line centre and a_0 is the absorbance at the same point. This relationship has been analytically verified to be equivalent to equation 2-17. The function $s_{2,\max}$ reaches its maximum when the modulation index, *m,* equals 2.2.

The procedure for determining the FM index involved measuring the maximum of the 2f signal $s_{2,\max}$ as a function of current modulation amplitude Δi (Figure 5-8).

A proportionality coefficient *K* between modulation index *m* and the current modulation amplitude Δi was determined from a fit of the experimental points by equation (5-1):

$$m = \frac{\nu_m}{\delta\nu} = K\Delta i \qquad \textbf{(5-2)}$$

where ν_m and $\delta\nu$ are the modulation amplitude and the half width at half maximum of the absorption line respectively. The fitting coefficient *K* was estimated to be 0.172/mA. The FM depth was then determined from the known $\delta\nu$ of methane by using the relation

$$\frac{\Delta\nu}{\Delta i} = K(\delta\nu) = 0.172mA^{-1} \times 2.2GHz = 0.38GHzmA^{-1} \qquad \textbf{(5-3)}$$

The optimum modulation amplitude (12mA) that was determined earlier in section 5.2.1 can now be converted to the frequency scale (0.38 GHz/mA × 12mA = 4.56 GHz. The experimentally determined modulation index is therefore given by 4.56 GHz/2.2 GHz = 2.1 ± 0.2 close to the theoretically predicted value of 2.2.

5.2.3 Determination of the temperature tuning coefficient.

The temperature tuning coefficient was determined in the following manner. The laser emission frequency was scanned across two methane absorption lines; the R3 and R4 branches of the $2\nu_3$ band (Figure 5-9(a)), by tuning the laser temperature. The laser operating current was set to 50mA. The second harmonic signal was then recorded as the temperature was stepped from 25°C to 53°C with a resolution of 0.1°C. Figure 5-9(b) shows the plot of the second harmonic signal against temperature that was obtained by temperature tuning the laser across the two methane lines shown in Figure 5-9(a).

The laser temperature tuning coefficient can be estimated by assigning the accurately known wavelength positions of peaks of the absorptions lines shown in Figure 5-9(a) to the peaks of the 2f plot of Figure 5-9(b). The tuning coefficient is then given by

$$\frac{1653.73\text{nm} - 1650.96\text{nm}}{51.9°\text{C} - 28.1°\text{C}} = 0.116 \pm 0.005\text{nm}/°\text{C} \tag{5-4}$$

This can be expressed in terms of frequency as 12.8 GHz/°C.

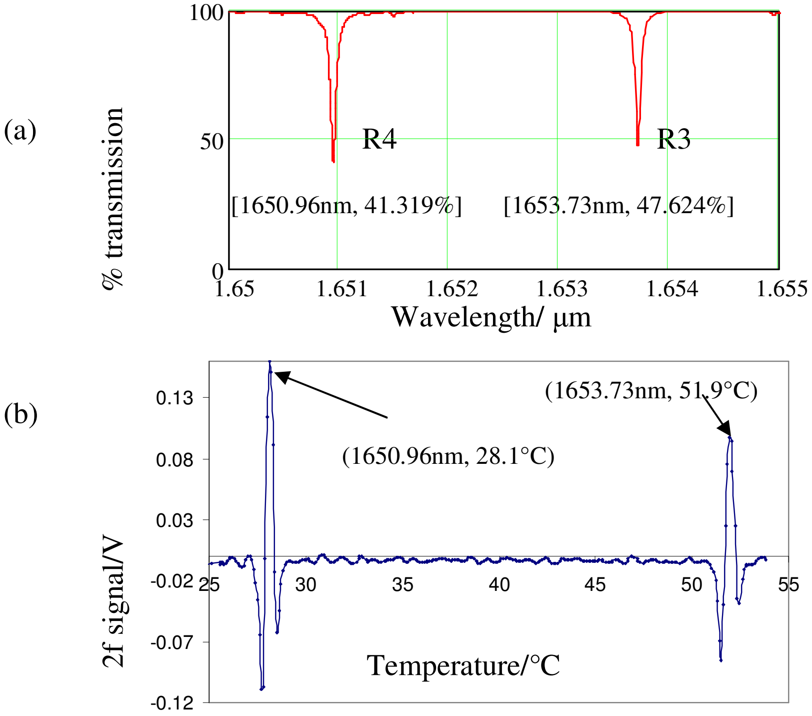

Figure 5-9: (a) Theoretical methane transmission lines (the R3 and R4 branches of the $2\nu_3$ band) obtained from the Hitran data base corresponding to 100% methane concentration in a path length of 1cm. (b) The 1651nm and 1654nm methane lines obtained by temperature tuning the DFB and monitoring the reference signal.

5.2.4 Determination of the intensity-frequency modulation (IM-FM) phase shift

In section Chapter 2, section 2.6.2, it was stated that in WMS, the detected signals are mainly due to the FM of the laser emission, whereas IM, often referred as RAM (residual amplitude modulation) in the literature, is an unwanted effect that distorts the signals. The level of distortion also depends on the IM–FM phase shift; therefore this parameter should be determined. The amplitude of the WMS signal detected at the *n*th harmonic varies periodically with the phase Φ_n of the lock-in detection. For each harmonic, the amplitude reaches maximum and minimum values at detection phases

$\Phi_{n,max}$ and $\Phi_{n,min}$, respectively, that are directly proportional to the **IM-FM** phase shift ψ[3]:

$$\Phi_{n,\max} = n\psi + k\pi, \tag{5-5}$$

$$\Phi_{n,\min} = n\psi + (2k+1)\pi/2. \tag{5-6}$$

The **IM-FM** phase shift ψ was experimentally determined by establishing the detection phase $\Phi_{n,min}$ that minimises the amplitude of the *n*th-harmonic signal:

$$\psi = \frac{\Phi_{n,\min} - (2k+1)\pi/2}{n} \tag{5-7}$$

The evolution of the maximum WMS signals (1f and 2f) as a function of detection phase of a lock-in amplifier (Stanford research SR850) was measured and plotted (Figure 5-10).

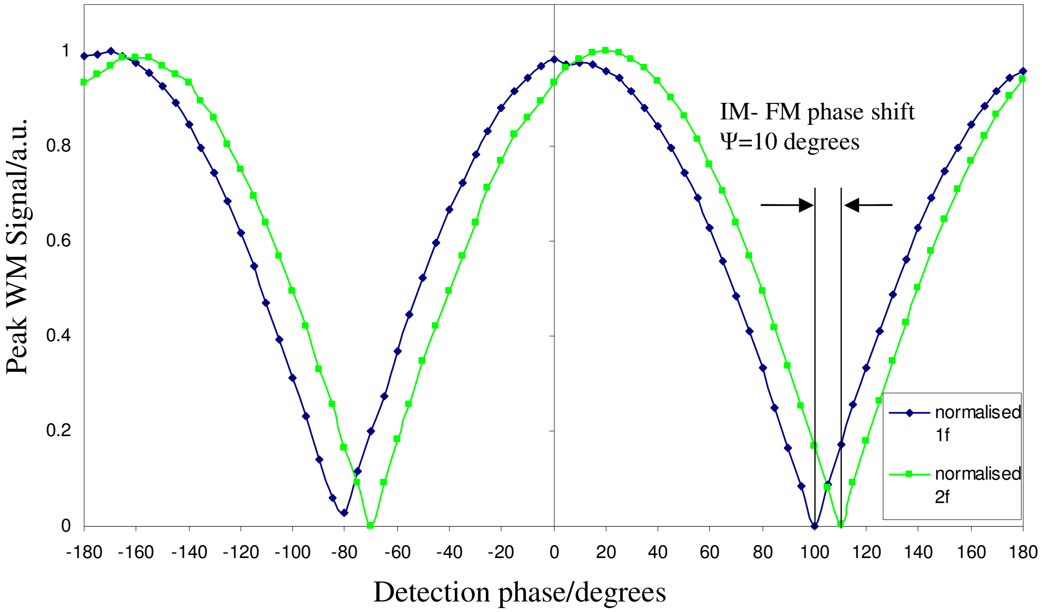

Figure 5-10: Evolution of the amplitude of the WMS signal as a function of detection phase. The IM-FM phase shift can be obtained from the difference in the position of the minima of two different harmonics[3]. Key: auk; arbitrary unit.

From the plot, the minimal amplitude of the signal at two different harmonics, n_1 and n_2 was determined, and the phase shift was obtained from the difference in the position of these minima by using the relation:

$$\psi = \frac{\Phi_{n_2,\min} - \Phi_{n_1,\min}}{n_2 - n_1} = \frac{110-100}{2-1} = 10 \pm 0.7 \text{ degrees} \tag{5-8}$$

The maximum amplitude of the 2f signal is obtained in the case of $\Phi_{2,max} = 2\psi \pm 180$ degrees

5.2.5 *Summary of the characterisation experiments*

The WMS system parameters established in the above experiments are summarised in Table 5-1. These parameters will be referred to in the following sections.

Table 5-1: Summary of experimentally determined system parameters

PARAMETER	VALUE
Optimum modulation current amplitude	12mA
D.C. frequency modulation coefficient	0.66GHz/mA
Frequency modulation coefficient at 6kHz	0.38GHz/mA
Temperature tuning coefficient	0.116±0.005 nm/°C
IM-FM phase shift	10±0.7 degrees

5.3 Investigation of interference effects in the system.

Interference effects were observed on the reference photodiode background signal during an experiment to determine the temperature tuning coefficient of the DFB module (section 5.2.3, Figure 5-9). The aim of this section is to investigate the source of the interference effects.

For convenience, Figure 5-9 is presented again here as Figure 5-11(a). The background signal (expanded in Figure 5-11(b)) appears to be modulated, consistent with the presence of interference effects.

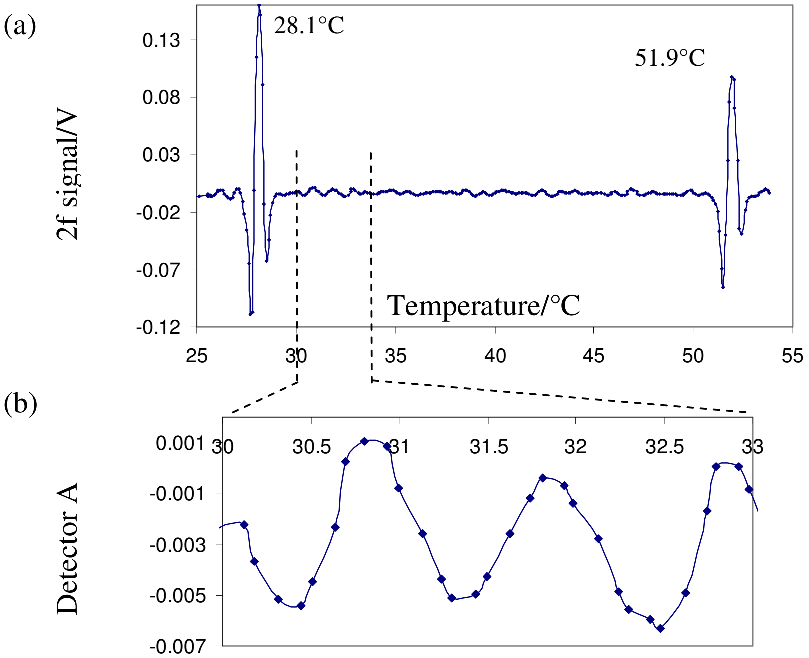

Figure 5-11: (a) The 2f harmonic signals corresponding to the 1651nm and 1654nm methane lines (the R4 and R3 methane lines of the 2v3 band) obtained by temperature tuning the DFB and monitoring the reference signal. (b) Expansion of (a) showing modulated background signal. The fringe spacing was approximately 1±0.2°C.

The interference fringe signal was observed to be repeatable. Figure 5-12 shows plots of the background signal obtained successively at intervals of at least five minutes.

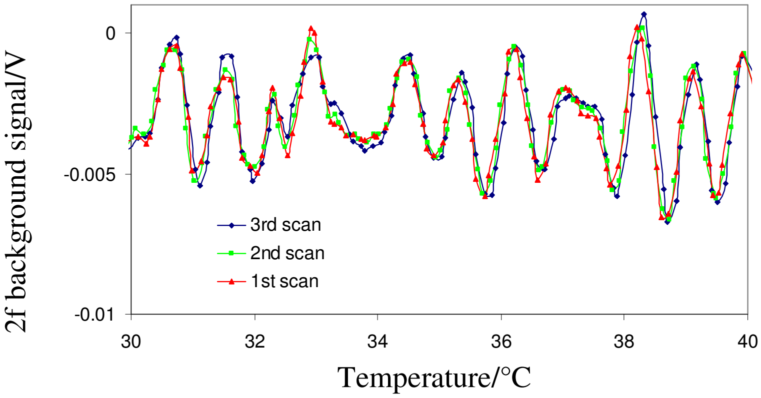

Figure 5-12: Plots of reference photodiode background signal obtained successively, separated by at least 5minutes. The signal was observed to be repeatable in the short term (5 minute intervals).

The fringes could be due to reflections from optical components within the laser module or external to it. There are two candidate mechanisms for generating the interference fringe; a Fabry-Perot etalon created by a pair of reflective optical components in the optical system (see Chapter 2; section 2.7.1 for more detail) or the self mixing effect (low optical feedback regime, see Chapter 2; section 2.7.2 for more detail). The following paragraphs describe the procedure that was taken to determine the components responsible for the observed fringes and the mechanism by which the fringes were generated.

The period of the fringe signal shown in (Figure 5-11(b) was used to determine the separation between the reflective surfaces giving rise to the fringes. The length *L* of the cavity (or external lasing cavity in case of self mixing) was calculated from the number of fringes in a given temperature span and from the temperature tuning coefficient (the relationship is valid for both Fabry-Perot cavities and the self mixing effect)

$$L = \frac{c}{2n\Delta\nu} \qquad \textbf{(5-9)}$$

where c is the free space speed of light and Δν is the fringe spacing, n is the refractive index of the cavity (n =1 for air spaced cavity). The fringe spacing was found to be 0.714°C (12 peaks in a span of 10°C), corresponding to an etalon spacing of 14±2mm.

The contribution of reflections from external components to the observed signal was ruled out after it was observed that the fringe signal was still detectable on the photodiode background signal after the removal of the external components. This was taken as confirmation that the fringe signals were generated within the DFB module itself. The following section reports experiments investigating interference effects in the DFB package.

5.3.1 Investigation of Interference effects in the DFB module

The DFB module (Figure 5-1(b)) was examined to identify the reflective surfaces that could give rise to interference effects.

An aspheric lens (Light path 350230D with a back focal length or working distance of 2.91mm, centre thickness of 2.94mm and an AR coating with a reflectivity of < 0.2% at 1651nm) is the only component in the path of the forward emission. Due to the distances and the curvature of the lens surface, it was considered that the source of the reflections was less likely to be in the forward path. A strong possibility was thought to be reflections from components in the path of the rear facet emission; in particular the photodiode chip or window (spacing of 11.9mm, **Error! Reference source not found.**). Due to the fragile nature of the components involved it was difficult to verify that these were the surfaces responsible by the usual means (e.g. changing the effective optical cavity length and observing the effect on the fringes) as there was a possibility of permanent damage to the laser module.

The next step that was taken was to establish the mechanism by which the fringes were being generated (i.e. self mixing or Fabry-Perot etalon).

5.3.2 Establishing mechanism generating fringes (self mixing or Fabry-Perot etalon)

Although the analytical treatment of fringes due to a Fabry-Perot etalon and self mixing is similar, the potential implications for the gas detection system would be more severe in the latter case. This is primarily due to the fact that if fringes were due to a Fabry-Perot cavity in the rear facet emission path, they would be present on the monitor photodiode signal only and not on the front facet emission. Therefore one solution to the problem would be not to use the integral reference cell. A beam splitter could be used to sample and direct a portion of the main beam to an external reference cell as conventionally implemented in many WMS systems. On the other hand if the fringes were caused by self mixing, they would be present on the front facet emission as well. This would rule out the solution described above if the fringes can not be eliminated. This is why it was imperative to establish the mechanism by which the fringes were generated.

As Fabry-Perot etalons are created between parallel reflective surfaces, angling the monitor photodiode with respect to the laser facet would result in reduction or elimination of the interference fringe signal, if this was the etalon giving rise to the fringes. However, angling of the reference cell with respect to the laser chip did not result in significant reduction of the visibility of the fringes. Figure 5-13 shows plots of the background photodiode signal obtained for a varying degree of tilt applied to the reference cell.

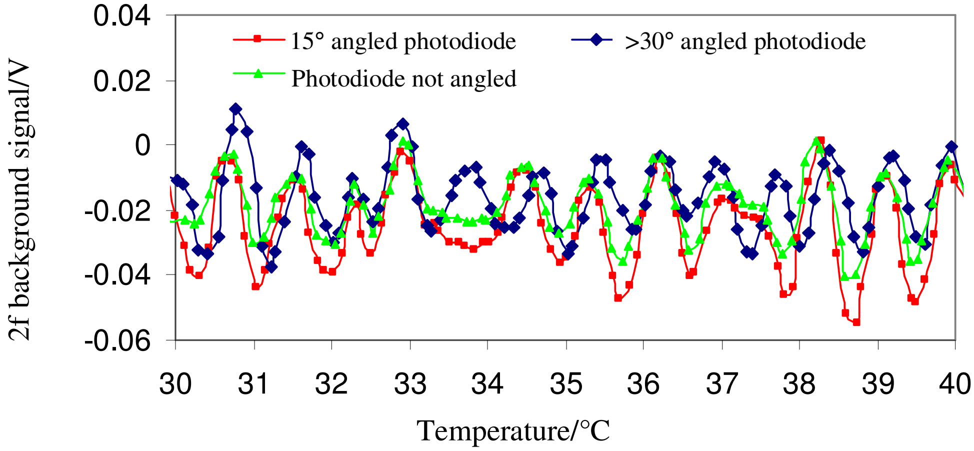

Figure 5-13: Normalised background signals obtained for different degrees of angling of the photodiode. Angling did not result in significant reduction of the visibility of the fringes.

This is consistent with the fringes not originating from an etalon where the reference gas cell is one of the parallel reflective surfaces. It should be pointed out that this experiment was made difficult by the diverging nature of the rear facet emission and the close proximity of the components involved.

As there are no other reflective parallel surfaces in the rear emission path with a spacing consistent with the fringes, a plausible explanation for the fringes is that the fringes are formed by self mixing due to back scattered light entering the laser cavity. The presence of the fringes of the same period on the main output beam would provide additional support for the self mixing case. The presence of the fringes on the main output beam was next investigated as described below.

An amplified detector (Thorlabs PDA400) was placed in the path of the main output beam (Figure 5-14).

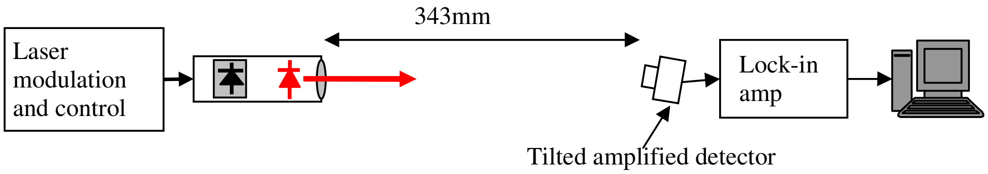

Figure 5-14: Schematic diagram of the experimental set up for investigating the effect of interference effects within the DFB module on the performance of the instrument.

Precautions were undertaken to prevent light backscattered or reflected from the detector from being coupled into the laser cavity. The distance between the laser and detector was 343mm. The detector signal was fed to a lock-in amplifier for second harmonic detection.

Interference fringes with the same period as those observed at the reference monitor photodiode were observed. Shown in Figure 5-15 (a) and (b) are fringes observed as the laser temperature and current were tuned respectively.

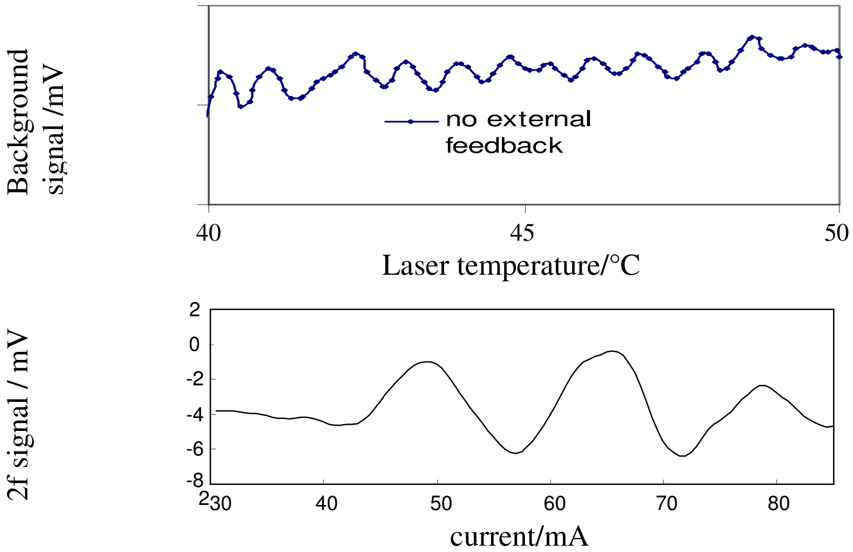

Figure 5-15: Plots showing modulation of the background signal without external feedback. The plots were obtained with the detector located 343mm from the emitter. Plots obtained by (a) temperature tuning the laser and (b) current tuning the laser.

This can be taken as further evidence that the fringes could be attributed to the self mixing effect rather than to a Fabry-Perot cavity as they are present on both the rear and front facet emissions of the laser. Wherever the cavity was (forward or rear path), only in the self mixing case would the fringes be visible in both the forward and rear emissions

The results of the investigations so far are consistent with the rear photodiode being the source of the observed fringes (from the calculated fringe spacing). The presence of the fringes on both the rear and front facet emission and the fact that misaligning the reference cell with respect to the laser chip did not result in significant reduction of the fringe visibility can be taken as evidence to support the hypothesis that the fringes are generated through the self mixing effect rather a Fabry-Perot etalon.

Due to the importance of the implications of self mixing fringes for TDLAS based gas sensing, the topic of self mixing was extensively investigated. This included investigations of self mixing effects due to diffuse reflections. The results of the investigation are reported separately in chapter 6.

In the following section an evaluation of the effects of the interference effects on the performance of the instrument is reported.

5.3.3 Evaluation of the effect of the interference effects in the DFB module on the performance of the instrument

The aim of this section is to establish the influence of interference fringes generated in the DFB module (Semelab) on the performance of the initial benchtop instrument. The effect of the interference fringes generated in the DFB module on instrument performance was investigated using the experimental set up shown in Figure 5-14.

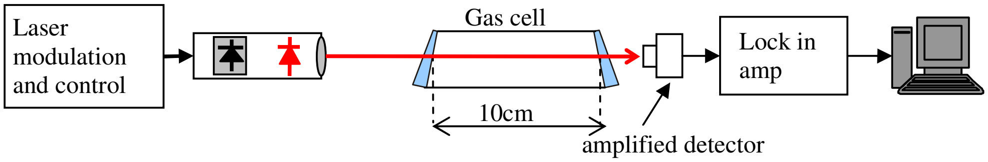

Figure 5-16: Schematic diagram of the experimental set up for investigating the effect of interference effects within the DFB module on the performance of the instrument.

A 10cm gas cell with wedged and AR coated windows was used for the investigations. Precautions were taken to prevent external feedback. Such measures included locating the detector and the cell at distances greater than 1 metre from the laser diode.

The gas cell was filled with 505ppm methane. Plots of the demodulated 2f signal and the background ((i) from the detector with the cell evacuated and (iii) from the monitor photodiode) were obtained by scanning the laser frequency across the gas absorption line. The frequency sweep was achieved by ramping the laser current from 30-80mA (approximately 26GHz range). As the monitor photodiode is enclosed in a TO18 can containing methane, the monitor photodiode background signal was obtained by setting the laser operating temperature such that the emission wavelength was “off” the gas absorption line (in this case 40°C).

Figure 5-17 shows plots of the 2f signal and the background recorded at the detector. The 2f signal has a significant offset and is distorted.

The offset and the distortion were removed by subtracting the background signal from the 2f signal (Figure 5-17). The period of the fringes on the background signal is comparable to that of fringes observed on the reference photodiode (Figure 5-18).

By comparing the background signals recorded at the detector with and without the gas cell, it was established that the contribution of the gas cell to the fringes observed at the detector was below the level of the fringes generated in the module and therefore could not be measured directly. The detection sensitivity is therefore expected to be limited by the fringes generated in the module rather than those created by the gas cell.

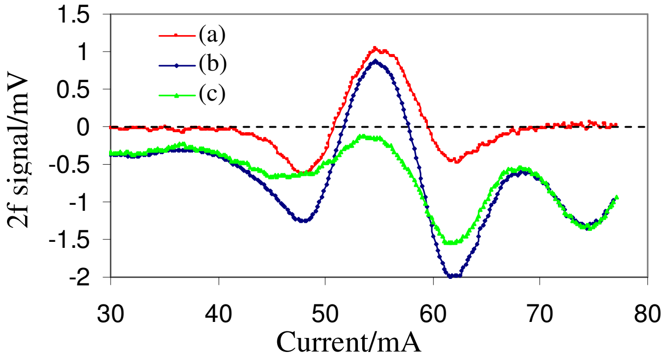

(b) 2f signal cell full of gas

(c) 2f signal (cell evacuated)

(a) Corrected signal (b) - (c)

Figure 5-17: Plots of the 2f and background signals obtained from a 10cm gas cell containing 505ppm methane. Detector gain was 0dB. The lock-in amplifier time constant was 300ms. Laser temperature was 28.5°C. DFB module.

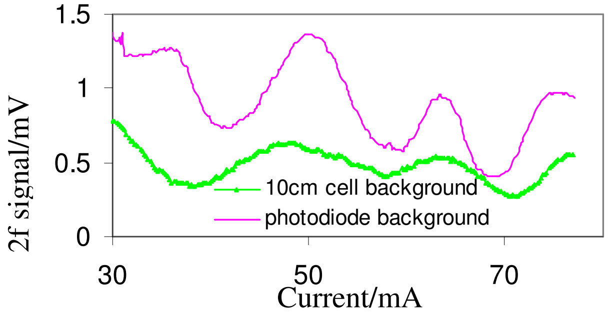

Figure 5-18: Plots of the photodiode and 10cm cell background signals. In both cases the background is dominated by interference effects within the DFB module.

For concentrations above 100ppm the output of the instrument was linear (Figure 5-19).

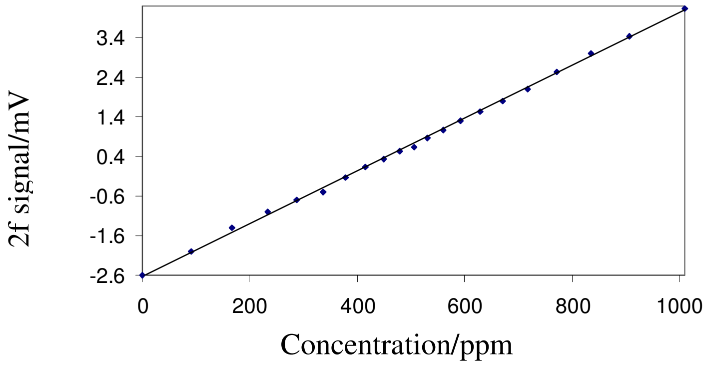

Figure 5-19: Plot of 2f signal against methane concentration for the DFB module. Time constant was 1 second. Detector (Thorlabs, PDA400) gain was 0dB (15kV/A).

However, as expected, at low concentrations, both the background and the measured signal were subject to drift (Figure 5-20).

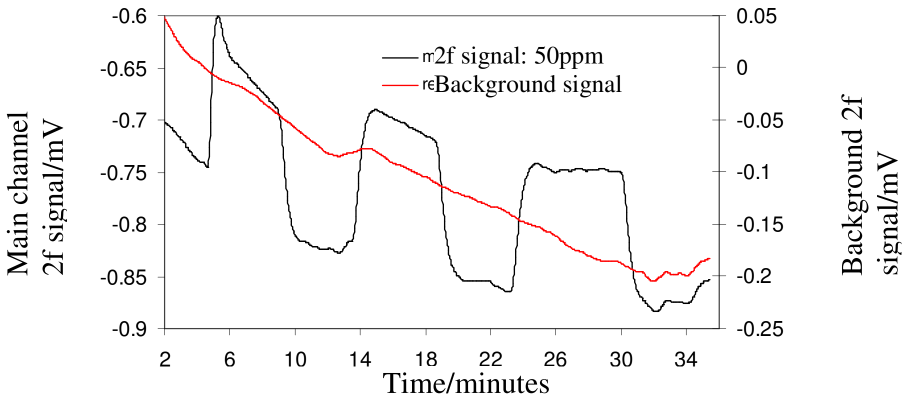

Figure 5-20: Plots of the 2f signal recorded for a series of 50ppm methane bursts, illustrating that the gas signal is affected by fringes in the module. The drift on the main channel is similar to the drift on the ref channel.

The following section describes efforts that were taken to reduce the amplitude of the fringes generated in the DFB module.

5.4 Evaluation of a revised benchtop demonstrator (MARK2)

As discussed in the previous sections, a number of revisions to the experimental configuration shown in Figure 5-2 were required to improve the performance of the system. The main changes are summarised below;

1. Removal of optical fibre: fibre was initially used in the system for its perceived convenience or flexibility in guiding the laser emission to the gas cell. However the efforts required to suppress interference effects due to Fabry-Perot Etalons and optical feedback in the fibre coupling system outweighed the benefits (experiments reported in Appendix D. Therefore fibre was removed from the system.
2. Modifications to the DFB package.
   a. Removal of the integral reference gas cell. This was thought to contribute to the fringes investigated in 5.3.
   b. Covering of reflective surfaces in the DFB module with absorbing material.
3. Use of external gas reference cell; the integral reference photodiode removed from the DFB package was used as an external reference cell.

The revised experimental setup is shown in Figure 5-21. A portion of the laser emission was sampled by a beam splitter and directed to photodiode enclosed in a T018 can for frequency stabilisation as described in 5.1.3. The beam transmitted through the beam splitter fell onto the detector after passage through the gas cell.

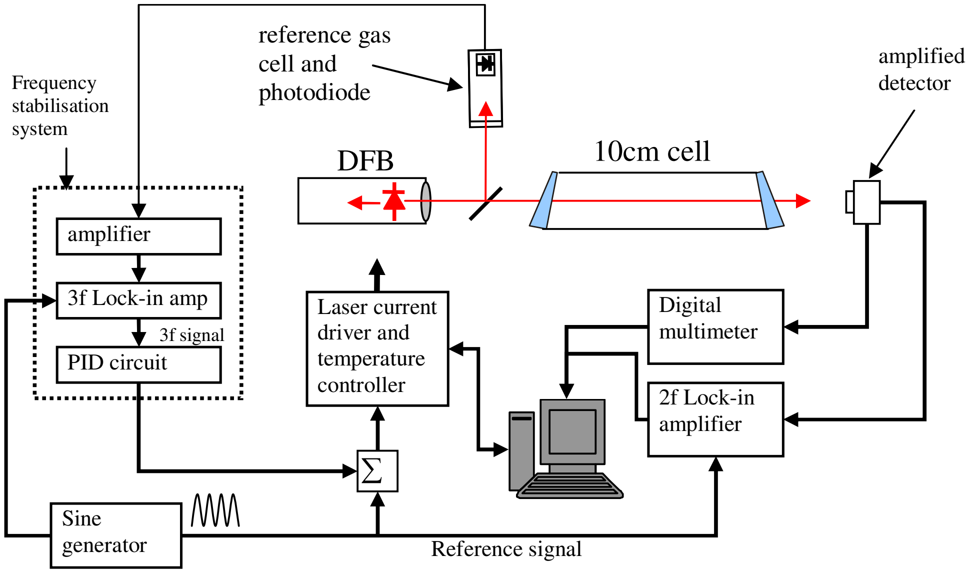

Figure 5-21: Scheme of the revised experimental set-up used with the DFB laser.

The following section reports a series of experiments that were conducted with the aim of reducing interference fringes generated in the DFB module.

5.4.1 Reduction of self mixing fringes in DFB module

Two main modifications were made to the DFB module in an attempt to reduce the interference fringe signal generated within the DFB module. The source of the fringes was suspected to be reflections from components in the path of the rear facet emission. The first modification involved removal of the monitor diode and second modification was to cover the reflective surfaces of the module with an antireflective material.

In a first experiment, the background signal at the detector (with reference to Figure 5-21, with the 10cm gas cell and the reference channel removed) obtained prior to the removal of the photodiode was compared to the background signal obtained after the removal (Figure 5-22). The background taken before removal of the photodiode (plot (a)) appears as if it is a superposition of more than one frequency component. This could be expected as there are at least three reflective components in the path of the rear facet emission, namely; the T018 can window, the monitor photodiode facet, and the back end of the laser module.

Upon close inspection of (Figure 5-22), it appears that removal of the photodiode resulted in a minor reduction of the amplitude of the background signal and a change in the appearance of the waveform (to just one distinct frequency component). A possible explanation is that there was only one dominant reflective surface in the optical path i.e. the gold finish on the back end of the case of the module. If this were the case, a reduction in the effective reflectivity of the back end of the module would lead to a reduction in the visibility of the fringes.

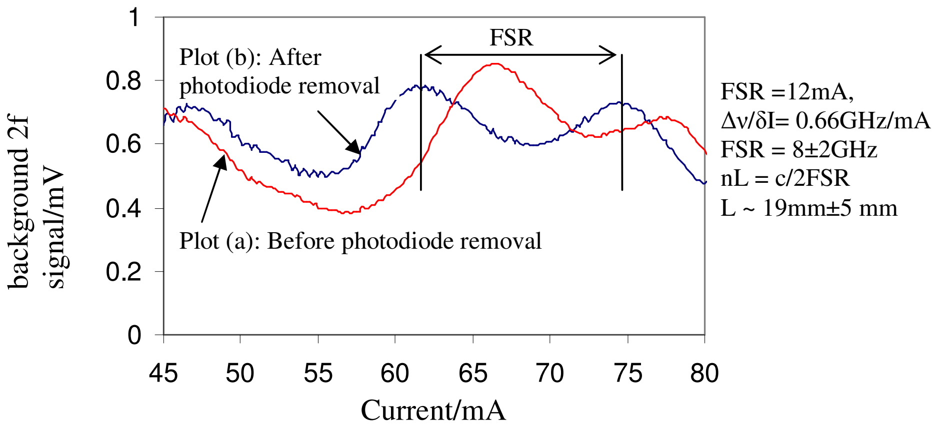

Figure 5-22: Plots of background signals obtained at detector. Plot (a) obtained with the reference gas cell in place. Plot (b) obtained with the reference gas cell removed Detector gain (Thorlabs PDA400) was 0dB (15kV/A). The lock-in amplifier time constant was 100ms.

This was tested in a second experiment by attaching an absorbing material onto the back surface of the module's case. Figure 5-23 shows a comparison of plots of the 2f demodulated signal recorded at the detector with and without the absorbing material.

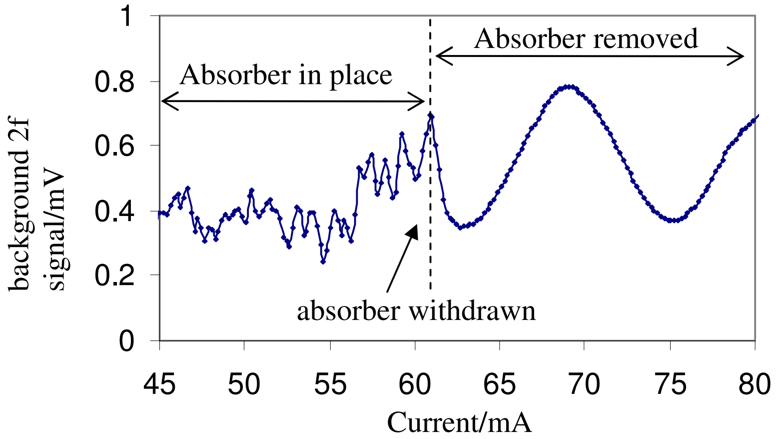

Figure 5-23. Plots of background signals recorded at detector A while an absorber was placed at the rear of the laser module and then removed. Detector gain was 0dB. The lock-in amplifier time constant was 100ms.

The first half of the plot was recorded with the absorber in place and the absorber was withdrawn for the later half of the signal acquisition. Reducing the effective reflectivity of the back end of the module's case by the use of the absorber resulted in an apparent reduction the amplitude of modulation of the background signal, confirming the hypothesis that the fringes are caused by backscattering from the components in the path of the rear facet emission.

In section 5.3, it was found that the contribution of the gas cell to the background signals could not be measured directly because it was below the level of the signal due to interference fringes from the DFB module. The experiment was repeated in the case of the modified DFB module. With reference to Figure 5-21, the detector background signal was recorded with the evacuated 10cm cell in place whilst the laser current was ramped from 45-80mA (approximately 23GHz). The result is shown in Figure 5-24.

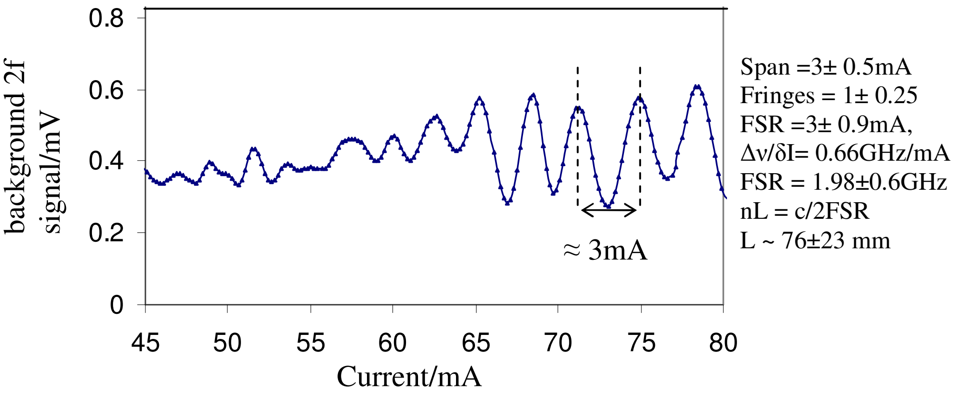

Figure 5-24: Plots of background signals recorded at detector B whilst the laser current was ramped from 45-80mA (approximately 23GHz). Detector gain was 0dB. The lock-in amplifier time constant was 1s.

Interference fringes with a period of 76 ± 23mm were observed. The fringes were only detectable for particular orientations of the gas cell. This is consistent with the fringes being caused by a residual Fabry-Perot cavity created between the two opposing windows of the 10cm cell. It is therefore expected that the detection sensitivity of the revised demonstrator would be limited by the stability of the mechanical alignment of the optical components and the gas cell.

The following sections reports experiments conducted to establish the detection sensitivity of the revised demonstrator.

5.4.2 Evaluation of the revised system

In an experiment to determine the detection limit of the system, the laser diode output was locked to the methane line and the 2f-demodulated output was recorded whilst different methane concentrations (0ppm, 25ppm and 50ppm) were delivered to the cell. Figure 5-25 shows the 2f demodulated output plotted as a time series against different methane concentrations.

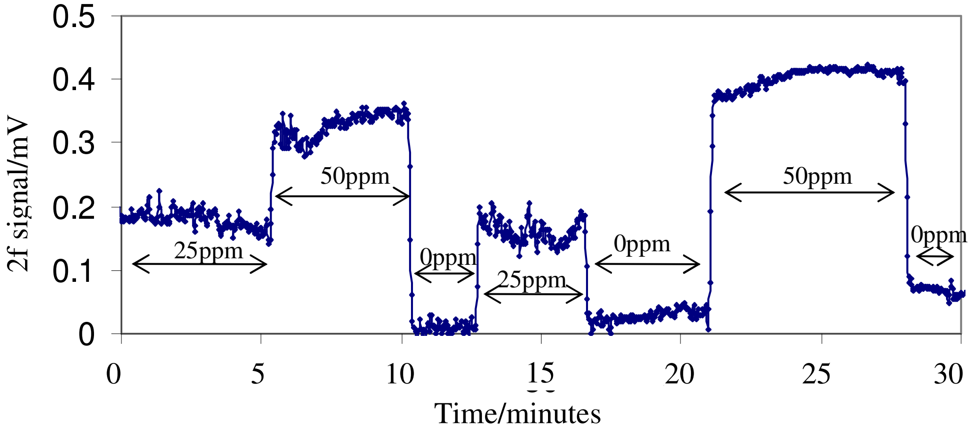

Figure 5-25: Plot of 2f signal showing short term drift in the instrument output. Time constant of the lock-in amplifier was 1 second. Detector (Thorlabs, PDA400) gain was 0dB (15kV/A).

The detection limit was estimated from calculations presented in Table 5-2 using data from the first 12.5 minutes of Figure 5-25 to evaluate short term noise and from the entire experiment to determine longer term drift.

Table 5-2: Signal to noise ratio calculations for data shown in Figure 5-25.

Concentration/ppm	**50**		**25**	
Calibration factor	152ppm/mV		139ppm/mV	
	mV	**ppm**	**mV**	**ppm**
Mean	0.33	50	0.18	25
Standard deviation (1σ)	0.02	3.04	0.013	1.81
SNR1[a]	16.2		14.3	
SNR2[b]	36		19.8	
Short term drift- 5minutes	3ppm			
Long term drift- 30minutes	11ppm			
Response time t_{90}	<10 seconds			
Dynamic range	0ppm-2.5%			

[a] SNR1 was calculated by dividing the background corrected methane signal by its standard deviation.

[b] SNR2 was calculated by dividing the background corrected methane signal by the standard deviation of the background.

[c] Cell volume = 5.1×10^{-3}L

Figure 5-26 shows the 2f demodulated output plotted against different methane concentrations in the range 0-50ppm.

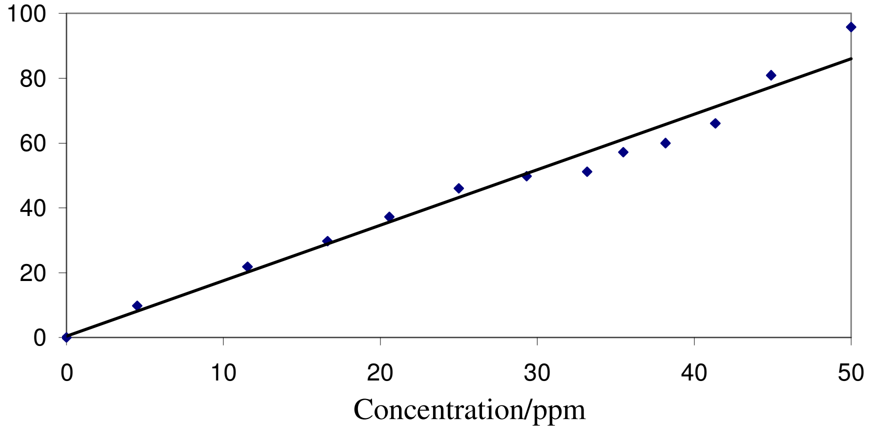

Figure 5-26: Plot of 2f signal against concentration for DFB. Time constant was 1 second. Detector (Thorlabs, PDA400) gain was 0dB.

Residual noise and drift in the detected signal is attributed to the residual etalon and self mixing effects described above.

In summary, the detection limit of the MARKI demonstrator was limited by interference fringes generated in the DFB module. The fringes were caused by light backscattered/back reflected from components in the path of the rear facet emission. The magnitude of the fringes was reduced in MARK2 by removing the integral reference cell in the module and covering the reflective surfaces in the path of the rear facet emission.

5.5 Discussion and Conclusion

In this chapter the design, build and evaluation of the performance of a bench top WMS methane gas sensor has been reported. The target sensitivity of the instrument was 2ppm corresponding to the UK's background methane concentration.

The performance of the MARKI instrument was limited by interference effects from the fibre coupling system (feedback effects and etalon effects) and from the DFB module (self mixing effect). After removing the fibre and modifying the DFB module, a detection sensitivity of 3ppm was achieved in 10cm gas cell for a demodulation time constant of 1 second. The detection limit was set by residual interference effects from the laser module and the gas cell. A long term drift of 11pm was recorded.

The effects of interference fringes due to Fabry-Perot etalons on the sensitivity of TDLAS is well known. In the experiments it was found that fringes due to the self mixing effect were equally if not more problematic. It was therefore surprising to find no systematic study of the implications of self mixing effect on TDLAS based sensors in the literature. Due to the importance of the subject, an extensive study of the self mixing effect was conducted and is reported in the next chapter.

5.6 References

[1] van Well, B., Murray, S., Hodgkinson, J., Pride, R., Strzoda, R., Gibson, G., and Padgett, M. (2005), 'An open-path, hand-held laser system for the detection of methane gas', *Journal of Optics A: Pure and Applied Optics*, V7, N6 pp. 420-4.

[2] Schilt, S. and Thevenaz, L. (2004), 'Experimental method based on wavelength modulation spectroscopy for the characterisation of semiconductor lasers under direct modulation', *Applied Optics*, V43, N22, pp. 4446-4453.

[3] Schilt, S., Thevenaz, L., and Robert, P. (2003), 'Wavelength modulation spectroscopy: combined frequency and intensity laser modulation', *Applied Optics*, V42, N33, pp. 6729-6736.

Chapter 6 Self mixing interference fringes

The theory of interference effects caused by weak optical feed back in semiconductor lasers was presented in section 2.7.2. For convenience, a summary is presented in 6.1.2.

This chapter reports observations of self-mixing induced spectral features in the measured absorption spectra for TDLS based gas detection. The features were almost identical in appearance to Fabry-Perot interference fringes and created equally problematic measurement uncertainties that limited detector performance.

The self mixing interference effect was observed in the laboratory gas detection instrument reported in Chapter 5 as well as in a commercial prototype instrument employing a VCSEL (Vertical Cavity Surface Emitting Laser) diode.

Experiments involving the commercial prototype instrument were conducted in collaboration with IR Microsystems (IRM), originally a spin-off company from the Federal Institute of Technology (EPFL) in Lausanne, Switzerland. IRM is now part of Leister Process Technologies, Switzerland. The experiments were conducted at IRM premises (EPFL science park, Lausanne) and are reported in section 6.3.

To the author's knowledge, a systematic study of self-mixing interference has not been previously reported in TDLS. However, it is likely to have been previously observed because (i) the effect is difficult to distinguish from etalon – induced interference fringes, and (ii) as it is shown, it can arise in a greater range of circumstances than is the case for etalons. In particular, this phenomenon is particularly relevant to the use of diffusely reflective surfaces within gas cells, the focus of the next chapter.

Before presenting the experimental results, a brief summary of the theory of interference effects due to low finesse Fabry-Perot etalons and self mixing is outlined below.

J. Hodgkinson[*] made a significant contribution to the following sections presented in this chapter: Summary of theory in 6.1, analysis of the results presented in 6.2.5 and 6.2.7 and the summary section presented in 6.4. The results reported in 6.3 were obtained in collaboration with Dr Stephane Shilt[†].

---

[*] Research supervisor

[†] Project manager at IR Microsystems (IRM). Originally a spin off company from Federal Institute of Technology (EPFL) in Lausanne, Switzerland. IRM is now part of Leister Process Technologies, Switzerland.

6.1 Brief summary of theory of interference from low finesse etalons and self mixing

6.1.1 Interference from low finesse etalons

Low finesse Fabry-Perot etalons within the optical path give rise to an intensity modulation that takes the form[1];

$$I = I_0 \{1 + K \cos\delta\} \qquad \textbf{(6-1)}$$

where I_0 is the incident intensity, K is a constant whose value lies between zero and one and δ is the optical phase of the cavity of length d, with $\delta=4\pi d/\lambda$ for a double pass (see Figure 6-1) and λ is the wavelength. The value of K is proportional to $\sqrt{r_1 r_2}$, where r_1 and r_2 are the reflectivities of the two surfaces forming the etalon. If the reflectivities of the two surfaces are equal, as might be expected in the case of windows, K varies in proportion to r.

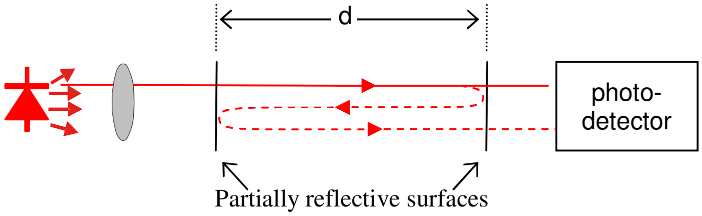

Figure 6-1: A low-finesse etalon in the optical path of a detection system; the partially reflective surfaces are often the windows of the gas sample cell.

The light reflected from the cavity is also modulated, such that it is out of phase by 180° in δ with respect to the transmitted intensity. The total level of light emitted from the diode (transmitted + reflected) is unchanged, as is the voltage across the laser diode at a given drive current.

6.1.2 Self-mixing interference

If a fraction of light backscattered or back reflected from optical components or a remote target is coupled into the laser cavity, modulation of both the amplitude and frequency of the lasing field can be generated[2]. Relative motion between the laser and the remote target or tuning the laser by ramping the injection current or operational temperature will result in generation of signals that are periodic in the optical phase difference.

This modulation can be monitored on the output from the rear facet, using the monitor photodiode which is often to be found in the laser diode package (Figure 6-2).

The laser output intensity takes the form

$$I = I_0 (1 + m \cos\delta) \qquad \textbf{(6-2)}$$

where I_0 is the output power from the diode in the absence of feedback, I is the modulated power output in the presence of feedback and m is a modulation index. m is a function of the so-called feedback parameter C (dependent on the characteristics of the laser) and, for very weak feedback, proportional to $\sqrt{r}$ where r is the proportion of light reflected back into the laser diode.

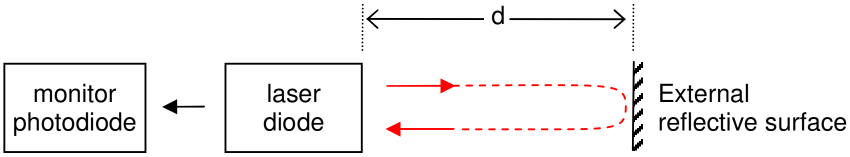

Figure 6-2: Typical schematic configuration for measurement of deflection using laser diode self-mixing. After Giuliani *et al*[2].

This form of the intensity modulation is therefore indistinguishable from that in equation 6-1, but the effects differ from those of etalon interference in two ways. Firstly, the result is a modulation of output intensity of the diode rather than of the intensity of light transmitted or reflected from the interfering cavity. Output from the rear facet is also modulated with a 180° phase change in δ, compared to the front facet. Secondly, while the laser drive current is ramped, a modulation can also appear on the voltage across the diode.

For a perfect Lambertian diffuse reflector, the level of light returned into a small solid angle $\delta\Omega$ is given by

$$r = \frac{\delta I}{I_0} = \frac{3}{4\pi} F \left(1 + \cos 2\theta\right) \delta\Omega \qquad \textbf{(6-3)}$$

F is the fraction of light backscattered in total by the diffuser (=0.99 for Spectralon$^{\text{TM}}$ and similar materials, as used in our experiments) and θ is the angle that the collection axis makes to the normal to the surface.

The following sections report experiments investigating the self mixing effect and its implications for TDLAS based gas absorption measurements.

6.2 Summary of experiments reported in this chapter.

The benchtop demonstrator described in section 5.4 was used for the experiments reported in this section.

A brief outline and justification for the experiments reported in this chapter follows;

a. Detection of the self mixing effect using a monitor photodiode enclosed in laser diode package as a means of distinguishing between fringes due to Fabry-Perot etalons and the self mixing effect.

b. Detection of the self mixing effect using the voltage drop across a laser diode as an alternative method to (a) where the laser package does not include a monitor photodiode.
c. Determination of the magnitude of self-mixing interference caused by a specular reflection from a 6° wedged, AR coated window.
d. Feedback from a diffuse reflector (Spectralon^{TM}) placed in the output beam at a range of distances from the laser diode. This is to show that the self mixing effect can arise from diffuse reflections as well as specular reflections.
e. Observations of self mixing in a VCSEL as confirmation that VCSELs are also susceptible to the self mixing effect.
f. Gas absorption measurements made in the presence of deliberately induced self mixing interference fringes. The purpose was to determine the amplitude of the self mixing fringes relative to the gas absorption signal.
g. Observations of interference effects (possibly caused by self mixing) in a commercial prototype instrument. To emphasise the significance of the implication of self mixing effect in the design of TDLAS based gas sensors.

6.2.1 Experimental setup

Figure 6-3 shows a schematic diagram of the laser diode modulation and detection apparatus, in this case configured for measurement of self-mixing modulation of the rear emission from the DFB laser diode.

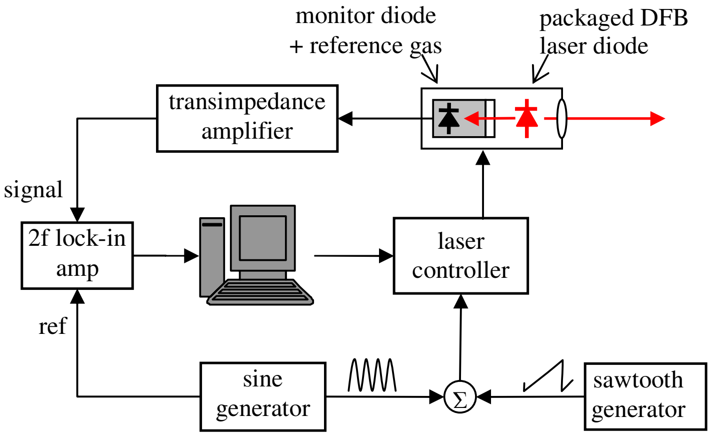

Figure 6-3: Schematic experimental configuration for 2f wavelength modulation spectroscopy, in this case measuring the output from the rear facet of the DFB laser in order to distinguish self-mixing interference. KEY; ref: reference signal.

A detector / amplifier (Thorlabs PDA400) was used to detect the forward emission from the laser diode, with a gain of 0dB (15kV/A). A lock-in amplifier (Stanford Research SR850) was used for 2f demodulation; its output voltage sampled using a data acquisition card and transferred to a PC for data processing. In the absence of gas, a reference measurement showed a rising output intensity with current, as expected. In the presence of methane, at the absorption line centre a depression was observed corresponding to the scale of the absorption. The peak absorption was measured by subtracting the received signal from the reference and normalising to the reference intensity. Single mode operation of the laser diodes used was confirmed using a confocal optical spectrum analyser (Toptica FPI100, FSR = 1GHz, Finesse >100).

Test gases were fed to the sphere from two certified cylinders (Scott Specialty Gases), one containing hydrocarbon (HC) free air and the other containing 1010ppm methane. A bank of mass flow controllers (Teledyne Hastings HFC-302 with THPS-400 controller) was used to control flow rates from the two cylinders, with downstream mixing generating a series of mixtures of different concentrations in the range 0-1010ppm.

The DFB laser emitted wavelength was scanned across the gas absorption line centre by applying a current ramp through a driver (ILX Lightwave, ILX LDC-3722B), the current varying between a minimum of 30mA and a maximum of 80mA (corresponding to a frequency range of 33 GHz). A sinusoidal dither was also applied at a frequency of 6 kHz and an amplitude of 24mA (peak to peak); giving a modulation λ_m of 6 GHz. Gross wavelength tuning was achieved by controlling the diode temperature using a Peltier element within the package.

For experiments using the 1686nm VCSEL (Vertilas, VL-1686-1-SP-A5 housed in a TO can with angled and AR coated front window), the ILX laser diode controller was replaced with a high precision current controller (Thorlabs LDC 200 VCSEL) and a temperature controller (Thorlabs TED 200). The modulation of the VCSEL current was achieved by supplying the current controller with a 6 kHz sine waveform from a signal generator (Hewlett Packard HP33120A). A ramp signal (2.5V peak to peak) derived from a second signal generator (Stanford Research DS345) was used to scan the laser DC current from 6mA to 8mA corresponding to a frequency range of approximately 80GHz.

6.2.2 Confirmation of the self mixing behaviour.

Figure 6-4 shows the experimental set up that was used to confirm the behaviour of interference effects due to self mixing.

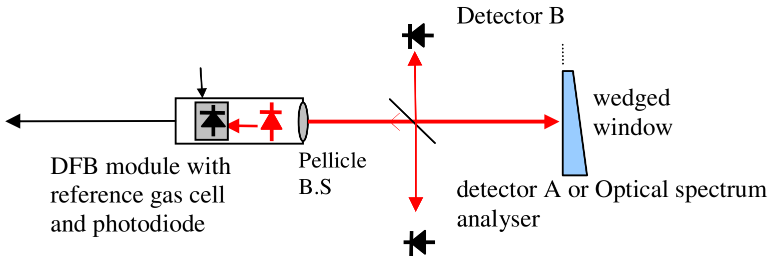

Figure 6-4. Scheme of the experimental set-up used with the DFB laser. Key: B.S; beam splitter

A fraction of the main beam (approximately 1%) was sampled by a beam splitter and directed to a confocal optical spectrum analyser (Toptica FPI100, FSR = 1GHz, Finesse >100) or a detector (detector A, Thorlabs PDA400). The output power of the module was approximately 14mW @ 28.5°C and 65mA. A slight tilt was applied to the spectrum analyser/ detector A to direct the reflected beam away from the DFB laser. A wedged window (10°, deviation angle) was placed in the path of the transmitted beam (128mm from laser, Figure 6-4). A fraction of back reflected light from the wedged window was sampled by the beam splitter and directed to a second detector (detector B, PDA400). After amplification, the signals detected by the reference monitor photodiode, detector A and detector B were then demodulated (2f).

Interference effects due to self mixing signals are carried by the laser emission and are therefore expected to be detected at the reference monitor photodiode as well as at detectors A and B. On the other hand, fringes caused by a classical etalon formed between the wedged window and a second surface in the DFB module would not be detected at the monitor photodiode. The results are plotted in Figure 6-5.

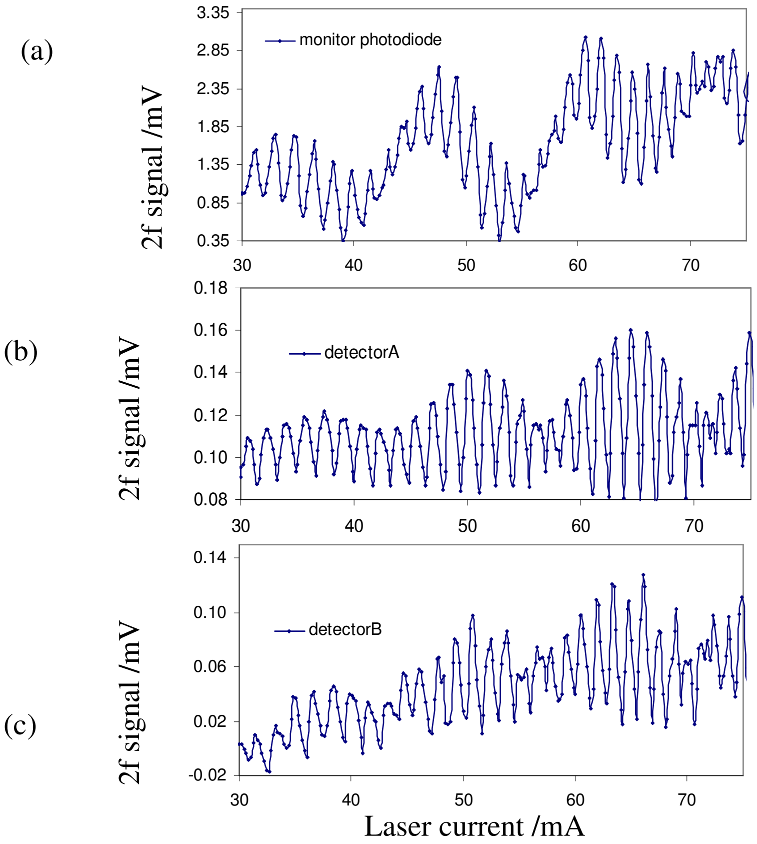

Figure 6-5: Background interferometric signals obtained due to feedback from a wedged window placed 128mm away from laser (a) the reference signal; transimpedance gain = 100kΩ. (b) Detector A signal; gain =0dB. (c) Detector B signal; gain =30dB.The laser temperature was set at 40 degrees (off the gas line). Note different scales.

Interference fringes (high frequency fringes superimposed on an underlying lower frequency period) were observed at all the 3 detector locations. The low frequency fringes are consistent with self mixing effects within the module, previously reported in 5.3.1. The period of the high frequency fringes was used to estimate the “cavity” spacing responsible for their generation (Table 7-2).

Table 6-1: Quantitative analysis of the self mixing interference fringes.

	Monitor photodiode	**Detector A**	**Detector B**
Current range / mA	30-70	30-70	30-70
No of fringes	25±2	25±1	25±1
calculated cavity length d_{calc}	142±11mm	142±6mm	142±6mm
Measured distance between laser and wedged window	128±5mm		

The presence of the high frequency fringes at the 3 detector locations is consistent with the self mixing effect.

6.2.3 Use of the voltage across a DFB laser to detect the self mixing effect

Typically a monitor photodiode enclosed in laser diode packages is used as the sensor for the rear facet emission which is directly proportional to the front facet emission. However, many packages (including VCSELs and DFBs for TDLAS) are supplied without a monitor photodiode. In such a case, it is difficult to distinguish between fringes due to self mixing and a Fabry-Perot etalon. It has been reported in the literature that the self mixing signal can also be detected across the laser diode voltage[3]. This section reports an experiment conducted to detect the self mixing signal utilising the voltage drop across the DFB laser diode.

Using the voltage drop across the laser diode to detect the self mixing effect results in a lower signal to noise ratio compared to using the monitor photodiode. As a result it was found necessary to increase the amount of optical feedback. A retro reflective tape was used in place of the wedged window to give a stronger back reflected intensity.

The voltage measured across the laser diode was fed directly to the lock-in amplifier. The voltage and the rear emission (monitor photodiode signal) were measured during consecutive experiments (it was not practical to measure these parameters simultaneously with the set-up). In both cases, for increased sensitivity the 2f component of the signal was recorded, and the lock-in amplifier phase was set so as to reduce the dc component of the voltage signal. To ensure that the voltage signal was not directly caused by the laser current modulation at f, a control experiment was conducted in the absence of external feedback.

Figure 6-6 shows the correspondence between 2f components of the voltage signal and the signal received by the monitor photodiode.

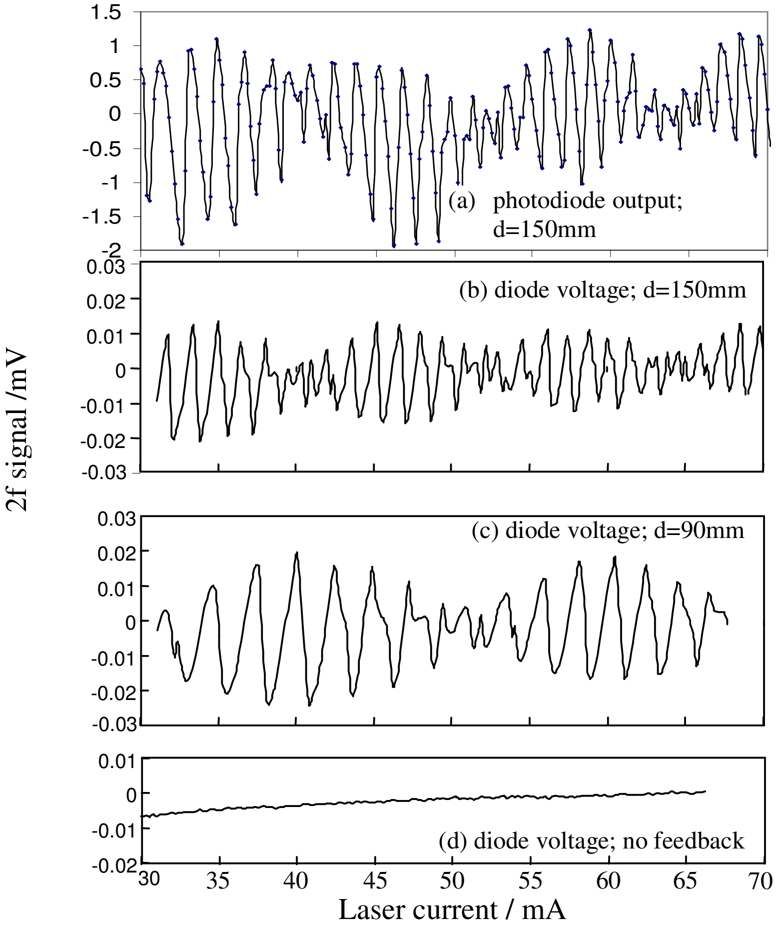

Figure 6-6: Comparison of the magnitudes of 2f signal components for self mixing conditions, (a) in the laser diode output, (b), (c) on the laser diode voltage, and (d) on the laser diode voltage in a control experiment with no external feedback.

This experiment confirms that the self-mixing interference effect can be observed as a small modulation of the laser diode voltage while ramping the drive current. However the detected signal is smaller in magnitude compared to the signal detected at the monitor photodiode. In the experiment the magnitude of the signal detected at the monitor photodiode was approximately 100 times larger than the signal detected on the voltage drop across the laser diode. The voltage modulation showed good correspondence with the modulated output intensity and increased its pitch with decreasing cavity length, as expected.

6.2.4 Self mixing fringes arising from feedback from a wedged, AR coated window

An experiment to confirm that the magnitude of self-mixing interference fringes behave according to equation (6.2) was conducted. A 6° wedged, AR coated window (Thorlabs PS812-C) was used as the external reflector. This type of window is routinely used in gas absorption cells to reduce the intensity of specular reflections that might give rise to etalon effects. Typically, the secondary reflection from the window is aligned away from the optic axis. In this case, a worst case scenario in which the reflection from the front face was directed straight back to the laser diode, was considered. The AR coating had a specified reflectivity of approximately 0.4% at 1650nm. A comparison was made with an uncoated window, whose reflectivity was estimated to be 4% (using a refractive index value of 1.5 at 1650nm for BK7 glass). The 2f component of the signal from the monitor diode was recorded while increasing the laser drive current. To observe weak feedback with a high signal to noise ratio, the forward emission from the laser diode was monitored using a pellicle beam splitter (Thorlabs BP245B3, 45:55) and a high sensitivity detector (Thorlabs PDA400) as shown in Figure 6-7.

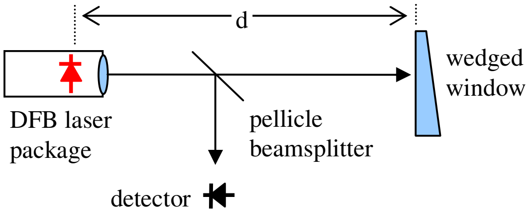

Figure 6-7: Schematic diagram of experiment to measure the effect of feedback from a wedged window. The pellicle beam splitter allowed separation of the forward emission from the window reflection.

A modulation was seen on the forward emission, shown in Figure 6-8. The fact that this modulation was observed on the full diode emission, yet depends on the cavity spacing in the forward path, confirms that we observed self-mixing induced interference rather than etalon – induced interference.

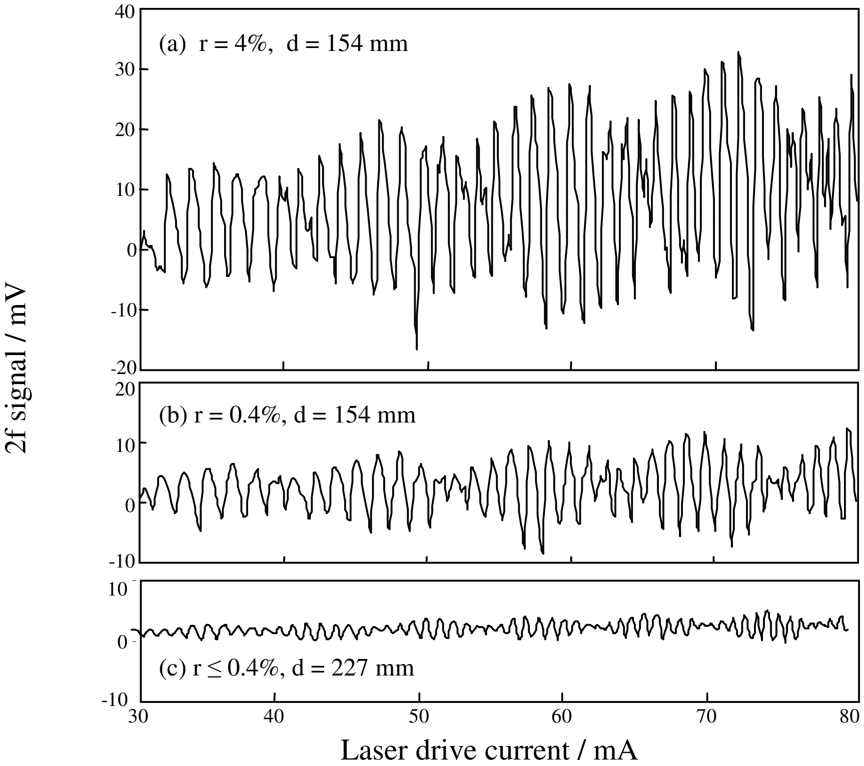

Figure 6-8: Self-mixing induced interference fringes observed in the laser diode forward emission for feedback from (a) an uncoated 6° wedged window at a distance of 154mm, (b) an AR coated 6° wedged window at a distance of 154mm, and (c) the latter at a distance of 227mm.

For self mixing interference, the magnitude of the modulation is expected to vary with $\sqrt{r}$, as shown here. At a distance of 154mm, reducing the surface reflectivity by a factor of approximately 10 has reduced the fringe amplitude by a factor of 2.5, in line with the expectation of a factor of 3.3. Increasing the distance to 227mm reduced the amplitude by a further factor of approximately 3, which may be a combination of two effects; (i) additional divergence of the laser beam, which at this distance had a diameter of approximately 6±2mm, and (ii) the additional effect of wavelength modulation averaging out narrower fringes from the larger cavity.

At a distance of 154mm, the fringe amplitude corresponded to a gas concentration of ±900ppm in a 100mm path length. Assuming equation (6.2) holds, to detect methane at the level of 1ppm would require reducing the level of feedback to below 1 part in 10^8.

6.2.5 Self mixing effects cause by diffuse reflections

In recent years, there has been increased interest in using diffusely scattering surfaces in TDLS[4]; for example in laser pointer style gas sensors where the light is backscattered from the surface topography[5-7] and the use of integrating spheres[8,9] where the source can be directly mounted onto the sphere and therefore get exposed to weak optical feedback. Therefore self mixing from diffuse reflections may have an impact on the design of such instrument.

Self mixing interference signals were recorded using the DFB monitor photodiode, for the case of feedback from a diffuse reflector (Spectralon^{TM}) placed in the path of the output beam at a range of distances from the laser diode. A sample of the results is shown in Figure 6-9. The modulation observed in the absence of external feedback is consistent with the findings of section 5.3.1 (fringes corresponding to a "cavity" of approximately12mm in the DFB module were reported).

Further experiments were conducted for d values covering the range 38mm – 268mm (see Table 6-2). For each recorded spectrum, the output was normalised. The fringe spacing was determined by counting fringes over a defined spectral region. The results are shown in Figure 6-10 and compared to the predictions of equation (6.2).

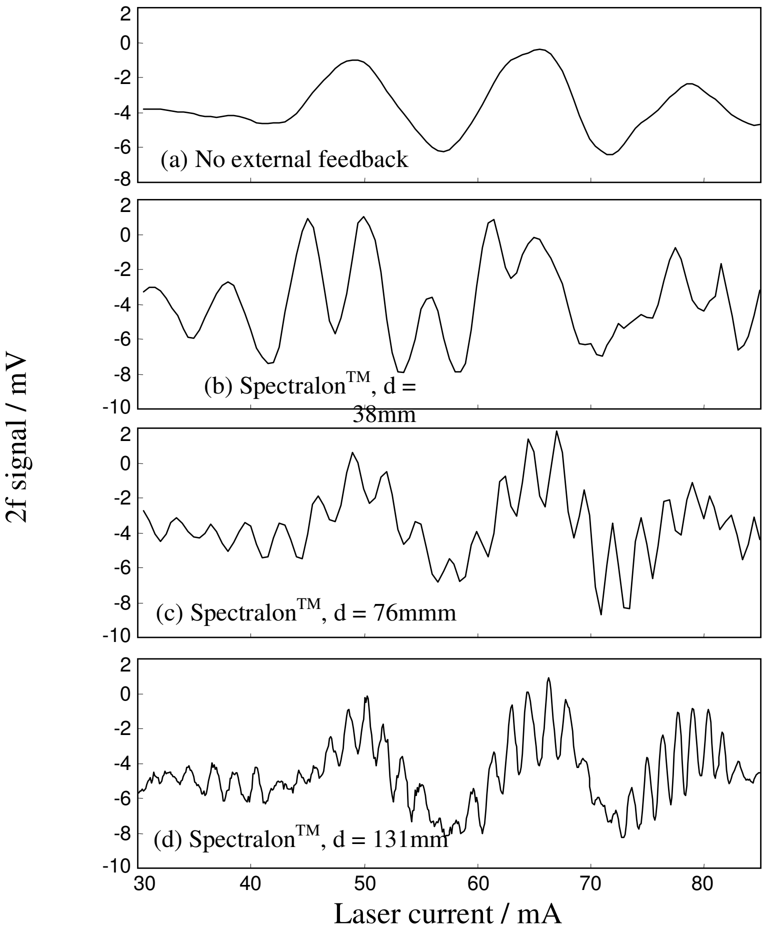

5

Figure 6-9: Self mixing modulation of the output from the DFB monitor photodiode by feedback from Spectralon^{TM}. (a) No external feedback, (b) d = 38mm, (c) d = 76mm, (d) d = 131mm.

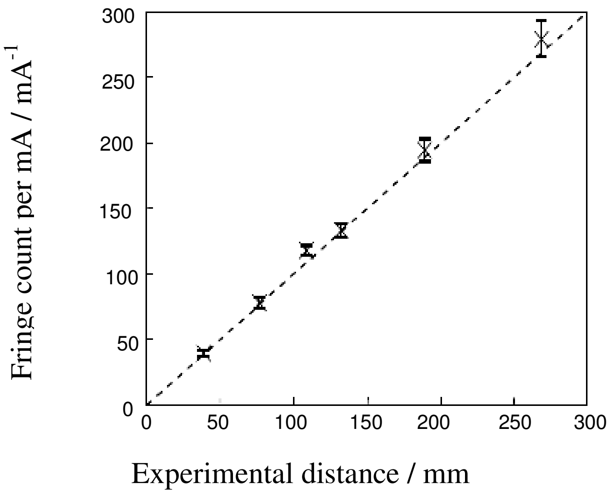

Figure 6-10: Results of self-mixing feedback from a diffuse reflector: distance estimated from fringe count versus measured experimental distance from reflector to laser diode.

Table 6-2: Quantitative analysis of the self mixing interference fringes.

Distance d_{exp} from diffuser to laser /mm	**38 + 3.5**	**76 + 3.5**	**108 + 3.5**	**131 + 3.5**	**188 + 3.5**	**268 + 3.5**
calculated cavity length d_{calc} / mm	44±4	91±4	141±8	150±8	230±11	341±15

These results show that the fringe amplitude decreases as the level of backscattered light decreases, in line with the prediction of section 6.1.2.

6.2.6 Observations of the self mixing effect in a VCSEL

In recent years, there has been increased interest in using VCSELs in TDLAS, primarily due to their lower cost, low power consumption and a wide mode hope free tuning range compared to DFB lasers (see Table 6-3, figures valid for lasers used in this project only).

Table 6-3: Comparison of DFB and VCSEL that were used in this project.

	COST £ (for small volume)	**POWER CONSUMPTION**	**TUNING COEFFICIENT**
DFB (NEL NLK1U5C1CA-TS)	£2000	0-150mA 10mW@60mA	1GHz/mA
VCSEL (Vertilas, VL-1686-1-SP-A5)	£700	0-10mA 3mW@5mA	40GHz/mA

An experiment was conducted to establish if VCSEL also suffer from interference effects. Confirmation of self-mixing modulation of the output from a VCSEL was hampered by the lack of a rear facet for this laser design. The voltage drop across the diode was used as described in 6.2.3, again using the retro reflective tape to increase the signal level. Figure 6-11 shows the results.

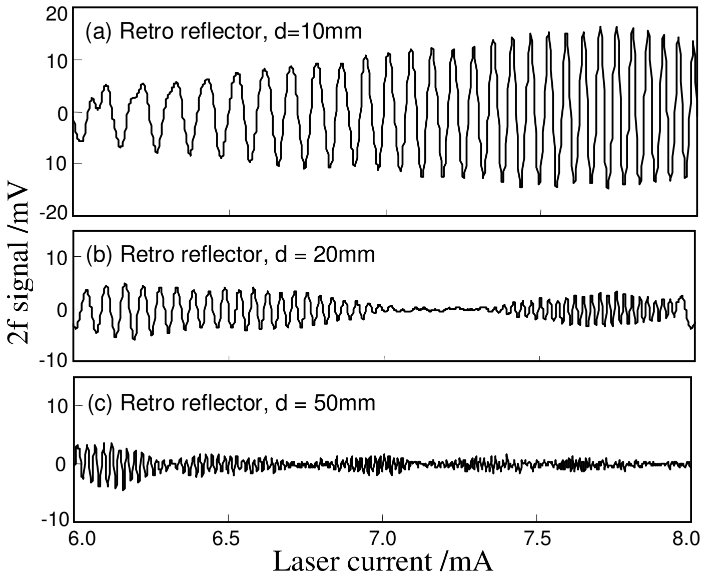

Figure 6-11: Self mixing interference observed as a modulation of the voltage across a VCSEL. Second harmonic signals obtained with retro reflective tape placed at distance d of (a) 10mm, (b) 20mm and (c) 50mm.

These results confirm self-mixing interference behaviour in our VCSEL. The change in fringe spacing with cavity length is again consistent with equation 6.2.

6.2.7 Effects of the self mixing interference fringes on the sensitivity of gas absorption measurements

A series of gas absorption measurements was made with relatively high levels of optical feedback. In order to separate the effects of feedback from possible etalon effects within the gas cell, the configuration in Figure 6-12 was used. A pellicle beam splitter (Thorlabs BP245B3, 45:55) was used to pass a proportion of the main beam emitted by the DFB laser diode towards a reference detector (D1). The main beam was then directed towards a wedged window, whose front surface was aligned to direct the reflected beam back towards the laser with a reflectivity of approximately 0.4%, the feedback being reduced to 0.1% of the initial intensity after traversing the beam splitter twice. A conventional gas cell was used with a 10cm path length and wedged AR coated windows to reduce etalon effects to an insignificant level compared with self-mixing feedback. Transmission though the cell was monitored with a second detector (D2). Signals from both detectors (Thorlabs PDA400) were demodulated at 2f using lock-in amplifiers as previously described. With hydrocarbon free air in the gas cell, the 2f output from each detector / lock-in amplifier combination was normalised so as to balance the two readings.

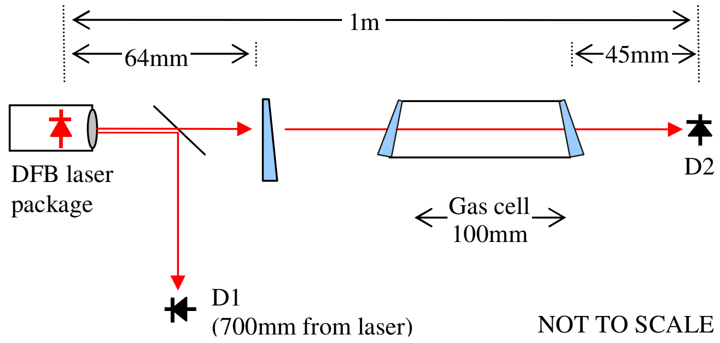

Figure 6-12: Configuration of experiments to investigate self-mixing feedback in gas absorption measurements.

In a first experiment, the laser drive current was ramped over the range 30-80mA in steps of 0.2mA, while 2f-demodulated outputs were recorded simultaneously for channels D1 and D2. Scans were taken with different concentrations of methane in air within the gas cell (all at atmospheric pressure). The results are shown in Figure 6-13 (a) and show self-mixing feedback on both detectors D1 and D2, with a fringe spacing dictated by the distance from the wedged window to the laser diode (64mm).

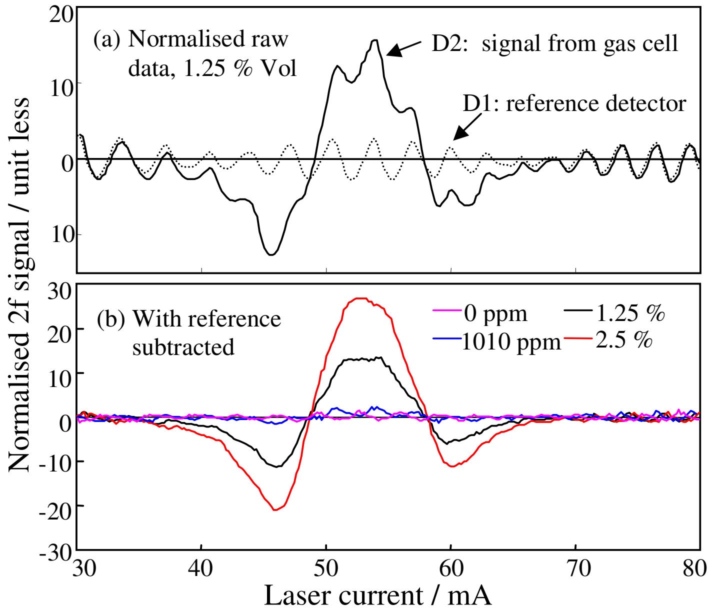

Figure 6-13: Results of wavelength scans through a methane line at different concentrations, while high levels of feedback were deliberately applied to the laser diode. (a) Normalised 2f signal components, (b) signals from D2 corrected by subtraction of the reference signal from D1. (Lock-in τ 100ms).

The fact that self-mixing feedback induces a modulation on the entire laser diode output allows for a straightforward reduction scheme. In this case, the normalised output from the reference channel D1 (after lock-in demodulation) was subtracted from that of the main signal channel D2. Figure 6-13 (b) shows that this removed the modulation to first order. A small residual modulation remains, caused by a slight phase change in δ observed between the two sets of fringes, the precise cause of which is uncertain. At 1010ppm, the methane line is just discernible.

In a second experiment, the laser diode output was locked to the methane line and 2f-demodulated outputs from both detectors were recorded simultaneously. Different methane concentrations were delivered to the cell; first hydrocarbon free air, then 1010ppm methane in air. The results are shown in Figure 6-14. Subtraction of the demodulated reference signal improved the signal to noise ratio by over a factor of 10, giving an estimated limit of detection of approximately 100ppm. Residual noise and drift in the corrected signal is attributed to imbalances between the two light paths leading to D1 and D2, possibly caused by etalon effects in the gas cell (previously reported in 5.4). A control experiment was conducted in the absence of self mixing (Figure 6-14(c)).

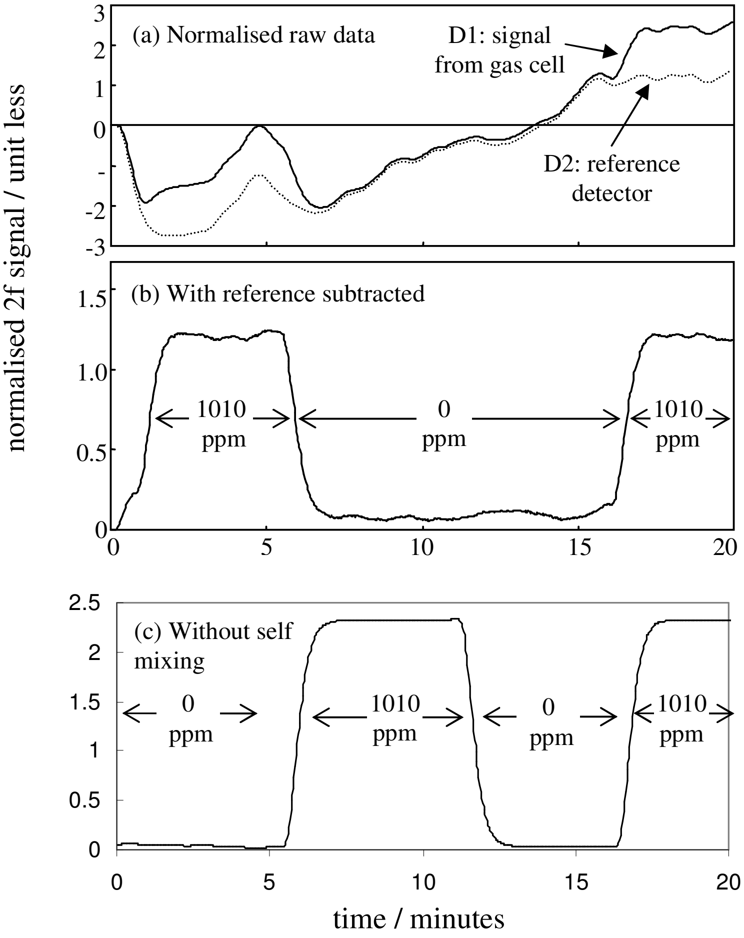

Figure 6-14: Normalised 2f-demodulated output from detectors D1 and D2 plotted as a time series while different methane concentrations (in air) were delivered to the gas cell. (a) Normalised raw data, (b) data corrected by subtraction of the reference, and (c) Raw data (no background subtraction) obtained in the absence of self mixing (Lock-in τ 10s.)

6.3 Results for a commercial VCSEL based instrument

This section reports observations of interference effects in a commercial prototype instrument (IR Microsystems microLGD^{TM}) made in collaboration with IR Microsystems (IRM).

The instrument employs a 1651 nm VCSEL (Vertilas VL-1651-1-SP-T5), mounted in a cell of 80mm physical length with a reflective geometry and a total path length of 160mm. The cell has been carefully designed so as to minimise the opportunity for etalons to arise in the optical path by tilting the photodiode to prevent direct specular reflection from the detector or its package to be redirected towards the laser.

A custom electronics board performed laser current and temperature control as well as second harmonic demodulation for WMS. Signals were transferred to a computer running Labview^{TM} software via a RS232 port. The VCSEL was modulated at a frequency f ≈ 20kHz to generate a WMS gas detection signal.

Because the instrument configuration was fixed, it was not possible to confirm self-mixing interference behaviour directly by any of the techniques used in the laboratory experiments. Instead 2f signals from the photodiode were recorded.

Figure 6-15 shows the results of a wavelength scan for a methane concentration of 100ppm within the cell. For straightforward WMS, a large fringe-like modulation can be observed superimposed on the gas line (Figure 6-15 (a)). The fringes could be efficiently reduced by applying a deliberate low amplitude modulation to the laser. In this case, suppression of a factor of 10 was achieved by applying a 6kHz low amplitude modulation (Figure 6-15 (b)).

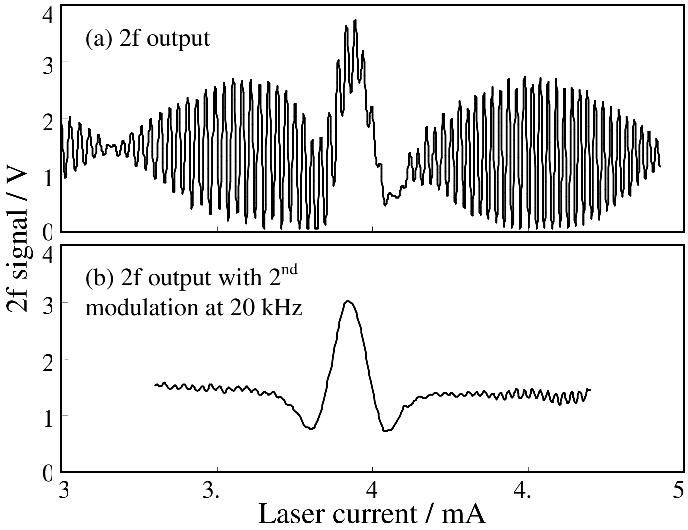

Figure 6-15: 2f WMS signals acquired by the microLGD^{TM} for a methane concentration of 100ppm. (a) Interference fringes superimposed on the absorption line for straightforward WMS at f=20kHz. (b) Suppression of fringes using a second modulation at 1.6 kHz.

The fringe spacing was found to correspond to a 16cm cavity, twice the physical length of the gas cell. Angling or misaligning either the laser or the photodiode did not significantly reduce the fringe visibility. This is consistent with two possible causes, (i) self mixing interference, possibly caused by a small fraction of the light reflected by the mirror falling directly onto the laser diode, (ii) a weak etalon in the optical path, formed between the photodiode and mirror or the laser diode and mirror. It was not possible to confirm unambiguously which of these causes was possible.

Following suppression of the fringes, the short-term rms noise was established to be approximately 1.8ppm over a period of 3 minutes, with a longer term zero drift of approximately 10ppm.

6.4 Summary

Both self mixing and Fabry-Perot etalon interference effects can create a modulation of the light intensity measured at a detector. For low levels of returned light and a given cavity length d, the resulting fringes take the same sinusoidal form. The effects of interference from low reflectivity etalons and from diffuse reflections are equivalent. Self-mixing interference can be caused by both specular and diffuse reflections with equivalent effects for the same levels of returned light and cavity length.

Interference caused by self-mixing in the laser diode cavity can be distinguished from classical etalon effects in two ways:

(i) Measuring a modulation of the output from the laser diode itself, which may conveniently be achieved at the rear facet by using a monitor diode.

(ii) Measuring a modulation of the voltage across the diode. This has a worse signal to noise ratio, but is more convenient for laser diodes with no rear emission, such as VCSELs.

The effects on WMS of interference fringes caused by etalons in the optical path of gas cells are well-known, but to the author's knowledge the effects of self-mixing interference have not been previously reported. With the DFB laser diode used in these experiments, feedback would have to be reduced to below the 1 in 10^8 level to permit detection of methane at 1ppm within a 200mm (double pass) gas cell.

In the experiments exaggerated levels of optical feedback were used in order to investigate the effect; in practice a good optical design would reduce this to give decreased modulation amplitudes. A good quality (60dB) optical isolator would circumvent the problem by reducing feedback, but for reasons of cost and simplicity, many workers prefer to avoid them, especially for industrial systems. It has indeed been experienced that in small quantities, isolators designed for use at non-standard wavelengths can cost more than the laser diodes themselves. Furthermore, the problem remains of feedback arising from reflections from the front face of the isolator. However, simple intensity referencing can remove the effects of the modulation to first order, which in these experiments improved the signal : noise ratio by over a factor of 10.

It has been shown that self mixing interference can arise from specular reflections, but perhaps more importantly from diffuse reflections (in our case, from Spectralon^{TM} and a retro reflective tape). This results means that the presence of dust or dirt within the optical path will also present a problem, and could be an issue for gas detectors designed for use in industrial environments. Air filters can be used to protect the optics, but these compromise response times and can themselves become blocked by dirt.

Thus, self-mixing interference fringes can arise in a greater range of circumstances than etalon-induced fringes. Furthermore, if etalons are created by gas cell windows, as is often the case, the two surfaces comprising the etalon have similar, low reflectivities and the resulting fringes have a modulation depth proportional to r. However, for self-mixing interference the modulation depth is proportional to $\sqrt{r}$. Therefore, as the value of r reduces, limited in practice by the quality of AR coatings, self-mixing interference is increasingly dominant.

6.5 Conclusion

To conclude, it has been shown that self mixing interference can cause spurious signals to arise in gas detectors based on wavelength modulation spectroscopy. As with etalon-induced fringes, the problem is particularly severe for this form of gas detection, which is highly sensitive to curved or periodic spectral features with a free spectral range of the order of the gas absorption linewidth. For methane this corresponds to an optical path difference of approximately 30 mm. In the very weak feedback regime, the effect is a cosine modulation of the laser diode output, whose amplitude is proportional to the square root of the level of reflected or backscattered light reaching the laser diode. The modulation can be observed on the forward and rear diode emission (for lasers with a rear facet) as well as, for strong signals, on the voltage across the diode.

6.6 References

[1] Santos, J. L., Leite, A. P., and Jackson, D. A. (1992), 'Optical fiber sensing with a low-finesse Fabry-Perot cavity', *Applied Optics*, V31, N34, pp. 7361-7366.

[2] Giuliani, Guido and others (2002), 'Laser diode self-mixing technique for sensing applications', *Journal of Optics A: Pure and Applied Optics*, V4, N6, pp. 283-294.

[3] 1995 *Frequency Stabilisation of Laser Diodes* Ikegami T, Sudo S and Sakai Y (Norwood, USA: Artech House, INC).

[4] Masiyano, D., Hodgkinson, J., and Tatam, R. P. (2008), 'Use of diffuse reflections in tunable diode laser absorption spectroscopy: Implications of laser speckle for gas absorption measurements', *Applied Physics B: Lasers and Optics*, V90, N2, pp. 279-288.

[5] van Well, B. and others (2005), 'An open-path, hand-held laser system for the detection of methane gas', *Journal of Optics A: Pure and Applied Optics*, V7, N6, pp. 420-424.

[6] Frish M B, Wainner R T, Green B D, Laderer M C and Allen M G 2005 *Infrared to Terahertz Technologies for Health and the Environment, Oct 24-25 2005* 6010 *Proceedings of SPIE - The International Society for Optical Engineering* (Boston, MA, United States: International Society for Optical Engineering, Bellingham WA, WA 98227-0010, United States) p 60100.

[7] Iseki, T., Tai, H., and Kimura, K. (2000), 'Portable remote methane sensor using a tunable diode laser', *Measurement Science and Technology*, V11, N6, pp. 594-602.

[8] Tranchart, S, Bachir, I. H., and Destombes, J-L. (1996), 'Sensitive trace gas detection with near-infrared laser diodes and an integrating sphere', *Applied Optics*, V35, N36, pp. 7070-7074.

[9] Hawe, E. and others (2007), 'An investigation into the use of an integrating sphere as a gas absorption cell', *Journal of Applied Optics A: Pure and Applied Optics*, V9, N6, pp. S12-S18.

Chapter 7 Gas cell design

As previously described in section 2.7.1, the sensitivity of many practical TDLAS systems is limited by the formation of unintentional Fabry-Perot interference fringes in the optical path between the source and detector[1]. The spacing between the maxima of these fringes can be in the same wavelength range as Doppler and pressure-broadened molecular line widths (10^{-3}-10^{-2}cm^{-1})[2]; this can lead to distortion or complete obscuring of the shape and strength of the absorption line[3]. Gas cell windows are often the worst culprits[4].

A detailed review of techniques employed to prevent/reduce interference effects due to Fabry-Perot etalons was presented in section 2.7.1. For convenience, a summary is presented here. Design techniques to reduce etalon formation include; the use of optical isolators, use of reflective rather than refractive optics, angling and antireflection coating of reflective surfaces[5]. Techniques for eliminating or reducing the amplitude of the fringe signal include: (a) mechanically oscillating the path length with external devices[1,6,7], (b) introduction of an asynchronous current in addition to the usual modulation current through the laser diode[8], (c) use of alternative waveforms[9,10] and (d) postdetection filtering[11]. The disadvantage of method (a) is that the detection bandwidth is limited by the mechanical motion and signal integration that is required[12]. Methods (b) and (c) are less effective and tend to wash out the gas absorption signal when the free spectral range (FSR) is comparable to the gas absorption linewidth[2]. Post detection filtering can only be applied where the signal and the interference spectra are distinguishable in the frequency domain[2].

In general, the alignment of the optical components is critical. This often leads to complex designs with tight tolerances on optical component alignment, and can therefore be difficult and expensive to maintain in field instruments.

As previously stated in the introduction, the main aim of this thesis is to investigate an alternative approach to gas cell design based on the use of diffuse reflections, known in some circumstances to reduce interference fringes[13]. However, their use introduces laser speckle that can contribute an intensity uncertainty to gas detection measurements. A systematic theoretical and experimental study of speckle effects and the associated intensity uncertainty have been reported in chapter 3 and 4.

The focus of this chapter is to apply the knowledge of speckle acquired in the aforementioned chapters to the design of gas cells utilising diffusive surfaces. The aims of the gas cell design exercise included;

1. Minimising Fabry-Perot interference effects associated with standard gas cell windows.

2. Designing gas cell configuration that are simple, easy to align and robust; in standard gas cells, design efforts to prevent formations of etalons often lead to complex designs that are sensitive to alignment.

This chapter has been structured as follows

I. Section 7.1 presents experiments; (a) demonstrating the detrimental effects of interference fringes due to Fabry-Perot etalons on the performance of a WMS instrument, (b) evaluating the effectiveness of common design efforts to prevent the occurrence of the etalons.
II. Section 7.2 presents a theoretical analysis and a discussion of several gas cell designs employing a diffusely scattering element. The performance of one such cell was also evaluated by conducting gas absorption experiments.
III. Section 7.3 reports experiments conducted to investigate techniques for reducing speckle related uncertainty by use of a moving diffuser.

7.1 Fabry-Perot etalon effects in standard gas cell designs

Optical windows used in gas cells can act as low finesse Fabry-Perot etalons. The transmission of a Fabry-Perot etalon is given by

$$\frac{I}{I_0} = \frac{1}{1 + F_{FP}\sin^2(\delta/2)} \qquad \textbf{(7-1)}$$

where F_{FP} is equal to $4R/(1-R)^2$, R is the reflectivity of the cavity, and δ is the optical phase of the cavity

$$\delta = \frac{4\pi}{\lambda_0} nl\cos\theta \qquad \textbf{(7-2)}$$

where n is the refractive index, l is the window thickness, λ_0 is wavelength and θ is the angle of incidence at the second surface, with $\cos\theta$ being equal to unity at normal incidence[5]. The cavity creates periodic fringes with an amplitude (peak-to-peak) of $4R$. The amplitude of the fringes scales linearly with the residual reflectivity, so that two surfaces with a residual reflectivity of 3.3% (Fresnel reflectivity of silica using n = 1.443 at 1650nm) induce fringes with an amplitude equivalent to an absorption of 13.2% volume in the direct transmission signal (Figure 7-1). When considering WMS with $2f$ demodulation, the amplitude of the $2f$ fringes signal depends on the modulation index m and FSR of the cavity[10].

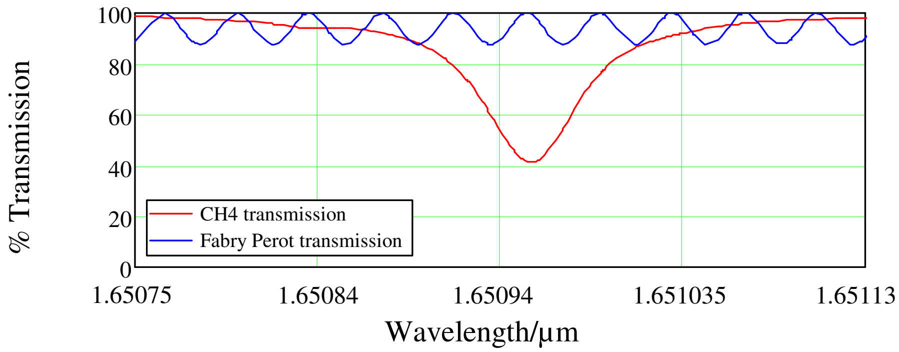

Figure 7-1: Theoretical plots of the 1651nm (Hitran data base; Rothman *et al,* L. S. (1992),see ref 10 in chapter 2), 100% concentration methane and 1cm path length) and Fabry-Perot transmission using equation 7-1 with l = 25.0 mm, n = 1.443, R= 3.3%. Key: CH_4; methane.

As previously discussed in section 2.7.1, the fringes can not be removed by background subtraction because optical depth (product of window thickness and refractive index, *nl* in equation 7-2) is a function of temperature[5].

$$\frac{dnl}{dT} = \frac{dn}{dT} + \frac{dl}{dT} \qquad \textbf{(7-3)}$$

Additionally, filtering techniques can not be applied when the FSR (ν = c/2nl) is close to the gas linewidth. For methane at room temperature the worst etalon spacing is 25mm as the corresponding FSR of 4.2GHz, which approximately equals the full-width-half-maximum of the gas 1651nm absorption line, Figure 7-1.

According to equation 7-2, the maximum fringe amplitude can only arise in the case of plane parallel windows. Therefore the use of wedged windows can reduce etalon effects. Figure 7-2 shows two 10cm cells used in this study, one employing plane parallel windows and the other employing wedged and AR coated windows.

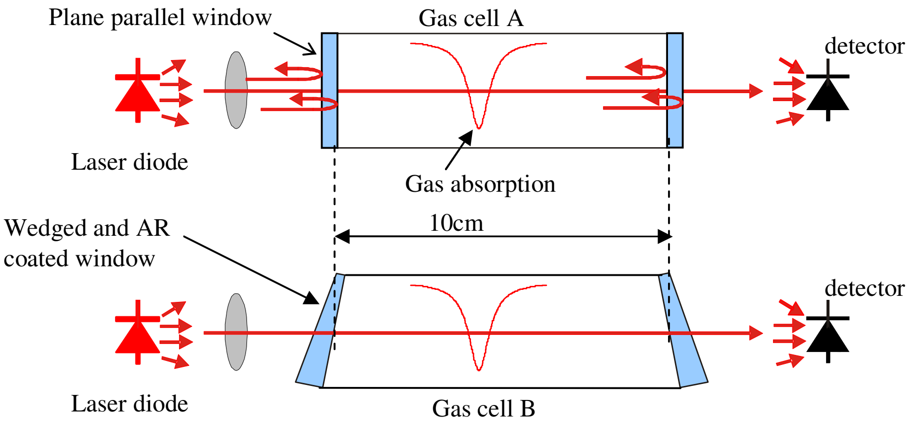

Figure 7-2: Gas cells implemented using: (a) Plane parallel windows (UV silica) with a refractive index of 1.443. (b) Wedged windows with a wedge angle of 3° 53' or 0.068radians that resulted in an angular beam deviation of 2° and were made of BK7 (n=1.5 at 1650nm), thin edge of wedge was 3mm; the thick edge was 4.7mm.

Gas cell A represents the worst case scenario (i.e. no design efforts made to reduce or prevent the occurrence of Fabry-Perot etalons). Etalons can be formed between any of the four surfaces of the gas cell windows giving rise to lower frequency fringes with an FSR of 16GHz (corresponding to window thickness l = 6.5mm and n= 1.443) and higher frequency fringes with an FSR of approximately 1.5GHz (corresponding to air spaced etalon formed between the two cell windows and n = 1,). This cell was used to illustrate the effects of Fabry-Perot Etalons on the performance of TDLAS based gas instrument.

In gas cell type B formation of fringes due to Fabry-Perot etalons was minimised by use of wedged and AR coated windows. The two windows were also tilted relative to each other such that the beam deviation through the cell was minimal and to avoid further tilted etalon. The AR coating reduced the reflectivity from 4% using a refractive index of 1.5 for BK7 at 1650nm to 0.4% (Thorlabs's C-coating). This cell was used to evaluate the effectiveness of common design efforts (AR coated and wedged /tilted windows) in reducing Fabry-Perot etalon formation.

The experimental setup was configured such that the measurements could be obtained simultaneously from the two cells (Figure 7-3).

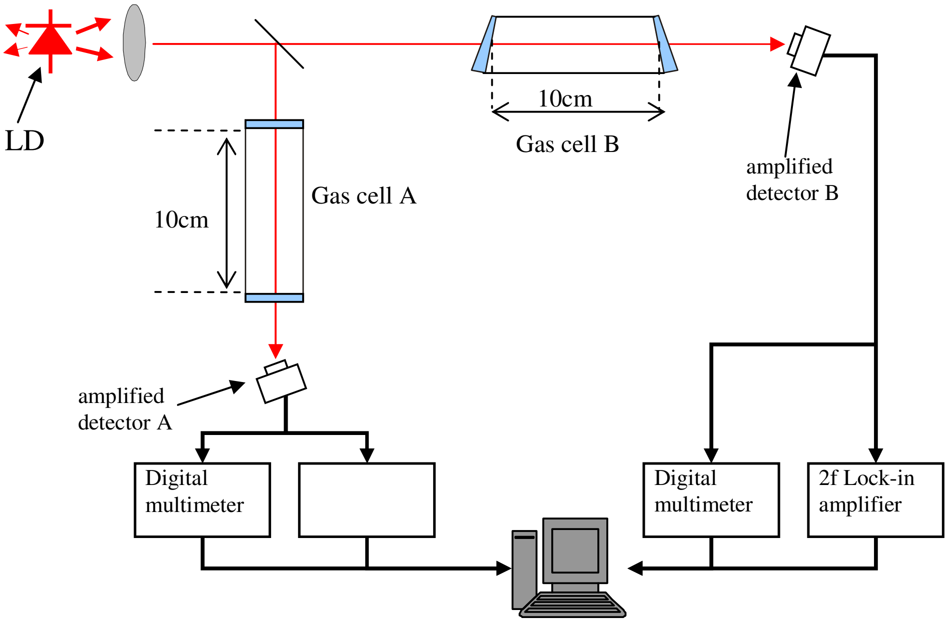

Figure 7-3: Schematic diagram of the experimental setup for investigating Fabry-Perot etalon effects in WMS.

In a first experiment, the cells were filled with 1010ppm methane. The 2f-demodulated outputs were recorded simultaneously for channels detector A and detector B (see annotation in Figure 7-3) while the laser drive current was ramped over the range 40-80mA in steps of 0.2mA. Two background signals were also recorded for each detector channel (1) background with the cells removed and (2) background with the cells filled with hydrocarbon free air. This was used to confirm that the observed fringes were associated with the gas cell.

The plots of the 2f signal corresponding to 1010ppm methane and background signals from the two gas cells are shown in Figure 7-4. Each channel was normalised by the DC signal to remove the dependence on the amount of light arriving at the detector. A quantitative analysis of the plots is presented in Table 7-2 and Table 7-2.

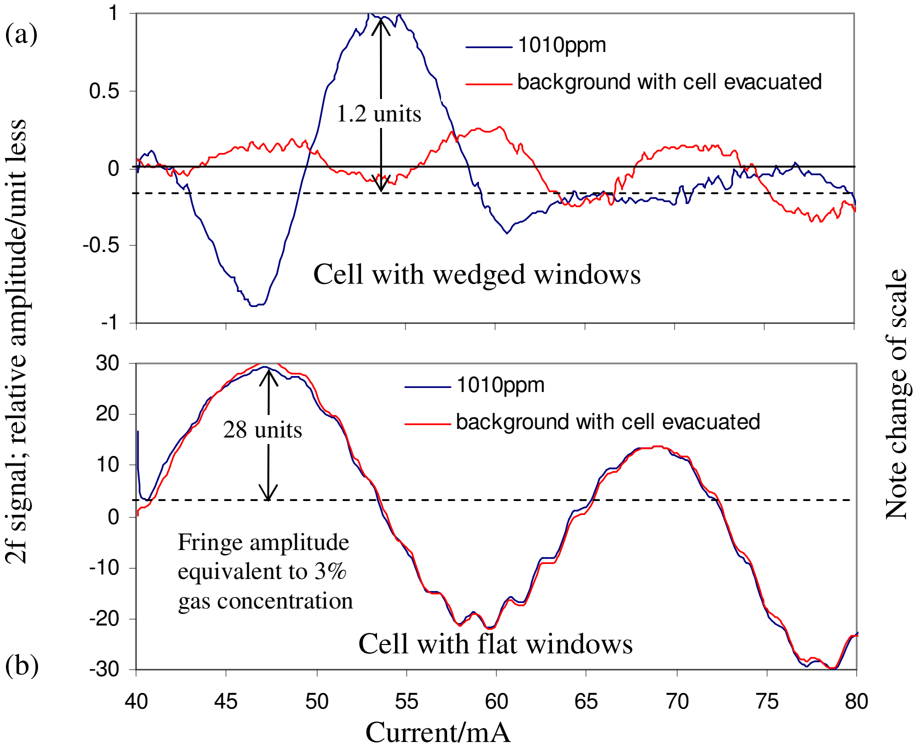

Figure 7-4: Comparison of the magnitudes of gas absorption and back ground signals (normalised) obtained from a gas cell with (a) a cell with wedged, AR coated and angled windows and (b) plane parallel windows. Note change of scale.

Table 7-1: Quantitative analysis of the observed fringes plotted in Figure 7-4.

	no cell	**cell with plane parallel windows**	**cell with wedged AR coated window**
uncertainty	170ppm	2.4% Vol	equal to or less than 170ppm

For both detectors, the background recorded with the cells removed (Figure 7-4(a)) is consistent with fringes due to self mixing in the DFB module (reported in detail in section 5.3).

In the case of the cell with wedged windows, the magnitude of the background signal recorded at the detector with the cell removed was comparable to background signal recorded with the gas cell in place. This is consistent with the level of fringes generated in the cell with wedged windows being lower than the fringes generated elsewhere in the system. The signal corresponding to 1010pm gas is readily distinguishable from the background signal (Figure 7-4(a)).

In the case of the gas cell with plane parallel uncoated windows, the signal corresponding to1010pm gas can not be distinguishable from the background signal (Figure 7-4(b)). The background obtained with the cell evacuated is much larger (2 orders of magnitude) than the signal recorded with the cell removed. Fringes of two different periods were superimposed on to the background signal (Figure 7-4(b)). The higher frequency fringes are consistent with an etalon formed between a surface from one window and a second surface from the opposite window (column 2 of Table 7-2). The lower frequency fringes are consistent with an etalon created between two opposing surfaces of one window (column 3 of Table 7-2).

Table 7-2: Quantitative analysis of the observed fringes plotted in Figure 7-4.

	High frequency fringes Figure 7-4(b)	**Low frequency fringes** Figure 7-4(b)	**Background with cells removed**
Calculated cavity length d_{calc}	128±33mm	7.4±4mm	19.4±6mm
Possible etalon causing fringes	100mm (reflections between the two windows)	6.5mm (Reflections within one window)	Consistent with findings of section 5.3 (self mixing in DFB module)

The unexpected large difference in amplitude between the lower and the higher frequency fringes could be due to imperfect alignment of the two windows relative to each other (etalon transmission depends on angle of incidence at second surface, equation 7.2).

In a second experiment, the laser diode output was locked to the methane line and 2f-demodulated outputs from both detectors were recorded simultaneously while different concentrations of 1010ppm methane in hydrocarbon free air were delivered to the cell. The results are shown in Figure 7-5.

The signal from the cell with plane parallel windows shows a large DC offset and background drift with time (Table 7-3). The output of the cell with the wedged window showed a much reduced offset and drift with time. In the case of the cell with plane parallel windows the output signal corresponding to concentrations below 100ppm could not be distinguished from the underlying the background signal. A detection limit of less than 10ppm was achieved using the AR coated wedged window cell in an earlier experiment (5.4.2).

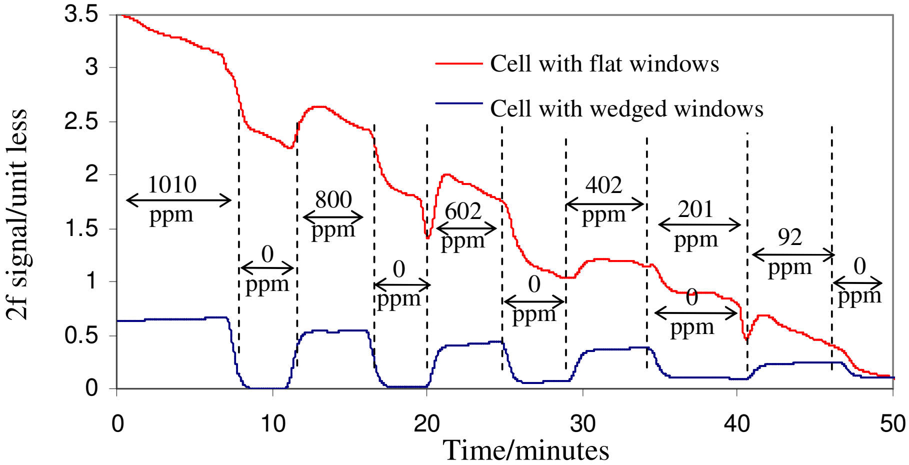

Figure 7-5: Normalised 2f-demodulated output from detector plotted as a time series while different methane concentrations (in air) were delivered to the gas cells. Simultaneous measurements from a cell with plane parallel windows and a cell with wedged and AR coated windows (Lock-in τ 10s).

Table 7-3: Analysis of short term and long term drift of the output from the cell with plane parallel windows and the cell with wedged window

	PERIOD	WEDGED WINDOW CELL		PLANE PARALLEL WINDOW CELL	
Calibration factor		1554ppm/unit		1554ppm/unit	
		Unit less	ppm	Unit less	ppm
Short term drift	5 minutes	0.022	34	0.3	466
Long term drift	50 minutes	0.109	169	3.4	5284

In summary, it has been shown that etalon effects in standard cells can limit the detection sensitivity of a TDLAS instrument. The use of AR coating and wedged windows can significantly reduce the magnitude of these features. However, several disadvantages still remain;

1. The requirement for custom optics/ AR coatings if working outside the telecom wavelengths. This is often expensive if bought in low volumes.
2. Alignment is critical; careful alignment of optical components was required to obtain the results for the wedged window cell reported in this chapter and in section 5.4.2. Whilst the four surfaces of the wedged windows of a standard cell can be misaligned with relative ease (with respect to each other) when the cell is considered in isolation, it becomes more challenging when other components (e.g. detector windows, laser windows, and lens) in the system have to be considered as well.
3. Glass surfaces have to be kept clean to avoid scattering that can lead to self mixing. This limits the environments where such a cell can be placed.

The following sections discuss gas cell designs employing a diffusive element with the aim of avoiding the problems discussed above.

7.2 Gas cells employing diffusive elements

Gas cells employing diffusive elements have the potential to overcome some of the disadvantages of standard cells discussed in the previous section. However as reported in section 4.3, the use of diffuse reflections can lead to speckle related intensity uncertainty and interference effects due to interferometric speckle. It was also shown in section 6.2.5 that diffuse reflections can also lead to interferometric noise caused by the so called self mixing effect.

The following sections report theoretical and experimental evaluation of a number of gas cell configurations employing diffusive elements. For all the designs presented the following noise sources were considered where relevant;

1. Subjective and objective speckle related intensity uncertainty of a single static speckle field.
2. Interference effects
    a. Interferometric speckle uncertainty.
    b. Low finesse Fabry-Perot etalons.
    c. Self mixing effects.

A number of gas cell designs that were considered are discussed in section 7.2.1. Section 7.2.4 reports an evaluation of one of the cells conducted by making gas absorption measurements.

7.2.1 Reflective type gas cell designs

A first gas cell geometry is shown in Figure 7-6, comprising of a reflective diffusely scattering surface in combination with one of a number of different types of window (a wedged window is illustrated).

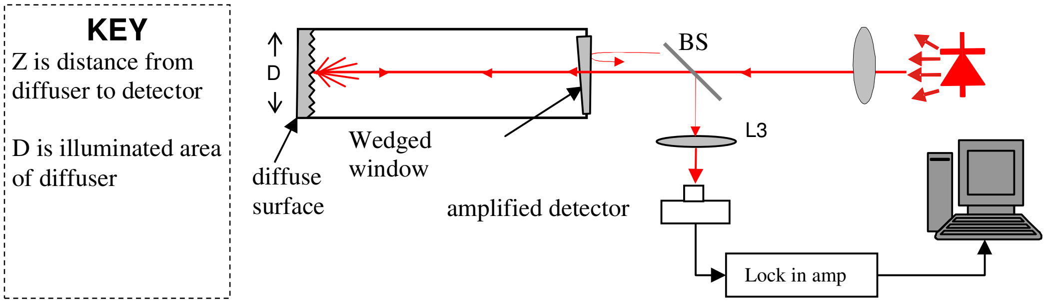

Figure 7-6: Experimental setup for investigating the use of diffuse reflections in WMS. Key, L1, L2, L3; lens, APC; angle polished connector, BS; beam splitter.

The speckle related intensity uncertainty for a single static speckle field arriving at the photo-detector with an area d is given by

$$\frac{\Delta I}{I} = \frac{1.22\lambda Z / D}{\mathrm{d}} \qquad \textbf{(7-4)}$$

for objective speckle (i.e. lens L3 removed from Figure 7-6) and

$$\frac{\Delta I}{I} = \frac{1.22\lambda\ (1+\Pi)\, F\#}{\mathrm{d}} \tag{7-5}$$

for subjective speckle (i.e. lens L3 used to gather light), where F# is the ratio of the focal length to aperture and Π the magnification at which the lens is operating. For a fixed value of F#, a lens with a smaller focal length (and therefore proportionally scaled diameter) is preferable to reduce the magnification Π of the system. However this results in reduced light collection efficiency. For both objective and subjective speckle, the uncertainty is inversely proportional to the detector size. Therefore use of a larger area detector will result in a proportional reduction in the speckle related intensity uncertainty.

Typical figures (approximation to order of magnitude) for the speckle related intensity uncertainty are presented in Table 7-4. Here, the lens parameters were chosen to minimise the uncertainty rather than optimise the light collection efficiency.

Table 7-4: Parameters used to calculate objective and subjective speckle related intensity uncertainty. The detector diameter = 5mm, λ = 1650nm.

	Parameters	Uncertainty ΔI/I
Objective speckle	• Illuminated area diameter D= 25.4mm • Distance from diffuser to detector, Z = 150mm	2.4×10^{-3}
Subjective speckle	• Lens diameter, D_{lens} = 25.4mm • Lens focal length, $f_{lens} = D_{lens}/2$, hence F# = 0.5 • Lens to detector distance, $S_{detector} = f_{lens}$ • Lens to diffuser distance, $S_{diffuser}$ = 150mm • Magnification, $\Pi = S_{detector}/S_{diffuser}$	2.2×10^{-4}

In the case of subjective speckle, in addition to improved light collection efficiency, use of the lens in this cell geometry reduces the uncertainty by an order of magnitude by optimising the geometry of the receiving lens. Objective speckle related intensity uncertainty can be reduced by increasing the illuminated area D. However this is limited by practical considerations such illumination geometry and increased response time (filling and evacuating a larger volume). For example, to achieve the same level of uncertainty as in the subjective speckle configuration requires a ten fold increase in the illuminated area D and a consequent ten fold increase in the cell volume.

Another potential source of uncertainty in the measured intensity in the cell design of Figure 7-6 is interferometric speckle. Interferometric speckle could arise if a partial reflection from one side of the wedged window combined coherently (i.e. giving rise to interferometric speckle) with the light scattered from the diffusive surface at the detector. The intensity modulation of interferometric speckle at the detector takes the form[14];

$$I = I_0\left(1 + k\sqrt{r_1 r_2}\cos 4\pi d/\lambda\right) \tag{7-6}$$

The fringe amplitude would be proportional to $\sqrt{r_1 r_2}$, where r_1 and r_2 are the surface reflectivities of the wedged window and the diffusive surface. The form of this equation is similar to the low finesse Fabry-Perot relationship previously discussed in section 6.1.1. In practice, interferometric speckle can be avoided with relative ease by misaligning the reference beam such that only the light scattered from the diffuser reaches the detector or using different gas cell geometry (see following sections). For this reason an analysis of interferometric speckle noise will be largely omitted. The focus will be on considering speckle related intensity uncertainty governed by equations 7.4 and 7.5.

The main advantage of the cell geometry presented in Figure 7-6 is that the effective path length of the cell is twice the physical length (i.e. 20cm path length from a 10cm long cell). The design has a number of potential disadvantages;

1. Light inefficiency due to losses at the beam splitter. To optimise the power arriving at the detector would necessitate the use of a 50/50 split beam splitter. This could potentially mean discarding 50% of the power incident on the beam splitter from the laser and 50% of the diffusely reflected light. An alternative configuration to improve light collection efficiency is presented in Figure 7-7.
2. In the experiments a Pellicle beam splitter was used to avoid stray reflections associated with plate or cube beam splitters. However, Pellicle beam splitters are fragile and relatively expensive.
3. The expected intensity uncertainty is above the target detection limit of several ppm.

In summary, the speckle related intensity uncertainty for a single static field depends on the gas cell geometry. For a given geometry, the uncertainty is inversely proportional to the detector size.

The foregoing analysis for the speckle related intensity uncertainty applies to many of the gas cell designs considered in this section and will therefore not be repeated for each cell. Only a summary of the results will be presented for the other cell designs.

The notation presented in Table 7-4 will be used in all the gas cell geometries to be considered in this section. In the case of subjective speckle, the lens will be configured to operate at F# = 0.5, the magnification will be defined as $S_{\text{detector}}/S_{\text{diffuser}}$ with the detector located at the focal point of the light collecting lens. A detector diameter of 5mm will be used in all the calculations.

Figure 7-7 shows a second optical cell geometry that overcomes the main disadvantages of the previous design (Figure 7-6) by using an off axis parabolic mirror (OAP) in place of the beam splitter. The OAP has hole in centre to accommodate a laser diode (ideally a 5.6mm can or a fibre tip for fibre coupled sources) mounted such that OAP forms one end of the gas cell. A highly reflective holographic/engineered diffuser with a diffusion angle matched to the F/# of the OAP can be used to improve the efficiency of the system. Highly reflective engineered diffusers are now commercially available (such as those manufactured by Luminit*). These have the added advantage that profile of the backscattered light can be shaped (cone angle as well as profile) to increase the light collection efficiency

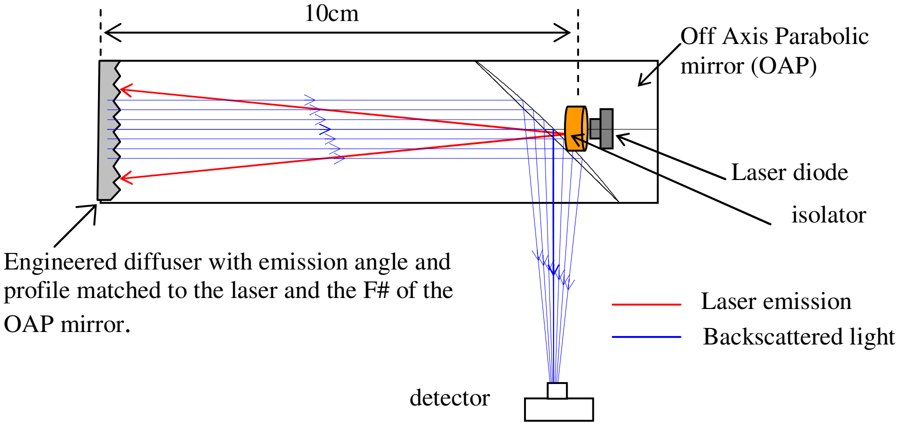

Figure 7-7: Use of an off axis parabolic mirror to improve light collection efficiency of the configuration shown in Figure 7-6.

Advantages of the cell configuration include; (a) simple and robust integrated geometry, (b) improved light collection efficiency, and (c) doubling of the effective path length.

The main disadvantage of such a system is self mixing interference if the laser is mounted in the OAP as shown in Figure 7-7. An isolator can be used to reduce the effect but at a considerable cost (>£1000) and the effectiveness of the isolator would be limited by the residual reflectivity of the entry aperture window facing the laser diode.

A third cell geometry is shown in Figure 7-8, in which single mode fibre is used to couple light to the cell.

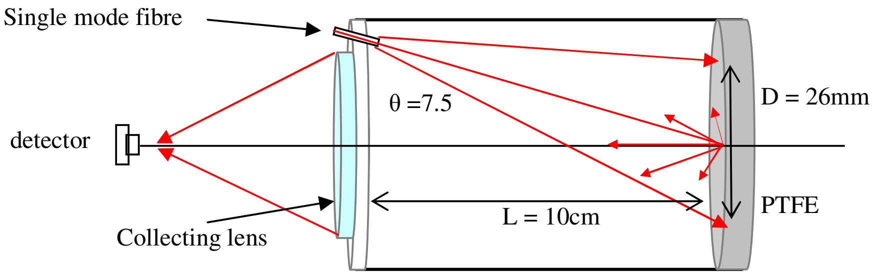

Figure 7-8: Reflection type gas cell model. Not to scale.

---

* http://www.luminitco.com/index.php/?item=hm: 20600 Gramercy Place, Building 203, Torrance, CA 90501-1821 (USA).

In the system shown in Figure 7-8 above the size of the illuminated area D will be given by

$$D = 2L\tan\theta \qquad \textbf{(7-7)}$$

where θ is the half angle derived from the NA of a single mode fibre. For L = 10cm, the diameter of the illuminated area D=26mm. This is comparable to D = 25.4mm used in calculations for the cell geometry (Figure 7-9, Table 7-5). Therefore the speckle related intensity uncertainty will be on the same scale (Table 7-5) for objective speckle and subjective speckle (if a similar lens configuration is used). The advantages of such as system include (a) effective path length is approximately double the physical path length, (b) flexibility of fibre; laser can be located remotely from cell allowing cell and (c) simple and robust. One main disadvantage is interference effects (Fabry-Perot as well as self mixing) associated with the use of fibre (often in the fibre coupling system).

7.2.2 Transmission type gas cell designs

Figure 7-9 shows a fourth gas cell geometry, employing a transmissive diffuser. The diffuser forms the first window of the gas cell. The detector and mount can be sealed to the opposite end of the cell such that front of the detector package forms the window.

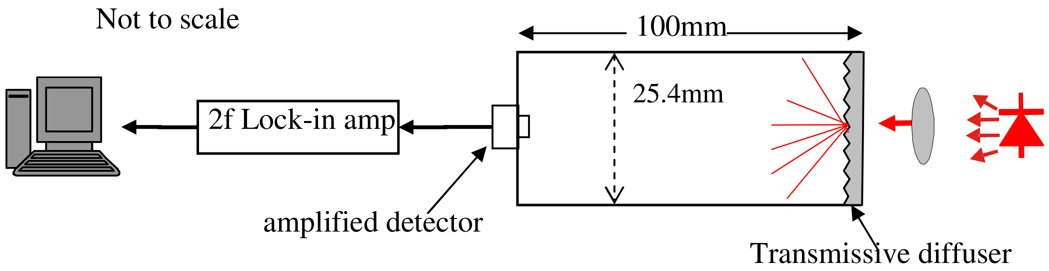

Figure 7-9: Scheme of gas cell geometry employing a transmission type diffuser.

Alternatively a lens can also be placed in front of the detector to improve the light collection efficiency. The estimated speckle related intensity uncertainty in the measured intensity at the detector is presented in Table 7-5.

Table 7-5: Parameters used to calculate objective and subjective speckle related intensity uncertainty. The detector diameter d = 5mm, λ = 1650nm.

	Parameters	Uncertainty ΔI/I
Objective speckle	D=25.4mm, Z = 100mm	1.6×10^{-3}
Subjective speckle	D_{lens} = 25.4mm, $S_{diffuser}$ = 100mm	2.3×10^{-4}

Different types of diffusely transmitting materials were investigated. A sample of the diffusers is presented in Table 7-6.

Table 7-6: List of transmissive type diffuser and their transmission properties.

Diffuser	comment
Ground glass • 120grit -22% transmission • 220 grit-22%, • 600grit-80% • 1500grit-100% (Transmission normalised to the 1500 grit sample)	• Gaussian diffuser • For the coarse diffuser (1500grit) the central portion of beam not diffusely scattered • Low transmission and strong reflected specular component for the fine grit diffuser (120 and 220)
Zenith^{TM} (100µm) thick or Spectralon^{TM}	• 100µm sample relatively fragile and • may not be gas tight; this can be both advantage/disadvantage • Transmission poor for samples > 100µm thick.
Holographic diffuser/engineered diffuser	• Engineered to shape light to a specified aspect angle • Scattered light at specified cone angle relatively high transmission

Advantages of the cell configuration include: (1) it is a simple and robust design (b) use of commercially available engineered/holographic transmissive diffusers that lead to a high system throughput (light shaping to a specified aspect ratio leading to high collection efficiency and relatively high transmission e.g. Luminit diffusers claim 85-92% transmission). The disadvantages include;

1. Potential for self mixing due to
    a. Specular reflection from the first surface of the diffuser.
    b. Diffusely backscattered light from the second surface of the diffuser.
2. The first surface can form an etalon with flat surfaces preceding it; AR coating/wedging should be considered in both cases.
3. There is only a single pass through the gas cell.

The following section summarises the gas cell designs discussed above.

7.2.3 Summary of the gas cell designs

In summary, a number of gas cell geometries employing a diffusive element have been discussed (summarised in Table 7-7). In all the gas cell designs considered here, the estimated speckle related intensity uncertainty for a single static speckle pattern remained in the range 1×10^{-3} to 1×10^{-4}. The speckle related intensity uncertainty is determined by the optical geometry of the gas cell and the light collection geometry.

Objective speckle noise can be reduced by

1. Use of a large detector (more speckles integrated over the detector aperture), however InGaAs detector chips are more expensive than silicon.
2. Use of large illuminated area. This is not practical in many situations due to difficulties in configuring the illumination geometry and light losses. This would also lead to cells with a relatively large volume and therefore longer response time of the sensor.

When a lens is used to gather light (i.e. subjective speckle), a number of advantages can be realised;

1. Speckle size is independent of illumination geometry, instead, it is governed by the geometry of the light collection lens.
2. Speckle size can be minimised by using large diameter optics(for collection efficiency) with short focal length(i.e. small F/# e.g. aspheric lens or Fresnel lens)

Table 7-7: Summary of gas cell designs.

CELL	ADVANTAGES	DISADVANTAGES	UNCERTAINTY
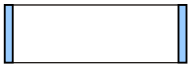	• simple design • low cost	• interference effects due to Fabry-Perot etalons • poor sensitivity	• worst case detection limit of 2.4% achieved in section 7.2
	• etalon effects reduced by use of AR coatings and wedging • high sensitivity can be achieved (3ppm demonstrated in section 5.4.2)	• coatings can be expensive at non standard wavelengths • alignment is critical	• 3ppm demonstrated in section 5.4.2
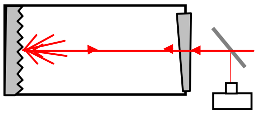	• effective path length is twice path length • simple geometry	• possibility of interferometric speckle. • Light inefficiency	• estimate for a single static speckle field 2.3×10^{-4}ppm
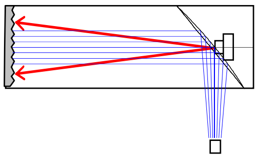	• effective path length is twice path length • simple and robust geometry • engineered diffuser can be used to achieve high light collection efficiency	• possibility of interferometric speckle. • Requires use of a 60dB isolator to prevent self mixing interference effects	•
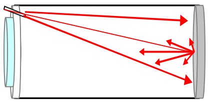	• effective path length is twice path length • simple and robust geometry • can be remotely located from source	• interference effects associated with fibre coupling	• estimate for a single static speckle field 2.3×10^{-4}ppm
	• simple geometry and robust geometry • engineered diffuser can be used to improve light efficiency	• single pass • reflected specular component from 1st window (can be reduced by AR coating/wedging)	• estimate for a single static speckle field 2.3×10^{-4}ppm

Formation of interferometric speckle can be prevented through good cell design practice. Precautions to avoid optical feedback (due to diffuse reflections) and the associated self mixing interference effects (reported in detail in section 6.2.5) should be undertaken. For cells with diffusive surfaces this procedure is simplified because one of the windows has been replaced.

In the following section, the performance of a gas cell utilising a diffusive element has been evaluated by performing gas absorption measurements.

7.2.4 Gas absorption measurements

This section reports an experiment conducted to evaluate the performance of a 10cm cell employing a diffusive element. The cell geometry discussed in Figure 7-9 with ground glass as the diffusive element was used as the test cell. The experimental set up is shown in Figure 7-10. For the cell geometry used, the expected intensity uncertainty for a single static speckle pattern was approximately (to order of magnitude) 1×10^{-3} (see Table 7-5).

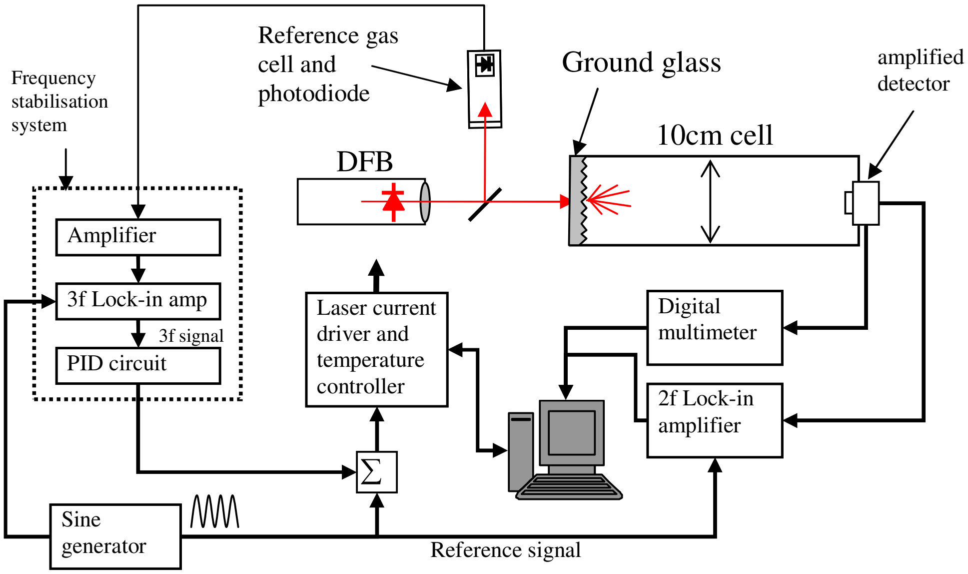

Figure 7-10: Scheme of the experimental set-up used to evaluate the performance of a gas cell employing a transmissive diffuser.

The modulated output light of a frequency stabilised DFB laser (Semelab) was directed onto an amplified detector (Thorlabs PD400) after passage through a 10cm long gas cell with a ground glass front window. The output of the detector amplifier was fed to a lock-in amplifier (Stanford Research Systems SR850) for phase sensitive detection at 12kHz (2f). The 2f signal was transferred to a computer running Labview^{TM} software through data acquisition card (National Instruments PCI 6259).

Methane (2.5% concentration) was gradually diluted with hydrocarbon free air using gas flow controllers (Telydyne THPS-400-230). The peak 2f was recorded for different concentrations; from an initial concentration of 1000ppm down to 25ppm (ppm, parts per million). The recorded demodulated 2f output is plotted against concentration in Figure 7-11.

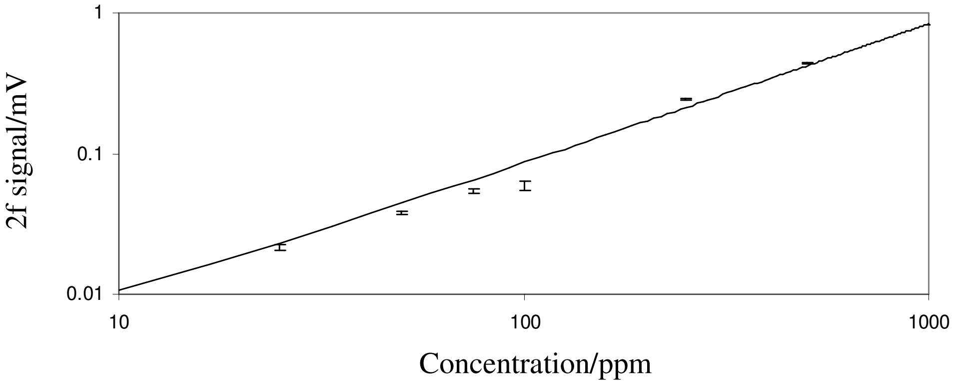

Figure 7-11: Plot of 2f signal against concentration. Time constant was 1 second. Detector (Thorlabs, PDA50EC) gain was 0dB. Note; log scale

Figure 7-12 shows a time series plot of the 2f demodulated output in the low concentration range. An analysis of the time series data is presented in Table 7-8 below.

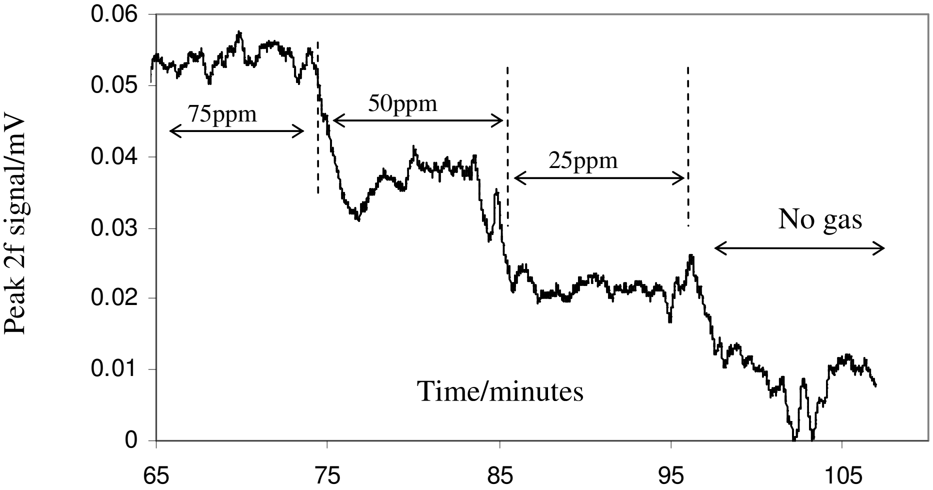

Figure 7-12: 2f-demodulated output from the detector plotted as a time series while different methane concentrations (in air) were delivered to the gas cell. Key: ppm; parts per million. Time constant = 100ms.

Table 7-8: Analysis of short term and long term drift of the output.

PARAMETER	VALUE
Calibration factor	1290ppm/mV
Detection limit	11ppm
Long term drift/100 minutes	56ppm

In summary, the performance of a gas cell utilising a diffusive element has been evaluated. The detection limit was found to be 11ppm. This is approximately 3 orders of magnitude lower than the expected speckle related uncertainty limit of 1×10^{-3}. One possible explanation is that, in practice, the measurements were obtained in a finite time interval set by the lock-in amplifier time constant. During this time interval, the speckle pattern at the detector is expected to vary in a random manner due to the high sensitivity of speckle to ambient vibrations. Therefore a reduction in the uncertainty (compared to that of a single static speckle pattern) is expected due to averaging. Another explanation is that if the speckle pattern as "seen" by the detector remains unperturbed during the measurement interval, equations 7.4 and 7.5 can not be used to estimate the uncertainty. The equations are relevant in estimating the measurement precision where there is perturbation of the speckle pattern (i.e. due to relative displacement between the detector and diffuser) between subsequent measurements or between subsequent wavelength modulations. The latter explanation is more likely than the former because in practice the speckle was observed (using a CCD camera) to be relatively stable over durations comparable to the lock in time constants used in the experiments (3ms-10s).

The following sections report experiments in which the speckle related intensity uncertainty was deliberately enhanced such that effectiveness of techniques investigated for suppressing it could be determined unambiguously.

7.3 Speckle noise reduction by averaging

Speckle related intensity uncertainty can also be reduced by reducing the contrast of the speckle pattern as previously discussed in section 3.2.8 and demonstrated in section 4.4.4. The contrast C or normalised standard deviation of a polarised speckle pattern was shown in chapter 3 (section 4.1) to be given by $C = \sigma / \langle I \rangle$. Adding M uncorrelated speckle patterns on an irradiance basis results in suppression of speckle contrast to

$$C = \sigma / \sqrt{M} \langle I \rangle \tag{7-8}$$

This is relevant where the detector integrates M uncorrelated speckle patterns during the measurement bandwidth. This can be achieved by rotating or vibrating the diffuser. The following section reports experiments investigating the reduction of speckle related intensity uncertainty by reducing the contrast of the speckle by rotating and vibrating a diffuser.

In the following experiments, the speckle related intensity uncertainty was deliberately exaggerated so that the effectiveness of the measures taken to suppress it could be quantified unambiguously. The speckle uncertainty was exaggerated by using a relatively small detector (1mm diameter) and appropriate optical geometry (i.e. objective speckle with large Z and relatively small D in equation (7.4)). Speckle suppression by means of a moving diffuser (rotating and vibrating) was investigated.

7.3.1 Rotating diffuser

Reduction of speckle contrast and therefore the related intensity uncertainty by using a rotating diffuser was investigated using the experimental set up shown in Figure 7-13.

A diffuser (a sample of Zenith$^{\text{TM}}$, 1mm thick) mounted on a rotating platform was illuminated off axis by the emission from a modulated DFB laser (beam approximately 8mm diameter). The backscattered light fell onto a 1mm diameter InGaAs detector

(Thorlabs PDA400) after passage through 10cm cell with wedged and AR coated windows.

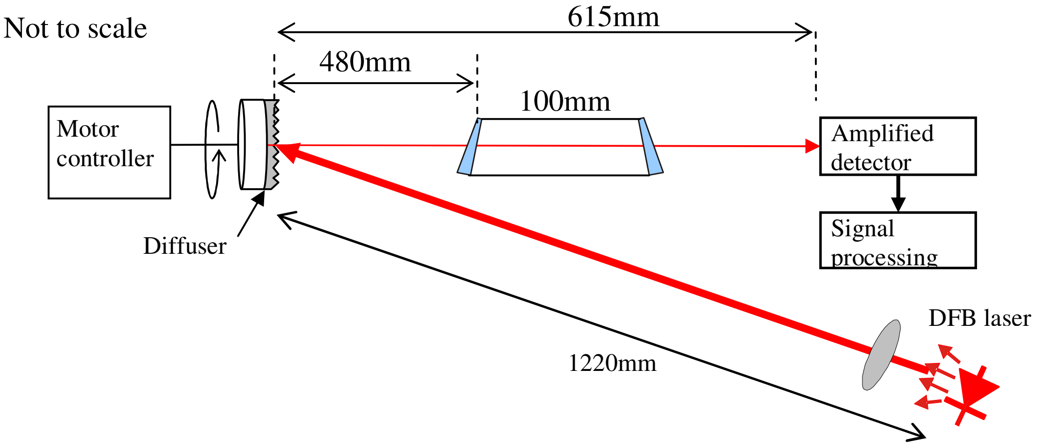

Figure 7-13: Experimental setup for characterising properties of speckle from various scattering materials. Key: f; focal length of lens L1 and L2.

The detector could be placed at two different locations L1=300 mm and L2 = 615mm that yielded an estimated speckle related uncertainty of 1.5×10^{-2} and 3.1×10^{-2} respectively for a single static frame (see Figure 7-14). This level of uncertainty is far above the uncertainty due to interference effects in the gas cell (characterised in section 7.1). Therefore in principle the presence of the cell can be largely ignored (only used to contain the gas in the laboratory), such that the system was equivalent to an open path system.

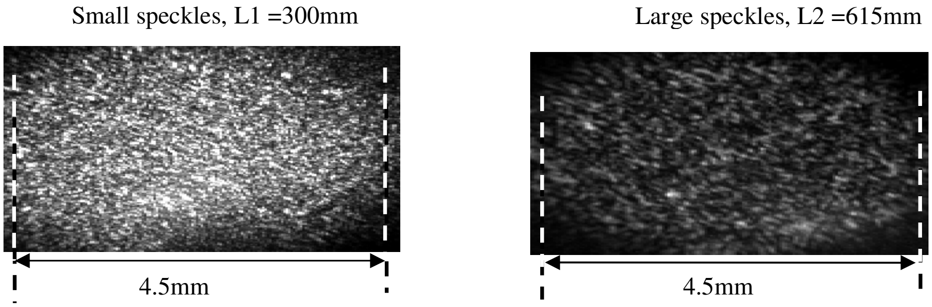

Figure 7-14: Images of large and small speckles taken with a camera located at 615mm and 300mm from the diffuser.

In a first experiment, the laser diode output was locked to the methane line. The 2f-demodulated output from the detectors was recorded. Different methane concentrations were delivered to the cell; first hydrocarbon free air, then 1.25% methane in air. The results obtained for rotating diffuser (1kHz) are shown in are shown in Figure 7-15 as a log plot signal of against concentration. Figure 7-16 shows a sample of the results plotted as a time series as different methane concentrations were delivered to the cell.

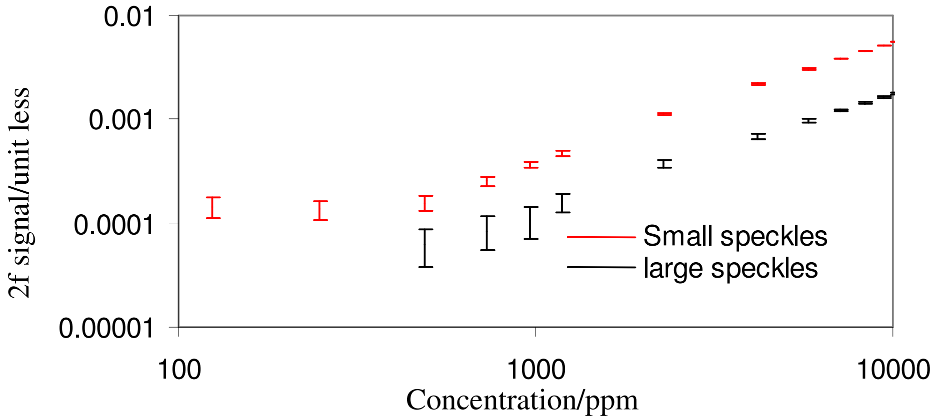

Figure 7-15: Log plot signal of against concentration obtained in the case of a rotating diffuser.

(a) Small speckles

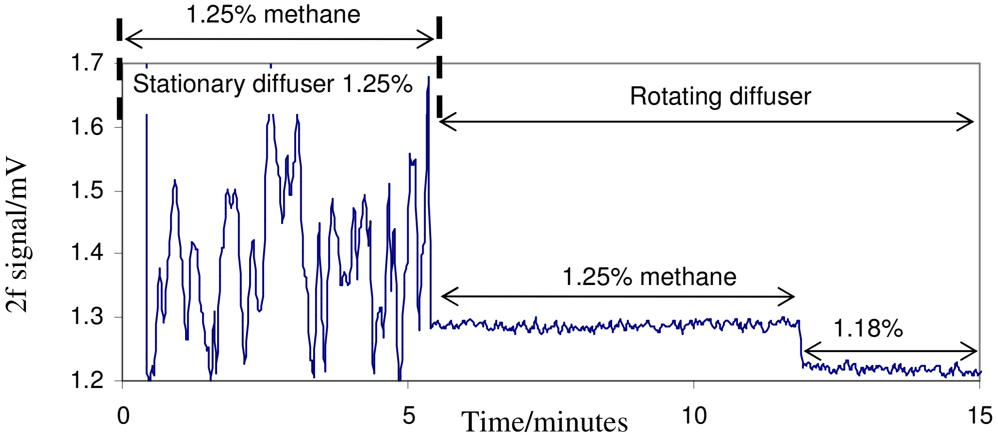

(b) Small speckles at low concentration; rotating diffuser

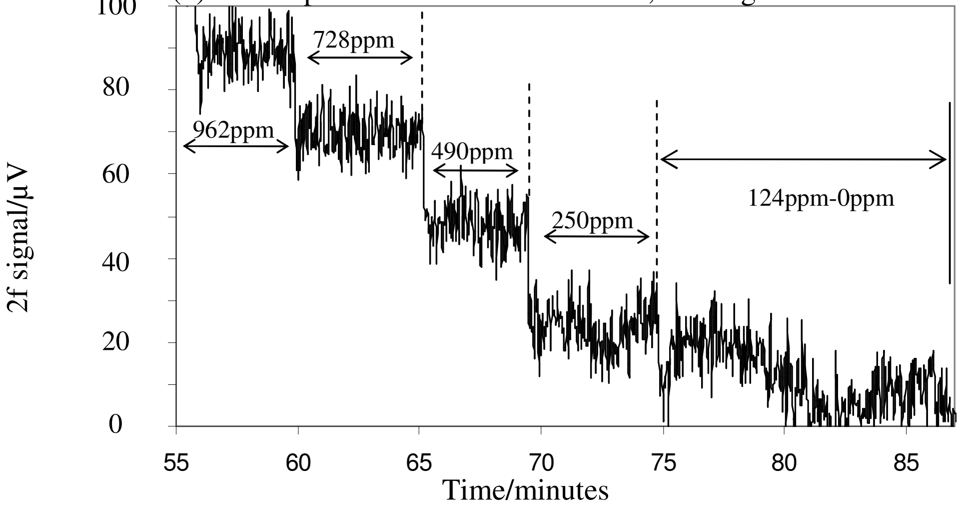

Figure 7-16: Plots of the 2f-demodulated output from the detector plotted as a time series while different methane concentrations (in air) were delivered to the gas cells. Plots obtained in the case of (a) small speckles and (c) small speckles in the low concentration range.

A quantitative analysis of the results in the case of large speckles and smaller speckles are presented in Table 7-9 and Table 7-10 respectively.

Table 7-9: A quantitative analysis of the results in the case of larger speckles.

Parameter	**1.25% Vol methane stationary diffuser**	**1.25% Vol methane rotating diffuser**
Mean value of intensity I	3.2×10^{-3}	2.2×10^{-3}
Standard deviation ΔI	5.1×10^{-4}	3.1×10^{-5}
Normalised Standard deviation (ΔI/I)	0.16	0.014
Expected speckle related uncertainty calculated from theoretical speckle size	0.031	

Table 7-10: A quantitative analysis of the results in the case of smaller speckles.

Parameter	**1.25% stationary diffuser**	**1.25% rotating diffuser**
Mean value I	1.39	1.29
Standard deviation ΔI	0.11	5.9×10^{-3}
Normalised Standard deviation (ΔI/I)	0.079	4.6×10^{-3}
Expected speckle related uncertainty calculated from theoretical speckle size	0.015	

In a second experiment (with the system configured for large speckles), the laser drive current was ramped over the range 35-70mA in steps of 0.2mA, while 2f-demodulated detector output was recorded in the case of a stationary and rotating diffuser. Scans were taken with the cell evacuated and also with the cell filled with 1.25% methane at atmospheric pressure. The results are plotted in Figure 7-17.

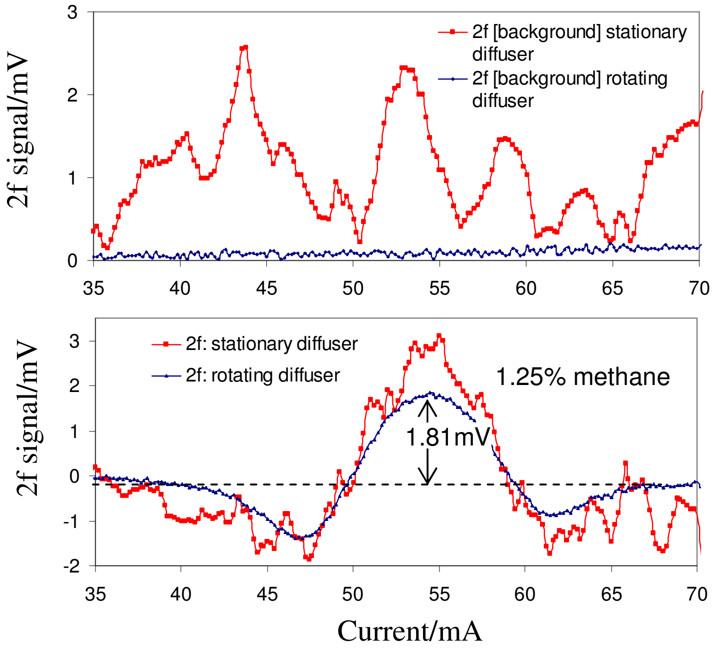

Figure 7-17: Results of wavelength scans obtained in the case of a stationary and rotating diffuser (a) through an evacuated gas cell. (b) through a methane line at 1.25% concentrations (Lock-in τ 100ms.). The estimated speckle related intensity uncertainty for a stationary diffuser was 3.1×10^{-2}.

A quantitative analysis of the plots in presented in Table 7-11.

Table 7-11: Quantitative analysis of the plots shown in Figure 7-17.

Parameter	**Background stationary diffuser**	**Background rotating diffuser**
Expected speckle related uncertainty	3.1×10^{-2}	
Normalised standard deviation	0.59	0.044
Calculated detection limit	4075ppm	304ppm

In summary reduction of speckle contrast and therefore the related intensity uncertainty by using a rotating diffuser was investigated. Use of a rotating diffuser was found to reduce the speckle related intensity uncertainty by a factor of 10.

The following section reports an experiment investigating the reduction of speckle related intensity uncertainty by means of a vibrating diffuser.

7.3.2 Vibrating diffuser

Reduction of speckle contrast and therefore the related intensity uncertainty by using a rotating diffuser was investigated using the experimental set up shown in Figure 7-18. A reflective diffuser (a sample of Zenith 1mm thick) was glued to a loudspeaker diaphragm. The speaker could be driven by a signal derived from the laser modulating signal. A 200Hz sine wave and an audio signal[15] were found to be suitable for driving the loud speaker. The signal selection process involved visually monitoring the contrast of the speckle as different signals were applied. The backscattered light fell onto a 1mm diameter InGaAs detector after passage through 10cm cell with wedged and AR coated windows.

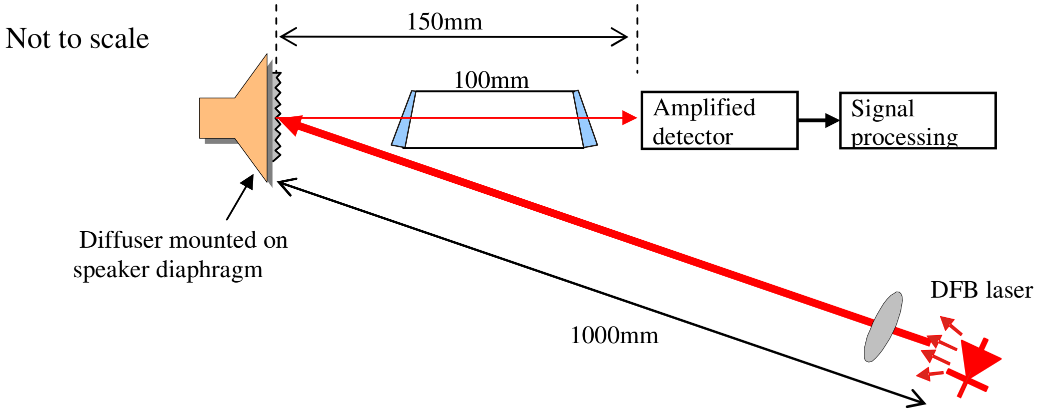

Figure 7-18: Experimental setup for characterising properties of speckle from various scattering materials. Key: f; focal length of lens L1 and L2.

In a first experiment the laser drive current was ramped over the range 30-80mA in steps of 0.2mA, while 2f-demodulated detector output was recorded in the case of a stationary and vibrating diffuser. Scans were taken with the cell filled with 1010ppm methane with the lock-in amplifier time constant set to 100ms. The results are plotted in Figure 7-19 and analysed in Table 7-12.

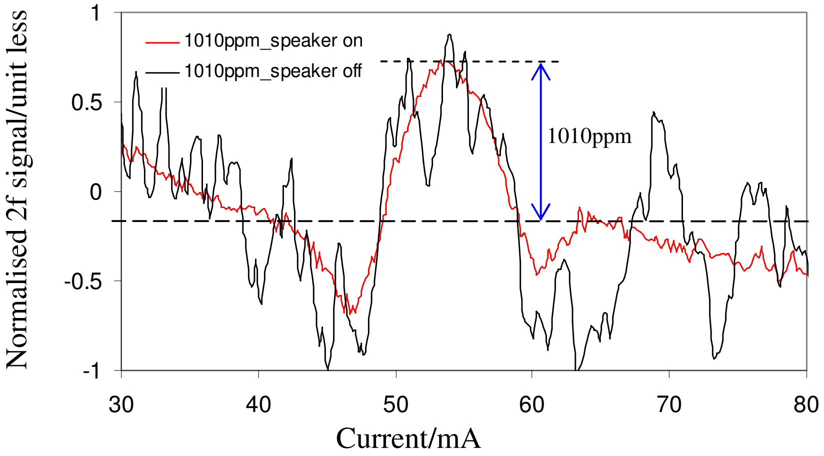

Figure 7-19: Results of wavelength scans obtained in the case of a stationary and rotating diffuser. In both cases the gas cell was filled with 1010ppm methane (Lock-in τ 100ms).

Table 7-12: A quantitative analysis of the results in the case of smaller speckles

Parameter	**stationary diffuser (1010ppm)**	**vibrating diffuser (1010ppm)**
Expected speckle related uncertainty	4×10^{-2}	
Calibration factor	1195ppm/unit	
Short term fluctuation (5 minutes)	1542ppm	160ppm

Use of the diffuser reduced the short term signal fluctuations by an order of magnitude (Table 7-12).

In a second experiment, the laser diode output was locked to the methane line. The 2f-demodulated output from the detectors was recorded. With the speaker turned on, the cell was filled with 1010ppm methane and then evacuated. The speaker was then turned off and the procedure repeated. The results obtained for a stationary and vibrating diffuser are shown in Figure 7-20 (Lock-in τ 10s).

In summary, use of a vibrating diffuser was found to reduce the speckle related intensity uncertainty by an order of magnitude in the first experiment (Figure 7-19). In the second experiment (where the laser was locked to the gas line, Figure 7-20), the magnitude of the improvement due to the vibrating diffuser can not be directly determined because the long lock-in amplifier time constant (τ 10s) that was used also contributed to the averaging out of the speckle related uncertainty.

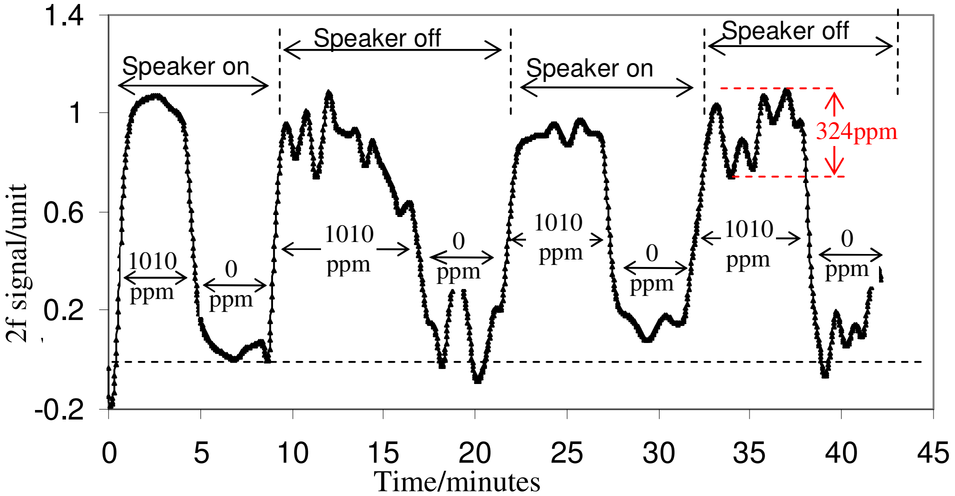

Figure 7-20: Normalised 2f-demodulated output from the detector as a time series while the gas cell was filled with 1010ppm methane and evacuated sequentially. The speaker was turned on in one interval and then turned off in the next (Lock-in τ 10s.)

7.4 Discussion and summary

The detrimental effects of Fabry-Perot etalon effects on the performance of a WMS instrument has been demonstrated (section 7.1). In a worst case scenario, fringes with an amplitude equivalent to 2.4% gas concentration were observed in the case of a 10cm gas cell with plane parallel windows. Use of a gas cell with wedged and AR coated windows improved the detection limit to 3 parts per million. However, this required careful alignment of the cell windows. The susceptibility to misalignment often leads to complex designs with tight tolerances on optical component alignment, and can therefore be difficult and expensive to maintain in field instruments. In addition, if the gas absorption line of interest lies outside the telecoms wavelengths, the optics and the AR coating can be expensive.

The deliberate use of diffuse reflections in gas cells as a means of eliminating interference effects due to Fabry-Perot etalons has been investigated. It has been shown that under the right circumstances (i.e. precautions taken against formation of interferometric speckle and self mixing effects) robust gas cell designs that do not suffer from Fabry-Perot etalon effects can be realised. However, the use of diffuse reflections lead to the formation of speckle and the consequent speckle related intensity uncertainty. Equations (7.4 and 7.5) were developed in chapter 3 to estimate the speckle related intensity uncertainty of a single static field. The expected speckle related intensity uncertainty of a number of gas cell geometries employing diffuse reflections that have been discussed was in the range 1×10^{-3} to 1×10^{-4} depending on the optical configuration. A detection limit of 11ppm was achieved using a single pass 10cm cell employing a ground glass diffuser (Table 7-8). This is significantly lower than the uncertainty as predicted by equation (7.4) possibly due to averaging effects as discussed in the summary of section 7.2.4. For convenience a comparison of the performance of the diffusive cell to the standard cells evaluated in section 7.1 is presented in Table 7-13.

Table 7-13: Summary of performance of different cell designs.

	CELL TYPE		
PARAMETER	**Plane parallel windows**	**AR coated and wedged windows**	**600 grit ground glass diffuser**
			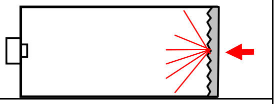
Detection limit	2.4%	3ppm	11ppm
Short term drift	470ppm/ 5minutes	34ppm/ 5minutes	11ppm/ 5minutes
Long term drift	5300ppm/ 50minutes	170ppm/ 50minutes	56ppm/ 100minutes

It has also been shown in section 7.3 that speckle related intensity uncertainty can be reduced by up to an order of magnitude by the use of a rotating or vibrating diffuser. In the experiments reported in this section the optimum vibration frequency and/or amplitude and optimum rotation frequency was selected dynamically by adjusting the frequency or amplitude to give rise to miminum rms noise in the system output (e.g. Figure 7-16 and Figure 7-19).

7.5 Conclusion

In conclusion, the feasibility of using diffuse reflections in gas cell designs as a means of eliminating Fabry-Perot etalon effects has been confirmed. The case for such cells is presented with the aid of an example cell design first presented in Figure 7-7 and presented here again for convenience as Figure 7-21. The design has not been realised in practice but the principles behind it have been experimentally evaluated.

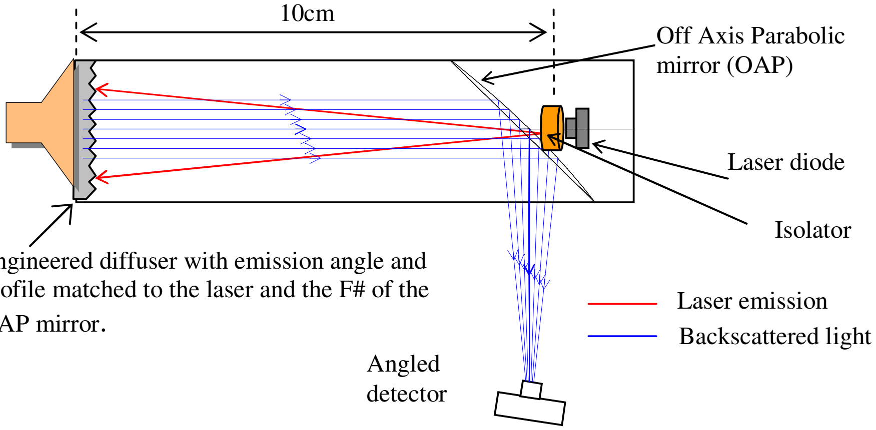

Figure 7-21: Schematic diagram of a preferred diffusive gas cell design.

This shows an ideal diffusive cell configuration based on the discussion and the results presented in the preceding sections. The design meets the key desired criteria outlined in the introductory remarks of this chapter (i.e. robust, simple, free from Fabry-Perot etalon effects, no use of transmissive optics). The added advantages are the high throughput due to the use of an engineered diffuser and the doubling of the effective path length. The uncertainty can be reduced by vibrating the diffusive element. This can be easily achieved by using a loud speaker or piezo electric transducer. This system has potential to achieve the target detection sensitivity of 2ppm. It is expected that detection limit will be determined by self mixing interference effects (reported in chapter 6). A 60dB Faraday isolator (small form factor; aspirin type) can be used in the system as shown in as Figure 7-21. However, its effectiveness will be limited by residual reflectivity of the isolator entry aperture window.

A number of studies[13,16-18] have reported the use of integrating spheres with diffusive surfaces as multipass optical cells. Several claims have been made regarding the potential advantages of using such cells. In the following chapter, the knowledge of diffuse reflections acquired in this thesis will be applied to a systematic study of the feasibility of using integrating spheres with internal diffusive surfaces as multipass optical cells in TDLAS.

7.6 References

[1] Silver, J. A. and Stanton, A. C. (1988), 'Optical interference fringe reduction in laser absorption experiments ', *Applied Optics*, V27, N10, pp. 1914-16.

[2] Schiff H I, Mackay G I and Bechara J 1994 *Air Monitoring by Spectroscopic Techniques* Editor Sigrist M W (New York: John Wiley and sons) pp 239-333.

[3] McManus, B. J and Kebabian, P. L. (1990), 'Narrow optical interference fringes for certain setup conditions in multipass absorption cells of the Herriott type', *Applied Optics*, V29, N7, pp. 898-900.

[4] Bomse, D. S., Stanton, A. C., and Silver, J. A. (1992), 'Frequency modulation and wavelength modulation spectroscopies: comparison of experimental methods using a lead-salt diode laser', *Applied Optics*, V31, N6, pp. 718-730.

[5] Mansfield, C. D. and Rutt, H. N. (1999), 'Evaluation of multiple beam interference effects in infrared gas spectroscopy', *Measurement Science and Technology*, V10, N3, pp. 206-210.

[6] Webster, C. R. (1985), 'Brewster-plate spoiler: a novel method for reducing the amplitude of interference fringes that limit tunable-laser absorption', *Journal of Optical Society of America B*, V2, N9, pp. 1464-1470.

[7] Chou, S., Baer, D. S., and Hanson, R. K. (1997), 'Diode laser absorption measurements of CH_3Cl and CH_4 near 1.65μm', *Applied Optics*, V36, N15, pp. 3288-3293.

[8] Reid, J. and others (1980), 'Sensitivity limits of a tunable diode laser spectrometer, with application to the detection of NO2 at the 100-pptv level', *Applied Optics*, V19, N19, pp. 3349-3354.

[9] Sano, H., Koga, R., and Kosaka, M. (1983), 'Analytical description of tunable diode laser derivative spectrometry ', *Japanese Journal of Applied Physics, Part 1 (Regular Papers & Short Notes)*, V22, N12, pp. 1883-8.

[10] Iguchi, T. (1986), 'Modulation waveforms for second-harmonic detection with tunable diode lasers', *Journal of the Optical Society of America B (Optical Physics)*, V3, N3, pp. 419-23.

[11] Capellani F, Mellandrone G and Restelli G 1987 *Monitoring of Gaseous Pollutants by Tunable Diode Lasers* editors Grisar R, H. Preier H, Schmidtke G and Restelli G (UK: Kluwer Academic Publishers) pp 51-60.

[12] Sun, H. C and Whittaker, E. A. (1992), 'Novel etalon fringe rejection technique for laser absorption spectroscopy', *Applied Optics*, V31, N24, pp. 4998-5002.

[13] Tranchart, S, Bachir, I. H., and Destombes, J-L. (1996), 'Sensitive trace gas detection with near-infrared laser diodes and an integrating sphere', *Applied Optics*, V35, N36, pp. 7070-7074.

[14] Sirohi, R. S. (2002), 'Speckle interferometry', *Contemporary Physics*, V43, N3, pp. 161-180.

[15] Marley, B and Wailers (1984), 'No Woman No Cry', *Legend*,

[16] Venkatesh, C. G., Eng, R. S., and Mantz, A. W. (1980), 'Tunable diode laser-integrating sphere systems: a study of their output intensity characteristics', *Applied Optics*, V19, N10, pp. 1704-1710.

[17] Tanaka H, Matsuura M, Tai H and Uehara K Tokyo Gas Co, LTD Tokyo Japan (13 April 1993), *Gas Detection Device*. USA. 5202570.

[18] Hawe, E. and others (2007), 'An investigation into the use of an integrating sphere as a gas absorption cell', *Journal of Applied Optics A: Pure and Applied Optics*, V9, N6, pp. S12-S18.

Chapter 8 Use of integrating spheres in TDLAS

The sensitivity of TDLAS systems is directly proportional to the gas absorption path length (at low concentration). For TDLAS systems operating in the near infrared, where the absorption coefficients can be up to 2 orders of magnitude weaker than of the fundamental absorption bands occurring in the mid infra red, the sensitivity can be improved by using long path lengths. Multipass optical cells (MOC) such as the White[1,2], Herriott[3] or Chernin type[4,5] cells are often used. These use highly precise and carefully aligned mirrors to fold the optical path. Path lengths of tens of metres to hundreds of metres have been reported[6]. A description of the operation of a simple implementation of the Herriot cell is given in Appendix G. The description also shows how this type of cell might lead to formation of undesirable interference fringes[6], which have been found to limit the sensitivity of TDLAS schemes employing this type of MOC. For example, Werle *et al*[7,8] found that the signal to noise ratio improvement of high frequency (200MHz) TDLAS over low frequency (typically <20kHZ) TDLAS reduced from 2 orders of magnitude to one order of magnitude when multipass cell are used. The problem of interference fringes coupled with the requirement of highly precise mirrors and complex alignment procedures in these type of MOC has led to interest in alternative MOC designs.

A number of studies[9-13](reviewed in a later section) have reported the use of integrating spheres (see Figure 8-1) as multipass optical cells.

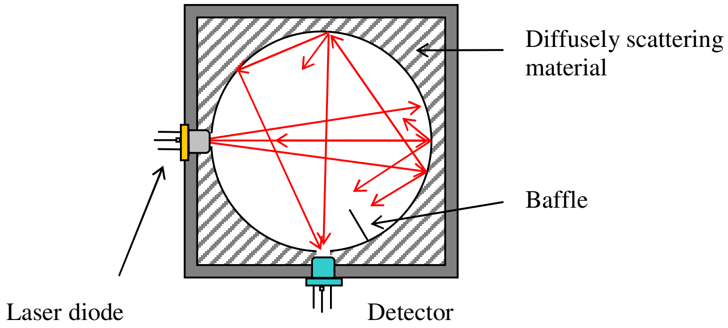

Figure 8-1: Schematic diagram of an integrating spheres showing the location of a baffle placed between output port and the so called "first-strike spot"[14].

An integrating sphere is a spherical cavity with highly reflective surfaces that is used to contain and diffuse input light so that it is evenly spread over the entire surface area of the sphere. The use of a Lambertian surface (the intensity from the incident radiation I_0 varies only as the viewing angle of the surface θ) in combination with a spherical enclosure leads to two unique properties of integrating spheres : (1) Every point within a sphere receives the same intensity of light as every other part of the sphere following the first bounce[15] and (2) any angular dependence of the intensity is removed[15].

When used as a gas cell, the highly reflective coating of the internal sphere surface allows multiple reflections through the sample and results in an equivalent absorption path length much larger than the diameter of the sphere.

8.1 Background

Integrating spheres have been traditionally used as devices for measuring optical radiation and are also widely used for recording spectra of scattering samples by placing the specimen inside or outside the sphere[16,17,18]. Although the use of integrating spheres as a multipass gas cell has been previously demonstrated[9], there is limited literature on their use in TDLAS (see section 8.2 for a summary of reported use). The aim of this chapter is to make a contribution to the body of knowledge on the use of integrating sphere in TDLAS in several areas including;

1. Speckle noise quantification; the interior surfaces of integrating spheres are often made of highly reflective diffusing materials that give rise to speckle. A systematic study of speckle effects has not been reported by the previous studies on the use of integrating spheres in TDLAS (reviewed section in 8.2)

2. Investigation of several claims that have been made by Tranchart et al[12] and other researchers regarding the potential advantages of using an integrating sphere as a multipass optical cell. The most important claims consistent with the theme of this thesis are outlined below.

a. *"The light source and the detector are coupled easily and no careful optical adjustments are needed, leading to a long-term mechanical stability"*[12].

b. *"An integrating device, such as an integrating sphere, is interposed optically between the tunable semiconductor laser and the detector. This integrating device is used to mitigate the effects of parasitic spectral noise, such as noise that is generated by speckle…"*[19]

There is the potential advantage that an integrating would lead to simple systems resulting in a relaxation of relaxation of design tolerances, which is the primary aim of this thesis.

c. "*Because of the infinite number of different optical paths, no optical interference fringes are expected. It has been verified experimentally that, if such effects are present, they represent a modulation of the baseline corresponding to an absorption coefficient smaller than* $5 \times 10^{-7} cm^{-1}$*"*[12].

Results obtained in chapter 6 (section 6.2.5) showed that diffuse reflections can lead to self mixing interference effects. Highly reflective diffusive surfaces (e.g. Spectralon^{TM}, Zenith^{TM}) are employed in integrating spheres. Experiments have shown that if reflected light from such samples is coupled into a laser diode, self mixing interference effects can be induced. The occurrence of self mixing effects in integrating spheres would have design implications that could contradict claim (a) above.

In summary, this chapter reports a systematic study on the feasibility of using integrating spheres as multipass optical cells in TDLAS.

The chapter is structured as follows

1. Section 8.2 presents a review of previous studies reporting the use of integrating spheres as multipass optical cells. The theory of integrating spheres is presented in section 8.3.
2. The experimental work is presented in the remaining sections and includes;
    a. Calibration experiments
        i. Effective path length determination.
        ii. Characterisation of the output nonlinearity (deviation from Beer's Law).
        iii. Quantification of speckle related intensity uncertainty.
    b. Experiments investigating the occurrence of self mixing effects in integrating spheres.
    c. Gas absorption experiments to determine the detection limit.

8.2 Review of the use of integrating spheres as multipass optical cells.

To the authors knowledge, the use of an integrating sphere as a MOC for gas absorption measurements was first reported in 1980 by Venkatesh et al[9]. They used a sphere machined out of aluminium. The aluminium surfaces had 180-grit SiC particles cemented to the inside walls and were gold over coated. The primary motivation for their work was to investigate the intensity profile of the integrating sphere output beam for various combinations of F#s of input and output coupling optics. They also used the sphere to measure carbon monoxide gas. Measurements of absorbance (A) were made on the P(29) line of CO (carbon monoxide) in the fundamental band (around 5µm) at pressures in the range 3-5 Torr.

Abdullin and Lebedev[11] reported the next case in 1988. A CO_2 laser was used for ammonia gas absorption experiments. They used a 10cm diameter sphere made of copper, and the experimentally determined effective path length was found to be 430±25cm. In comparing an integrating sphere to a standard MOC, Abdullin and Lebedev[11] concluded that in addition to path lengths that were more than ten times the sphere dimensions, the inherent disadvantages of standard MOCs do not exist in an integrating sphere (i.e. complex alignment procedure).

Tranchart *et al*[12] claimed that they were the first to use an IS to measure light absorption in gases. This is inaccurate as they are at least two earlier published papers on the subject[9,11]. They were probably the first to use a Spectralon™ coated sphere as it was developed by Labsphere in 1990. Gas absorption experiments were conducted for (1) broad band absorption of butane using a 1.2µm-multimode laser diode and (2) water vapour in air at atmospheric pressure with the use of an 830-nm single longitudinal mode laser diode. Equivalent path lengths of 203cm - 442cm were achieved from a sphere with an internal diameter of 10cm.

More recently the OFSRC research group (Limerick University, Ireland) has investigated the use of a 2 inch internal diameter integrating sphere (with Spectralon™ internal wall) in as a gas cell[13]. They have used single mode and multimode fibre (up to 1mm core) to couple narrow and broad band sources into the sphere respectively. The pointed out that due to the near uniform reflectivity of Spetralon™, one sphere could be used for absorption measurements from UV to mid infrared.

Table 8-1 provides a summary of papers reporting the use of integrating spheres as multipass optical cells for gas absorption measurements.

Table 8-1: Summary of papers reporting the use of integrating spheres as multipass optical cells for gas absorption measurements.

Authors	Year	Material/ Internal Diameter	Gas used	pathlength
Venkatesh *et al*[9]	1980	• machined aluminium surfaces that had 180-grit SiC particles cemented to the inside walls and gold over coated • tandem spheres each with a diameter of 3.81cm with a 1.27cm coupling hole diameter	Carbon monoxide in the 5µm region using a lead-salt laser	• 62.2cm
Abdullin and Lebedev[11]	1988	• machined copper • Diameter = 10cm	• Ammonia at 9.303µm using a CO_2 laser	• 430±25cm.
Tranchart *et al*[12]	1990	• Spectralon™ • Diameter = 10cm	• butane at 1.2µm using a multimode laser diode • water vapour in air at 830-nm using single-mode laser diode	• 203cm for butane • 442cm for H2O
Hawe *et al*[13]	2007	• Spectralon™ • Diameter = 5cm	• Ozone using a deuterium/halogen source with a spectrometer at 603nm • Nitrogen at 370nm using UV LED • CO2 lines (1530 to 1610 nm)	• 70cm for Ozone • 55cm for nitrogen

The following section presents the integrating sphere relations governing the throughput and the effective path length, relevant to its use as an MOC.

8.3 Integrating sphere relations

For an empty sphere, the ratio of the total light output to total light in is given by[14]

$$\frac{\Phi_{exit}}{\Phi_{in}} = \frac{\rho f_{exit}}{1-\rho(1-f_{total})} \qquad \textbf{(8-1)}$$

where Φ_{exit} is total flux exiting a given port (Watts); Φ_{in} is total incident flux (Watts), f_{exit} is exit port fraction (area of exit port /surface area of sphere), f_{total} is total port fraction (sum of all port areas/surface area of sphere), and ρ is sphere wall reflectance ($0 \leq \rho \leq 1$). A sphere containing an absorbing medium has an effective reflectance that is given by[12]

$$\rho[1-\alpha(\upsilon)L_{once}] \qquad \textbf{(8-2)}$$

where L_{once} is the average single pass through the IS, and $\alpha(\upsilon)$ is the gas absorption coefficient.

Equation (8-1) can therefore be modified accordingly to include the effects of an absorbing medium in the gas cell.

$$\frac{\Phi_{exit}(\alpha)}{\Phi_{in}} = \frac{\rho[1-\alpha(\upsilon)L_{once}]f_{exit}}{1-\rho[1-\alpha(\upsilon)L_{once}](1-f_{total})} \qquad \textbf{(8-3)}$$

The dependence on Φ_{in} and the exit port fraction can be eliminated by dividing equation (8-3) by (8-1) giving

$$\frac{\Phi_{exit}(\alpha)}{\Phi_{exit}} = \frac{[1-\alpha(\upsilon)L_{once}][1-\rho(1-f_{total})]}{1-\rho[1-\alpha(\upsilon)L_{once}](1-f_{total})} \qquad \textbf{(8-4)}$$

The fractional power absorbed by a sample in a sphere can be expressed as

$$\frac{\Delta\Phi}{\Phi_{exit}} = \frac{\Phi_{exit}-\Phi_{exit}(\alpha)}{\Phi_{exit}} = 1-\frac{\Phi(\alpha)}{\Phi_{exit}} \qquad \textbf{(8-5)}$$

Equation (8-5) can be manipulated to give an expression for the fractional absorption[12]

$$\frac{\Delta\Phi}{\Phi_{exit}} = \frac{\alpha(\upsilon)L_{once}}{1-\rho[1-\alpha(\upsilon)L_{once}](1-f_{total})} \qquad \textbf{(8-6)}$$

For a single pass through a weakly absorbing gas, $L_{once} = 2/3$ of sphere diameter (D)[12] and $\alpha(\upsilon) L_{once} << 1$. Equation (8-6) therefore simplifies to

$$\frac{\Delta\Phi}{\Phi_{exit}} = \alpha(\upsilon)L_{once}\left[\frac{1}{1-\rho(1-f_{total})}\right] \qquad \textbf{(8-7)}$$

The term in brackets on the right hand side of equation (8-7) is often termed the sphere multiplier (M)[20] resulting in further simplification of the fractional absorbance equation

$$\frac{\Delta\Phi}{\Phi_{exit}} = \alpha(\upsilon)L_{once}M = \alpha(\upsilon)(2/3D)M \quad \textbf{(8-8)}$$

The throughput at a port is given by

$$\Phi_{OpenPort} = \frac{\Phi_{in}}{\pi A_s} \times M \times A_{port} \times \Omega_{out} \quad \textbf{(8-9)}$$

where Ω_{out} is equal to π steradians or 180 degrees full hemisphere and A_s is the internal surface area of the integrating sphere. If the output flux is sampled with a detector with a defined field of view, the throughput is given by

$$\Phi_{\det ector} = \frac{\Phi_{in}}{\pi A_s} \times M \times A_{\det ector} \times \pi \sin^2\theta \quad \textbf{(8-10)}$$

where θ is the half angle of the field of view of the detector. However if a lens is used with the detector, it may be more convenient to estimate Ω_{out} from the F# of the system. In this case the sphere throughput is given by

$$\Phi_{\det ector} = \frac{\Phi_{in}}{\pi A_s} \times M \times A_{\det ector} \times \frac{\pi}{(2F\#)^2} \quad \textbf{(8-11)}$$

Optical fibre can also be used to couple light out of the sphere. Since fibre ends are highly polished, their reflectivity is taken into account and the solid angle is estimated from the numerical aperture (NA).

$$\Phi_{fibre} = \frac{\Phi_{in}}{\pi A_s} \times M \times A_{core}(1 - R_{reflect}) \times \pi NA^2 \quad \textbf{(8-12)}$$

8.4 Sphere calibration experiments

This section reports a number of experiments that were conducted to prepare and calibrate integrating spheres that were used for gas absorption experiments and to confirm relations presented in section 8.3.

Three commercially sourced integrating spheres were used for the investigations. The details including the standard port sizes are given in Table 8-2. Also presented in Table 8-2 are the expected theoretical path lengths calculated using the standard port sizes. In practice, the port sizes could be reduced using port reducers/adapter to increase the path length.

Table 8-2: Details of the integrating spheres used.

Internal diameter	Supplier	Coating	Standard port sizes
1 inch sphere	SphereOptics	Zenith^{TM}	3 ports with diameters of 12.7mm
2 inch sphere	Thorlabs	Zenith^{TM}	3 ports with diameters of 12.7mm Detector port = 3 mm
4 inch sphere	SphereOptics	Zenith^{TM}	4 ports with diameters of 25.4mm

Several sources were used in this chapter including (1) the 1651nm DFB module previously described in section 5.1.1, (2) a 1651nm fibre coupled DFB and (3) an 823nm Fabry-Perot laser diode in a 9mm T0 can, (4) a 1651nm VCSEL in a MTE package. The commercially available InGaAsP VCSEL diode module is mounted in a standard 8 pin T046 package and consisted of;

- a 1651nnm DFB laser diode chip mounted on a thermoelectric cooler (TEC) element for heating or cooling the diode
- a negative temperature coefficient thermistor (NTC) for sensing the operating temperature of the laser

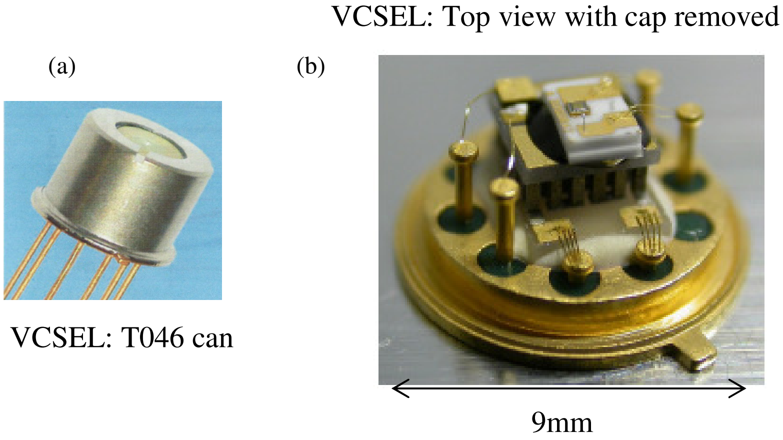

Figure 8-2: The 1651nm VCSEL diode (a) Picture of T046 can (b) Picture taken with cap removed.

Light from the sources could be coupled into the spheres in a number of ways. As illustrated in Figure 8-3(a) a collimated beam was injected into the sphere as in the case of the DFB module (previously described in section 5.1.1). In this case the first strike spot becomes the virtual source. If the first strike spot is in the field of view of a detector mounted onto the sphere as depicted in Figure 8-3(a), artificially high level of signal will be recorded. In the experiments the detector port was shielded from the first strike spot by

1. Use of a baffle made of the same material as the sphere internal wall located between the first strike spot and the detector (Figure 8-3(a)).
2. Deliberately limiting the field of view of the detector by stopping down or recessing the detector.

In a second configuration, the laser diode (9mm and MTE packages) could be mounted directly onto the integrating sphere (illustrated in Figure 8-3(b)) using a custom mounting adapter (pictured in Figure 8-5(a), such that a diverging beam is incident on the first strike spot. In this case the baffle was placed between source and detector to prevent light from reaching the detector directly before striking the sphere wall.

The 1 inch and 4 inch spheres had integral baffles to shield the detector from the source or first strike spot as shown in Figure 8-3.

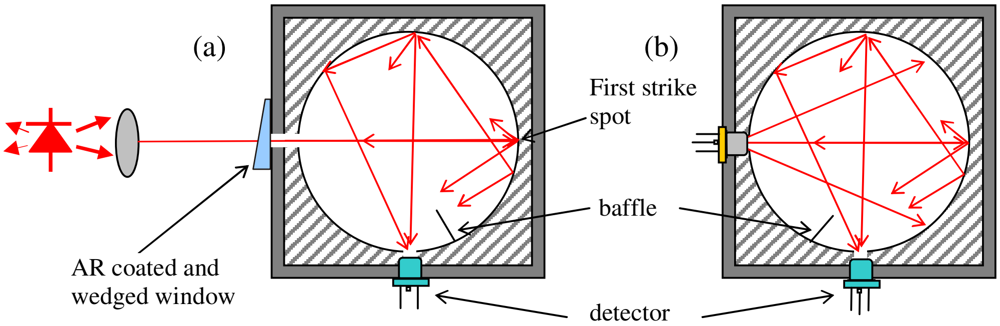

Figure 8-3: Schematic diagrams of integrating spheres showing the location of baffles placed between output port and the so called "first-strike spot"[14]. (a) The input beam is collimated. (b) The input beam is expanding.

The 2 inch sphere used a recessed detector port. A schematic diagram of the 2 inch sphere is shown in Figure 8-4.

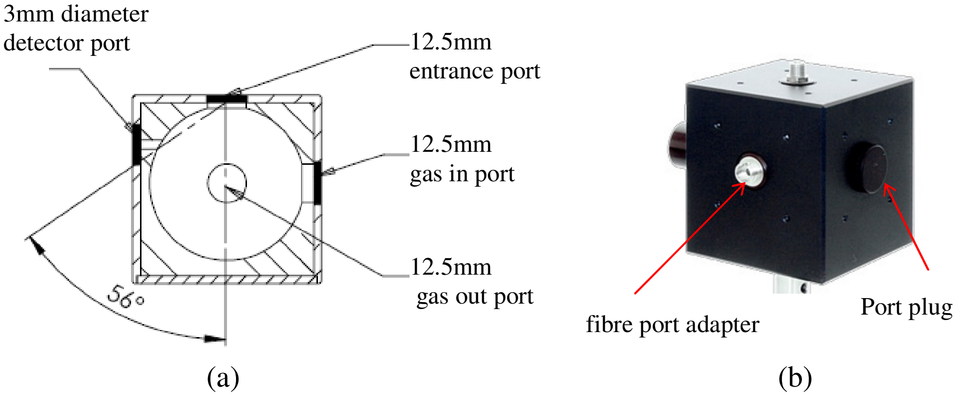

Figure 8-4: (a) Schematic diagram of an integrating sphere with a 2inch internal diameter. Image taken from Thorlabs document IS200-E01. The 3mm diameter detector port was configured such that sources with a divergence half angle of up to 56 degrees can be used without requiring a baffle. (b) Picture of integrating sphere taken from Thorlabs^{TM} website.

The location of the detector port and entrance port was such that the detector was not in the field of view of sources with a divergence half angle of up to 56 degrees or 0.83NA (NA, numerical aperture), negating the need for a baffle.

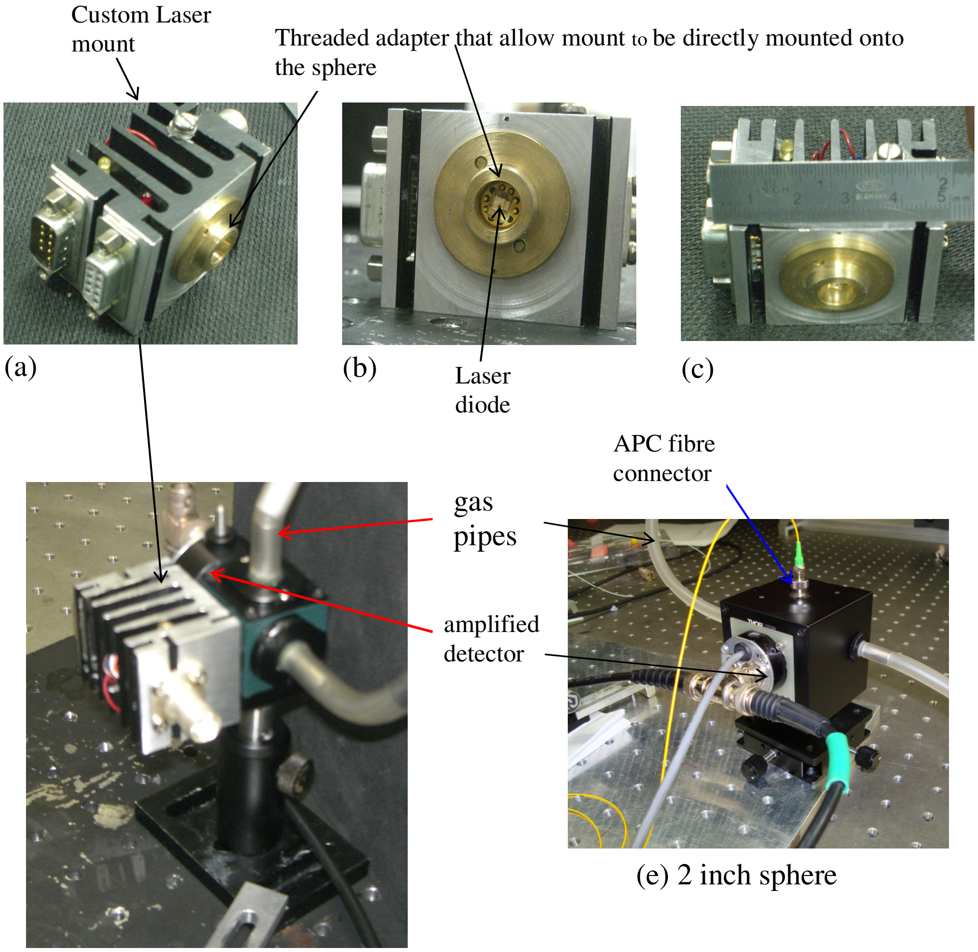

(d) 1 inch sphere

(e) 2 inch sphere

Figure 8-5. (a), (b) and (c) pictures of custom laser diode mount for attaching laser diode directly onto the sphere. (d) One inch integrating sphere with a laser diode mount and detector directly attached to it. (e) Picture of the 2 inch integrating sphere showing gas pipes, a detector modified to be attached to the sphere directly and light coupled to the sphere via fibre. Key; APC: angle polished connector.

The following section reports a series of sphere calibration experiments including

1. speckle related intensity uncertainty,
2. determination of the effective path length of the sphere,
3. characterisation of the output linearity.

8.4.1 Speckle noise in integrating spheres

A systematic study of speckle effects in TDLAS was reported in chapter 7 (sections 7.2 and 7.3). This section discusses the implications of speckle related intensity uncertainty in a TDLAS system employing an integrating sphere as a gas cell.

The speckle related intensity uncertainty (for a single static speckle pattern) in an integrating sphere is governed by the relations presented in section 4.1. In the case of objective speckle the illuminated area is defined by the field of view of the detector. The relationship for subjective speckle is unchanged (i.e. the uncertainty is inversely proportional to the F# of the light collection system).

Figure 14 shows objective speckle images obtained by a camera placed at a port of a 2 inch internal diameter integrating sphere with (a) 12.7mm aperture, (b) 7mm aperture, (c) 600μm aperture, and (d) 200μm aperture. The theoretical size of subjective speckle was estimated by using the equation $\varepsilon_s = 1.22\lambda(1+M)F\#$.

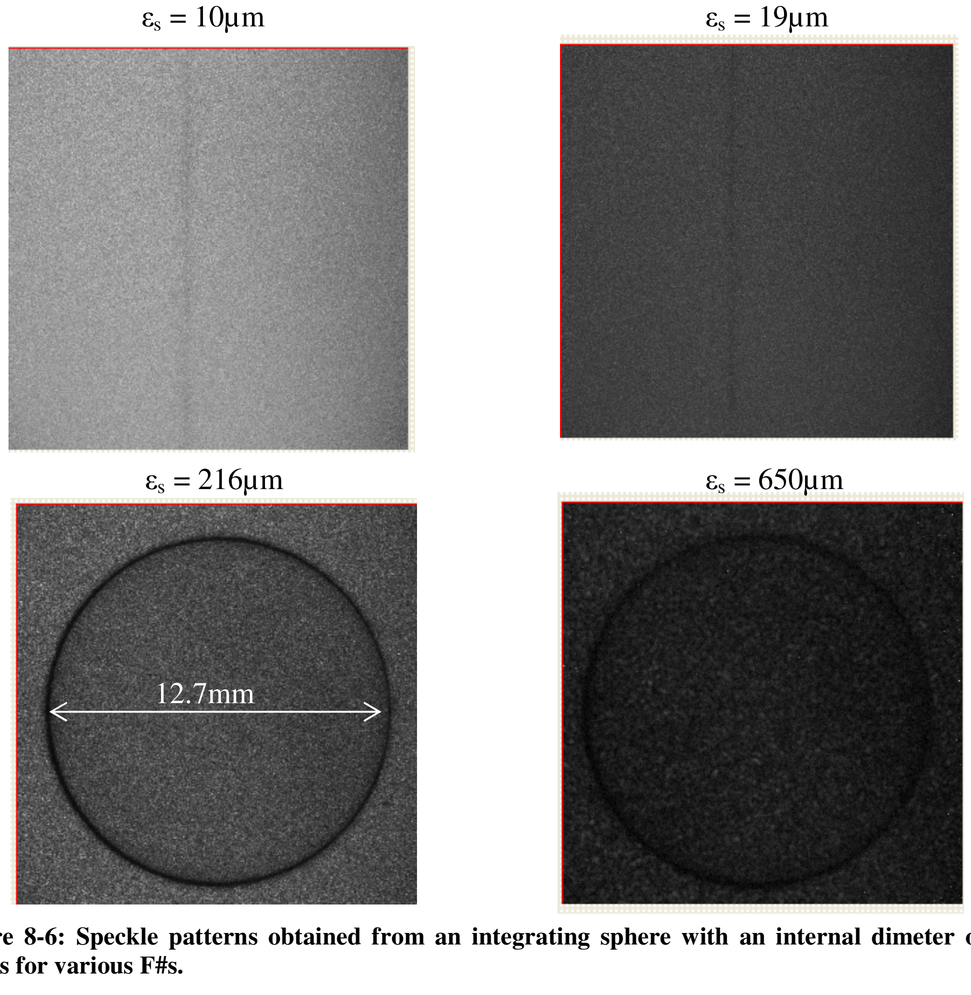

Figure 8-6: Speckle patterns obtained from an integrating sphere with an internal dimeter of 2 inches for various F#s.

Figure 8-7 shows a multimode fibre (Edmund Optics59289) coupled to the integrating sphere using an aspheric lens (Thorlabs F230SMA). The fibre output was recorded by a CCD camera. The recorded images are shown in Figure 8-8. The features (thought to be a combination of speckle and modes) in the recorded image shown in Figure 8-8(a) could be washed out by lightly tapping the fibre (Figure 8-8(b)). This shows that agitating the fibre (easily implemented) can be used as a means of reducing speckle related intensity uncertainty as previously discussed in 7.3.

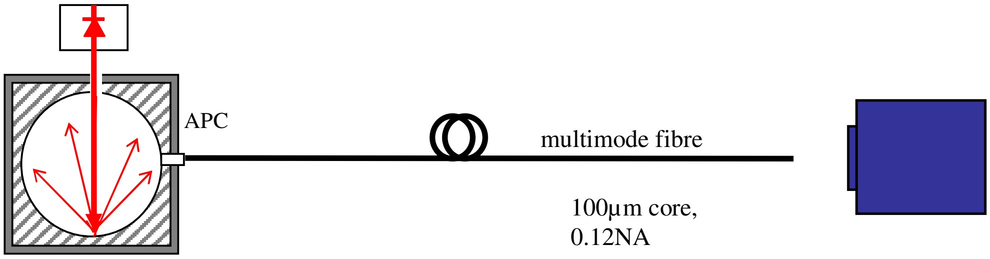

Figure 8-7. Schematic diagram of an experimental set up that was used to record the output of a multimode fibre coupled to an integrating sphere with an internal diameter of 2 inches.

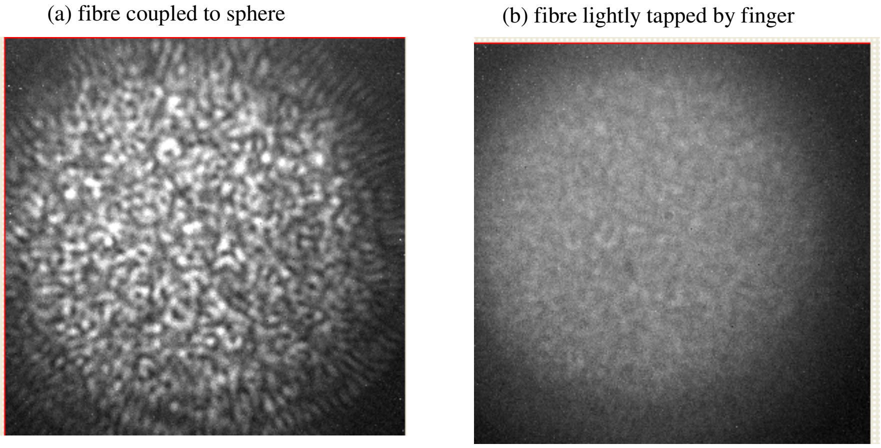
(a) fibre coupled to sphere

(b) fibre lightly tapped by finger

Figure 8-8: Images of light coupled out of multimode fibre (100µm core, 0.12NA).

8.4.2 Effective absorption path length

A description of the effective path length determination procedure is presented with the aid of the experimental setup shown in Figure 8-9.

The effective path length was estimated from Beer's Law written in terms of absorbance A

$$A = \ln(I_0 / I) = \alpha CL \tag{8-13}$$

where α is the absorption coefficient and C is the gas concentration, L is the path length, I_0 is the initial intensity and I is the transmitted intensity. With reference to Figure 8-9, if the path length of the cell (L_{cell}) is precisely known, the effective path length of the sphere (L_{sphere}) can be calculated by simultaneously measuring absorbances for the cell (A_{cell}) and the sphere (A_{sphere}). The ratio of the absorbances is equal to the ratio of the path lengths (valid only for the linear region of the Beer's law).

$$L_{sphere} = \frac{A_{sphere}}{A_{cell}} L_{cell} \qquad \textbf{(8-14)}$$

A_{sphere} and A_{cell} were calculated from the simultaneous measurements of I_0 and I for various gas concentrations.

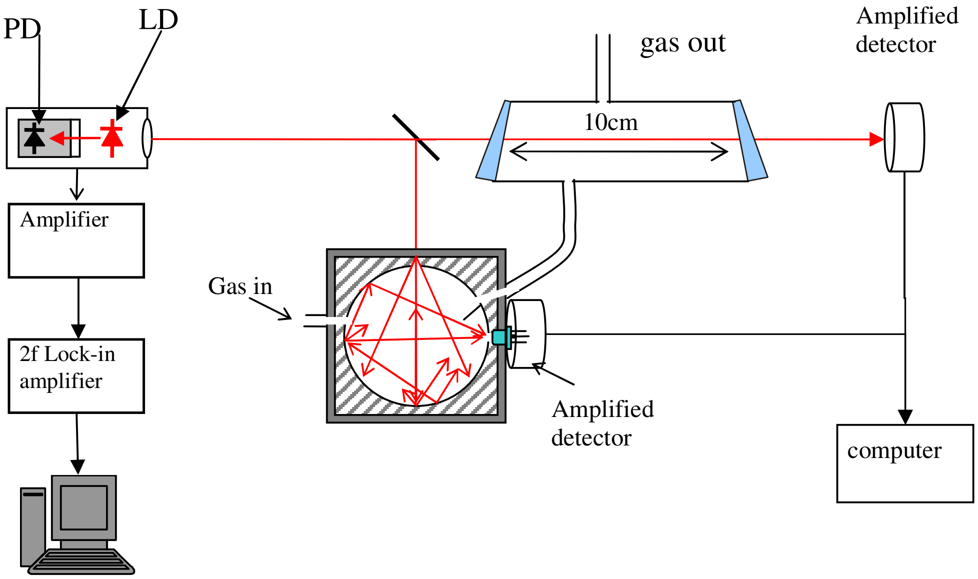

Figure 8-9. Schematic diagram of the experimental setup that was used to determine the effective path length of the integrating sphere. The gas cell series configuration was first used by Abdullin and Lebedev[11].

In one configuration, optical fibre was used to couple light into the sphere. Port plugs with the same inner reflective material (Zenith^{TM}) as the sphere were used to reduce the effective port diameters and thereby increase the effective path length of the integrating sphere. The port sizes (diameters) were as listed below;

1. light entrance port (via adapted port plug)= 1.5mm,
2. gas in port (pipe attached to adapted port plug)= 1.5mm,
3. gas out port (pipe attached to adapted port plug) = 1.5mm,
4. detector port = 1.5mm. Multimode fibre (Thorlabs BFH48-1000) with core diameter of 1mm and 0.48NAwas used.

The values listed above yield $f_{total} = 1.28\times 10^{-3}$. The reflectivity of the sphere at 1650nm was estimated to be $0.983 < \rho < 0.985$ from the manufactures data sheet. The effective path length L was calculated using equation (8.8) to be in the range 183cm < L < 205cm (see in Table 8-3).

Table 8-3: Estimates of effective pathlength calculated for different reflectivities for a 50.8mm internal diameter sphere.

REFLECTIVITY	THEORETICAL MULTIPLIER M	THEORETICAL EFFECTIVE PATH LENGTH
0.983	54	183cm
0.984	57	193cm
0.985	61	205cm

The path length of the 2 inch integrating sphere was determined experimentally as follows. The experimental setup shown in Figure 8-9 was used. The output of the laser was divided by a beam splitter. One path was coupled into an integrating sphere with a diameter of 50.8mm and the other path was directed onto a detector after passage through a 100mm gas cell. Gas inlet and outlet pipes were attached such the sphere and the 100mm cell were connected in series. This ensured that the integrating sphere and the 100mm gas cell were filled with the same gas. The absorption peak was located by adjusting the laser current until the reference transmitted signal was minimum. The detector signal was recorded before (equivalent to I_0) and after (equivalent to I) introducing methane gas of a known concentration into the cells. A sample plot is shown in Figure 8-10.

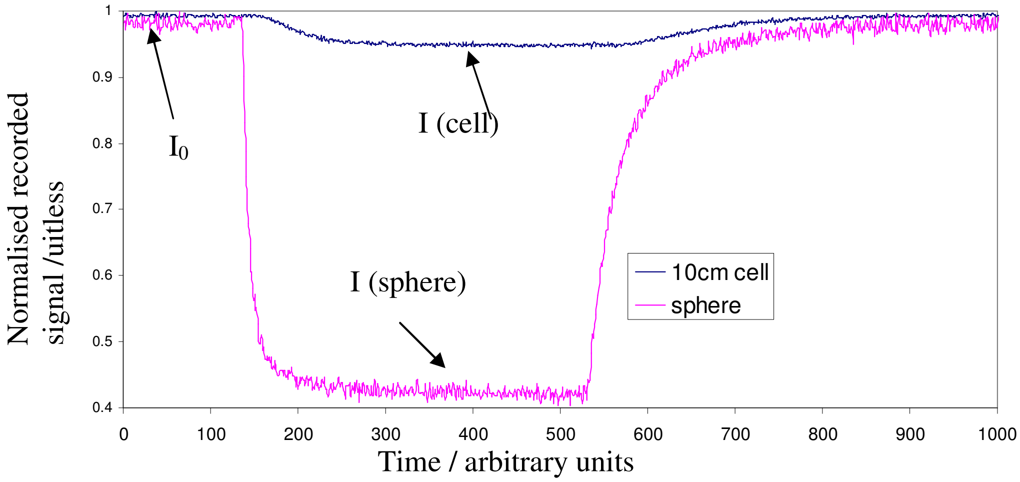

Figure 8-10: Plots of the detector signal corresponding to the transmitted signal in the cell and the sphere. Initially the sphere was full of hydrocarbon free air, 12,500ppm methane was then introduced into the cells.

The recorded signals corresponding to I and I_0 were then used to calculate the Absorbance A, from which the effective absorption path length of the sphere was estimated by applying equation (8.14). A sample of the results is presented in Table 8-4 below.

Table 8-4: Experimentally determined effective absorption path length calculated from simultaneous measurements of absorbance from the 2 inch sphere and a 10cm gas cell for different methane gas concentrations.

CONCENTRATION	A_{cell}	A_{sphere} (2 inch)	L_{sphere} /cm
12,500ppm	0.046	0.85	184
7,140ppm	0.026	0.49	187
12,500ppm	0.051	0.94	183
9,500ppm	0.040	0.72	176
3,500ppm	0.013	0.25	183

For the configuration used the average path length was found to be 183±4mm. This result is comparable to the theoretical path length estimated in Table 8-3 for a reflectivity ρ of 0.983.

Table 8-5 provides port sizes that were typically used to optimise path length as well as throughput of the integrating spheres. Also shown in the table are the expected theoretical effective path lengths.

Table 8-5: Typical port dimensions that were used in the experiments and the theoretical expected path lengths calculated using ρ = 0.983.

Sphere diameter	Practical port sizes	THEORETICAL MULTIPLIER M For ϱ = 0.983	THEORETICAL EFFECTIVE PATH LENGTH
25.4mm	Source = 6.35 Detector =12.7mm Gas in = 1.5mm Gas out = 1.5mm	10.1	170mm
50.8mm	Source = 6.35 Detector =12.7mm Gas in = 1.5mm Gas out = 1.5mm	26	900mm
101.6mm	Source = 6.5 Detector =6.6mm Gas in = 1.5mm Gas out = 1.5mm	51	3440mm

In summary, a method that was used to determine the effective path length of the sphere has been presented. The theoretical and the experimental results were in good agreement.

In section 2.6.1, it was stated that the 2f output is only linear for small concentrations (i.e. $\alpha CL \ll 1$). For the methane line at 1650nm, the product αL ($0.38\text{cm}^{-1} \times 183\text{cm}$) is approximately 70. Therefore for the 2 inch sphere configured as described above (i.e. L = 183cm), the output of the system is expected to be nonlinear at relatively low methane concentrations. This was confirmed by obtaining a plot of the 2f signal against concentration with the sphere configured as above and using a modulation index[*] m = 2.2. The result is shown in Figure 8-11.

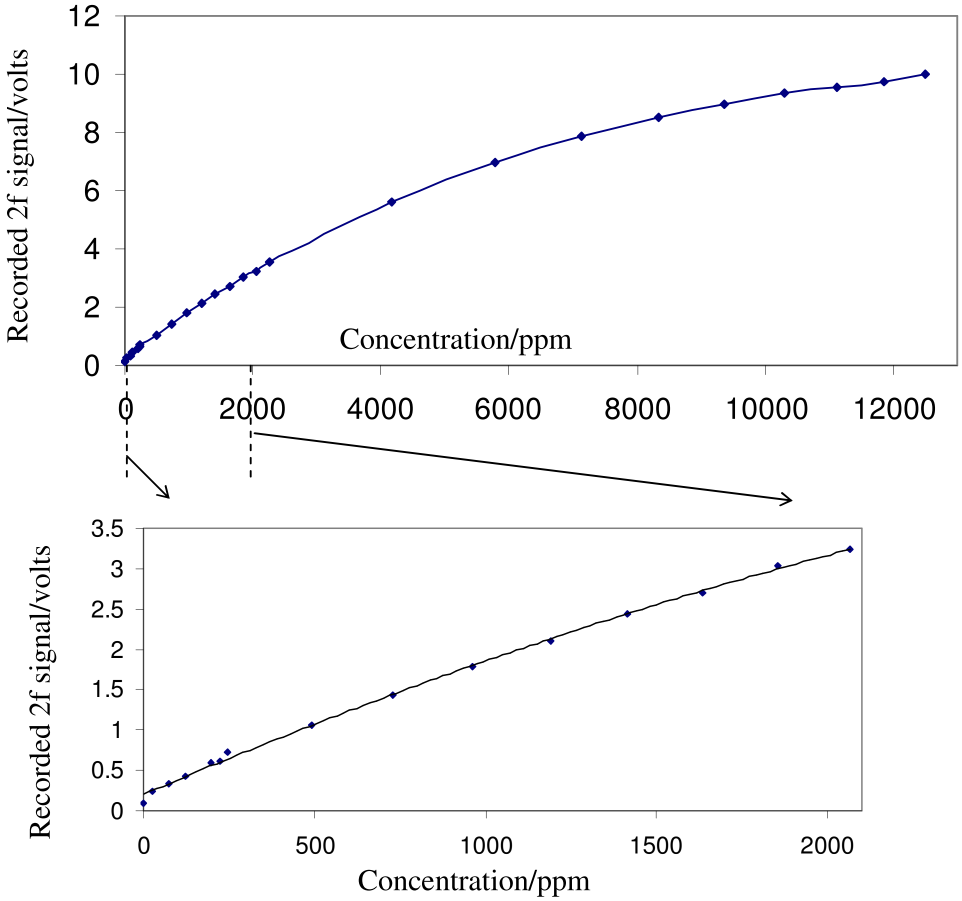

Figure 8-11: (a)Plot of 2f signal against concentration;. (b) Plot of the 2f signal for concentration below 2000ppm extracted from (a). The effective path length was 183cm, m = 2.2 and the detector (PDA400) gain was 40dB.

As expected, Figure 8-11(a) and (b) show that the output is nonlinear at relatively low values of methane concentration. In the next section, a series of experiments conducted to investigate the nonlinear output of the system is reported.

8.4.3 Investigation of nonlinear effects in an integrating sphere

The output of a WMS instrument using the 2f demodulated signal as the system output is taken to be linear by making the assumption that the Beer's law transmittance T

$$T = e^{-\alpha CL} \tag{8-15}$$

can be approximated by

---

[*] Ratio of the modulation amplitude to the half width half maximum of the gas absorption line.

$$T_{approx} = 1 - \alpha CL \tag{8-16}$$

if $\alpha CL << 1$, where α is the absorption coefficient, C is gas concentration and L is the path length over which the light interacts with gas (See section 2.6.1 for detailed theoretical description of WMS). This is justified by the fact that in most practical situations the concentration of the gas being measured is small.

At high concentrations or long path lengths, the assumption no longer holds true, therefore to accurately model the 2f output, the transmittance expression given by equation (8.15) must be used in the WMS formalism. Figure 8-12(a) shows the theoretical plots of equations (8.15), annotated "Beer's law", and (8.16), annotated "approximation", for path lengths of 10cm and 100cm. Equations (8.15) and (8.16) are in agreement only for values of $\alpha CL << 1$. Figure 8-12(b) shows a plot of the percentage error in the reported transmittance associated with using T_{approx} for L =100cm and $\alpha = 0.38\text{cm}^{-1}$.

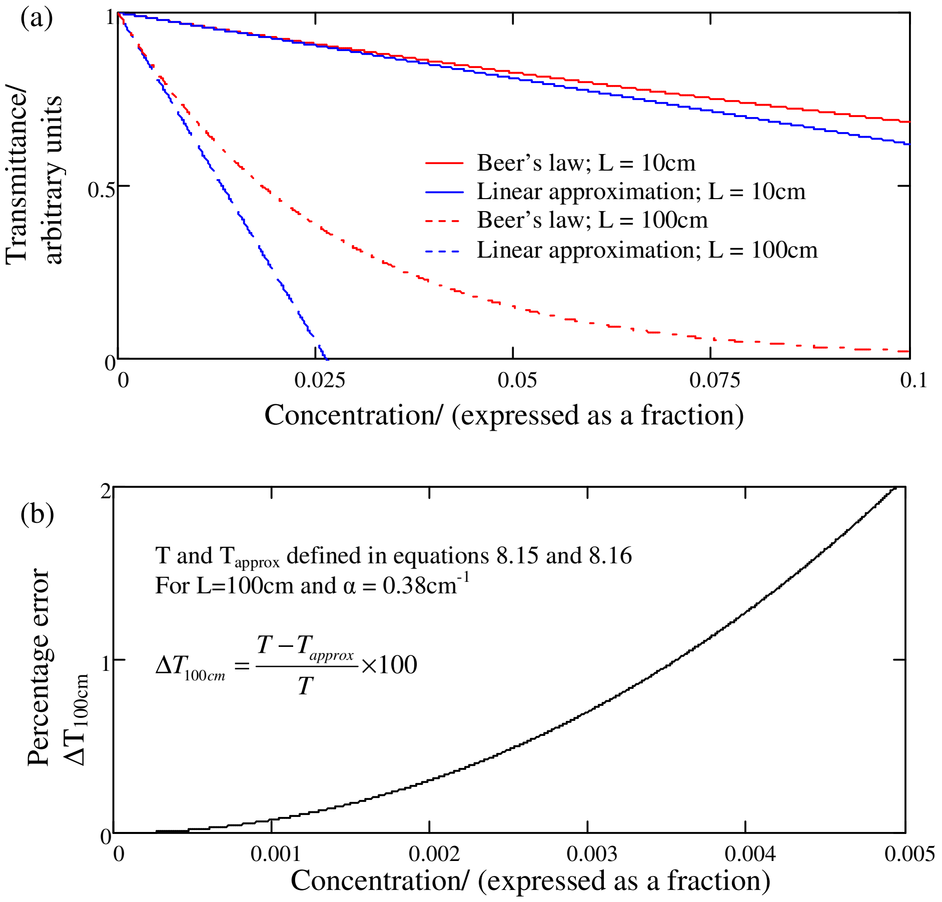

Figure 8-12: Theoretical plots of transmittance using equations (8.15) and (8.6) for path lengths of 10cm and 100cm. $\alpha = 0.38\text{cm}^{-1}$. (b) Plot of error ($\Delta T = T_{approx} - T$) in transmittance against concentration.

In section 8.3 the fractional absorbance in an integrating sphere was given as

$$\frac{\Delta\Phi}{\Phi_{exit}} = \alpha(\upsilon)L_{once}M = \alpha(\upsilon)(2/3D)M \qquad \textbf{(8-17)}$$

Where M was defined as

$$M = \frac{1}{1-\rho[1-\alpha(\upsilon)(2/3D)](1-f_{total})} \qquad \textbf{(8-18)}$$

Which, $\alpha L << 1$ reduces to

$$M_{est} = \frac{1}{1-\rho(1-f_{total})} \qquad \textbf{(8-19)}$$

It is worth pointing out two observations,

1. The multiplier in (8-18) was arrived at by making the small concentration assumption that $e^{-\alpha L}$ can be approximated by $1-\alpha L$. If this condition is not satisfied then the sphere multiplier depends on the gas concentration.
2. There is potentially an error in the path length calculated associated using equations (8-18) and (8-19) which depends on the magnitude of α(ν)(2/3)D.

The experimental setup to characterise the nonlinearity of the integrating sphere is shown in Figure 8-13.

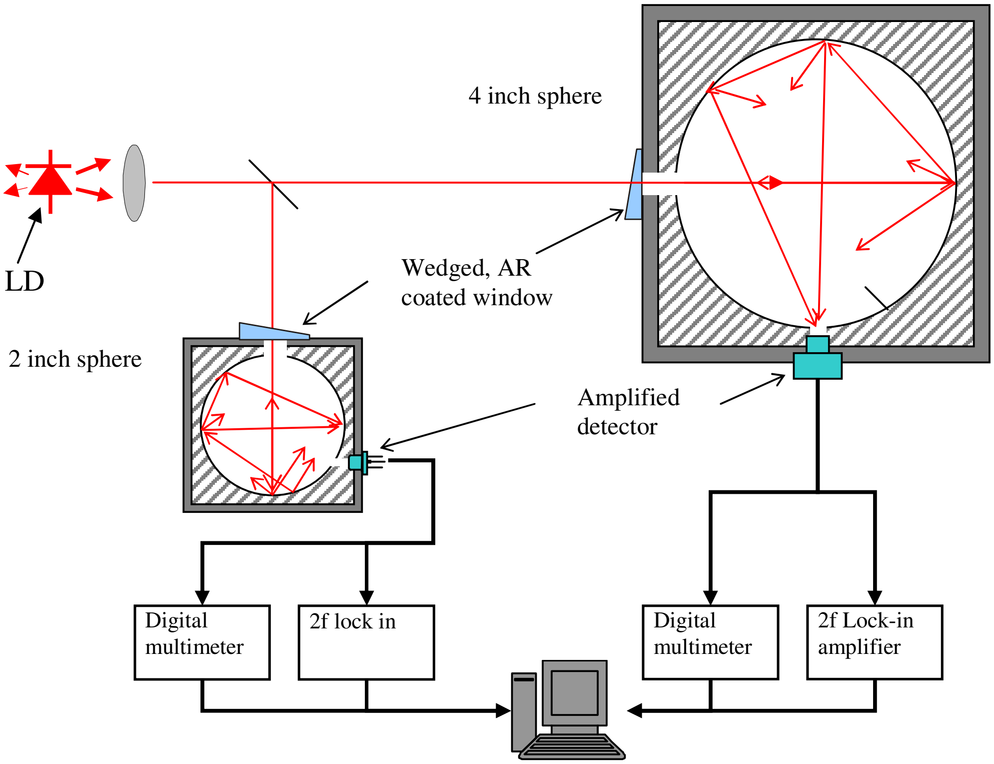

Figure 8-13: Experimental setup used to characterise the nonlinearity of the integrating sphere.

In a first experiment, the integrating sphere nonlinearity was characterised by obtaining a plot of absorbance A (defined as ln(1/T)) against concentration. The detector signal was recorded as the laser emission frequency was slowly scanned (3mHz ramp frequency) across the gas absorption line to obtain a record of the transmitted signal from which I_0 and I could be determined. The scan was performed for gas concentrations in the range 490-12500ppm. The 2 inch sphere was used for this experiment. Figure 8-14 shows direct absorption plots (only a small sample shown for clarity) after normalising with the DC plot obtained with the gas cell filled with hydrocarbon free air.

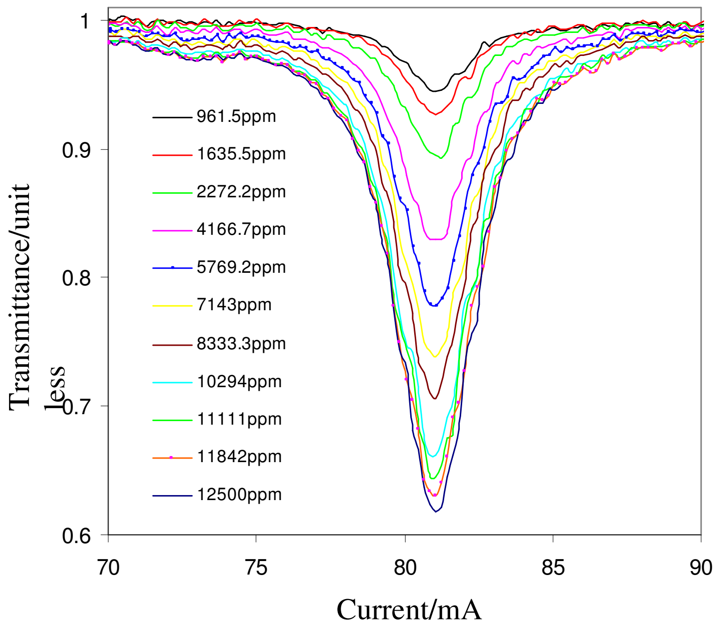

Figure 8-14. Normalised direct absorption signals (transmittance). The detector (Thorlabs PDA400) transimpedance gain was 0dB.

The minima of the normalised plots were taken to be the transmittance (I/I_0). A plot of absorbance A against concentration is shown in Figure 8-15. For comparison, also shown in Figure 8-15, is a plot of peak 2f signal against concentration obtained with the same sphere configuration. The 2f experiment was conducted immediately after the absorbance experiment with no changes made to the experimental setup.

Both the plots of absorbance and 2f against concentration were observed to be nonlinear with the nonlinearity more pronounced in the latter. The nonlinearity is an apparent deviation from Beer's law behaviour, which could be caused by the following effects:

- The path length distribution is non-uniform.
- WMS using 2f as system output is more nonlinear as both the peak height and line shape are affected.

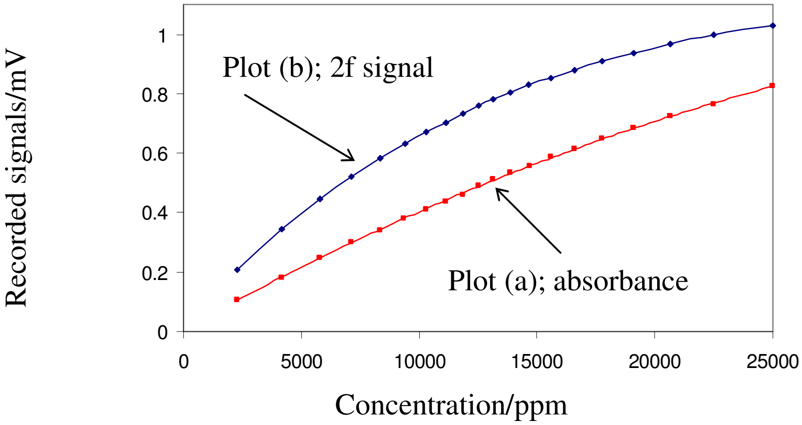

Figure 8-15: Plots of (a) absorbance against concentration (b) 2f signal (m = 2.2) against concentration. The detector (Thorlabs PDA400) transimpedance gain was 0dB (4.7×10^5V/A).

In a second experiment, the 2f output nonlinearity of the 2 inch and 4 inch integrating spheres was characterised using the experimental setup shown in Figure 8-13 in the following manner. The 2f demodulated signals were recorded for different methane concentrations in the range 1000ppm to 2.5% with the laser frequency locked to the peak of the gas absorption line. The 4 inch and 2 inch spheres configured such the expected theoretical path lengths were 344cm and 90 cm respectively (Table 8-5). The results are shown in Figure 8-16.

The demodulated 2f output of both the 2 inch and 4 inch sphere exhibit a response that is nonlinear in concentration. As the experimental data for both plots were obtained simultaneously, the product αC is the same in both cases. Therefore the difference in the response curves can be attributed to the difference in the effective path lengths of the spheres.

In summary, it has been shown that the output of the sphere will be nonlinear. It is expected that the output curvature will depend on the path length distribution which is a function of sphere reflectivity and the port sizes. Therefore for each sphere configuration, a calibration is required. In practical WMS systems calibration is required any way as 2f output is not a direct measure of concentration.

In conclusion, due to the long path lengths, the condition $\alpha CL << 1$ (for which the 2f output is assumed to be linear) is not satisfied at relatively low concentrations in integrating spheres (Figure 8-16(b)). In addition, in an integrating sphere, there are multiple path lengths from entry port to detector port due to multiple reflections. For each path, there is a Beer's law response curve associated with it. Therefore to accurately model the integrating sphere nonlinearity, a model of the path length distribution is required.

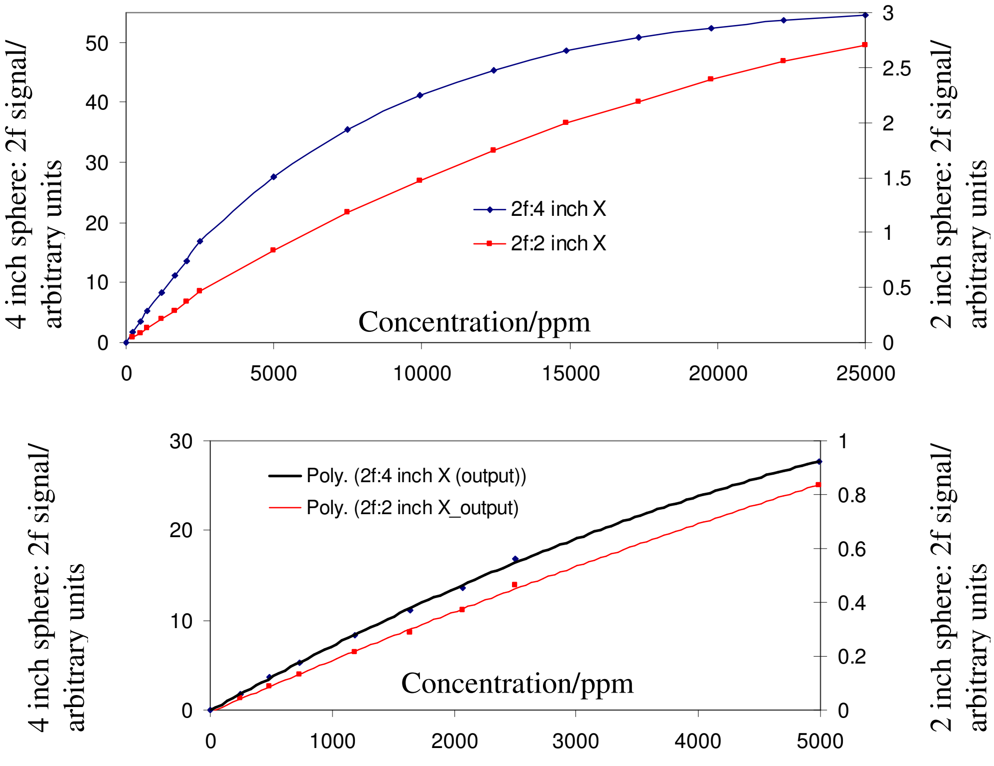

Figure 8-16: (a) Plots showing the nonlinear 2f demodulated output from a 4 inch sphere and a 2 inch sphere. (b) Plots for concentrations below 5000ppm.

8.5 Self mixing interference fringes in integrating spheres

The aim of this section is to investigate the presence of self mixing effects in integrating spheres. Self mixing interference fringes from diffusely reflecting samples were observed in section 6.2.5 using the experimental configuration shown in Figure 8-17(a). The period of the fringes was found to correspond to the distance d between the diffuser and the laser diode. The amplitude of the fringes was found to be proportional to the level of light coupled into the laser cavity. For a perfect Lambertian diffuse reflector, the level of light returned into a small solid angle $\delta\Omega$ is given by

$$r = \frac{3}{4\pi}\rho\left(1+\cos 2\theta\right)\delta\Omega \qquad \textbf{(8-20)}$$

Where ρ is the fraction of light backscattered in total by the diffuser and θ is the angle that the collection axis makes to the normal to the surface.

Integrating sphere surfaces approach perfect Lambertian diffuse reflectors with $F = 0.99$ (for Spectralon$^{\text{TM}}$ and Zenith$^{\text{TM}}$, as used in the experiments). Therefore it is expected that self mixing interference effects will be observed in an integrating sphere if a laser diode were to be mounted onto the sphere as shown in Figure 8-17(b).

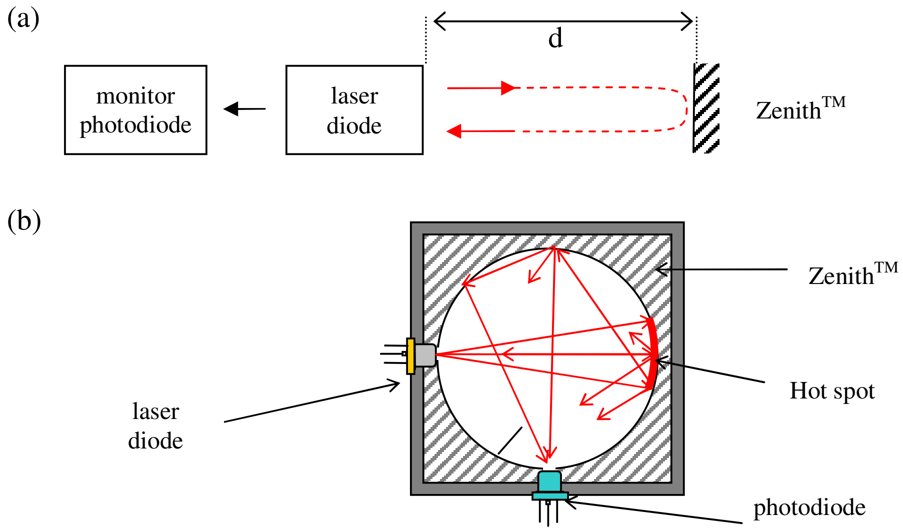

Figure 8-17: (a) Schematic diagram of a typical experimental setup for detecting the self mixing effect using a monitor photodiode integrated in a laser diode package. (b) Schematic diagram of a sphere configuration which may be susceptible to the self mixing effect due to backscatter from the so called "first-strike spot"[14] or hot spot.

In the absence of a hot spot in the integrating sphere, the light coupled into the laser diode would be governed by integrating sphere throughput relations presented in section 8.3. The throughput (in this case light coupled into the laser) of an empty integrating sphere (as arranged in Figure 8-17 (b) is given by equation

$$\Phi_{exit} = \frac{\Phi_{in}}{\pi A_s}\left(\frac{\rho}{1-\rho(1-f_{total})}\right)A_{emitter} \times \Omega \qquad \textbf{(8-21)}$$

Where in this case, $A_{emitter}$ is the emitter area and $\Omega = \pi \sin^2 \theta$. This assumes that the sphere is uniformly illuminated after the first bounce. This assumption is valid in the case of a detector port that can be shielded from the first strike spot by the use of a baffle. However, in the configuration shown in Figure 8-17 (b), the laser diode emitter is not shielded from the first strike spot. Therefore in practice, one would expect that the first strike spot makes a significant contribution to the optical feedback. The system can be approximated by the configuration of Figure 8-17 (a) by assuming that the first strike spot is perpendicular to the collection axis. Therefore it is expected that the level of light fed back into the laser due the first strike spot is approximately given by equation (8-20).

8.5.1 Confirmation of self mixing in integrating sphere with a Fabry-Perot laser diode

A series of experiments was conducted to investigate the occurrence of self mixing interference effects in an integrating sphere in the case of a laser diode directly mounted onto the sphere as shown in Figure 8-17(b). For this set of experiments, a 150mW single longitudinal mode Fabry-Perot laser diode (Spectra Diode Labs 5400 series) emitting at 823nm was used for the following reasons:

1. The module has a photodiode, which was used to monitor the laser emission. Using a detector mounted on the sphere means the measured intensity is affected by multiple scattering effects and speckle related intensity uncertainty.
2. The DFB module would exaggerate the effect in two ways
    - The collimated output leads to an intense first strike spot.
    - The collimating lens also enhances optical feedback as it collects light and focuses it at the emitter facet.
3. The VCSEL has no photodiode. Although the voltage drop across the VCSEL can be used to monitor self mixing effects, the signal to noise ratio is poor (demonstrated in section 6.2.3).

A first experiment was conducted to confirm that self mixing interference fringes could be observed on the monitor photodiode of the Fabry-Perot laser diode in the straight forward case of diffuse reflections from samples of Spectralon^{TM} and Zenith^{TM}. The experimental set up shown in Figure 8-18 was used. The samples of Spectralon^{TM} and Zenith^{TM} were placed at distances of 25.4mm, 50.8mm and 101.6mm. The distances were chosen so that the results could be compared with results from a following experiment in which the diffusive samples were replaced by integrating spheres of internal diameters of 25.4mm, 50.8mm and 101.6mm. The 2f demodulated monitor photodiode signal was recorded as the laser diode was slowly scanned (several mHz) from 95-125mA. This corresponded to a tuning range of 30mA×1.3GHz/maA= 39GHz.

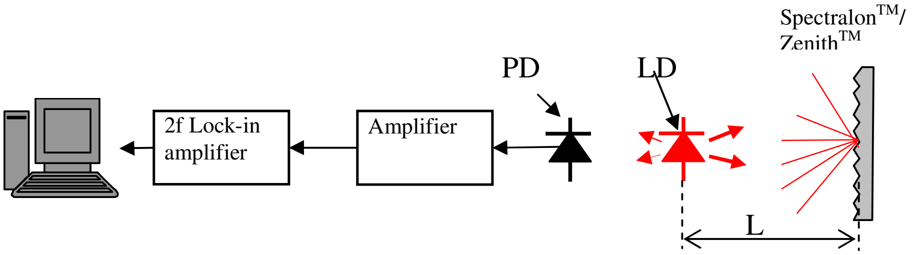

Figure 8-18: Schematic diagram of experimental setup for investigating optical feedback from diffusive samples (Spectralon^{TM} and Zenith^{TM}) placed at distances L (25.4mm, 50.8 and 101.6mm) from the laser.. Key; PD: photodiode, LD: laser diode.

The results from the experiment using the diffusive samples are presented in Figure 8-19.

The results are consistent with interferometric fringes due to self mixing. A quantitative analysis of the fringes is presented in Table 8-6. Similar results were obtained in the case of Spetralon^{TM} and Zenith^{TM}.

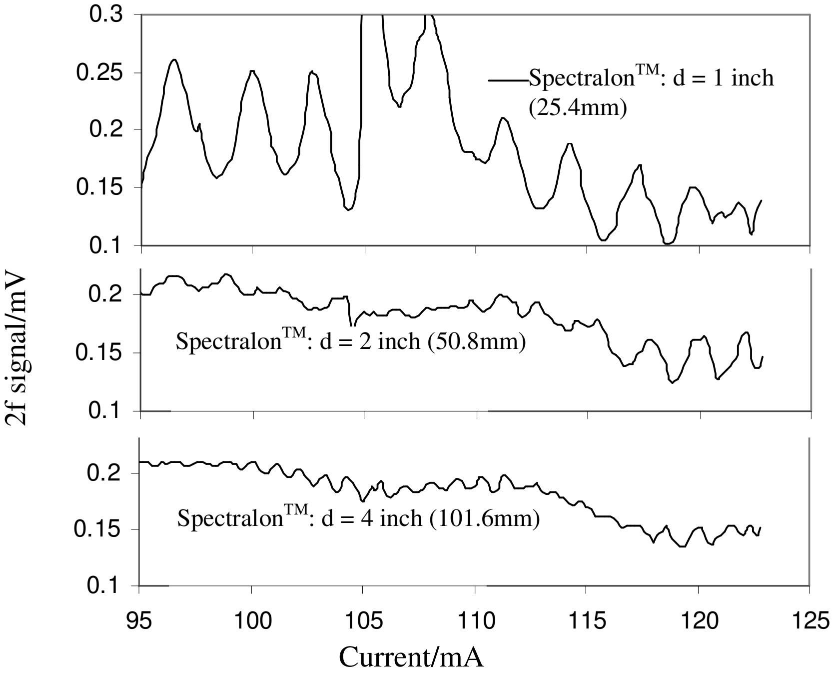

Figure 8-19: Self mixing interference fringes detected at the monitor photodiode. Fringes caused by optical feedback from a sample of Spectralon^{TM} placed at distances d (24.5mm, 50.8mm and 101.6mm) from the laser.

Table 8-6: Quantitative analysis of the self mixing interference fringes.

Distance d_{exp} from diffuser to laser /mm	**25.4**	**50.8**	**101.6**
Current range / mA	95-120	95-120	95-120
No of fringes	8±2	11±2	22±2
calculated cavity length d_{calc} / mm	36±12	49.6±15	99.2±26

This was taken as confirmation that the Fabry-Perot laser diode was suitable for conducting investigations of self mixing interference effects in the integrating spheres.

In a second experiment the laser was directly attached to the sphere input port as shown in Figure 8-20. A detector/amplifier (Thorlabs PDA400) was attached to a port orthogonal to the input port. A baffle, located between the source and detector port prevented the laser emission from directly impinging on the detector. The detector and monitor photodiode outputs were recorded simultaneously as the laser operating DC current was ramped from 95mA-125mA.

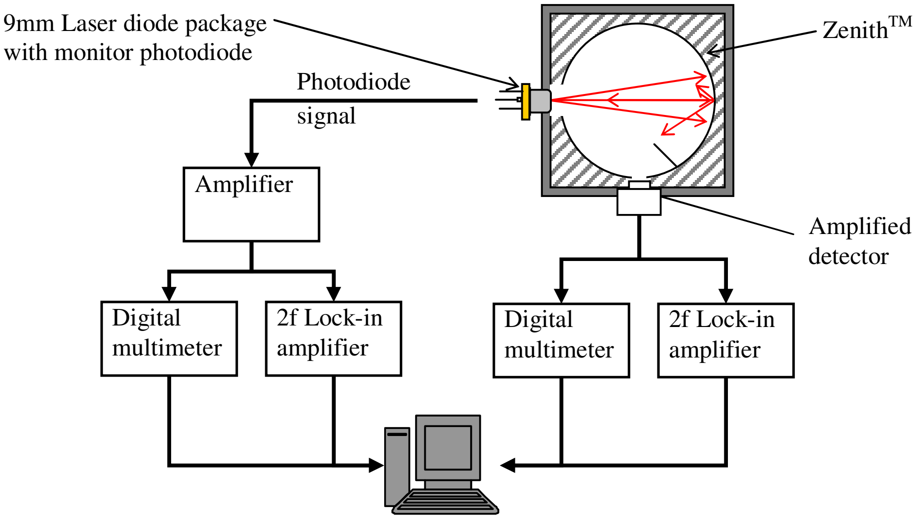

Figure 8-20: Schematic diagram of experimental setup for investigating optical feedback from integrating spheres of diameters (25.4mm, 50.8 and 101.6mm) from the laser.

Figure 8-21 shows the demodulated monitor photodiode output for the three integrating spheres.

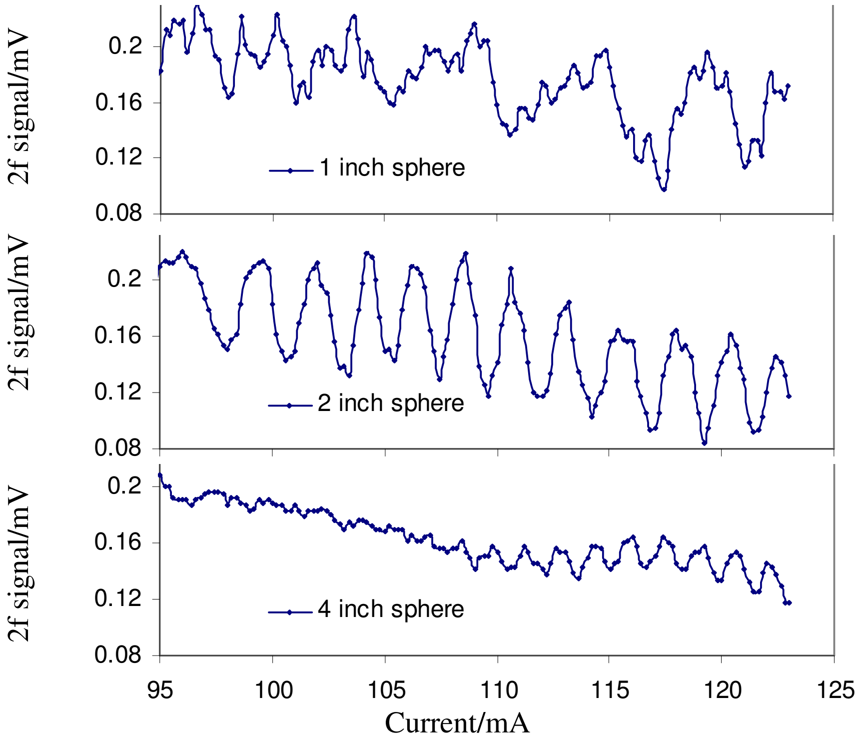

Figure 8-21: Normalised self mixing interference fringes detected at the monitor photodiode. Fringes caused by optical feedback from integrating spheres of diameters; 24.5mm, 50.8mm and 101.6mm.

In the case of the 2 inch and the 4 inch integrating spheres, interference fringes with a FSR corresponding to the diameter of the integrating sphere were obtained (Table 8-7).

The results are consistent with the behaviour of self mixing interference fringes. In the case of the 1 inch integrating sphere, the recorded plot appeared to have two distinct frequency components (Table 8-7). The lower frequency fringe could be attributable to self mixing from the first strike spot. The source of the higher frequency fringes is uncertain.

Table 8-7: Quantitative analysis of the self mixing interference fringes.

Sphere diameter/mm	**25.4**		**50.8**	**101.6**
	Period 1	**Period 2**		
Current range / mA	95-120	95-120	95-120	95-120
No of fringes	6±1	22±5	11±1	17±3
FSR/mA	4.2±0.7	0.93±0.2	2.3±0.2	1.1±0.1
Laser current tuning (DC) / GHz/mA	1.33±0.3	1.33±0.3	1.33±0.3	1.33±0.3
FSR / GHz	5.5±1.6	1.2±0.4	3±0.7	1.5±0.4
calculated cavity length d_{calc} / mm	27±2.6	122±35.5	49.6±11	81.1±22.8

Figure 8-22 shows a comparison of the monitor photodiode signals (previously shown in Figure 8-21 and the amplified photo detector signals obtained simultaneously.

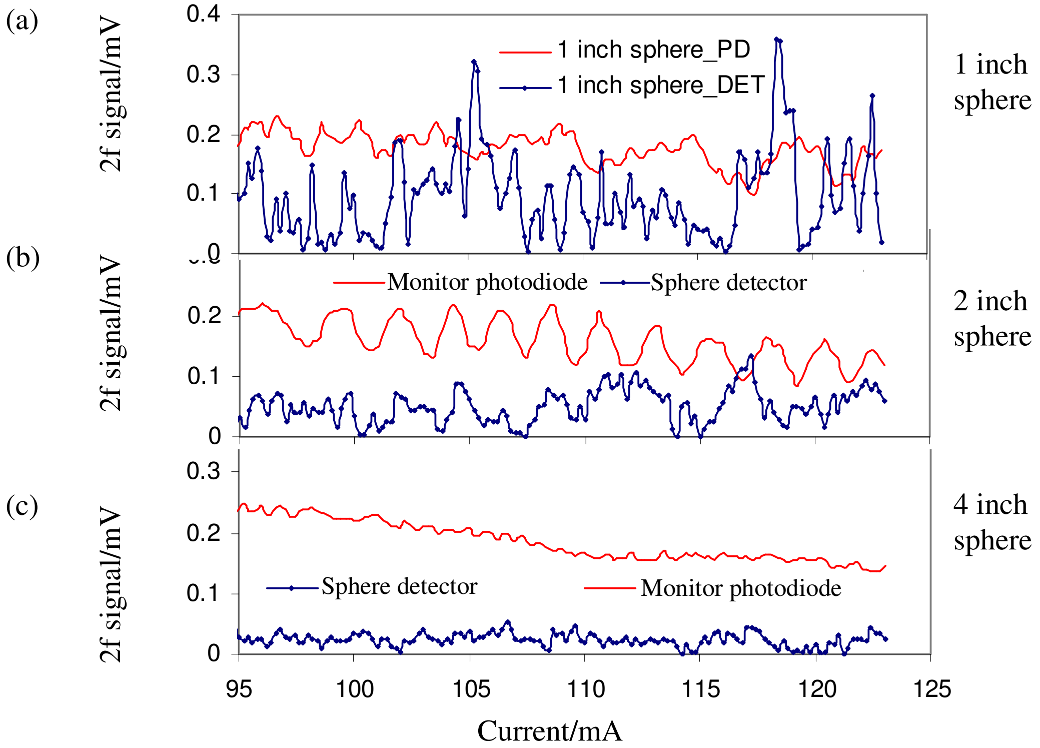

Figure 8-22: Self mixing interference fringes detected at the monitor photodiode. Fringes caused by optical feedback from integrating spheres of diameters; (a) 25.4mm, (b) 50.8mm and (c)101.6mm.

In the case of the 2 inch and 4 inch spheres, the signals recorded at the photo detector mounted onto the sphere appear to be “scrambled” versions of the signals recorded at the monitor photodiode. The washing out of the periodicity could be attributable to the effects of speckle noise or multiple scattering or a combination of both. Similarities between the signals obtained from the 1 inch sphere were not obvious.

The following section reports experiments investigating self mixing effects in a 2 inch integrating sphere using the DFB laser with the collimated output.

8.5.2 Self mixing with DFB laser

The experimental setup was arranged as shown in Figure 8-23. The approximate distance from the laser to the ‘first strike spot’ was approximately 10cm. The first strike spot is effectively the port directly opposite the entry port. This will be referred to as the 180 degree port (annotated in Figure 8-23).

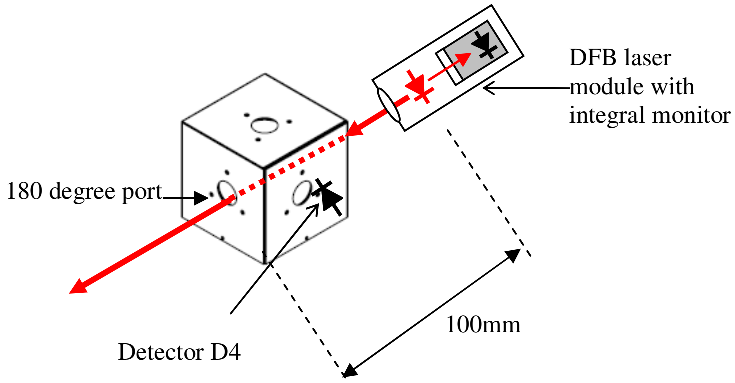

Figure 8-23: Experimental setup for investigating the self mixing effect in the 2 inch integrating sphere.

Plots of the monitor photodiode and detector D4 signals were recorded simultaneously in the presence and absence of feedback from sphere. This was achieved by locating the sphere at distances of 10cm and >1m from the laser respectively. The field of view and therefore the amount of light arriving at D4 was controlled by a calibrated iris diaphragm (variable from 1mm to 12mm with a resolution of 0.5mm). The detector D4 signals was recorded for 1mm and 10mm aperture.

Figure 8-24 shows the normalised 2f plots of the monitor photodiode signal with and without feedback. The plot obtained in the presence of feedback from the sphere is consistent with self mixing interferometric fringes (calculated cavity spacing = 104±6mm).

A similar result (to Figure 8-24) was obtained when the reference signal (monitor photodiode) was recorded with the 180 degree port open with laser located 10cm from sphere first strike spot (Figure 8-23). This was effectively recording the reference signal with no external feedback as the collimated beam is transmitted straight through the sphere (beam diameter < 8mm and sphere port= 12.7mm). The reference signal was then recorded with the 180 degree port plugged (i.e. with feedback from the sphere). The port plug was made of the same material as the sphere interior.

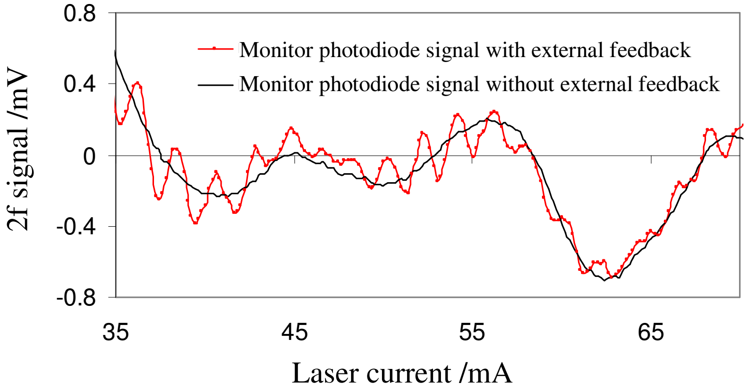

Figure 8-24: Reference monitor photodiode signals. (a) no external feedback, obtained with entry port and 180 degree port open. The plot with external feedback obtained with 180 degree port closed with SpectralonTM port plug. (b) The normalised plots of figure (a). The laser temperature was set at 40 degrees (off the gas line).

The plots of the 2f demodulated output of detector D4 obtained with and without feedback are shown in Figure 8-25(a) and (b) respectively. The plots corresponding to "without feedback" in Figure 8-25(b) were recorded with 180 degree port plugged, but with laser located a distance of greater than 1 metre from laser.

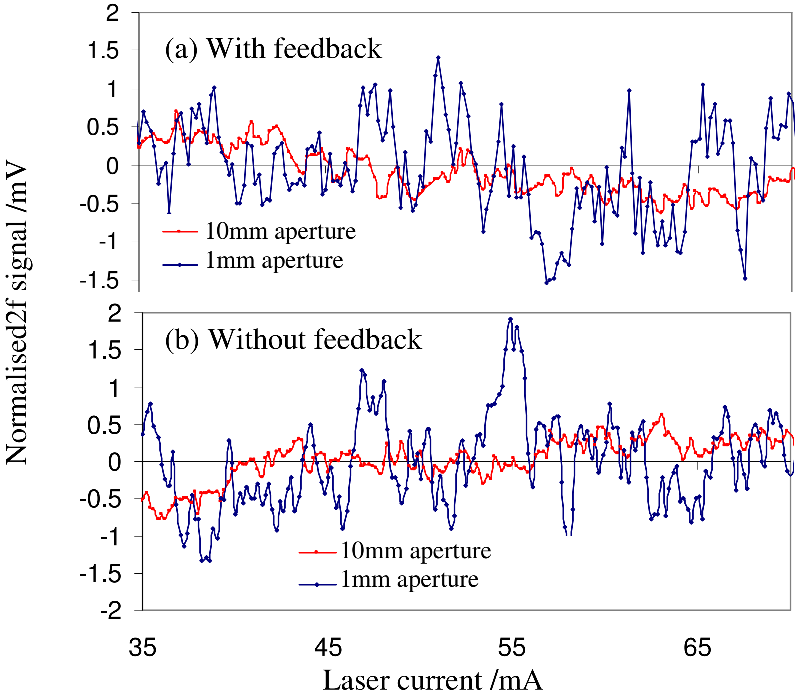

Figure 8-25: 2f demodulated signals obtained from D4 with 1mm and 10mm apertures placed on detector. Signals recorded at detector D4 (a) in the presence of feedback from the sphere (b) in the absence of external feedback. PDA400 gain = 40dB.

Both the plots (with and without feedback) exhibit a comparable intensity uncertainty that is not periodic in phase as the signal detected at the monitor photodiode. However, the intensity uncertainty is lower in the case of the plots obtained with a large aperture (i.e. 10mm).

The result shown in Figure 8-22 and Figure 8-25 are consistent with multiple reflections or speckle related intensity uncertainty in the sphere causing a reduction in the contrast of interference fringes. This hypothesis was tested in the following section.

8.5.3 Effect of integrating sphere on fringe visibility

The principle of the test involved coupling into the sphere an interferometric signal with "good" fringe visibility or contrast. By comparing the contrast at the entry port (before entering the sphere) and at the exit port, the effects of the sphere on fringe visibility could be observed.

The effect of the integrating sphere on self mixing signals was investigated by using a modified experimental setup of Figure 8-23 as shown in Figure 8-26 below.

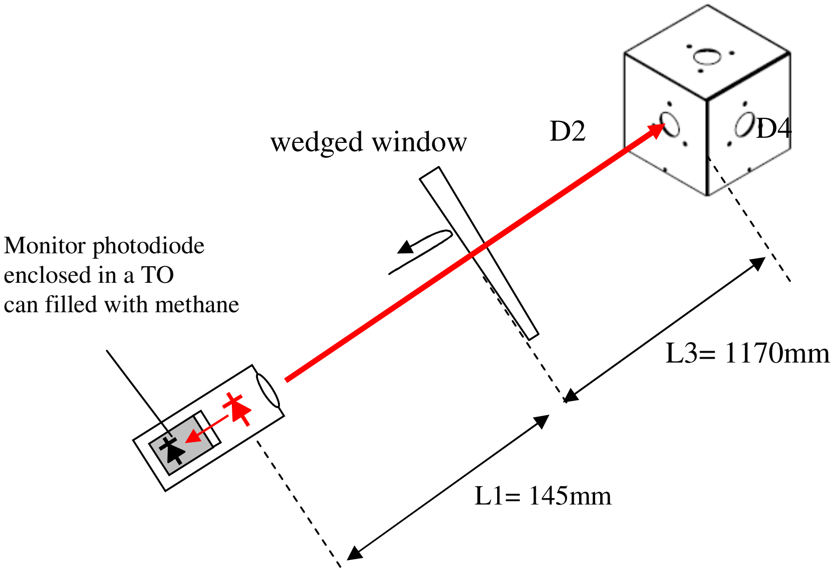

Figure 8-26: Experimental setup for investigating the effect of the sphere on externally generated interferometric self mixing signals.

An uncoated wedged window was placed in the path of a collimated DFB laser beam. The Fresnel reflection from an uncoated wedged window (4%, reflectivity of BK7 at 1650nm) was directed into the laser and the transmitted beam was coupled into the sphere via an open port (entry port hereinafter). The reason for this arrangement was to generate an interferometric signal that was large in magnitude in comparison to the intensity uncertainty recorded at detector D4. As a precaution, the sphere was deliberately located a long way from the laser (> 1 metre) to minimise the effects of scattering from components placed at the entry port or the sphere external surface.

An integral monitor photodiode was used to monitor the DFB laser emission to confirm the Fresnel reflection from the wedge induced self mixing interference fringes. A detector D2 (Thorlabs PDA400) could also be placed between the wedged window and the sphere to monitor the signal entering the sphere. A second amplified photo detector D4 was directly mounted onto the integrating to monitor the sphere throughput.

The plots of the demodulated 2f monitor photodiode and detector D2 outputs are shown in Figure 8-27. The results are consistent with self mixing interference fringes (calculated fringe period = 169±13mm).

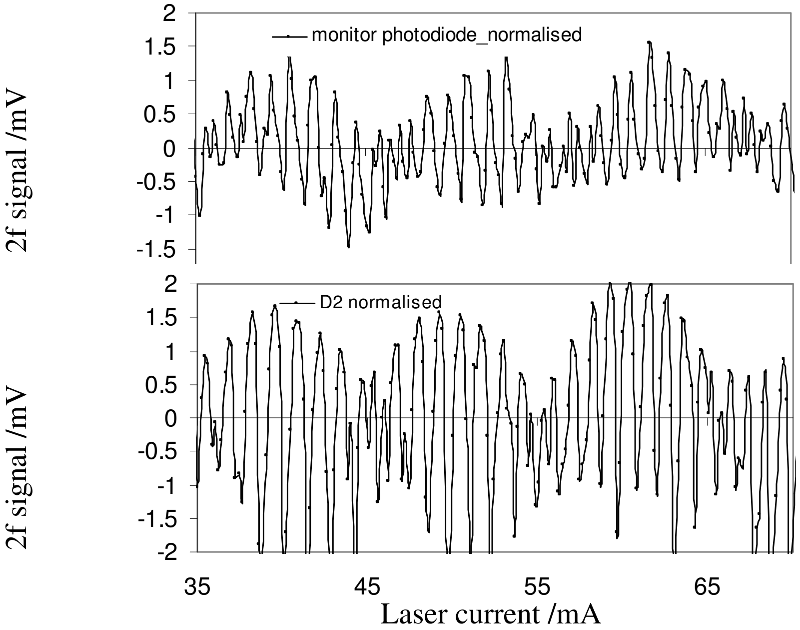

Figure 8-27: Confirmation of the presence of self mixing interference fringes due to Fresnel reflection from a wedged window. (a) Monitor photodiode signal. (b) Detector D2 placed in the path of the transmitted beam between wedged window and the integrating sphere.

Signals from detector D4 were obtained in the presence external feedback from the wedge for the following aperture sizes; 1mm, 5mm, and 10mm and also with no aperture on the sphere port (i.e. detector with a field of view of approximately 180 degrees). The results are shown in (Figure 8-28). As the aperture or field of view of the detector increases, the visibility of fringe signal improves (Figure 8-28).

One possible explanation is that when the amount of light arriving at the detector is relatively low or when the detector field of view is small, the interference signal is dominated by intensity uncertainty due to laser intensity noise, RIN or speckle noise. This uncertainty reduces the fringe contrast.

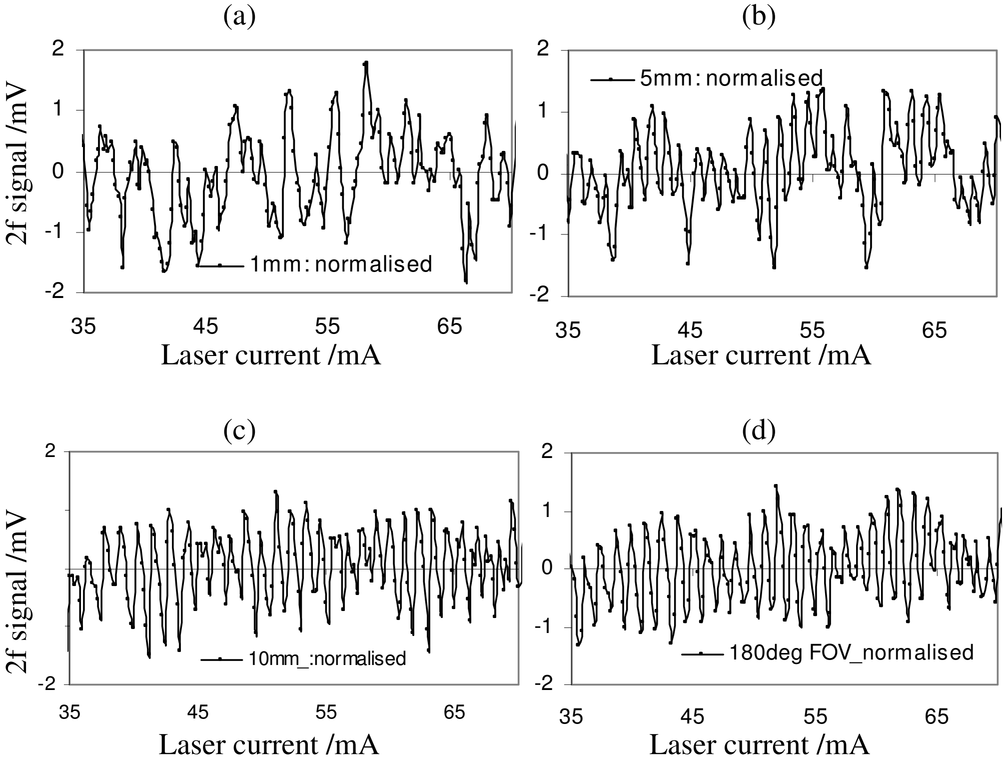

Figure 8-28: Second harmonic signals obtained from D4 for various aperture sizes (a) 1mm. (b) 2mm. (c) 5mm. (d) 8mm. (e) 10mm. Detector PDA400 gain = 40dB.

The following section reports experiments that were conducted to investigate the implications of self mixing effects for gas absorption measurements using integrating spheres.

8.5.4 Use of the 1650nm VCSEL with the 2 inch integrating sphere

The results reported this section were obtained in collaboration with Dr Stephane Shilt[*]. The experiments involved conducting gas absorption experiments using a VCSEL (Vertilas type VL-1651-1-SP-T5, # XLXR-RSOA-SLSE-F) and a 2 inch integrating sphere. The VCSEL and an amplified photo detector (Thorlabs PDA400) were mounted on the sphere as shown in Figure 8-29. The theoretical path length in this configuration was estimated to be 90cm.

In a first experiment, plots of the 2f signal corresponding to 100ppm CH4 concentration and background signal were obtained by locking the laser emission frequency to the peak of the gas absorption line and current tuning the VCSEL from 2-6mA. The results are shown in Figure 8-30.

---

[*] Project manager at IR Microsystems (IRM). Originally a spin off company from Federal Institute of Technology (EPFL) in Lausanne, Switzerland. IRM is now part of Leister Process Technologies, Switzerland.

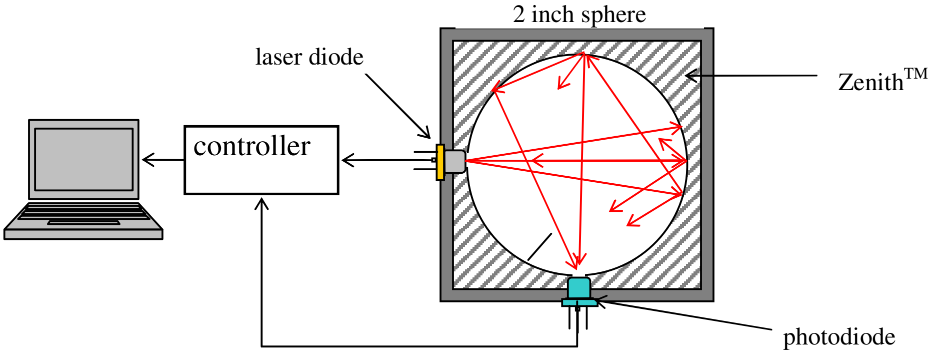

Figure 8-29: Scheme of the experimental set-up used with the VCSEL laser.

The effective path length was determined by comparing the normalised 2f peak signal from the integrating sphere to that of a standard cell of a known path length (16cm). The normalized signal was calculated by dividing the measured 2f signal by the detector DC signal at the centre of the CH_4 line. A signal enhancement by a factor ~5.4 was obtained compared to the 16cm cell corresponding to an effective pathlength of 86 cm in the sphere (Figure 8-30(a)).

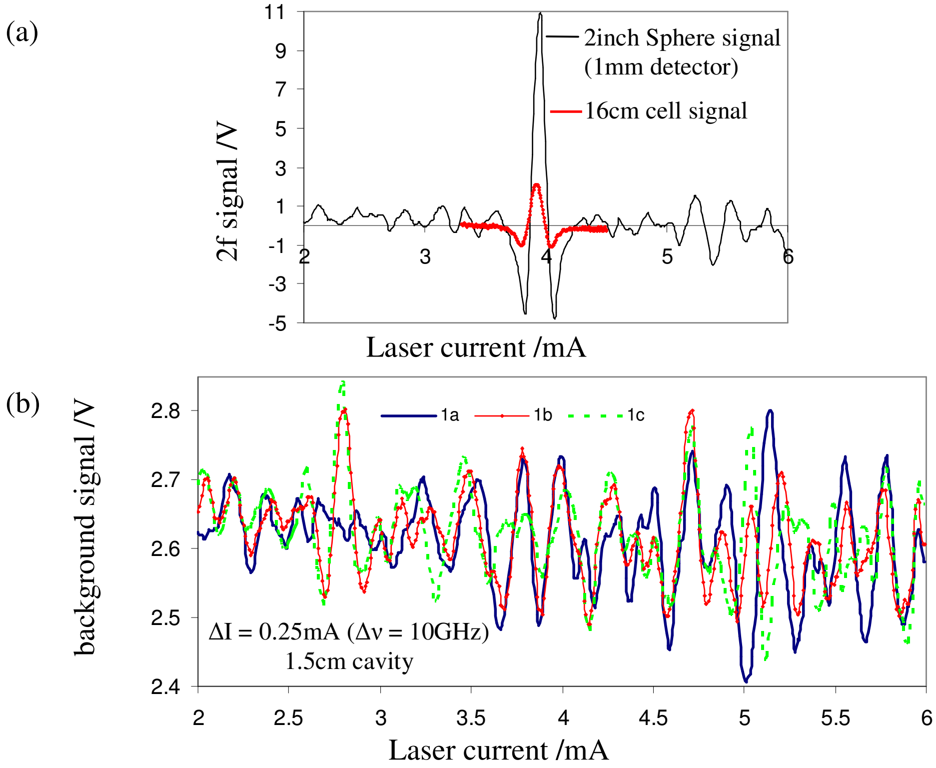

Figure 8-30: Comparison of the CH4 [100ppm] signals in a 16cm cell and in the sphere. (a) 2f signals normalised by D.C component, offset subtracted. (b) Successive background signals. Laser temperature = 22.5°C, Detector PDA400 gain = 10dB.

An interference fringe like pattern was observed superimposed on the background signal. Successive measurements of the background signal were then performed to analyze the fringe pattern. The interference fringe signal was observed to be irreproducible, but a general trend was observed in each measurement, showing a rather periodic structure with a period of ~10 GHz, corresponding to a "cavity" of ~1.3 cm (see Figure 8-30.(b)). This result was unexpected as the source of such a cavity is not immediately apparent from examining Figure 8-29. The detector was recessed such that there no direct line of sight to the VCSEL.

In a second experiment, the Ø1mm detector was replaced with a large area germanium detector (PDA50B-EC, Ø5mm). The rest of the system (as set up in the first experiment) was left undisturbed and the experiment repeated. The results are shown in Figure 8-31.

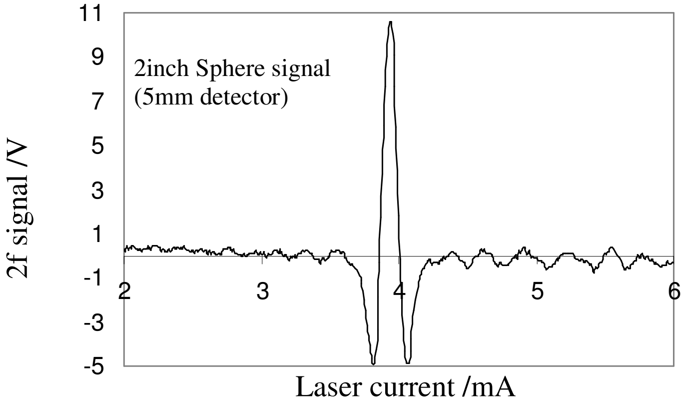

Figure 8-31: Plot of the 2fsignal corresponding to CH4 [100ppm] signals in the sphere. (a) 2f signals normalised by D.C component, offset subtracted. Laser temperature = 22.5°C, Detector (PDA50B-EC, Ø5mm). Gain = 10dB.

In the case of the large area detector, the signal was more noisy (detector noise), but the contrast of the fringes was reduced compared to the Ø1mm detector ((Figure 8-30(a)). The same effective path length (86cm) was obtained as in the previous experiment.

8.5.5 Discussion.

The occurrence of interference effects in integrating spheres has been investigated. Self mixing interference fringes were observed in the case of a DFB laser and a Fabry-Perot laser diode. Although periodic signals were also observed in the case of the VCSEL it was difficult to establish conclusively that the observed fringes/signals were due to the self mixing effect due to the lack of monitor photodiode in this type of package.

In an experiment in which a VCSEL was directly mounted on a 2 inch integrating sphere (path length approximately 100cm), the magnitude of the background signal (thought to be a self mixing interferometric signal) was found to correspond to a signal from 9ppm methane (Figure 8-30).

In experiments using the collimated DFB laser, the self mixing signal generated by reflection by backscatter from the integrating sphere were easily detectable on the monitor photo diode signal (Figure 8-24). However, the intensity uncertainty on the signal recorded at the sphere output port D4 in the absence of external optical feedback was on the same scale as in the case of self mixing (Figure 8-25). As a consequence, the signals recorded at D4 in the presence of feedback from the sphere appear to be dominated by this intensity noise (Figure 8-25) for all aperture sizes used in the experiment.

On the other hand, the self mixing signal caused by reflection from the wedged window was clearly visible at the sphere output, D4, for large apertures (Figure 8-28). This was possibly because the signal was larger than the intensity noise recorded in the absence of feedback (Figure 8-25(b)).

It appears that for small apertures at D4, there was a significant amount of intensity uncertainty (Figure 8-25(b)). This could be due to speckle noise or laser intensity noise or a combination of both. The case for speckle noise is supported by the fact that the intensity noise is significant even in the absence of external optical feedback. Furthermore, the uncertainty was observed to reduce with increasing field of view of detector (Figure 8-25) or using a large are detector (see Figure 8-30 and Figure 8-31).

It is worth pointing out at this point that because of the optical feedback effects within the DFB module, it is not possible with this module to distinguish speckle related intensity from intensity noise (RIN) due to optical feedback from within the module.

In the case of the DFB laser with a collimated output, feedback from the sphere was found to be negligible if the sphere was located at distances greater than 1 metre from the laser. Precautions should be taken to avoid feedback from the collimating optic.

For sources directly mounted onto the sphere, as in the case of the Fabry-Perot laser and the VCSEL, a practical means of reducing optical feedback from the sphere is use of an isolator. At NIR wavelengths, small isolators (size comparable to aspirin tablet) are commercially available due to large Verdet[*] constant and high transmission of some materials (e.g. bismuth-iron-garnet has transmission of >96% at 1550nm and 30-50% between 750 and 850nm). In practice, the effectiveness of the isolator will be limited by the residual Fresnel reflectivity of the isolator aperture window facing the laser diode.

8.6 Gas absorption measurements/sensitivity limits

This section reports a number of gas absorption experiments that were conducted using the 2 inch and the 4 inch integrating spheres with the collimated DFB laser as the source. The experimental set up that was used is shown in Figure 8-32. The modulated

---

[*] The magnetic field, ***B***, applied to the Faraday rotator causes a rotation in the polarization of the light due to the Faraday effect. The angle of rotation, β, isdirecIty proportional to the Verdet constant

output light of a frequency stabilised DFB laser was coupled into the integrating sphere via a wedged and AR coated window located at the entry port. The output of a detector amplifier (Thorlabs PDA400) which was directly mounted on the sphere was fed to a lock-in amplifier (Stanford Research Systems SR850) for phase sensitive detection at 12kHz (2f) and digital multimeter for recording the DC output. The multimeter and lock-in amplifier signals were transferred to a computer running Labview^{TM} software via GPIB to high speed USB cable.

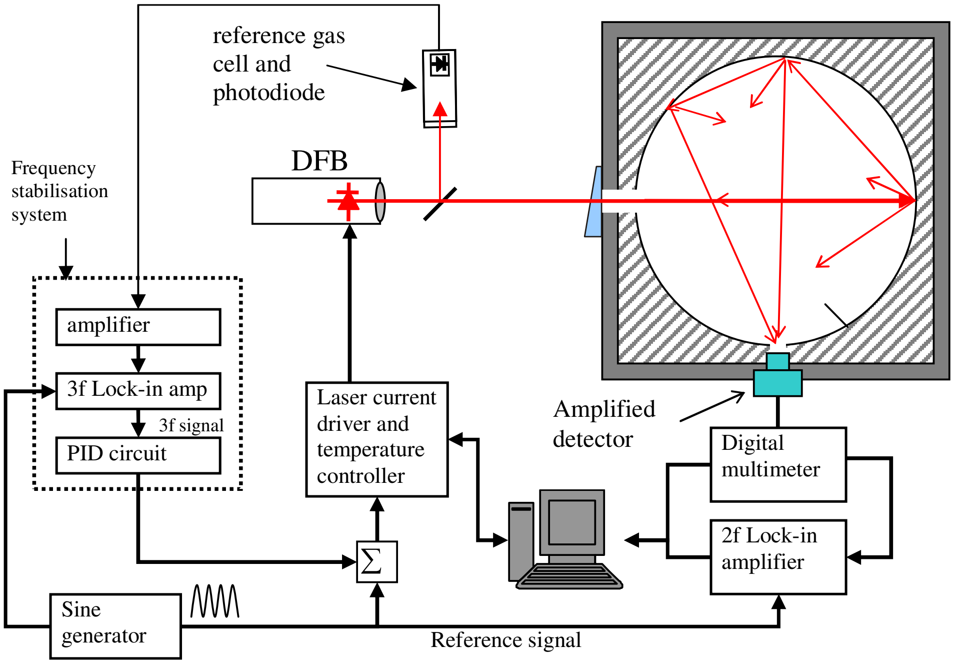

Figure 8-32: Scheme of the experimental set-up used for conducting gas absorption experiments using integrating spheres.

8.6.1 Gas absorption experiments using a 2 inch sphere

In a first experiment plots of the 2f signal corresponding to 500ppm CH_4 concentration and background signals were obtained by setting the DC current at 65mA and temperature tuning the laser. The sphere configuration yielded an effective path length of approximately 100cm. The results are shown in Figure 8-33. The detection limit was determined to be approximately 8ppm. This was calculated by dividing the standard deviation of the background signal by the peak 2f signal and multiplying the quotient by 500ppm.

In a second experiment the laser emission frequency was locked to the peak of the absorption line. The peak 2f was recorded for different concentrations; methane (1010ppm concentration) was gradually diluted with hydrocarbon free air using gas flow controllers (Telydyne THPS-400-230). The recorded demodulated 2f output was plotted against concentration (Figure 8-34).

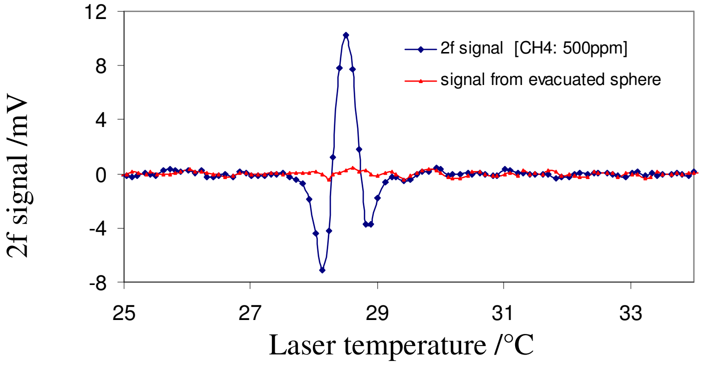

Figure 8-33: Plots of CH_4 (500 ppm) and background 2*f* signals observed with a direct coupling of the DFB laser beam into the sphere. I_{DC} = 65mA. PDA400 gain = 0dB, lock-in amplifier time constant = 100mS, power in = 14mW

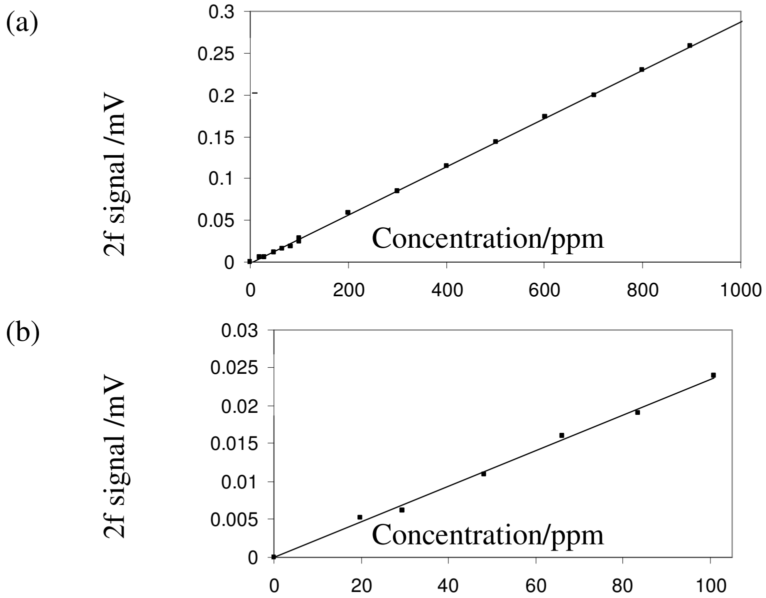

Figure 8-34: Plots of 2f signal against concentration obtained with the 2 inch integrating sphere configured for a pathlength of approximately 100cm. (a) 2f signal for concentration in the range 0-1000ppm. (b) 2f signal for concentration in the range 0-100ppm.

In this configuration (effective path length = 100cm), the output appears to be linear for concentrations below 1000ppm.

The following section reports gas absorption experiments conducted using the 4inch internal diameter integrating sphere.

8.6.2 Gas absorption experiments using a 4 inch sphere

In a first experiment plots of the 2f signal corresponding to 50ppm CH_4 concentration and background signals were obtained by ramping the laser operating current from 40-75mA at a fixed operating temperature. The theoretical effective path length was estimated to be 344cm. The results are shown in Figure 8-35. The detection limit was determined to be approximately 1.6ppm. This was calculated by dividing the standard deviation of the background signal by the peak of the 2f signal and multiplying the quotient by 50ppm.

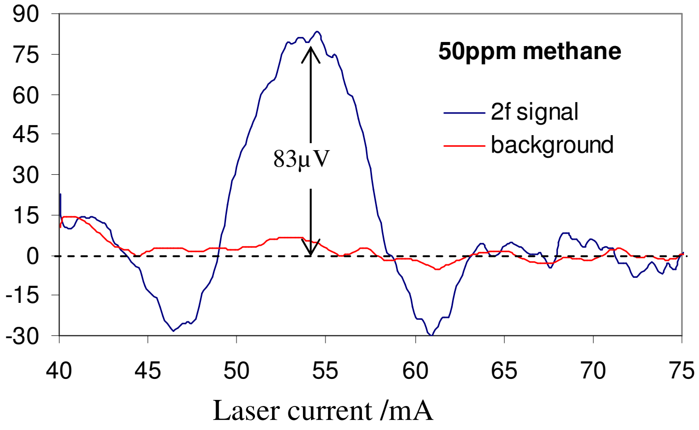

Figure 8-35: Plots of CH_4 (50 ppm) and background 2*f* signals observed with a direct coupling of the DFB laser beam into the sphere. PDA400 gain = 0dB, lock-in amplifier time constant = 100mS.

In a second experiment, the laser diode output was locked to the methane line and 2f-demodulated output was recorded whilst different methane concentrations (0ppm, 25ppm and 50ppm) were delivered to the cell. Figure 8-36 shows the 2f demodulated output plotted as a time series against different methane concentrations. A quantitative analysis of the plot is presented in Table 8-8.

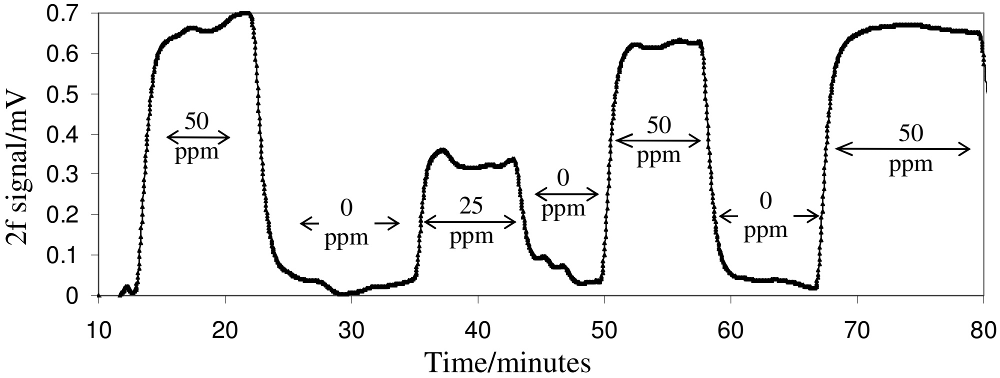

Figure 8-36: Normalised 2f-demodulated output from detector plotted as a time series while different methane concentrations (in air) were delivered to the gas cells. (Lock-in τ 10s.)

Table 8-8: The SNR was calculated by dividing the background corrected methane signal by its standard deviation.

	50ppm	25ppm
Mean	0.66	0.33
Standard deviation	0.01	0.014
SNR	66	24
Detection limit	0.5ppm	0.35ppm

The detection limit was estimated to be 0.4ppm.

In a final experiment to determine the detection limit of the system, the laser diode output was locked to the methane line and 2f-demodulated output was recorded while different methane concentrations were delivered to the integrating sphere. Figure 8-37 shows a plot of 2f signal against concentration.

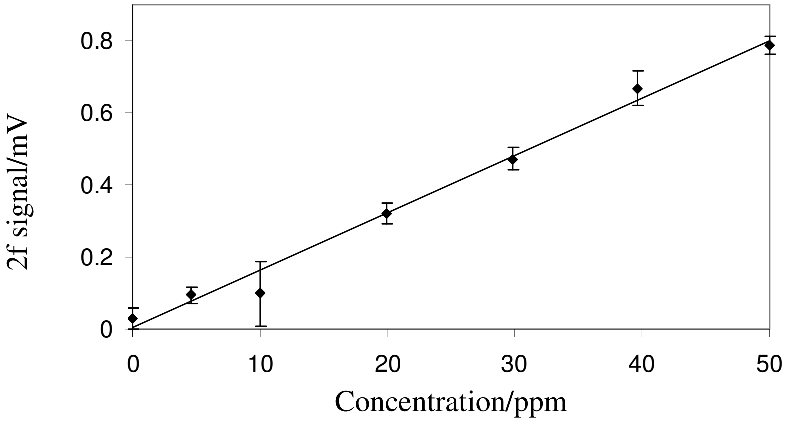

Figure 8-37: Plot of 2f signal against concentration (Lock-in τ 10s).

The detection limit in this experiment was approximately 4ppm. This was set by intensity uncertainty from the source (confirmed by measurements on the reference channel) and not by uncertainty generated in the sphere.

8.7 Discussion

In summary, gas absorption experiments were conducting using a 2 inch and 4 inch internal diameter sphere. The detection limit was found to be in the range 0.4 to 4ppm. The performance of the system was limited by interference effects from elsewhere in the system (thought to be the source) and not the integrating spheres.

In addition to a discussion of the results presented in this chapter, this section will also consider a number of claims made by other researchers on the potential advantages of using integrating spheres as multipass cells in TDLAS

8.7.1 Ease of alignment

In practice coupling the emission from the source to the detector via an integrating sphere was found to be a relatively easy task for all the configurations considered here (sample shown in Figure 8-38(a), (b) and (c)). In an experiment using the configuration shown in Figure 8-38(a), input powers as low as 20µW were detected.

By comparing Figure 8-38 (a-c) to (d) it is apparent that less alignment effort to avoid formation of Fabry-Perot etalon is required in the case of the sphere compared to the standard cell configuration. The same conclusion is arrived at when an inspection of Figure 8-39 (a) and (d) is made.

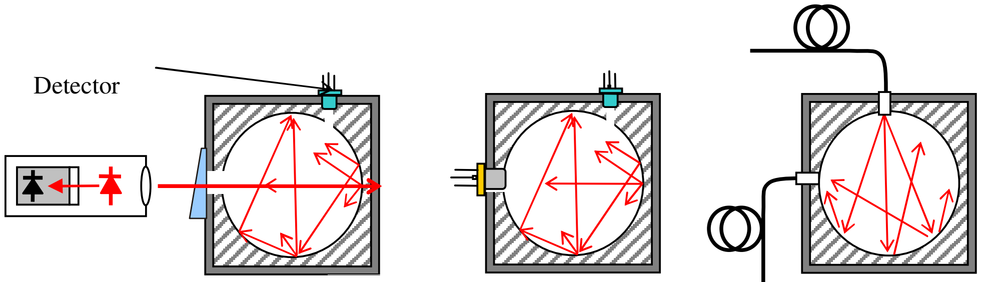

(a) collimated beam launched into sphere

(b) laser directly mounted on sphere

(c) Fibre coupling

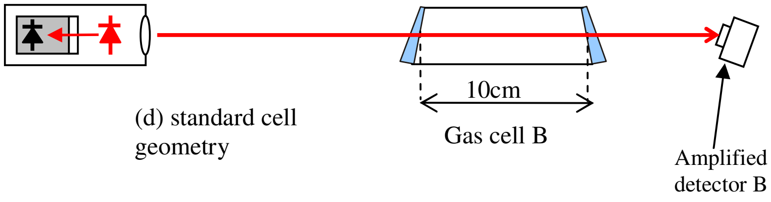

(d) standard cell geometry

Figure 8-38: Schematic diagrams of a sample of integrating sphere configurations that were used for conducting gas absorption experiments.

> *"For remote detection and for differential measurements, light from several lasers can be coupled easily to the sphere with optical fibres"*

The advantages of an integrating sphere over a standard cell for fibre coupled systems can be appreciated by examining Figure 8-39. In system (b) the sensitivity of the system will be limited by the effectiveness of the measures taken to suppress Fabry-Perot etalon and self mixing effects in the fibre launch system. In addition to the above described limitation, in system of Figure 8-39 (a), precautions against formation of Fabry-Perot etalons have to be undertaken; (1) when coupling the single mode fibre out put the cell, (2) gas cell windows and (3) when coupling from gas cell to multimode fibre.

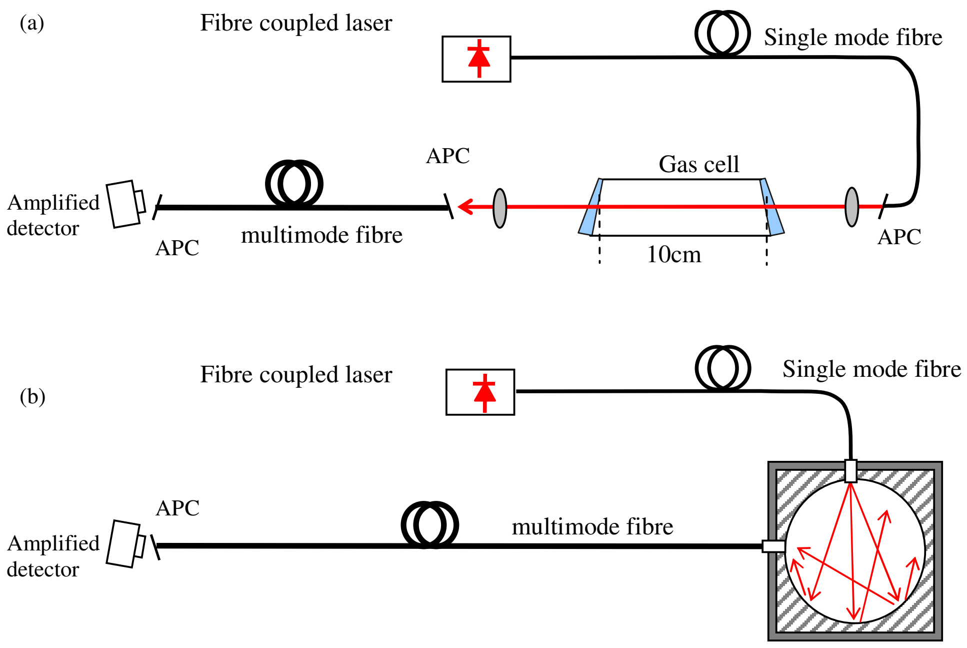

Figure 8-39. Schematic diagram of a remote detection system employing optical fibre to couple light from the source to a detector. (a) scheme employing a standard cell (b) scheme employing a sphere.

In the experiments only one source channel was used at a time. However, in several experiments, two detector channels were used by mounting the detectors directly onto the sphere or using multimode fibre to couple the sphere output to the detectors. Use of fibre offered greater flexibility and also lead to a longer pathlength by minimising the port fraction (a pathlength of 180cm (best case scenario) was achieved using a fibre configuration with a 2 inch sphere, Table 8-4).

8.7.2 Interference effects

> Tranchart *et al*[12] claimed that *"Because of the infinite number of different optical paths, no optical interference fringes are expected. It has been verified experimentally that, if such effects are present, they represent a modulation of the baseline corresponding to an absorption coefficient smaller than* $5 \times 10^{-7} cm^{-1}$*"*.

Neither a description of the experiment or results were presented in the paper relating to the above claim. It is therefore difficult to make a comment on this claim.

In the experiments shown here, interference effects due to self mixing were found to be more problematic than Fabry-Perot etalon effects. Interference fringe signals with an amplitude equivalent to 9ppm gas signal were observed in an experiment (reported in Figure 8-30) using a VCSEL and a 2 inch integrating sphere configured as Figure 8-39 (b).

For experiments using a collimated source as shown in Figure 8-38 (a), it was found necessary to locate the sphere at distances greater than 1 metre from the laser in order to minimise self mixing effects.

8.8 Conclusion

The feasibility of using integrating spheres as multipass optical cells has been investigated. In practice using integrating spheres lead to simple and robust systems. Fabry-Perot etalon effects could be easily designed out of the systems without requiring a great amount of alignment effort.

However, the use of highly reflective diffusive surfaces (e.g. Spectralon^{TM}, Zenith^{TM}) in integrating spheres can induce self mixing interference effects that were found limit the detection sensitivity in several configurations that were considered. Design precautions against optical feedback have to be considered.

A second source of intensity uncertainty was found to be speckle related. This was found to be of the same order of magnitude as the self mixing interference effects. In the configurations where a detector was mounted directly onto the sphere, the speckle related intensity uncertainty could be reduced by using large area detector or wide field of view. Using multimode fibre to couple light out of the integrating sphere can also lead to a reduction in speckle related intensity uncertainty (Figure 8-8).

A discussion and conclusion of the thesis is given in Chapter 9**.** Also presented in this Chapter are suggestions for further work. This is followed by a list of publications arising from this research and appendices.

8.9 References

[1] White, J. U. (1942), 'Long Optical Paths of Large Aperture', *Journal of Optical Society of America*, V32, N5, pp. 285.

[2] White, J. U. (1976), 'Very long optical paths in air', *Journal of Optical Society of America*, V66, N5, pp. 411–416.

[3] Herriott, D. R., Kogelnik, H., and Kompfner, R. (1964), 'Off-Axis Paths in Spherical Mirror Interferometers', *Applied Optics*, V3, N4, pp. 523.

[4] Chernin, S. M. and Barskaya, E. G. (1991), 'Optical multipass matrix system', *Applied Optics*, V30, N1, pp. 51-58.

[5] Herriott, D. R. and Schulte, H. J. (1965), 'Folded Optical Delay Lines', *Applied Optics*, V4, N8, pp. 883.

[6] Silver, J. A. (2005), 'Simple dense-pattern optical multipass cells', *Applied Optics*, V44, N31, pp. 6545-6556.

[7] Werle, P. and others (1989), 'Wideband noise characteristics of a lead-salt diode laser: possibility of quantum noise limited TDLAS performance', *Applied Optics*, V28, N9, pp. 1638.

[8] Werle, P. and Slemr, F. (1991), 'Signal-to-noise ratio analysis in laser absorption spectrometers using optical multipass cells ', *Applied Optics*, V30, N4, pp. 430-434.

[9] Venkatesh, C. G., Eng, R. S., and Mantz, A. W. (1980), 'Tunable diode laser-integrating sphere systems: a study of their output intensity characteristics', *Applied Optics*, V19, N10, pp. 1704-1710.

[10] Tanaka H, Matsuura M, Tai H and Uehara K Tokyo Gas Co, LTD Tokyo Japan (13 April 1993), *Gas Detection Device*. USA. 5202570.

[11] Abdullin, R. M. and Lebedev, A. V. (1988), 'Use of an integrating sphere as a multipass optical cell', *Soviet Journal of Optical Technology*, V55, N3, pp. 139-41.

[12] Tranchart, S, Bachir, I. H., and Destombes, J-L. (1996), 'Sensitive trace gas detection with near-infrared laser diodes and an integrating sphere', *Applied Optics*, V35, N36, pp. 7070-7074.

[13] Hawe, E. and others (2007), 'An investigation into the use of an integrating sphere as a gas absorption cell', *Journal of Applied Optics A: Pure and Applied Optics*, V9, N6, pp. S12-S18.

[14] Labsphere 200 *Sphere Systems and Instrumentation* Catalogue II (USA: Labsphere, INC).

[15] SphereOptics-Hoffman LLC 2004 *Integrating Sphere Design and Applications* (USA: SphereOptics-Hoffman LLC).

[16] Fry, E. S., Kattawar, G. W., and Pope, R. M. (1992), 'Integrating cavity absorption meter', *Applied Optics*, V31, N12, pp. 2055-65.

[17] Pope, R. M. and Fry, E. S. (1997), 'Absorption spectrum (380-700 nm) of pure water. II. Integrating cavity measurements', *Applied Optics*, V36, N33, pp. 8710-23.

[18] Elterman, P. (1970), 'Integrating cavity spectroscopy', *Applied Optics*, V9, N9, pp. 2140-2.

[19] Atia W A and Flanders D C Axsun Technologies, Inc (27 March 2006), *Method and System for Reducing Parasitic Spectral Noise in Tunable Semiconductor Source Spectroscopy System*. USA. 20060187457.

[20] Hawe E, Dooly G, Chambers P, Fitzpatrick C and Lewis E 2006 *Photonic Applications for Aerospace, Transportation, and Harsh Environments, Oct 3 2006* 6379 *Proceedings of SPIE - The International Society for Optical Engineering* (Boston, MA, United States: International Society for Optical Engineering, Bellingham WA, WA 98227-0010, United States) p 63790.

Chapter 9 Conclusion and Future work

The advantages of using tunable diode laser absorption spectroscopy (TDLAS) for trace gas sensing include; fast response times, high sensitivity and high target gas selectivity. However, it is widely acknowledged that the sensitivity of many practical TDLAS systems is limited by the formation of unintentional Fabry-Perot interference fringes in the optical path between the source and detector[1]. This was also experienced in this thesis. The effect partly explains why field deployment of instruments based on TDLAS is relatively low, despite the large number of studies on TDLAS and the many advantages of using the technique.

Common design techniques to reduce etalon formation include; the use of optical isolators, use of reflective rather than refractive optics, angling and antireflection coating of reflective surfaces[2]. Techniques for eliminating or reducing the amplitude of the fringe signal include: (a) mechanically oscillating the path length with external devices[13,4], (b) introduction of an asynchronous current in addition to the usual modulation current through the laser diode[5], (c) use of alternative waveforms[6,7] and (d) postdetection filtering[8]. The disadvantage of method (a) is that the detection bandwidth is limited by the mechanical motion and signal integration that is required[9]. Methods (b) and (c) are less effective and tend to wash out the gas absorption signal when the free spectral range (FSR) is comparable to the gas absorption linewidth[10]. Post detection filtering can only be applied where the signal and the interference spectra are distinguishable in the frequency domain[10].

In general the alignment of the optical components is critical. This often leads to complex designs with tight tolerances on optical component alignment, and can therefore be difficult and expensive to maintain in field instruments. This presents a barrier in transferring the technology from the laboratory to field applications.

This thesis set out to investigate an alternative technique for eliminating Fabry-Perot etalon interference fringes that lead to simple and robust designs thereby easing manufacturing tolerances. A technique based on the use of diffuse reflections in the optical path between the source and the detector has been investigated. The focus was on gas cell design, as these are often the worst culprits[11].

However, the use of diffuse reflections introduced laser speckle that contributed an intensity uncertainty to gas detection measurements. This lead to a systematic study of speckle effects including;

1. Development of a methodology for investigating speckle effects in TDLAS.
2. Quantification the intensity uncertainty due to laser speckle.

3. Investigation of methods of reducing speckle related intensity uncertainty.

For a single static speckle pattern, the uncertainty is approximately given by ratio of the average speckle size ε to the detector diameter d (i.e. ε/d). The average speckle size is determined by the optical geometry of the gas cell and the light collection geometry. The uncertainty was minimised by integrating a large number of speckles over the detector area. This was achieved by arranging the geometry such that the speckle size was minimised and using a large area detector. In all the gas cell designs considered in this thesis, the estimated speckle related intensity uncertainty for a single static speckle pattern was in the range 1×10^{-3} to 1×10^{-4} equivalent ppm.

Changes in the speckle pattern due to external factors (ambient vibrations, cooling fans in electronic equipment, pumps etc) will not worsen speckle noise for a sufficient number of speckles arriving at the detector. Although the speckle pattern will be non stationary, the detector will effectively 'see' the same number of speckles (i.e. average intensity is constant). Therefore in worst case, the speckle related uncertainty will be on the same level as that of a static speckle field.

Speckle related intensity uncertainty can be actively suppressed by averaging a sufficient number of uncorrelated speckles during the detector integrating period. Adding M independent speckle patterns was shown to reduce the uncertainty by $\sqrt{M}$. Uncorrelated speckle patterns were generated by applying a dither or rotation to the diffuser. In either case, the speckle related uncertainty in gas absorption measurements was reduced by a factor of 10.

A worst case scenario in which speckle could lead to interference effects was also considered. Coherent combination of a polarised speckle field with a specular beam or another speckle pattern at the detector gave rise to interferometric speckle. Interferometric speckle contributed an intensity uncertainty that behaved in a similar manner to a low Finesse Fabry-Perot etalon. The visibility of the fringes was significantly reduced by integrating a large number of speckles over a detector area. The explanation for this result is that although the intensity of each speckle is periodic in phase, the distribution of the phases of individual speckles is random. Therefore this amounted to averaging random variables. In practice, it took considerable efforts to align the system to achieve interferometric speckle. Therefore formation of interferometric speckle can be avoided relatively easily through good design practice (i.e. ensuring that only the diffusely scattered light from the gas cell was directed at the detector).

In the course of the experiments it was found that low level optical feedback gave rise to interferometric fringes in a phenomenon commonly referred to as the self mixing effect[12]. Interference fringes due to the self mixing effect were found to be equally if not more problematic. It is therefore surprising to find no systematic study of the implications of self mixing interference fringes on TDLAS based sensors in the literature. A systematic study of self mixing interference effects was conducted.

Both self mixing and Fabry-Perot etalon interference effects create a modulation of the light intensity measured at a detector. The effects of interference from low reflectivity etalons and from self mixing (in the case of low feedback) are equivalent. For a given cavity length d, the resulting fringes take the same sinusoidal form with a period that is equal to c/2d.

Self mixing interference can arise from specular reflections (back reflection) and diffuse reflections (backscatter) with equivalent effects for the same levels of returned light and cavity length. Self mixing due to diffuse reflections has the important implication that the presence of dust or dirt within the optical path (including AR coated surfaces) will also present a problem.

A Fabry-Perot cavity is formed by two parallel surfaces and the amplitude of resulting fringes scales linearly with the residual reflectivity of the surfaces, so that a 100-fold reduction of the reflectivity results in a decrease of the fringe visibility by the same factor. In contrast, only a single reflecting or backscattering surface is required to produce self-mixing interferometric fringes. The amplitude of the modulated power scales with the square root of the external cavity attenuation (in the case of weak feedback) so that if the backscattered or back reflected light is reduced by a factor 100, the amplitude of the modulated power is reduced by a factor 10 only.

Thus, self-mixing interference fringes can arise in a greater range of circumstances than etalon-induced fringes and can be more difficult to eliminate. It is possible that self mixing interference fringes are routinely observed but are mistakenly attributed to Fabry-Perot etalons.

Self-mixing fringes in a laser diode cavity can be distinguished from Fabry-Perot etalon fringes in two ways:

(i) Self mixing results in modulation of the output from the laser diode itself whereas Fabry-Perot fringes are only present on the beam that has transversed the etalon. Therefore the self mixing effect may conveniently detected on the rear facet emission of Fabry-Perot and DFB lasers using a monitor photodiode.

(ii) Self mixing also results in modulation of the voltage across the diode. This has a worse signal to noise ratio so that only relatively high levels of feedback can be detected, but is more convenient for laser diodes with no rear emission, such as VCSELs.

A good quality (60dB) optical isolator would prevent the problem by reducing feedback. However, the effectiveness of the isolator is limited by feedback arising from residual reflections or backscatter (due to dust or dirt) from the front face of the isolator. Simple intensity referencing can remove the effects of the modulation to first order, which in the experiments improved the signal to noise ratio by over a factor of 10. Intensity referencing is effective in the case of self mixing fringes since the modulation is on the laser emission itself and any changes in the fringes will be common to the reference and main path. In the case of Fabry-Perot etalons intensity referencing requires matching the reference path to the sensing path, which is often difficult to achieve in practice.

In recent years, there has been increasing interest in using integrating spheres as multipass optical cells in TDLAS. The knowledge of diffuse reflections acquired in this thesis was applied to a study on the feasibility of using integrating spheres with diffusive internal surfaces as multipass optical cells. A number of claims made by previous workers regarding the potential advantages of using such cells were also investigated.

In practice using integrating spheres lead to simple and robust systems. Fabry-Perot etalon effects could be easily designed out of the systems without requiring a great amount of alignment effort. Furthermore, effective path lengths that were several multiples of the sphere diameters were achieved. In a best case scenario a path length of 180cm was achieved in a 5cm internal diameter sphere (practical path lengths of 100cm were routinely achieved in several configurations).

However, the use of highly reflective diffusive surfaces (e.g. Spectralon^{TM}, Zenith^{TM}) in integrating spheres was found to induce self mixing interference effects that limited the detection sensitivity in several configurations that were considered. Design precautions against optical feedback have to be considered.

A second source of intensity uncertainty in integrating spheres was found to be speckle related. In the configurations where a detector was mounted directly onto the sphere, the speckle related intensity uncertainty could be reduced by using large area detector or wide field of view. Using multimode fibre to couple light out of the integrating sphere can also lead to a reduction in speckle related intensity uncertainty.

In summary the deliberate use of diffuse reflections in gas cells as a means of eliminating interference effects due to Fabry-Perot etalons has been investigated. It has been shown that under the right circumstances (i.e. precautions taken against formation of interferometric speckle and self mixing effects) robust gas cell designs that do not suffer from Fabry-Perot etalon effects can be realised.

The technique could potentially simplify instrument design, thereby aiding the transfer of technology to industry.

9.1 Future work

9.1.1 Speckle size dependence on surface structure

The statistical properties of speckle presented in section 3.2 and summarised in 4.1 are based on the assumption that the surface height deviations of the diffuser are large in comparison to the wavelength of the radiation illuminating it, and that the resultant speckle field is completely polarised.

It was pointed out in section 4.4 that

1. Bulk diffusers (surfaces into which light penetrates and is multiply scattered) such as matt white paint or opal glass depolarise the light and thus do not generate a fully developed speckle pattern[13].
2. The statistics of speckle from singly scattering surfaces with height deviations less than the illuminating wavelength have been shown to depend on the surface roughness[14].

Evidence was provided (see section 4.4) to show that speckle size and contrast depended on the type of sample that was used[15]. However, it was not possible to establish whether the observed effects where due to surface structure or bulk micro structure or multiple scattering effects. This was in part because singly scattering surfaces with deviations less than the illuminating wavelength were not readily available. Further work is required in this area to investigate if diffusers of this type can lead to reduction in speckle related intensity uncertainty.

In the case of bulk scatterers, it is envisaged that the effects of surface structure or bulk micro structure or multiple scattering on speckle related intensity uncertainty will be difficult to distinguish.

9.1.2 Laser diode packaging

The DFB laser module used in this thesis (with integrated monitor photodiode enclosed in a reference cell, section 5.1.1) had several advantages over standard laser packages;

- Absolute wavelength calibration.
- The integral reference cell negated the need for a beam splitter in the forward path to sample a portion of the beam for the frequency stabilisation system.

However it suffered from self mixing interference effects that limited the instrument sensitivity. However experiments reported in section 5.4.1 demonstrated that by observing good design practice, the self mixing fringes can be significantly reduced or eliminated. As the module is a hermetically sealed unit, it will be immune from feedback due to scattering caused by gradual accumulation of dust or dirt. Further development of this type of module is highly recommended.

In recent years, there has been increasing interest in using VCSELs in TDLAS mainly due to lower cost in comparison to DFBs. It has been shown in sections 6.2.6, 6.3 and 8.5.4 that VCSELs are also susceptible from the self mixing effect. However, in many cases, VCSEL packages do not have a monitor photodiode. Without a monitor photodiode, it is difficult to distinguish interference effects due to low level feedback from low finesse Fabry-Perot etalons. Use of a commercially available VCSEL with an integral monitor (Emcore, Gigalase 8585-8312) has been reported in the literature[16]. An important area for further work is the development of VCSELs packages with an integral photodiode suitable for use in TDLAS.

9.1.3 Use of integrating spheres in TDLAS

The feasibility of using integrating spheres in TDLAS has been demonstrated. However the cost of commercially available integrating spheres is relatively high (around £1000).

Abdullin and Lebedev[17] demonstrated the use of a home made 10cm internal diameter sphere machined out copper that had an effective path length of 430mm (4mm diameter ports). Further work is required on materials (surface scatters or bulk diffusers from which integrating spheres can be made to reduce cost.

9.2 References

[1] Silver, J. A. and Stanton, A. C. (1988), 'Optical interference fringe reduction in laser absorption experiments ', *Applied Optics*, V27, N10, pp. 1914-16.

[2] Mansfield, C. D. and Rutt, H. N. (1999), 'Evaluation of multiple beam interference effects in infrared gas spectroscopy', *Measurement Science and Technology*, V10, N3, pp. 206-210.

[3] Webster, C. R. (1985), 'Brewster-plate spoiler: a novel method for reducing the amplitude of interference fringes that limit tunable-laser absorption', *Journal of Optical Society of America B*, V2, N6, pp. 1464-1470.

[4] Chou, S., Baer, D. S., and Hanson, R. K. (1997), 'Diode laser absorption measurements of CH_3Cl and CH_4 near 1.65μm', *Applied Optics*, V36, N15, pp. 3288-3293.

[5] Reid, J. and others (1980), 'Sensitivity limits of a tunable diode laser spectrometer, with application to the detection of NO2 at the 100-pptv level', *Applied Optics*, V19, N19, pp. 3349-3354.

[6] Sano, H., Koga, R., and Kosaka, M. (1983), 'Analytical description of tunable diode laser derivative spectrometry ', *Japanese Journal of Applied Physics, Part 1 (Regular Papers & Short Notes)*, V22, N12, pp. 1883-8.

[7] Iguchi, T. (1986), 'Modulation waveforms for second-harmonic detection with tunable diode lasers', *Journal of the Optical Society of America B (Optical Physics)*, V3, N3, pp. 419-23.

[8] Capellani F, Mellandrone G and Restelli G 1987 *Monitoring of Gaseous Pollutants by Tunable Diode Lasers* editors Grisar R, H. Preier H, Schmidtke G and Restelli G (UK: Kluwer Academic Publishers) pp 51-60.

[9] Sun, H. C and Whittaker, E. A. (1992), 'Novel etalon fringe rejection technique for laser absorption spectroscopy', *Applied Optics*, V31, N24, pp. 4998-5002.

[10] Schiff H I, Mackay G I and Bechara J 1994 *Air Monitoring by Spectroscopic Techniques* Editor Sigrist M W (New York: John Wiley and sons) pp 239-333.

[11] Bomse, D. S., Stanton, A. C., and Silver, J. A. (1992), 'Frequency modulation and wavelength modulation spectroscopies: comparison of experimental methods using a lead-salt diode laser', *Applied Optics*, V31, N6, pp. 718-730.

[12] Giuliani, Guido and others (2002), 'Laser diode self-mixing technique for sensing applications', *Journal of Optics A: Pure and Applied Optics*, V4, N6, pp. 283-294.

[13] Ennos A E 1975 *Laser Speckle and Related Phenomena* (Berlin: Springer-Verlag) pp 203-53.

[14] Fujii, H. and Asakura, T. (1974), 'Effect of surface roughness on the statistical distribution of image speckle intensity', *Optics Communications,* V11, N1, pp. 35-38.

[15] Masiyano, D., Hodgkinson, J., and Tatam, R. P. (2008), 'Use of diffuse reflections in tunable diode laser absorption spectroscopy: Implications of laser speckle for gas absorption measurements', *Applied Physics B: Lasers and*

Optics, V90, N2, pp. 279-288.

[16] Tucker J R, Leng L and Rakic A D 2003 *Optoelectronic and Microeletronic Materials and Devices*: IEEE) pp 583-6.

[17] Abdullin, R. M. and Lebedev, A. V. (1988), 'Use of an integrating sphere as a multipass optical cell', *Soviet Journal of Optical Technology*, V55, N3, pp. 139-41.

List of publications

Peer reviewed journal papers

[1] Masiyano D, Hodgkinson J, and Tatam R P, Use of diffuse reflections in tunable diode laser absorption spectroscopy: Implications of laser speckle for gas absorption measurements, Applied Physics B: Lasers and Optics, V90, No. 2, pp. 279-288 (2008)

[2] Masiyano D, Hodgkinson J, Schilt S, and Tatam R P, Self-mixing interference effects in tunable diode laser absorption spectroscopy, submitted to Applied Physics B: Lasers and Optics in December 2008.

Conferences

[1] Masiyano, D., Francis, D., Hodgkinson, J. and Tatam, R.P. (2006), 'Use of Diffuse Reflections in Tunable Diode Laser Absorption Spectroscopy ', *Journal of Physics: Conference Series,* Photon 06, Manchester, UK, September 2006.

[2] Masiyano, D., Hodgkinson, J., and Tatam, R. P. Use of diffuse reflections in TDLAS: implications of laser speckle for gas absorption measurements. Poster presentation at the 6th International Conference on Tunable Diode Laser Spectroscopy, Reims, France, July 2007.

[3] Masiyano, D., Hodgkinson, J. and Tatam, R.P. (2007), 'Methodology for investigation of diffuse reflections in tunable diode laser absorption spectroscopy', *Journal of Physics: Conference Series,* V. 76, pp. 012052, Sensors & their Applications XIV, Liverpool, UK, September 2007.

[4] Masiyano, D., Francis, D, Hodgkinson, J., and Tatam, R. P. Use of Diffuse Reflections in Tunable Diode Laser Absorption Spectroscopy. Oral presentation at Photonex 07, Birmingham, UK, October 2007.

[5] Masiyano, D., Hodgkinson, J., and Tatam, R. P. Interferometric Noise Reduction in TDLAS by the Use of Diffuse Reflections. Oral presentation at the 59th Pittsburgh Conference on Analytical Chemistry and Applied Spectroscopy, New Orleans, USA, March 2008

[6] Masiyano, D., Hodgkinson, J., and Tatam, R. P. Use of diffuse reflections in TDLAS: implications of laser speckle for gas absorption measurements. Oral presentation at the 41st GASG (Gas Analysis and Sensing Group) Colloquium, ‘Air Analysis - out of the laboratory and into the field', National Physics Laboratory, UK. May, 2008

Appendix A Theoretical description of WMS

A.1 Model that only considers frequency modulation (intensity diode intensity modulation ignored)

If the laser diode driving current is modulated sinusoidally, the current $i(t)$ is given by

$$i(t) = i_0 + i_m \sin \omega t \tag{A-1}$$

where i_0 the average laser current, i_m is the amplitude of the current modulation, ν is the frequency of the current modulation in Hz where $\omega = 2\pi\nu$. The frequency and intensity of emission from the laser may be expressed as

$$\nu = \nu_0 + \nu_m \sin \omega t \tag{A-2}$$

$$I(t) = I_0[1 + \eta \sin \omega t] \tag{A-3}$$

where I_0 and $\nu_0(= c / \lambda_0)$ represent, respectively, the average laser output power and the average laser carrier frequency. ν_m is the amplitude of the frequency modulation and η is an intensity modulation index. At this point, it is necessary to recall that Beer's law is given by

$$I(\nu) = I_0(\nu)\exp[-\alpha(\nu)CL]$$

The output light intensity of modulated laser light passing through a gas sample with an absorption coefficient $\alpha(\nu)$ is given by combining equations (A-2), (A-3) and Beer's law.

$$I(t) = I_0(1 + \eta \sin \omega t)\exp[-\alpha(\nu_0 + \nu_m \sin \omega t)CL] \tag{A-4}$$

Jin *et al*[1] approximated the light intensity after passing through the gas cell to be

$$I(t) = I_0[1 + \eta \sin \omega t - \alpha(\nu_0 + \nu_m \sin \omega t)CL] \tag{A-5}$$

by making two assumptions;

- $\alpha(\nu)CL << 1$, justified by the fact that in most practical situations the concentration of the gas being measured is small
- $\eta << 1$, usually the residual intensity modulation is also small

A.2 Theoretical description of WMS (Frequency and intensity modulation accounted for)

A theoretical description of WMS that includes the IM–FM phase shift follows.

The Lorentzian line distribution, can be rewritten in the form

$$\alpha(\nu) = \frac{\delta\nu^2 \alpha_0}{\delta\nu^2 + \left(\nu - \nu_{line}\right)^2} \tag{A-6}$$

Substituting equation (A-6) in the equation for transmittance $T = 1 - \alpha(\nu)CL$, gives

$$T = 1 - \frac{\delta\nu^2 \alpha_0 CL}{\left(\nu - \nu_{line}\right)^2 + \delta\nu^2} \qquad \textbf{(A-7)}$$

Equation (A-2) can be re written as

$$\nu = \nu_0 + \nu_m \cos\omega t \qquad \textbf{(A-8)}$$

Substituting (A-8) in (A-7) and expanding the transmittance T with respect to the frequency modulation amplitude ν_m, one obtains[2]

$$T = T_0 + \frac{{\nu_m}^2}{4} T_2 + \nu_m T_1 \cos\omega t + \frac{{\nu_m}^2}{4} T_2 \cos(2\omega t) \qquad \textbf{(A-9)}$$

where T_1 and T_2 are the first and second derivatives of the transmittance respectively at $\nu = \nu_0$ in equation (A-7) and

$$T_0 = 1 - \frac{\delta\nu^2 \alpha_0 CL}{\left(\nu_0 - \nu_{line}\right)^2 + \delta\nu^2} \qquad \textbf{(A-10)}$$

$$T_1 = \frac{-2\left(\nu_0 - \nu_{line}\right)\delta\nu^2 \alpha_0 CL}{[\left(\nu_0 - \nu_{line}\right)^2 + \delta\nu^2]^2} \qquad \textbf{(A-11)}$$

$$T_2 = \frac{-2[3\left(\nu_0 - \nu_{line}\right)^2 - \delta\nu^2]\delta\nu^2 \alpha_0 CL}{[\left(\nu_0 - \nu_{line}\right)^2 + \delta\nu^2]^3} \qquad \textbf{(A-12)}$$

Figure 1 shows the plots of the transmission factor and the first two derivatives.

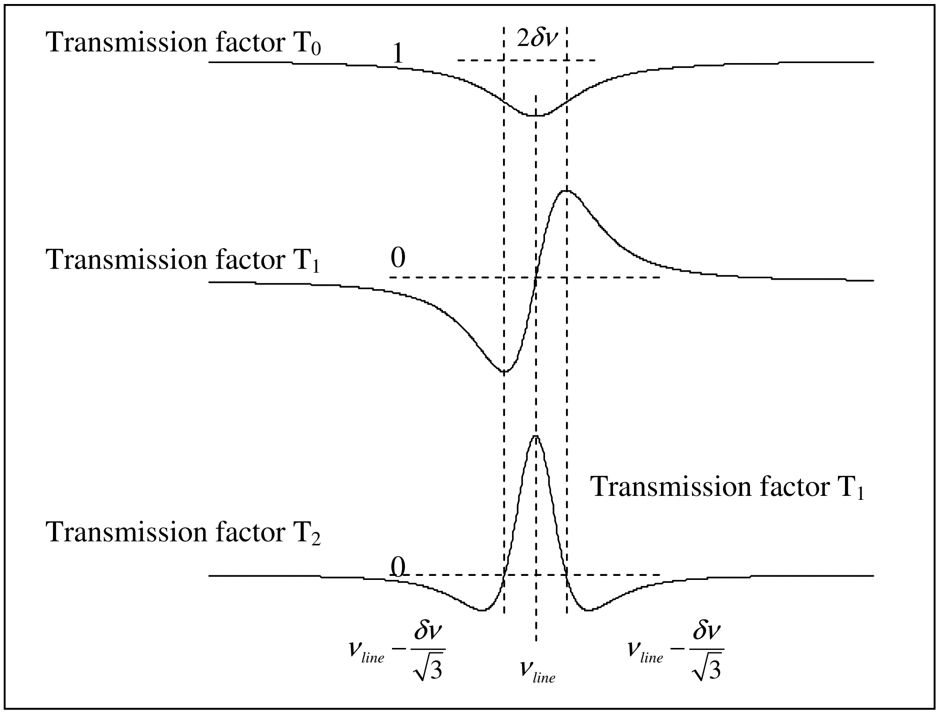

Figure 1: Plots of the transmission factor. The plots were generated by plotting the equations for T_0, T_1 and T_2 in MathCAD™ software. After Tanaka[2].

The laser output power equation requires modifying to include the IM-FM phase shift.

$$I = I_0 + \eta I_0 \cos(\omega t + \phi) \qquad \textbf{(A-13)}$$

where ϕ is the IM-FM phase difference. The IM contributes an additional phase sensitive signal which is unrelated to the gas absorption[2].

After passage through an absorbing gas, the intensity *P* of the DFB laser is related to the initial intensity *I* and transmittance in the following manner

$$P = AIT \qquad \textbf{(A-14)}$$

where A is a constant coefficient that accounts for other losses in the system.

By substituting equations (A-9) and (A-13) into equation (A-14), the intensity P becomes[2]

$$P = A\left[\left(I_0 + \eta I_0 \cos(\omega t + \phi)\right)\left(C_0 + \nu_m T_1 \cos \omega t + \frac{\nu_m{}^2}{4} T_2 \cos(2\omega t)\right)\right] \qquad \textbf{(A-15)}$$

where C_0 is given by

$$C_0 = T_0 + \frac{\nu_m{}^2}{4} T_2 \qquad \textbf{(A-16)}$$

By expanding equation (A-15) and ignoring the higher order terms, the components of *P* changing at the fundamental frequency *ω* are given by[2]

$$P(\omega) = AC_0 \eta I_0 \cos(\omega t + \phi) + AI_0 \nu_m T_1 \cos \omega t \qquad \textbf{(A-17)}$$

Since the two terms have different phases, their contribution can be manipulated by appropriate selection of detection phase in phase sensitive detection[2]. The contribution form the first term can be maximised by setting $\omega t + \phi = \pm n\pi$ in equation (A-17) to yield

$$P(\omega)_1 = A\left[\eta I_0 C_0 + I_0 \nu_m T_1 \cos \phi\right] \qquad \textbf{(A-18)}$$

And similarly, the contribution from the second term can be maximised by setting $\omega t + \phi = \pm \frac{n\pi}{2}$ in equation (A-17) to yield

$$P(\omega)_2 = AI_0 \nu_m T_1 \sin \phi \qquad \textbf{(A-19)}$$

It is worth pointing out that the IM contribution (η) is absent in $P(\omega_2)$.

From the foregoing considerations, Tanaka *et al*[2] has shown that if the laser frequency ν_0 is locked to the centre of the gas absorption line ν_{line}, the second harmonic component of the detected signal $P(2\omega)$ is given by

$$P(2\omega) = AI_0 \nu_m{}^2 T_2 / 4 \qquad \textbf{(A-20)}$$

$$P(2\omega) = \frac{AI_0 \nu_m{}^2 \alpha_0 CL}{2\delta\nu^2} \qquad \textbf{(A-21)}$$

$P(2\omega)$ is proportional to the concentration path length product *CL*. If *A* is constant, then a quantitative measurement of the absorbing gas can be made from $P(2\omega)$ [2]. To remove the dependency on A, the ratio R of $P(2\omega)$ and $P(\omega)$ is utilised. $P(\omega)$ is derived from (A-17), which at the line centre reduces to

$$P(\omega) = A\left[\eta I_0 C_0\right] \tag{A-22}$$

since T_1 given by (A-11) equals zero. At the line centre C_0 (A-16) is given by

$$C_0 = 1 - \left[\alpha_0 CL + \frac{\nu_m^{\ 2}}{4} 2\alpha_0 CL / \delta\nu^2\right] \tag{A-23}$$

The term in brackets on the right hand side of equation (A-23) is very small; therefore C_0 is approximately equal to one. The ratio $P(2\omega)/P(\omega)$ is therefore given by

$$R = \frac{P(2\omega)}{P(\omega)} = \frac{\nu_m^{\ 2}\alpha_0}{2\eta\delta\nu^2} \times CL \tag{A-24}$$

Substituting $x = \nu_m / \delta\nu$ in (A-24) using notation defined in WMS theoretical description of Jin *et al*[1] in section 2.6.1 to facilitate comparison gives

$$R = \frac{x^2}{2\eta} \times \alpha_0 CL \tag{A-25}$$

It can be seen that the 2f/1f ratio derived by Jin *et al*[1] (equation (2-18)) and Tanaka *et al*[2] (equation (A-24)) give the same result. The advantage of the formalism by Tanaka *et al* is most apparent when the 1f signal is used as the sensors output. If the IM-FM phase shift is known, then the component of the 1f signal that is due to the intensity modulation can be nulled by using equation (A-19) as the sensors output. Indeed this has been exploited by Johnstone *et al*[3] to eliminate RAM.

Appendix B Laser speckle

B.1 Addition of laser speckle field

The correlation coefficient of two random variables X and Y is defined as[4]

$$\rho_{XY} = \frac{\langle XY \rangle - \langle X \rangle \langle Y \rangle}{\sigma_X \sigma_Y} \tag{B-26}$$

where

$$\sigma_X = \left(\langle X^2 \rangle - \langle X \rangle^2 \right)^{1/2}, \quad \sigma_Y = \left(\langle Y^2 \rangle - \langle Y \rangle^2 \right)^{1/2} \tag{B-27}$$

If X and Y are independent variables, then

$$\langle XY \rangle = \langle X \rangle \langle Y \rangle \tag{B-28}$$

When this is the case the correlation coefficient is zero. The correlation coefficient of two interferometric speckle patterns I_a and I_b that have a phase difference δ between them is therefore

$$\rho_{I_a I_b} = \frac{\langle I_a I_b \rangle - \langle I_a \rangle \langle I_b \rangle}{\left(\langle I_a{}^2 \rangle - \langle I_a \rangle^2 \right)^{1/2} \left(\langle I_b{}^2 \rangle - \langle I_b \rangle^2 \right)^{1/2}} \tag{B-29}$$

According to Jones and Wykes[4], equation (B-29) is evaluated by noting the following points

4. I_a, I_b and δ are independent variables and can be averaged separately
5. The average of $\cos\theta = 0$
6. $\langle I^2 \rangle = 2 \langle I \rangle^2$

When these points are taken into consideration, the correlation coefficient in equation (B-29) therefore reduces to

$$\rho(\delta) = \frac{1 + r^2 + 2r\cos\delta}{(1+r)^2} \tag{B-30}$$

where $r = \frac{\langle I_b \rangle}{\langle I_a \rangle}$ is the ratio of the intensity of the interferometric speckle patterns, and δ is the phase difference between them.

B.2 Speckle pattern correlation fringe formation by electronic signal subtraction

In subtraction ESPI the image from an object in its initial state is recorded and stored electronically. The object is then displaced and the digitized live camera signal of the deformed state of the object is subtracted pixel by pixel from the stored signal. Areas of the two images where the speckle pattern remains correlated will give a resultant signal of zero, while uncorrelated areas will give non-zero signals[4].

This is demonstrated by considering the intensities I_a and I_b given by equations (3-19) before and (3-20) after displacement respectively.

If the output camera signals V_1 and V_2 are proportional to the input image intensities, then the subtracted signal V_s is given by[[4]]

$$V_s = V_1 - V_2$$

$$V_1 - V_2 \propto I_a - I_b \tag{B-31}$$

$$I_a - I_b = 2\sqrt{I_1 I_2}[\cos\Psi - \cos(\Psi + \Delta\delta)]$$

$$\therefore V_s \propto 2\sqrt{I_1 I_2}[\sin(\Psi + \Delta\delta/2) + \sin(\Delta\delta/2)] \tag{B-32}$$

In this analysis the electronic noise introduced by the camera and the image processing unit has been ignored. The signal V_s has negative and positive values and therefore requires rectification before being displayed on the monitor to avoid loss of signal. The rectification is achieved by taking the rms (root mean square) value of $V_{s.}$ If the brightness B on the monitor is assumed to be proportional to the rectified signal $|V_s|$, then the brightness at a given point in the monitor image is given by

$$B = 4K[I_1 I_2 \sin^2(\Psi + \Delta\delta/2)\sin^2(\Delta\delta/2)]^{1/2} \tag{B-33}$$

where the constant $K= g\gamma$, γ is the degree of resolution and g is the slope of the transfer function of the camera[5]. The term $4KI_1I_2$ represents the background intensity and the term $\sin(\Psi + 1/2\Delta\delta)$ represents the high frequency random speckle noise in the image, while last term, $\sin(1/2\Delta\delta)$, gives the fringe pattern profile[6][7]. The last point is perhaps more obvious when equation (B-33) is presented in the alternative form

$$B = 4K[I_1 I_2 \sin^2(\Psi + \Delta\delta/2)((1 - \cos\Delta\delta)/2)]^{1/2} \tag{B-34}$$

Due to the subtraction process the DC speckle terms $2I_1+2I_2$ have been removed from equation (3-21) resulting in a much improved fringe contrast.

The fringe contrast can be further enhanced by appropriate band pass filtering to remove low-frequency background effects caused by variable illumination across the surface and the high frequency random noise contained in the second term[6][8],[4].

The brightness B varies between maximum and minimum values B_{max} and B_{min} if it is averaged along a line of constant $\Delta\delta$ [4]:

$$B_{\max} = 2K\sqrt{I_1 I_2},\ \ \Delta\delta = (2n+1)\pi,\ n = 0,1,2 \tag{B-35}$$

$$B_{\min} = 0,\quad \Delta\delta = 2n\pi,\ \ n = 0,1,2 \tag{B-36}$$

The bright fringes are formed wherever two speckle patterns corresponding to the initial and deformed states of the object are fully uncorrelated. "Therefore the image of the object appears covered with dark and bright regions, which represent the well-known correlation fringes"[7]. Due to the subtraction process the conditions for bright and dark fringes are reversed compared with conventional speckle interferometry.

As the processing is done in software, a program can be written to continuously subtract live speckle interferometric speckle patterns after object deformation from the stored initial reference frame at set intervals and display the result. This means that speckle correlation fringes can be observed in pseudo-real time. Speckle correlation fringes can continue to be produced until the current speckle pattern becomes "decorrelated" with the initial reference pattern. Here the term decorrelated refers to the live speckle pattern losing touch with the stored reference frame due to unwanted motions in the measurement system leading to a loss of the displacement information. This type of decorrelation is known as "memory loss"[9] and should be distinguished from phase decorrelation.

Appendix C Frequency stabilisation scheme

In WMS, when the laser frequency is tuned to coincide with the methane absorption line centre, the 2f signal has maximum amplitude and the 3f signal is zero (Figure 2). Near the zero crossing, the 3f signal can be approximated to be linear. By using the deviation from the zero crossing of the 3f signal as an error signal in a feedback control loop, the laser frequency can be locked to the peak of the 2f signal. The deviation of the 3f signal from the zero crossing corresponds to the deviation of the laser frequency from the centre of the absorption line, and locking the laser frequency to the peak of the 2f signal corresponds to locking to the centre of the absorption line.

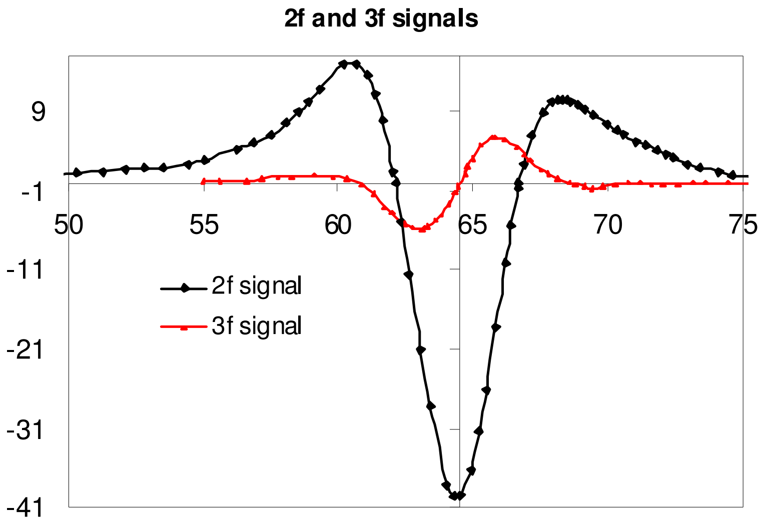

Figure 2: The second and third harmonic WMS signals, at gas line centre the 2f signal has maximum amplitude and 3f signal is zero.

The experimental setup for locking the laser frequency to the absorption line of methane in the reference gas cell is shown in Figure 3.

The light beam emitted from the back facet of the laser passed through the reference gas cell and was detected by the Ge photodiode. This signal was amplified by the transimpedance amplifier (self-made) and fed to the lock-in amplifier (Stanford Research SR850) for third harmonic (3f) extraction. The 3f was used as the error signal described above.

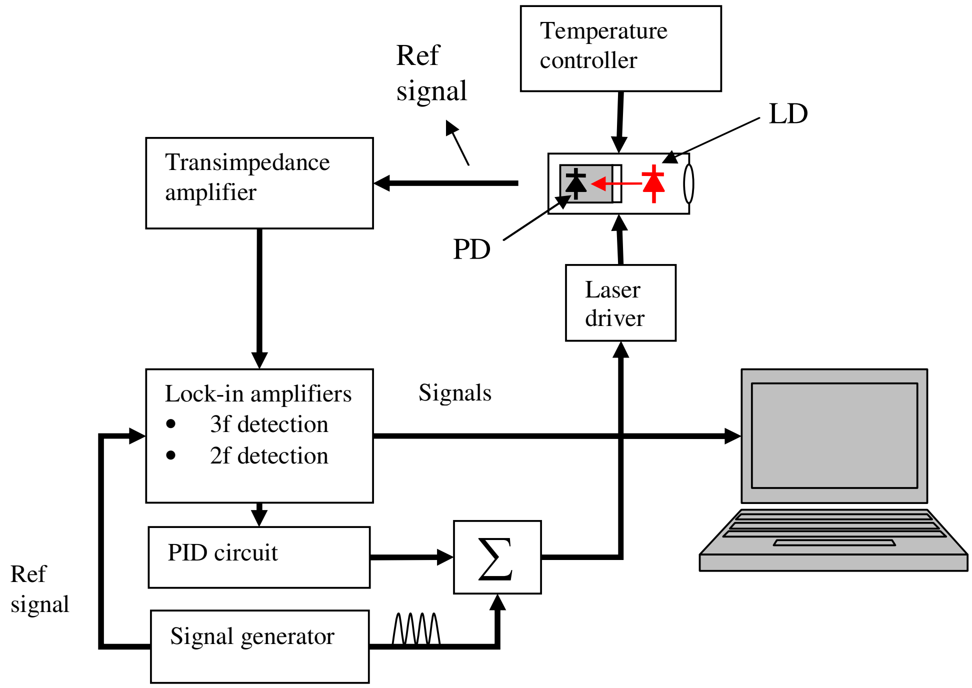

Figure 3: Experimental set up for gas line locking

The schematic diagram of the feedback control circuit is show in Figure 4 below.

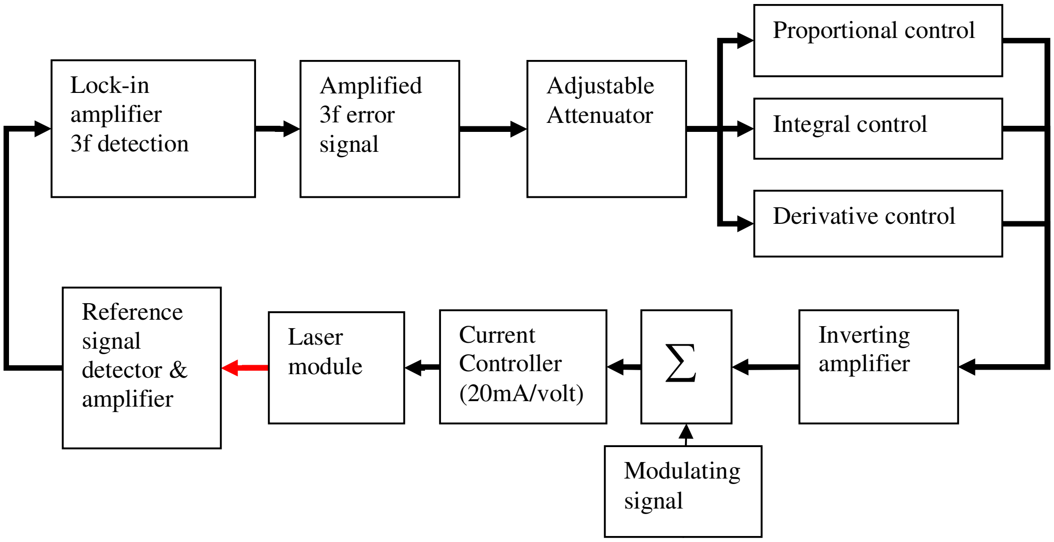

Figure 4: schematic diagram of the DFB laser frequency stabilisation circuit

An adjustable attenuator was used to scale the error signal from the lock-in amplifier to a level that is compatible with the 20 mA/V internal voltage to current converter of the laser diode driver (Profile LD-202). The output signal from the attenuator was then fed to the proportional, integral and differential (PID) gain stage. The proportional amplifier with a near-unity adjustable gain was used to damp out error signal oscillations, whilst the integrator output settled at a level that corresponds to zero output from the lock-in amplifier, but continued to compensate for slow frequency drifts of the laser with a time constant of around 1s. The differentiator corrects for high frequency fluctuations of the error signal. The respective gains of the proportional, integral and differential components are set by the 20 kΩ, 20 kΩ and 330 kΩ resistors corresponding to the values used in the PID system of Bradley *et al*[10].

In a practical circuit, the output of the integrator tended to drift slowly even after the error signal had been removed because op-amp offsets and bias currents continued to charge the 2.2 pF feedback capacitor. The integrator could be zeroed temporarily, by shorting its input to ground, by closing the push-button switch across the feedback capacitor. The correcting signal from the PID circuit was inverted before being fed to the laser current controller so that the control effort acts in the direction that reduces the error signal. For experiments lasting less than 30minutes, only the PI control actions were used for convenience.

A summing was used to add the correction term from the PID circuit and the modulation signal so that the two signals could be fed synchronously to the current controller. The modulation signal was first filtered with a passive high pass filter with a 3 dB point at 1 kHz to remove any low frequency mains noise that could otherwise disturb the error correction signal from the PID circuit.

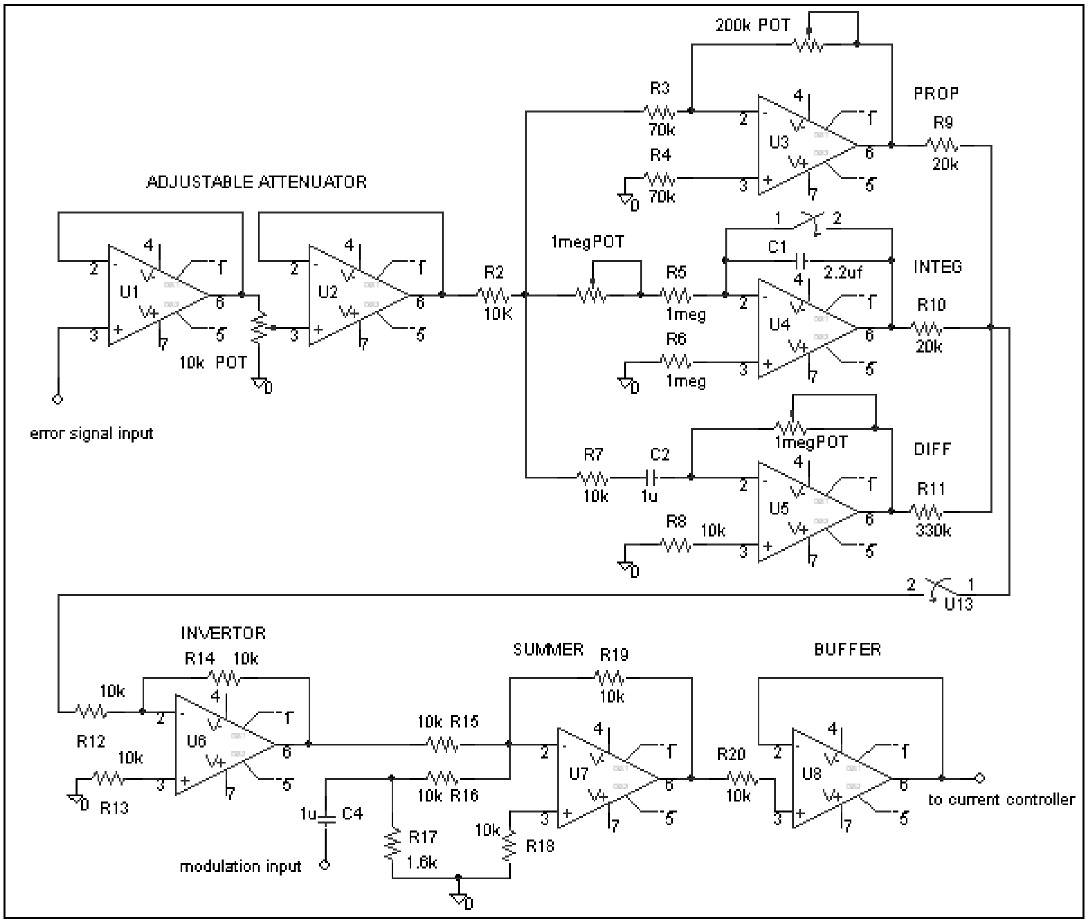

Figure 5: PID control circuit for laser frequency stabilisation drawn in MicroSim Pspice software

Appendix D The fibre coupling system; description and evaluation

This section is concerned with examining the effectiveness of the design precautions that were undertaken to prevent optical feedback and formation of Fabry-Perot etalons in the fibre coupling system. Such measures included; use of an optical isolator, AR coated of optics, angle polished fibre ends and wedged windows for gas cell, angling reflective surfaces such that reflected components were not directed back along the optical axis.

The schematic diagram of the fibre coupling system is shown in Figure 8.

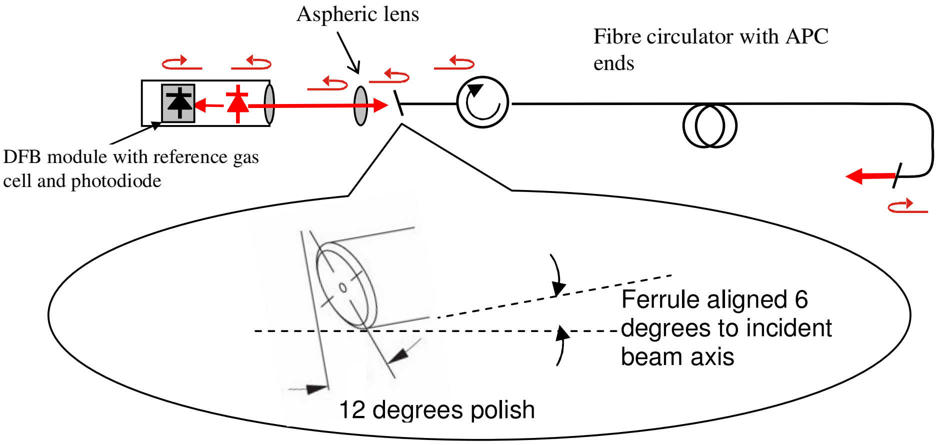

Figure 8: The experimental setup for investigating interference effects in the fibre coupling system. Key: APC, angle polished connector:

The focussing lens (Thorlabs C280TM aspheric lens) used to launch the beam into the fibre had an anti-reflective coating with a specified reflectivity of < 0.5% at 1650nm. An optical circulator (Fiberlogix FCIR-65-2-L-1) was used as an isolator (specified 45dB isolation) to prevent light reflected at the fibre output from being coupled back into the laser. The launch end face of the circulator into was angle polished at 12 degrees and angled away from the incident beam at 6 degrees (see inset in Figure 8). The angle of the polished end face is based on the work done by Ulrich and Rashleigh[11] in which they reduced the residual reflections from the tilted fibre end face by -66dB.

Optical feedback from optical elements placed in the optical path of the DFB laser was detected by monitoring the presence of interference effects on the monitor photodiode signal.

The effectiveness of the AR coating of the fibre coupling lens in preventing optical feedback into the DFB laser was investigated by comparing the reference monitor photodiode 2f signal without the lens and with the lens in place (Figure, with the fibre removed). Interference fringes were observed at lock-in amplifier time constants less than 100ms. Longer averaging time led to washing out of the fringes.

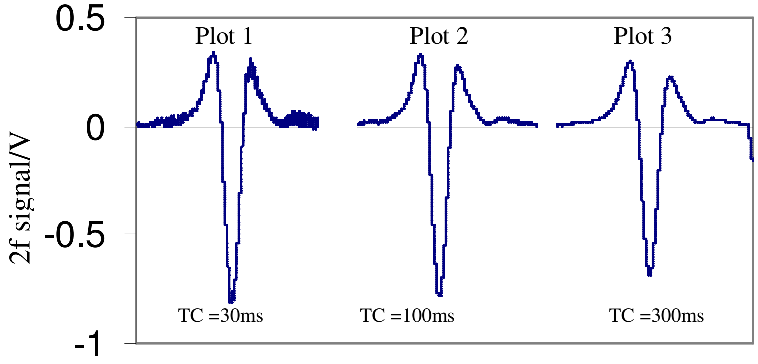

Figure 9-1: 2f plots recorded at different lock-in amplifier time constants under feedback due to reflections from the lens. The time constants for plots (1), (2), and (3) are 30ms, 100ms, and 300ms respectively.

To improve the visibility of the fringes, the laser was temperature tuned off the gas line. Figure shows a plot of the 2f background signal obtained in the presence of optical feedback from the lens. The fringes were eliminated by applying a slight tilt to the lens with respect to the laser. However this resulted in a lower coupling efficiency.

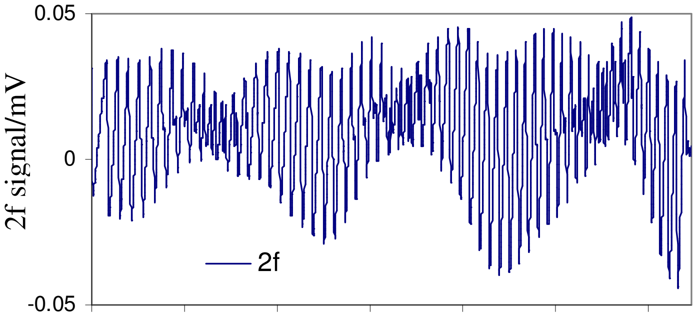

Figure 10: Feedback due to reflections from the lens. 2f background signals "off" gas line. Lock-in amplifier time constant = 3ms.

Figure 11 shows the worst and best case scenarios. In Figure 11(a), no attempt was made to minimise optical feedback (i.e. lens not tilted, FC rather than APC fibre connector). In the Figure 11(b), the lens was tilted and the 12 degrees APC fibre connector was tilted at 6 degrees with respect to the optical axis (see insert in Figure 8).

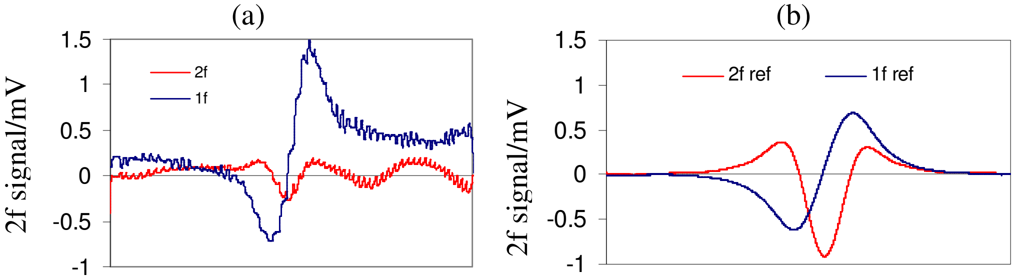

Figure 11: (a) 1f and 2f signals from the reference channel obscured by combination of optical feedback and etalon created by AR coated lens and FC fibre. (b) Feedback/fringes minimised by angling lens. Scan duration = 30ms, Time constant = 3ms.

The in-fibre circulator was found to be effective in eliminating interference effects due to Fresnel reflections from the fibre output. To analyse the observed background modulation, the 2f signal was obtained whilst temperature tuning the laser over a range outside methane absorption line. Large etalon fringes were observed in the fibre-coupled configuration corresponding to a cavity of approximately 13mm (Figure 12).

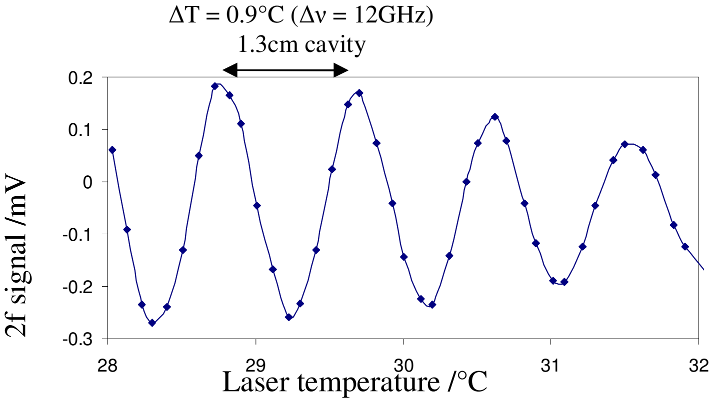

Figure 12: Etalon fringes measured in background signal due to the optical circulator. DC current = 65mA. PDA400 gain = 10dB, lock-in amplifier time constant = 100mS.

By observing the sensitivity of fringe pattern to touch and misalignment of the components in the optical path, it was noticed the fringes exhibited high sensitivity to disturbance (touch or heating) applied to the circulator. This could be taken to indicate that the circulator was the source of the etalon. However, the period of the fringes is comparable to the fringes generated in the DFB module. It is therefore difficult to establish without ambiguity whether the circulator is source of the fringes. Because of the sensitivity to alignment of the fibre coupling system for effective prevention of both optical feedback and Fabry-Perot etalon effects, it was decided the disadvantages of using the fibre system outweighed the advantages (mainly convenience of guiding the light to the detector). The fibre coupling system was therefore removed from the instrument.

.

Appendix E Herriot multipass optical cell

An excellent review of MOCs can be found else where in the literature[12]. Here, only a brief description of the operation and limitations of a Herriott cell is given.

The simplest form of a Herriott cell consists of two spherical mirrors separated by $d \leq 4f$, where f is the focal lengths of the mirrors (Figure 13).

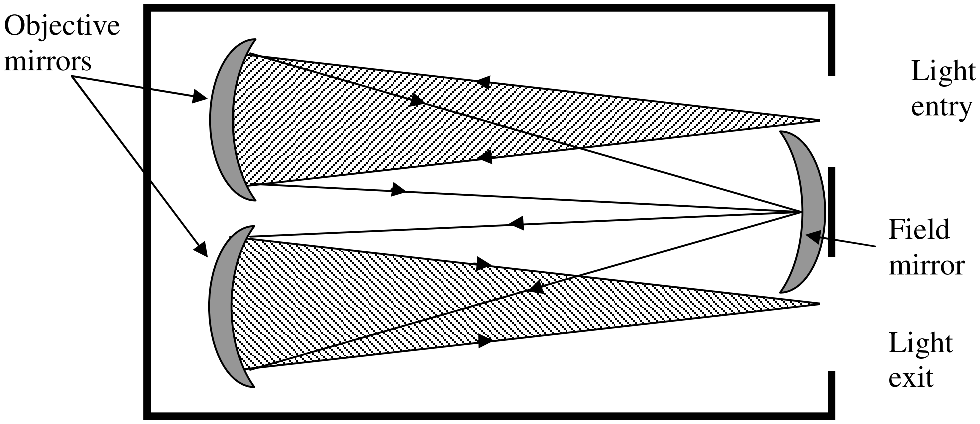

Figure 13: White optical system; basic set of four passes. After Sigrist[13].

A collimated laser beam is coupled into the system through a hole in one of the mirrors. “The beam is periodically reflected and refocused between the mirrors and then, after a designated number of passes N, exits through the input hole (corresponding exactly to the entry position of the input beam, defining the re-entrant condition) in a direction (slope) that is different from the entry slope. As a result, the total optical path traversed in the cell is approximately N × d”[14]. The pattern of reflected spots observed on the mirrors in these cells defines an ellipse. The number of passes is therefore limited by the number of spots one can fit on the circumference *C* of the ellipse without the spot adjacent to the output hole being clipped by or exiting that hole at a pass number less than N[14]. The maximum number of passes can be approximated by *C/*hole diameter[14]. The requirement of highly precise mirrors and complex alignment procedures in these types of MOCs has led to interest in the use of integrating spheres.

References

[1] Jin, W., Xu, Y. Z., Demokan, M. S., and Stewart, G. (1997), 'Investigation of interferometric noise in fiber-optic gas sensors with use of wavelength modulation spectroscopy', *Applied Optics*, V. 36, N. 28, pp. 7239-46.

[2] Tanaka, H., Matsuura, M., Tai, H. and Uehara, K. (inventors) Tokyo Gas Co, L.T.J., (Apr 13, 1993), *Gas detection device*. USA. 5202570.

[3] Johnstone, W. , Duffin, K., McGettrick, A., Stewart, G., Cheung, A., and Moodie, D. (2005), 'Tuneable diode laser spectroscopy over optical fibres for gas measurements in harsh Industrial environments', in Jaroszewicz, L. R. et al. *Optical Fibers: Applications,* V. 5952 International Society for Optical Engineering, United States, Warsaw, Poland, pp. 1-8.

[4] Jones, R. and Wykes, C. (1989), *Holographic and Speckle Interferometry* (2nd edition), Cambridge University Press, Cambridge, UK.

[5] Joenathan, C. (1991), 'Vibration fringes by phase stepping on an electronic speckle pattern interferometer: an analysis', *Applied Optics*, V. 30, N. 32, pp. 4658-65.

[6] Gorecki, C. (1994), 'Phase-correlation techniques for quasi real-time measurement of deformations with digital speckle interferometry', *Applied Optics*, V. 33, N. 14, pp. 2933-8.

[7] Sirohi, R. S. (2002), 'Speckle interferometry', *Contemporary Physics*, V. 43, N. 3, pp. 161-80.

[8] Schmitt, D. R. and Hunt, R. W. (1997), 'Optimization of fringe pattern calculation with direct correlations in speckle interferometry', *Applied Optics*, V. 36, N. 34, pp. 8848-57.

[9] Cloud, G. (1995), *Optical Methods of Engineering Analysis*, Cambridge University Press, New York.

[10] Bradley, C. C., Chen J., and Hulet , R. G. (1990), 'Instrumentation for the stable operation of laser diodes', *Review of scientific instruments* , V. 61, N. 8, pp. 2097-101.

[11] Ulrich, R. and Rashleigh, S. C. (1980), 'Beam-to-fiber coupling with low standing wave ratio', *Applied Optics*, V. 19, N. 14, pp. 2453-6.

[12] Robert, C. (2007) A simple, stable and compact multiple-reflection optical cell, for very long optical paths. *Applied Optics* (In Press)

[13] Hanst, P. L. H. S. T. (1994), 'Gas measurement in the fundamental infrared region', in Sigrist, M. W. *Air monitoring by spectroscopic techniques*, John Wiley and sons, New York, pp. 335-470.

[14] Silver, J. A. (2005), 'Simple dense-pattern optical multipass cells', *Applied Optics*, V. 44, N. 31, pp. 6545-56.